Design of Indoor Communication Infrastructure for Ultra-high Capacity Next Generation Wireless Services

George S. D. Gordon

Trinity College
University of Cambridge

A thesis submitted for the degree of
Doctor of Philosophy

May 30, 2013

Abstract

The proliferation of data hungry wireless devices, such as smart phones and intelligent sensing networks, is pushing modern wireless networks to their limits. A significant shortfall in the ability of networks to meet demand for data is imminent. This thesis addresses this problem through examining the design of distributed antenna systems (DAS) to support next generation high-speed wireless services that require high densities of access points and must support multiple-input multiple-output (MIMO) protocols.

First, it is shown that fibre links in DAS can be replaced with low-cost, broadband free-space optical links, termed radio over free-space optics (RoFSO) links. RoFSO links enable the implementation of very high density DAS without the need for prohibitively expensive cabling infrastructure. A 16m RoFSO link requiring only manual alignment is experimentally demonstrated to provide a spurious-free dynamic range (SFDR) of $> 100\text{dB/Hz}^{2/3}$ over a frequency range from 300MHz- 3.1GHz. The link is measured to have an 802.11g EVM dynamic range of 36dB. This is the first such demonstration of a low-cost broadband RoFSO system.

Following this, the linearity performance of RoFSO links is examined. Because of the high-loss nature of RoFSO links, the directly-modulated semiconductor lasers they use are susceptible to high-order nonlinear behaviour, which abruptly limits performance at high powers. Existing measures of dynamic range, such as SFDR, assume only third-order nonlinearity and so become inaccurate in the presence of dominant high-order effects. An alternative measure of dynamic range called dynamic-distortion-free dynamic range (DDFDR) is then proposed. For two different wireless services it is observed experimentally that on average the DDFDR upper limit predicts the EVM knee point to within 1dB, while the third-order SFDR predicts it to within 6dB. This is the first detailed analysis of high-order distortion effects in lossy analogue optical links and DDFDR is the first metric able to usefully quantify such behaviour.

Next, the combination of emerging MIMO wireless protocols with existing DAS is examined. It is demonstrated for the first time that for small numbers of MIMO streams (up to ~ 4), the capacity benefits of MIMO can be attained in existing DAS installations simply by sending the different MIMO spatial streams to spatially separated remote antenna units (RAU). This is in contrast to the prevailing paradigm of replicating each MIMO spatial stream at each RAU. Experimental results for two representative DAS layouts show that replicating spatial streams provides an increase of only $\sim$1% in the median channel capacity over merely distributing them. This compares to a 3-4% increase of both strategies over traditional non-DAS MIMO. This result is shown to hold in the multiple user case with 20 users accessing 3 base stations. It is concluded that existing DAS installations offer negligible capacity penalty for MIMO services for small numbers of spatial streams, including in multi-user MIMO scenarios.

Finally, the design of DAS to support emerging wireless protocols, such as 802.11ac, that have large numbers of MIMO streams (4-8) is considered. In such cases, capacity is best enhanced by sending multiple MIMO streams to single remote locations. This is achieved using a novel holographic *mode division multiplexing (MDM)* system, which sends each separate MIMO stream via a different propagation mode in a multimode fibre. Combined channel measurements over 2km of mode-multiplexed MMF and a typical indoor radio environment show in principle a 2×2 MIMO link providing capacities of 10bit/s/Hz over a bandwidth of 6GHz. Using a second experimental set-up it is shown that the system could feasibly support at least up to a 4×4 MIMO system over 2km of MMF with a condition number $\leq$15dB over a bandwidth of 3GHz, indicating a high degree of separability of the channels. Finally, it is shown experimentally that when a fibre contains sharp bends (radius between 20mm and 7.2mm) the first 6 mode-groups used for multiplexing exhibit no additional power loss or cross-coupling compared with unbent fibre, although mode-groups 7, 8 and 9 are more severely affected. This indicates that at least 6×6 multiplexing is possible in standard installations with tight fibre bends.

Design of Indoor Communication Infrastructure for Ultra-high Capacity Next Generation Wireless Services

George S. D. Gordon

Trinity College

University of Cambridge

A thesis submitted for the degree of

Doctor of Philosophy

May 30, 2013

To my fiancée, Sarah

Preface

This dissertation is the result of my own work and includes nothing which is the outcome of work done in collaboration except where specifically indicated in the text.

This dissertation contains 61,557 words and 99 figures, including appendices, bibliography, footnotes, tables and equations.

George Gordon

Acknowledgements

I owe much gratitude to my supervisor Prof. Ian White and my advisor Prof. Richard Penty for their helpful advice and guidance throughout my Ph.D. I would also particularly like to thank Dr. Michael Crisp for his unwavering support and assistance with countless experiments, particularly during the early years. For their financial support, I would like to thank the Rutherford Foundation of the Royal Society of New Zealand, the Cambridge Commonwealth Trust and the EPSRC.

I would like to thank Adrian Wonfor for his help in sourcing equipment and for sharing his immense experimental expertise. I would also like to thank Kun Zhu for his advice in conducting MIMO experiments and building the MIMO testing kit, as well as Dr. Jonathan Ingham for so attentively proof-reading the chapter on this work.

I am very grateful to Dr. Joel Carpenter and Dr. Timothy Wilkinson for being supportive of our collaboration on my most recent project using the mode-division multiplexing system built by Joel. Dr. Wilkinson welcomed and supported my contribution to his group's research and provided helpful feedback on the final chapter of this thesis. Joel has exhibited endless patience with my incessant questions and we have continued to collaborate very effectively from afar.

I am indebted to my family for their support during my many years of study. Finally, I would like to thank my fiancée Sarah, for her unwavering support and love, particularly in the final stages of writing.

Abstract

The proliferation of data hungry wireless devices, such as smart phones and intelligent sensing networks, is pushing modern wireless networks to their limits. A significant shortfall in the ability of networks to meet demand for data is imminent. This thesis addresses this problem through examining the design of distributed antenna systems (DAS) to support next generation high-speed wireless services that require high densities of access points and must support multiple-input multiple-output (MIMO) protocols.

First, it is shown that fibre links in DAS can be replaced with low-cost, broadband free-space optical links, termed radio over free-space optics (RoFSO) links. RoFSO links enable the implementation of very high density DAS without the need for prohibitively expensive cabling infrastructure. A 16m RoFSO link requiring only manual alignment is experimentally demonstrated to provide a spurious-free dynamic range (SFDR) of $> 100\text{dB/Hz}^{2/3}$ over a frequency range from 300MHz- 3.1GHz. The link is measured to have an 802.11g EVM dynamic range of 36dB. This is the first such demonstration of a low-cost broadband RoFSO system.

Following this, the linearity performance of RoFSO links is examined. Because of the high-loss nature of RoFSO links, the directly-modulated semiconductor lasers they use are susceptible to high-order nonlinear behaviour, which abruptly limits performance at high powers. Existing measures of dynamic range, such as SFDR, assume only third-order nonlinearity and so become inaccurate in the presence of dominant high-order effects. An alternative measure of dynamic range called dynamic-distortion-free dynamic range (DDFDR) is then proposed. For two different wireless services it is observed experimentally that on average the DDFDR upper limit predicts the EVM knee point to within 1dB, while the third-order SFDR predicts it to within 6dB. This is the first detailed analysis of high-order distortion effects in lossy analogue optical links and DDFDR is the first metric able to usefully quantify such behaviour.

Next, the combination of emerging MIMO wireless protocols with existing DAS is examined. It is demonstrated for the first time that for small numbers of MIMO streams (up to ~ 4), the capacity benefits of MIMO can be attained in existing DAS installations simply by sending the different MIMO spatial streams to spatially separated remote antenna units (RAU). This is in contrast to the prevailing paradigm of replicating each MIMO spatial stream at each RAU. Experimental results for two representative DAS layouts show that replicating spatial streams provides an increase of only $\sim$1% in the median channel capacity over merely distributing them. This compares to a 3-4% increase of both strategies over traditional non-DAS MIMO. This result is shown to hold in the multiple user case with 20 users accessing 3 base stations. It is concluded that existing DAS installations offer negligible capacity penalty for MIMO services for small numbers of spatial streams, including in multi-user MIMO scenarios.

Finally, the design of DAS to support emerging wireless protocols, such as 802.11ac, that have large numbers of MIMO streams (4-8) is considered. In such cases, capacity is best enhanced by sending multiple MIMO streams to single remote locations. This is achieved using a novel holographic *mode division multiplexing (MDM)* system, which sends each separate MIMO stream via a different propagation mode in a multimode fibre. Combined channel measurements over 2km of mode-multiplexed MMF and a typical indoor radio environment show in principle a 2×2 MIMO link providing capacities of 10bit/s/Hz over a bandwidth of 6GHz. Using a second experimental set-up it is shown that the system could feasibly support at least up to a 4×4 MIMO system over 2km of MMF with a condition number $\leq$15dB over a bandwidth of 3GHz, indicating a high degree of separability of the channels. Finally, it is shown experimentally that when a fibre contains sharp bends (radius between 20mm and 7.2mm) the first 6 mode-groups used for multiplexing exhibit no additional power loss or cross-coupling compared with unbent fibre, although mode-groups 7, 8 and 9 are more severely affected. This indicates that at least 6×6 multiplexing is possible in standard installations with tight fibre bends.

Publications

G. S. D. Gordon, M. J. Crisp, R. V. Penty, and I. H. White, "Effects of High-Order Laser Distortion Products in Radio over Free-Space Optical Links," in *Conference on Lasers and Electro-Optics*, 2011, Baltimore.

G. S. D. Gordon, M. J. Crisp, R. V. Penty, and I. H. White, "High-Order Distortion in Directly Modulated Semiconductor Lasers in High-Loss Analogue Optical Links with Large RF Dynamic Range", *IEEE/OSA Journal of Lightwave Technology*, 2011.

G. S. D. Gordon, J. Carpenter, M. J. Crisp, T. D. Wilkinson, R. V. Penty and I. H. White, "Demonstration of Radio-over- Fibre Transmission of Broadband MIMO over Multimode Fibre using Mode Division Multiplexing", in *European Conference on Optical Communications*, 2012, Amsterdam.

G. S. D. Gordon, M. J. Crisp, R. V. Penty and I. H. White, "Experimental Evaluation of Layout Designs for 3×3 MIMO- Enabled Radio-over-Fibre Distributed Antenna Systems", *IEEE Transactions on Vehicular Technology*, 2013.

K. Shi, **G. S. D. Gordon**, M. Paskov, J. Carpenter, T. Wilkinson and B. Thomsen, "Degenerate Mode-Group Division Multiplexing using MIMO Digital Signal Processing" in *IEEE Photonics Society Summer Topical Meetings*, July 2013, Waikoloa.

G. S. D. Gordon, M. J. Crisp, R. V. Penty and I. H. White, "Experimental Investigation of Antenna Selection and Transmit Beamforming for Capacity Enhancement in 3×3 MIMO-enabled Radio-over-Fiber DAS" [Accepted for publication at *2013 IEEE International Topical Meeting on Microwave Photonics (MWP)*].

Contents

List of Figures **xi**

List of Tables **xvii**

List of Acronyms **xix**

1 Introduction **1**

1.1 Modern wireless communication 1

1.1.1 The wireless revolution 1

1.1.2 Principles of wireless 4

1.1.3 Wireless protocols 6

1.2 Improving indoor wireless performance 8

1.2.1 Repeaters 8

1.2.2 Small cells 9

1.2.3 Distributed antenna systems 10

1.2.4 Other methods 13

1.3 Distributing analogue radio signals 14

1.3.1 Coaxial cable 14

1.3.2 Radio over Fibre 14

1.3.3 Radio over Free-Space Optics 18

1.3.4 Comparison of methods 22

1.4 Increasing backhaul capacity 22

1.4.1 Optical fibres 23

1.4.2 Mode-division multiplexing 27

1.5 Infrastructure for next generation wireless protocols 29

1.6 Overview of thesis 31

2 Radio over Free-Space Optical Links 33

2.1 Introduction 34

2.2 RoFSO System Description and Setup 35

2.3 Link budget modelling 36

2.3.1 Gain 36

2.3.2 Noise 40

2.3.3 Nonlinearity 43

2.3.4 Dynamic Range 47

2.3.5 Spreadsheet model 50

2.4 Experimental Link 52

2.4.1 Fibre testing 52

2.4.2 Free-space testing 61

2.5 Conclusions 71

3 High-Order Distortion in Directly-Modulated Semiconductor Lasers in High-Loss Analogue Optical Links 75

3.1 Introduction 76

3.2 High-RF-power high-loss optical links 77

3.2.1 Free-Space Optical Links 77

3.3 Theory of nonlinear behaviour in lasers 80

3.3.1 Causes of nonlinearity 80

3.3.2 Effects on third-order SFDR 83

3.4 Experimental investigation 87

3.4.1 Setup 87

3.4.2 High-Order Dynamic Distortion 88

3.4.3 DDFDR Performance 91

3.5 Conclusion 93

4 Evaluation of Layout Designs for 3×3 MIMO-Enabled Radio-over-Fibre Distributed Antenna Systems 95

4.1 Introduction 96

4.2 Theory of MIMO wireless systems 98

4.2.1 Single-user MIMO systems 98

4.2.2 Multi-user MIMO systems 103

4.3 Simulated comparison of $N \times N$ DAS layouts 104

4.4 Experimental set-up . . . 107
4.4.1 Layout comparison tests . . . 107
4.4.2 Tri-polarised antennas . . . 110
4.5 Single user results . . . 111
4.5.1 Capacity . . . 111
4.5.2 Throughput . . . 116
4.5.3 Effects of antenna polarisation . . . 117
4.6 Multiple user results . . . 121
4.6.1 Single base station . . . 121
4.6.2 Multiple base stations . . . 121
4.7 Conclusions . . . 123

5 Broadband Radio-over-Fibre Transmission of Wireless MIMO using Mode-Division Multiplexing 127
5.1 Introduction . . . 128
5.2 Theory . . . 129
5.2.1 Mode division multiplexing . . . 129
5.2.2 Fibre dependent effects . . . 133
5.2.3 Holographic excitation of modes . . . 134
5.3 Experimental set-up . . . 137
5.3.1 2×2 MIMO set-up . . . 137
5.3.2 Higher order MIMO set-up . . . 140
5.3.3 Fibre bend radius test setup . . . 143
5.4 Results . . . 144
5.4.1 2×2 MIMO . . . 144
5.4.2 Higher-order MIMO . . . 145
5.4.3 Effects of fibre bend radius . . . 150
5.5 Conclusions . . . 158

6 Conclusions and Future Work 159
6.1 Overall Conclusions . . . 159
6.1.1 Radio over Free-Space Optical Links . . . 160
6.1.2 High Order Distortion in RoFSO links . . . 160
6.1.3 Layout Designs for MIMO-enabled DAS . . . 161
6.1.4 Broadband MIMO-enabled RoF systems using Mode-Division Multiplexing 162
6.2 Areas of Future Research . . . 163

References **169**

List of Figures

1.1 Graph showing the annual increase in the number of mobile subscriptions, wireless internet capable devices and RFID tags. 2
1.2 Predicted shortfall in network capacity for a 3G mobile network operator. 3
1.3 How destructive multipath interference can create dead zones where there is little or no signal. 5
1.4 Some common indoor wireless services and their radio frequencies. 7
1.5 Graph showing the drop-off in spectral efficiency of emerging wireless services. . 8
1.6 Block diagram of a radio repeater for improving wireless coverage. 9
1.7 Illustration of how a combination of small and large cells can be used to provide improved wireless coverage in a building. 11
1.8 Comparison of: (a) traditional collocated antenna system and (b) distributed antenna system. 12
1.9 Schematic of a generic radio over fibre system. 15
1.10 Intensity modulating a laser using (a) direct modulation and (b) external modulation 16
1.11 Typical commercial digital FSO transceivers 19
1.12 Illustration of the trade-off between beam divergence, power loss and ease of alignment in a FSO link. 20
1.13 Schematic of a generic RoFSO system. 21
1.14 Tracking system used for the transmitter/receiver of the RoFSO system. 22
1.15 Graph showing measured and predicted increase in backhaul demand per cellular site accumulated from several 3G/LTE operators 24
1.16 Refractive index profiles for different types of industry standard fibre. Also shown is the ray optics approximation of how light propagates in such fibres. 25

1.17 Graph showing percentage of installed fibre base in buildings by type of fibre. . . 26
1.18 Graph showing the increase of record capacities for single-fibre communication systems as a function of year. 26
1.19 Cross-sectional profiles of the three lowest order square Hermite-Gaussian modes that can be used for selective mode excitation in MMF. 28
1.20 Schematic of a mode-multiplexer for 6 modes launched into few-mode fibre. . . . 28
1.21 Example layouts for MIMO DAS with K RAUs supporting two base stations each with 3 spatial channels. 30

2.1 Schematic diagram of the proposed RoFSO system showing both the uplink and downlink. 35
2.2 Flow chart showing equations used to model gain and noise for the full RoFSO link. 37
2.3 Gaussian profile beam converging to a beam waist. 38
2.4 Schematic showing modelled noise sources in optical link. 41
2.5 Measured light vs. current curve for a typical 1310nm laser diode showing the linear and nonlinear regions of operation. 44
2.6 Power spectrum and input power vs. output power graphs showing third-order only IMD products. 46
2.7 Illustration of the standard two-tone test to determine the SFDR showing how the IMD products are formed. 47
2.8 Graph of input power vs. output power for a system showing a geometric representation of third-order only SFDR. 48
2.9 Illustration of the constellation diagram for a complex modulation scheme. 49
2.10 Example graph of EVM vs. received signal power for 802.11g showing a typical EVM curve shape and the dynamic range. 51
2.11 Sample screenshot of uplink RoFSO link budget spreadsheet showing device parameters and cascading of noise and gain. 51
2.12 Graph showing simulated graph of third-order SFDR vs. optical loss for 1550nm laser. 52
2.13 Experimental set-up used to verify and test RoFSO uplink in fibre. 55
2.14 Graph of measured noise vs. optical attenuation for RoFSO link. 56
2.15 Graph of output power vs. input power for a two-tone test of the 1310nm link showing higher order distortion for 15.6dBo optical attenuation. 57

2.16 Graph of third-order SFDR vs. optical attenuation for (a) 1547nm link at 868MHz with 10dBm CW output and (b) 1310nm link at 2.4GHz with 10dBm CW output using the estimated lower bound of third-order SFDR. 58
2.17 802.11g EVM curves at 2.4GHz with different optical attenuations for (a) 1547nm link and (b) 1310nm link. 60
2.18 802.11g EVM dynamic range vs. optical attenuation at 2.4GHz for (a) 1547nm link and (a) 1310nm link. 61
2.19 Experimental set-up for free-space testing of the RoFSO uplink at 1310nm. . . . 62
2.20 Illustration of matching of numerical apertures (NA). 63
2.21 Photograph of experimental set-up of RoFSO system. 64
2.22 Illustration of how angular misalignment at the receiver causes power loss. 65
2.23 Illustration of field of view. 66
2.24 Illustration of how a drop of index matching gel prevents reflections back into the fibre. 68
2.25 Comparison of two different methods of reducing fibre-air coupling reflections. . . 68
2.26 Cross-sectional profile of laser beam at 16m from the transmitter. 70
2.27 Graph showing third-order SFDR vs. frequency for RoFSO link of length 16m. . 71
2.28 Graph showing 802.11g EVM of a 16m RoFSO link. 72

3.1 Graph showing output power and EVM vs. peak RF input power for a demonstration RoFSO uplink. 79
3.2 Simulation results illustrating different types of distortion. 82
3.3 Graph showing how power of harmonics varies as peak input power (or equivalently OMI) is increased for a single-tone input. 83
3.4 Graph of output power vs. peak input power for a two-tone input with tones at 950MHz and 1.05GHz. 84
3.5 Graph showing received electrical output power vs. input power of a single tone for a two-tone test illustrating the inaccuracies of conventional SFDR and highlighting the improvement offered by use of DDFDR. 86
3.6 Experimental set-up used for testing of RoF link. 88
3.7 Graph showing output power vs. peak input power for a two-tone SFDR test with the 1310nm Sumitomo SLV521A DFB. 89
3.8 Graph showing high-order IMD products at output of test link under a two-tone test. 90
3.9 Measured graph of light power vs. time showing turn-on delay, τ_d, followed by relaxation oscillations, both hallmarks of dynamic distortion. 90

3.10 Graph showing output power vs. input power for two-tone SFDR test with two different lasers. 92
3.11 Graph showing comparison of two-tone SFDR power curve and EVM curves for several modulation schemes at 2.4GHz. 93

4.1 Layout of two theoretical MIMO DAS scenarios: a) 4×4 system with replication $R = 1$ and b) 4×4 system with replication $R = 4$ 105
4.2 Graph showing the SNR gain for an $N \times N$ MIMO DAS with replication $R = N$ as N is increased. 106
4.3 Experimental set-up of 3×3 MIMO channel measurement system. 109
4.4 Experimental set-up of 3×3 MIMO 802.11n throughput testing system. 109
4.5 Test propagation environments showing location of transmit antennas and receiver test points. 110
4.6 Tested propagation environments showing location of transmit antennas and receiver test points for examing the effect of tri-polarised antennas. 111
4.7 Ergodic channel capacity, as calculated from channel measurements, plotted as a function of transmit power relative to the receiver noise floor. This represents an average of measurements taken across many fading scenarios and measurement locations in the LOS propagation scenario. 112
4.8 CDF of aggregate network capacity for a single user for two propagation scenarios: (a) LOS case and (b) NLOS case. 114
4.9 CDF of condition number for a single user with in two scenarios: (a) LOS case and (b) NLOS case 115
4.10 CDF showing improvement in throughput of using MIMO DAS with 3×3 802.11n compared with CAS 117
4.11 Graph showing the jitter, i.e. the standard deviation of packet arrival times, for 802.11n throughput testing using 3×3 MIMO DAS with $R = 1$ and 3×3 MIMO CAS. 118
4.12 Ergodic channel capacity, as calculated from channel measurements, plotted as a function of transmit power relative to the receiver noise floor comparing different antenna polarisation configurations. 119
4.13 CDF of channel capacity for a single user showing the effect of single and tri-polarised antenna configurations in MIMO DAS and CAS systems. 120
4.14 CDF of condition number for a single user showing the effect of single and tri-polarised antenna configurations in MIMO DAS and CAS systems. 120

4.15 CDF of aggregate network capacity comparing capacity for a single base station with multiple base stations in the LOS scenario for two cases: (a) collocated antenna system and (b) distributed antenna system. 122
4.16 CDF of aggregate network capacity for multiple users with multiple base stations for two scenarios: (a) LOS and (b) NLOS. 124

5.1 Illustration of multiple fibre solution for implementing MIMO DAS for: (a) a non-MIMO DAS and (b) an 8×8 MIMO DAS. 129
5.2 Cross-sectional intensity profiles of possible LP propagation modes for a multimode fibre with a parabolic refractive index profile. 131
5.3 Illustration of far-field or replay-field patterns produced by various binary-phase holograms. 136
5.4 (a) Experimental set-up of 2×2 MIMO RF system (b) DAS RF test environment showing test points. 138
5.5 Set-up of mode division multiplexing system. 139
5.6 Set-up of advanced mode division multiplexing system with mode selective output. 141
5.7 Graphical representation of an ideal mode transfer matrix with no mixing between mode groups. 142
5.8 Illustration of how LP modes are aggregated to form a mode-group transfer matrix. 143
5.9 Graph showing coupling between multiplexed modes at the output of the fibre vs frequency. 145
5.10 Graph showing channel capacity of the 2×2 MIMO system detailed in figures 5.4 and 5.5 vs frequency. 146
5.11 Graph depicting the mode transfer matrix for a 1m MMF patch cord. 146
5.12 Graph depicting the mode transfer matrix for 2km of OM2 MMF. Because of the longer length it is seen that there is now substantial coupling between mode groups. 147
5.13 Graph showing the magnitudes of the mode-group coupling coefficients vs. frequency for a 3×3 mode-group division multiplexing system using mode-groups 1, 2 and 3. 148
5.14 Graph showing the magnitudes of the mode-group coupling coefficients vs. frequency for a 5×5 mode-group division multiplexing system using mode-groups 1, 2, 3, 4 and 5. 149
5.15 Graph showing the condition number of particular submatrices of the mode-group transfer matrix as the number of MIMO channels is increased. 150
5.16 Mode-group transfer matrix of the unbent 10m OM3 patchcord used for bend radius testing. 151

5.17 Total received power aggregated across all mode groups for different launched mode groups as fibre curvature is increased. 152
5.18 Total power received in mode-groups 1-6 when mode-groups 7-9 are excited as fibre curvature is increased. 153
5.19 Ratio of power received in the same mode-group that is launched to power received in other mode-groups as fibre curvature is increased. 154
5.20 Histograms of the absolute value of the polarisation angles across all received modes for different transmitted mode-groups and fibre bend radii. 156
5.21 Standard deviation of received polarisation angles as fibre curvature is increased. Solid lines indicate trends. 157

6.1 Illustration of the proposed principle for the new MDM system transmitter module. 165
6.2 Illustration of the conversion of a conventional plane wave light beam to a twisted ‘corkscrew’ or helicoidal beam using a spatial light modulator (SLM). 166

List of Tables

1.1 Performance comparison of coaxial cable, RoF using multimode optical fibre and RoFSO as DAS signal distribution mechanisms. 23

2.1 Common estimated third-order SFDR requirements for wireless services. 49
2.2 Parameters for the link budget simulation of third-order SFDR using 1550nm laser. 53
2.3 Parameters for the experiment using two different lasers 55
2.4 Parameters for the 1310nm free-space experiment 63

3.1 Parameters for experimental set-up 88
3.2 Offsets of third-order SFDR and DDFDR upper limits from EVM knee points . . 92

4.1 Parameters of throughput testing setup 110

5.1 Radii of dowel used for testing fibre under different bend conditions. 144

List of Acronyms

10GbE	10 gigabit Ethernet
3G	third generation mobile
4G/LTE	fourth generation long term evolution mobile
ACG	automatic gain control
AWGN	additive white Gaussian noise
BPSK	binary phase-shift keying
CAS	collocated antenna system
CATV	cable television
CDF	cumulative probability distribution function
CSI	channel state information
CWDM	coarse wavelength division multiplexing
CW	continuous wave
DAS	distributed antenna system
DDFDR	dynamic distortion-free dynamic range
DMD	digital micromirror device
DPC	dirty paper coding
EDFA	Erbium-doped fibre amplifier
EVM	error vector magnitude
FMF	few-mode fibre
FOV	field of view
HCS	hard-clad silica fibre
IIP3	third-order input intercept point
IM-DD	intensity modulation and direct detection
IMD	intermodulation distortion
ITU	International Telecommunication Union

LIST OF ACRONYMS

LCOS	liquid crystal on silicon
LOS	line-of-sight
LSAS	large scale antenna system
MCS	modulation and coding scheme
MDM	mode-division multiplexing
MIMO	multiple-input multiple-output
MMF	multi-mode fibre
MMSE	minimum mean square error
MRC	maximal ratio combining
NA	numerical aperture
NLOS	non line-of-sight
OFDM	orthogonal frequency division multiplexing
PAPR	peak-to-average power ratio
PBS	polarising beam splitter
PDF	probability density function
PDV	packet delay variance (or jitter)
POF	plastic or polymer optical fibre
QAM	quadrature amplitude modulation
QPSK	quadrature phase-shift keying
RAU	remote antenna unit
RFID	radio frequency identification
RIN	relative intensity noise
RoFSO	radio over free-space optics
RoF	Radio over Fibre
SCM	sub-carrier multiplexing
SDH	synchronous digital hierarchy
SDM	space-division multiplexing
SFDR	spurious-free dynamic range
SIC	successive interference cancellation
SISO	single-input single-output
SLM	spatial light modulator
*SmC**	chiral smectic C phase liquid crystal
SMF	single-mode fibre
SM	spatial multiplexing
SNR	signal-to-noise ratio
TCP	transmission control protocol

TDM	time division multiplexing
TEC	thermoelectric cooler
TIA	transimpedance amplifier
UDP	user datagram protocol
VCSEL	vertical-cavity surface-emitting laser
WDM	wavelength division multiplexing
WLAN	wireless local area network
ZF	zero forcing

Chapter 1

Introduction

1.1 Modern wireless communication

1.1.1 The wireless revolution

Telecommunication has revolutionised the modern world and continues to impact our lives in a multitude of new ways. Wireless communication in particular is experiencing phenomenal growth. Currently there are over 5.9 billion mobile subscriptions worldwide [1]. Additionally, it is estimated that there are over 1.5 billion wireless internet (WLAN) capable devices worldwide [2]. Increasingly, everyday items are gaining wireless capability leading to the creation of an intelligent *internet of things*, in which huge amounts of data about the world around is collected wirelessly and processed in real time [3]. This has been greatly facilitated by the increasingly ubiquitous use of *radio frequency identification (RFID)* tags to wirelessly track all manner of things. In 2009 alone over 2.4 billion RFID tags were produced [4]. The growth in the use of mobile devices, wireless internet devices and RFID tags is summarised in Figure 1.1.

The increasing size of this global network of wireless devices of varying degrees of complexity has far-reaching implications. If analysed effectively and quickly, the huge amounts of data produced by this network could create an unparalleled opportunity to create a more intelligent and efficient world. This concept of gaining important new insights through analysis of large amounts of data, termed *big data*, has recently gained much attention as an area of key importance in the next few years and already the industry is already estimated to be worth US$100 billion [5].

An example application where analysis of real-time data from wireless capable devices will have a major role to play is in the implementation of smart grids. Household appliances, switch

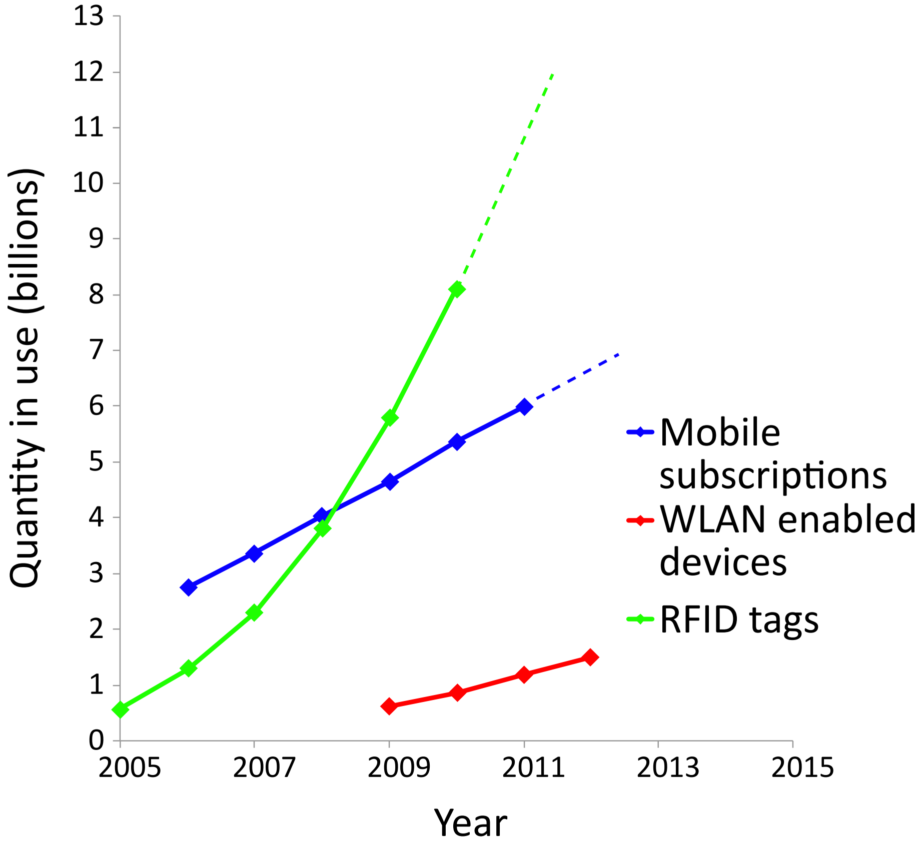

Figure 1.1: Graph showing the annual increase in the number of mobile subscriptions, wireless internet capable devices and RFID tags [1, 2, 4].

boards, solar panels and electricity meters could all be controlled wirelessly with the aim of creating a much more efficient energy supply system [6]. This increasing demand for and reliance upon wireless services translates into huge commercial value and in 2011 revenue from mobile data services totalled over US$310 billion [7].

Coupled with this increase in the number of wireless device is a significant increase in demand for data from these devices. It is predicted that mobile data usage will increase 18 fold from 2011 to 2016 [8]. Growth in mobile video traffic is largely responsible for this increase and it is estimated that by 2014 video will make up over 66% of all mobile traffic [9]. As mobile users become more reliant on wireless services there is a corresponding increase in expectations of their performance. New generations of users expect to be able to stream high quality videos to mobile devices anywhere, any time.

One of the greatest problems faced in the field of telecommunications is how to keep pace with this exploding demand. The US Federal Communications Commission has predicted that soon wireless networks will fall well short of being able to deliver the data speeds demanded by users, in what they have termed a looming "spectrum crisis" [10]. In fact, mobile operators have estimated that by 2014 there will be a 97% shortfall in capacity for wireless networks, as illustrated in Figure 1.2. This problem is of particular concern in buildings, where 80-90% of mobile data traffic originates [11]. Addressing this problem for indoor environments would then go a long way towards bridging this shortfall in capacity.

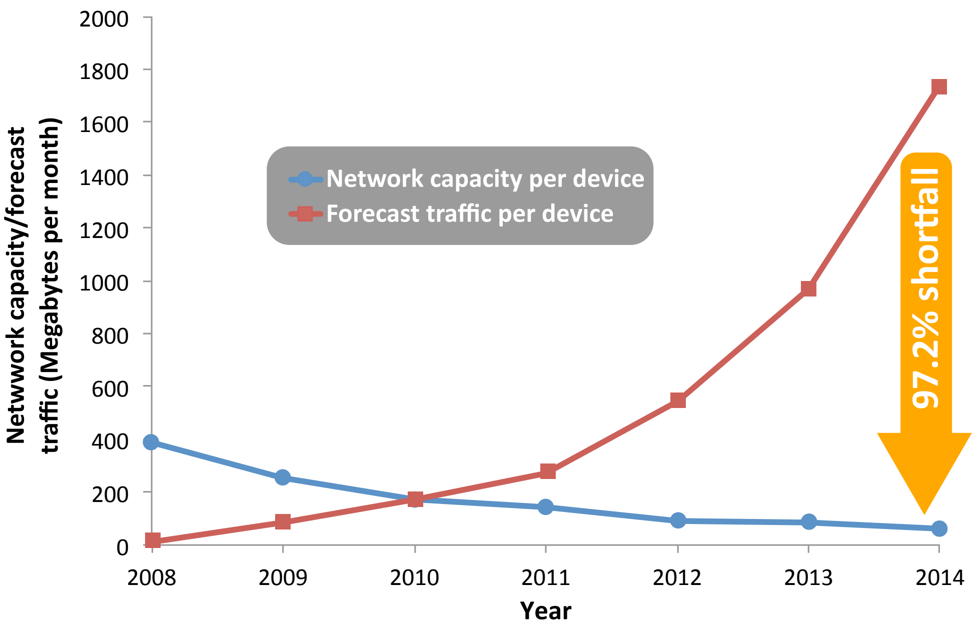

Figure 1.2: Predicted shortfall in network capacity for a 3G mobile network operator [12].

1.1.2 Principles of wireless

The most accurate model for predicting the behaviour of electromagnetic phenomena is that of quantum electrodynamics. However, for behaviour over macroscopic distances using large number of photons, such as in wireless systems, Maxwell's equations provide extremely accurate descriptions of propagation of electromagnetic radiation as waves. In the simplest possible case when radiation is transferred from a single transmitting antenna to a single receiving antenna via only one direct line of sight path, this wave model produces a simple relationship between power transmitted and received, termed the *Friis transmission equation* [13]:

$$\frac{P_r}{P_t} = G_r G_t \left(\frac{\lambda}{4\pi R} \right)^2 \tag{1.1}$$

where P_r and P_t are the received and transmit power respectively, G_r and G_t are the gains of the receive and transmit antenna respectively relative to an isotropic radiator, λ is the free-space wavelength and R is the distance between the antennas. It is worth noting that the power transferred is dependent on the square of the wavelength, or equivalently the inverse square of the frequency. This is because of the reduction in effective aperture of the antennas - in order to maximise received/transmitted power the antenna must have dimensions comparable to the wavelength. A result of this is that in systems with single transmit and receive antennas, small wavelengths require smaller antennas and hence power is only collected over a small area. This can, of course, be counteracted by using arrays of small antennas so that the total power-collecting area is increased.

The Friis equation is for an ideal case where there is only a single direct line-of-sight path between transmit and receive antennas. In reality radio waves bounce off objects as they propagate and arrive at the receiver via many different paths, an effect termed *multipath interference*. In the worst case, the two paths can differ in length such that the two received signals are completely out of phase and cancel each other out as illustrated in Figure 1.3. The resultant random variation in power is called *fading*. This destructive interference of signals creates *dead zones*, where no signal can be detected. Because the phase difference between two propagation paths is a function of frequency, different wireless services will create dead zones at different places in a building. These dead zones are unpredictable and unavoidable due to the complex nature of the wireless environment. This is a key factor limiting the coverage quality and hence limiting the performance of indoor wireless systems [14, 15].

Fading is a function of the exact propagation environment and all the reflective objects contained within it. This is unpredictable and so fading is modelled statistically at the receive antenna using Gaussian distributed in-phase and quadrature components for the received fields, or equivalently a Rician distribution for the received power, which simplifies to a Rayleigh distribution if the direct line-of-sight propagation is negligible.

Due to the complexity of developing such fading models for indoor environments, empirical formulas are used to determine approximate mean power levels. The most common of these is the International Telecommunication Union (ITU) Model for Indoor Attenuation [16]:

$$L_{total} = 20 \log_{10} f + N \log_{10} d + L_f(n) - 28 \quad \text{dB} \tag{1.2}$$

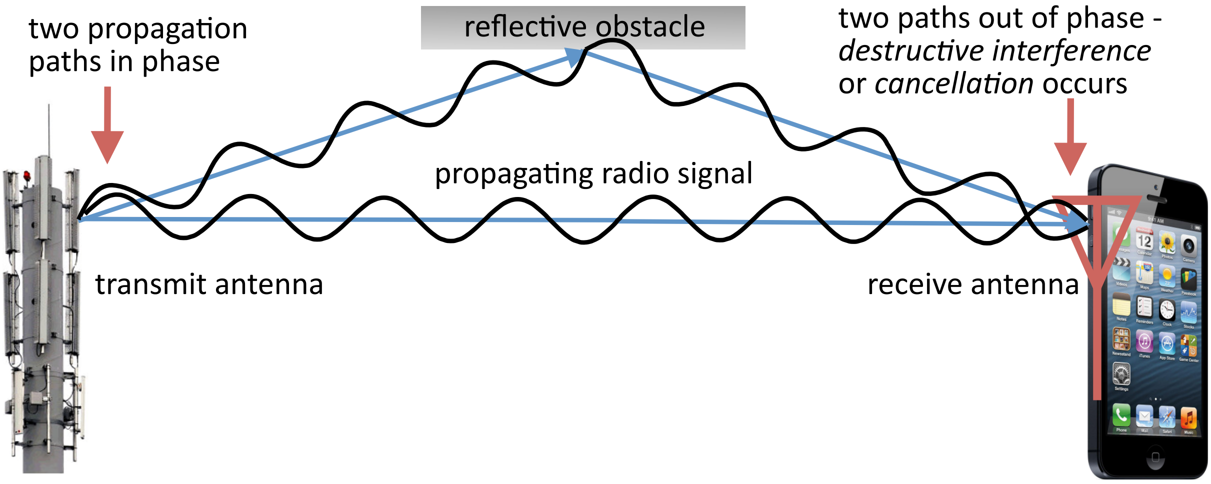

Figure 1.3: How destructive multipath interference can create dead zones where there is little or no signal.

where L_{total} is the total path loss in dB, f is the frequency, N is the power loss coefficient, d is the propagation distance, L_f is the floor penetration loss factor and n is the number of floors between the transmitter and receiver. It should be noted that because of multipath reflections and absorptions, the loss now increases with the $N/10^{th}$ power of distance. For the Friis model, $N = 20$ producing an inverse square law but in real office or residential environments N is typically measured to be between 28 and 30, giving a much greater power loss with distance.

Combining both these effects, in a typical indoor environment it is then expected that there are dead zones due to multipath fading, and that the average received power is significantly lower everywhere due to increased loss with distance. Equivalently stated, the wireless *coverage* inside buildings is expected to be poor compared with outdoor environments with fewer obstacles. Furthermore, the propagation loss increases with the square of frequency and so for emerging services using higher frequencies the coverage is expected to be further reduced [17], although it is worth noting that due to the recent reallocation of analogue television spectrum some new services (for example some implementations of 4G cellular) actually make use of lower frequency spectrum than their predecessors.

A result of reduced power due to poor coverage is that the *signal-to-noise ratio (SNR)* is significantly reduced in much of the building. According to the noisy channel coding theorem proved by Shannon, it is possible to derive a theoretical maximum rate at which a given communication channel can operate with arbitrarily low probability of error [18]. Using a simple approximation of a continuous-time analogue *single-input single-output (SISO)* wireless communication channel, under the assumptions that the channel is linear, has bounded signal power, S, is stationary (i.e., has time-invariant statistical properties), and the noise present on the channel is *additive white Gaussian noise (AWGN)* of known variance (or noise power), this maximum rate can be expressed neatly by the Shannon-Hartley theorem:

$$C = B \log_2 \left(1 + \frac{S}{N}\right) \tag{1.3}$$

where C is the maximum channel capacity in bit/s, B is the bandwidth of the channel in Hertz, S is the signal power in Watts, and N is the noise power of the channel in Watts. It can be seen that the maximum capacity of this channel is directly linked to SNR. Clearly then coverage is linked to the data rates available to users of a wireless network

To date the main challenge in indoor wireless has been *coverage*, i.e., trying to improve the SNR everywhere in an area. However, with increasing demand for data from users the focus has shifted to ways in which the *capacity* of wireless networks can be drastically increased for large numbers of users. Because the total signal power per radio transceiver (or *base station*) must be fixed due to interference requirements (and increasingly energy usage requirements), this demand for capacity cannot be met by increased SNR alone. Further, each base station only has a limited bandwidth allocation that must be divided between all the users attached to it. If all the users are using their maximum allocated power and bandwidth resources, the base station becomes a bottleneck. The only solution to adding capacity for large numbers of users is to introduce more base stations. There are several ways of doing this that are discussed in this thesis and there are many issues related to the implementation of such systems also discussed here. In short, wireless networks of the future must deliver both coverage and capacity - that is, large numbers of users should all be able to have high-speed connections simultaneously everywhere in a building.

The commercial importance of addressing this problem is huge and as a result it is predicted that revenue from the deployment of in-building wireless systems will grow to more than US$15 billion in 2013, up from US$3.8 billion in 2007 [19].

1.1.3 Wireless protocols

In addition to the increasing numbers of wireless users there is also an increasing range of wireless services available to these users. Figure 1.4 shows some of the wireless services commonly used indoors and the frequency bands they occupy.

Some of these protocols may not be used directly by users, such as RFID and ZigBee, but will play a crucial role in implementing new large scale intelligent networks such as the smart grid or the Internet of Things. The protocols that will experience the highest increase in demand directly from users are those used for mobile devices and wireless internet, namely 4G/LTE and 802.11n/ac protocols.

Recently there have been many improvements in wireless protocols that have enabled higher access speeds. This is evidenced, for example, by the shift from 3G to 4G mobile services that has brought a 7-fold increase in available wireless capacity [21]. Because available bandwidth in the RF spectrum is very limited and is heavily regulated these protocols aim to maximise data rates per unit bandwidth, a quantity known as *spectral efficiency.* Over the past several years there have been many different techniques adopted to improve spectral efficiency. In 3G systems spectrum spreading techniques such as code-division multiple access (CDMA) were used to enable improved efficiency when sharing between users. Spread-spectrum techniques have now largely been superseded by frequency techniques such as orthogonal frequency division

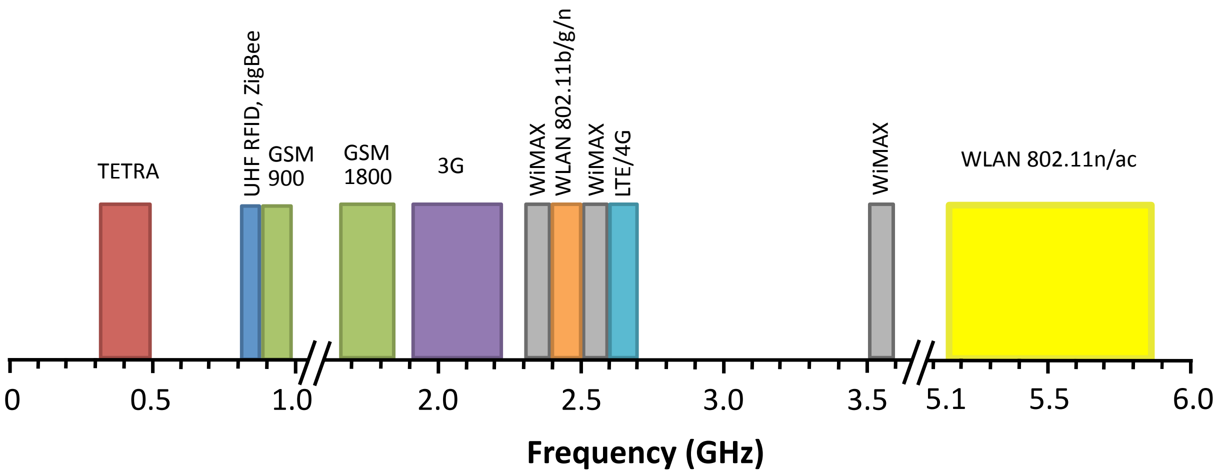

Figure 1.4: Some common indoor wireless services and their radio frequencies [20].

multiplexing (OFDM), which splits the available spectrum into small chunks to create many parallel communication channels. Each of these can transmit with different coding schemes depending on the SNR in it, thus making optimum use of the available spectrum.

More recently *space-division multiplexing (SDM)* has gained widespread adoption in emerging wireless services such as 4G mobile and 802.11n wireless-LAN. SDM relies on using multiple transmit and multiple receive antennas to create multiple communication channels and so in wireless applications is often termed *multiple-input multiple-output (MIMO)* communication.

MIMO works by sending independent streams of data, called *spatial streams*, from different elements of an M element array of transmit antennas to an N element array of receive antennas. This is termed an $M \times N$ MIMO system. Such systems enable simultaneous transmission of multiple data streams without using extra bandwidth or transmit power, hence greatly increasing the spectral efficiency and available data rate [22]. MIMO is presently being adopted in both wireless LAN (IEEE 802.11n) and mobile (LTE/4G) standards, which allow up for to 4×4 MIMO though only 2×2 and 3×3 systems are commercially available at the time of writing. Standards for future 8×8 MIMO are currently under development, for example IEEE 802.11ac [23]. MIMO wireless theory is discussed in more detail in Chapter 4.

However, as each of these new protocol improvements has been introduced and deployed the gains in spectral efficiency have begun to level off, as evidenced in Figure 1.5. This suggests that wireless protocols are approaching their theoretical upper capacity limits, defined by the Shannon-Hartley theorem, and as a result it is becoming increasingly difficult to obtain higher data rates in the same bandwidth and using the same power levels. This cannot be addressed simply by using more bandwidth as the radio spectrum is a very scarce resource that is tightly regulated, although emerging techniques such as cognitive radio are able to use intelligent sensing algorithms to make optimal use of available unlicensed spectrum as mentioned in Section 1.2.4. Similarly, the power cannot simply be increased as this would cause interference with neighbouring wireless systems reducing their performance.

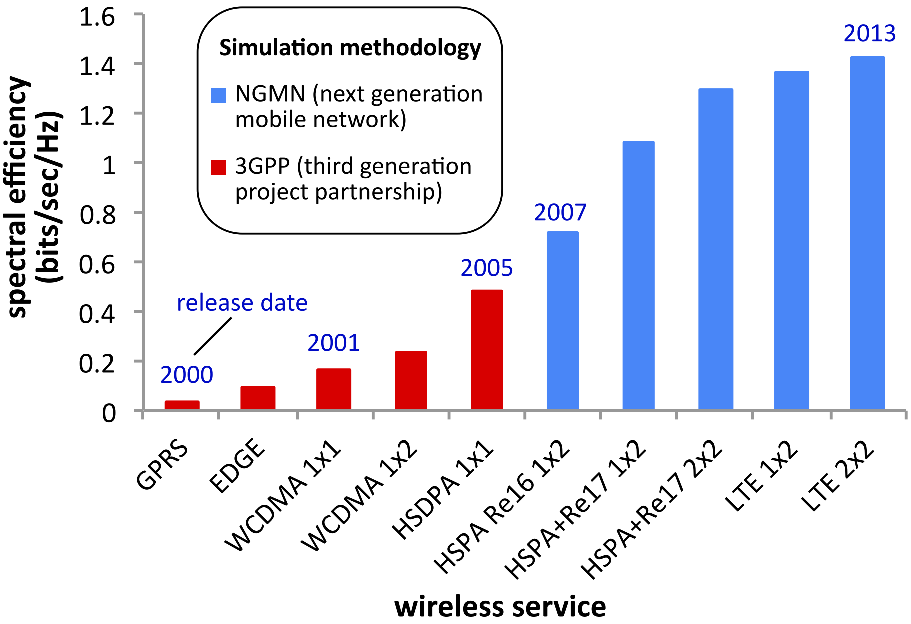

Figure 1.5: Graph showing the drop-off in spectral efficiency of emerging wireless services [24].

Consequently, to bridge this shortfall in wireless capacity it is necessary to consider radical new designs of the wireless distribution infrastructure. At a minimum it is necessary to design an infrastructure that enables the creation of ultra-dense networks of sources of wireless signals so that users are never far from a wireless signal source and each source need serve only a few users. This means each user will have a high SNR and will have to share bandwidth with as few other users as possible. This is in fact the key to being able to cope with the huge demand placed on networks by users. To achieve this requires careful planning of the location of these sources, design of the infrastructure required to link them all and development of algorithms able to intelligently coordinate them for optimal performance.

1.2 Improving indoor wireless performance

There have been a number of strategies proposed to improve indoor wireless coverage and capacity. All of these involve the introduction of additional sources of radio signal inside the building, but the nature of these sources and the strategies for coordinating them are quite different.

1.2.1 Repeaters

One of the most commonly used devices for improving indoor wireless coverage is the *repeater* or *relay*. This device essentially consists of a radio receiver, amplifier and transmitter as shown in Figure 1.6. The repeater receives, amplifies and retransmits weak radio signals, a process called *amplify and forward*, effectively extending the range of the original transmitter. This process is replicated twice in each repeater: once for the uplink and again for the downlink. Very little additional infrastructure is required to install radio repeaters as they operate wirelessly. The devices are also simple in design making them a cost effective solution. Repeaters in buildings are often fixed units but in some advanced networks mobile terminals can also be used as repeaters. Repeaters have been shown to be effective and economical in improving wireless coverage [25, 26, 27]. Intelligent repeaters can be used to create cooperative networks offering improved performance, such as in the IEEE 802.16 WiMAX standard [28].

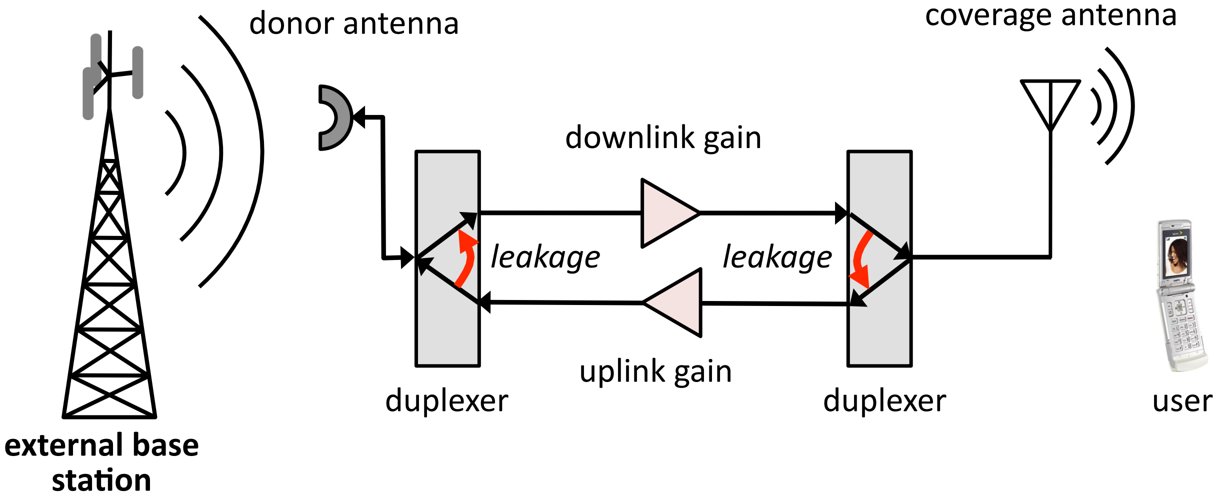

Figure 1.6: Block diagram of a radio repeater for improving wireless coverage [29].

The main problem with radio repeaters is the poor isolation between the uplink and downlink. Repeaters can often have very high gain (over 90dB) and so relative to the incoming signal, which is often weak, the transmitted signal is very powerful. There is often some leakage of this transmitted signal from the output back into the input, where it is amplified again and the cycle continues as illustrated in Figure 1.6. This problem can be alleviated by improving isolation between signal paths by using high quality duplexers or directional antennas but it is still very difficult to remove this problem [29]. Another problem is that the SNR of the retransmitted signal can only be as good as that at the input of the repeater, which is often fairly low due to large free-space attenuation. An alternative is to use repeaters that demodulate and regenerate the signal, but this adds additional cost and requires the repeater to be tailored to specific services. Further, low SNR on the input signal still results in an increased probability of bit error in the data stream. Finally, repeaters do not mitigate multipath effects. In fact, their effectiveness can be greatly reduced if there is destructive interference occurring at their input.

1.2.2 Small cells

The term *small cell* refers to any cell, or coverage area of mobile network, that is smaller than the standard size used in traditional deployments of mobile networks, called *macrocells*. This includes femtocells, picocells and microcells, which are named according to their sizes. At the centre of each of these cells is a small cellular base station with lower power output and hence shorter range than a standard base station.

Picocells tend to offer ranges of between 4-200m and are usually controlled by a centralised base station controller. Femtocells, on the other hand, tend to offer ranges of around 10m and contain their own internal base station controller [30]. The base station hardware is generally somewhat expensive owing to its complexity. If using picocells, there is an additional cost associated with setting up a backhaul infrastructure to link the cell to the centralised base station controller. Many femtocells are capable of connecting to the network provider via a standard broadband internet connection so although backhaul infrastructure is required, it is of a cheaper nature and is likely to have been installed previously for other applications. Because femtocells and picocells perform RF modulation themselves based on digitally received data, they are able to produce an SNR of a level comparable to the original base station wherever they are located, creating better quality coverage. This also means they add capacity to a wireless system as each small cell can support additional users. The relatively low-cost and ease of deployment of femtocells has seen a surge in their use. In fact it is estimated that by 2016 over 90% of all cellular base stations will be small cell [31].

However, there are some shortcomings of the small cell approach, most notably that smaller cells can create significant adjacent cell interference. It is then necessary to carefully manage the allocation of frequencies or other resources used for multiplexing between cells, a significant challenge in network design [33]. Another shortcoming is that small cells must be tailored to provide a particular service, for example 4G. Because they perform the modulation themselves it is potentially expensive and complex to develop hardware to do this for multiple radio services. Nowadays, new wireless protocols are introduced at regular intervals and existing services are frequently upgraded. For femtocells to support this they would need to have their software upgraded regularly and if there were a change in radio spectrum use, a new network of femtocells with updated hardware would have to be deployed.

1.2.3 Distributed antenna systems

Another way of creating a highly distributed network of signal sources is to distribute just the antennas of a transceiver, creating what is known as a *distributed antenna system (DAS)* or *distributed antenna network (DAN)*. Traditional wireless systems operate on the paradigm of having two antennas on the base station (or just one if duplexing is used) – one for the uplink and one for the downlink. These antennas are typically attached to the base station or are located very close by and so in the context of DASs these systems are often referred to as *collocated antenna systems (CAS)*. A DAS, by contrast, operates on quite a different paradigm whereby a single base station may transmit and receive radio signal via one or more remotely located antennas as illustrated in Figure 1.8. If this concept were taken to its extreme, albeit impractical, a DAS would radiate from every single point in a coverage area creating a perfectly uniform signal distribution. In this way, a DAS enables better coverage for a single radio transceiver because the signal can be transmitted simultaneously from several different locations [34]. When used in this fashion, a DAS is actually a spatial diversity scheme. For an ideal case it can be shown theoretically that when using a DAS the coverage area of a base station increases to:

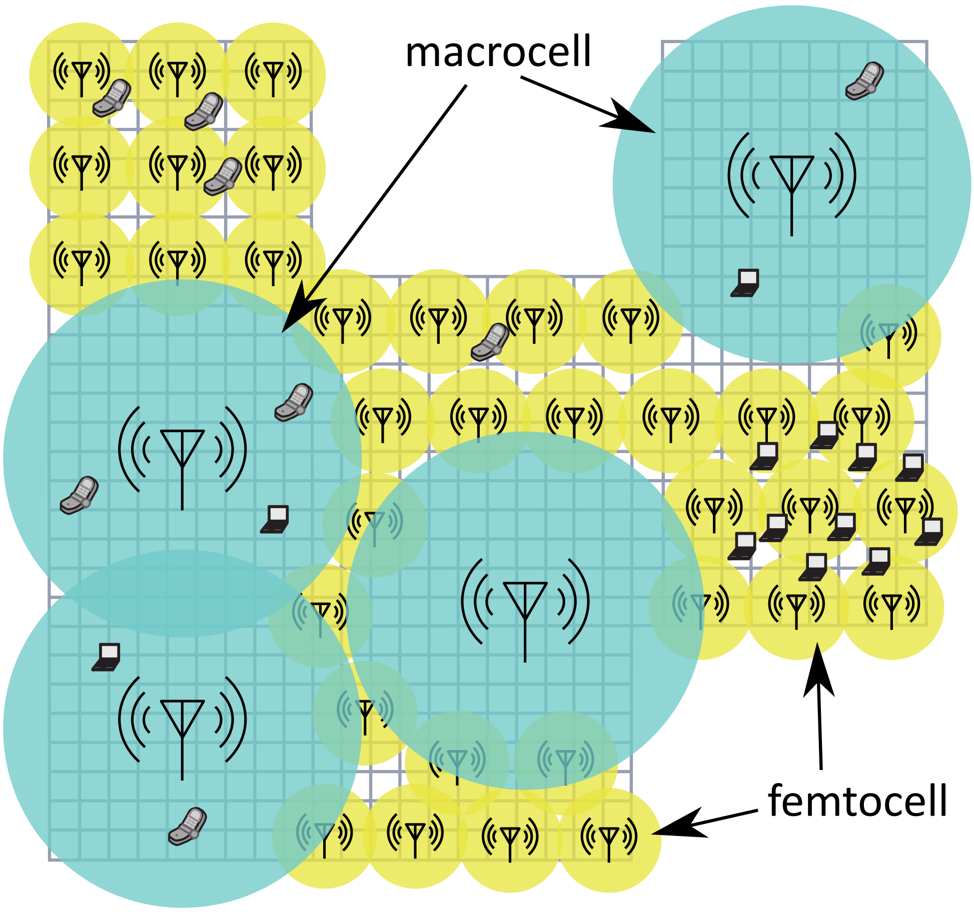

Figure 1.7: Illustration of how a combination of small and large cells can be used to provide improved wireless coverage in a building [32].

$$A_{total} = N^{\left(1-\frac{2}{\gamma}\right)} A_{\gamma} \tag{1.4}$$

where A_{total} is the new total coverage area, N is the number of antennas, A_{γ} is the coverage area for the original single antenna CAS and γ is the path loss exponent (usually ranging from 2-5 depending on the environment) [35]. Another related property of DASs is that if the coverage area is held constant they can made to be more power efficient than equivalent single antenna CASs. DASs have been demonstrated to reduce transmitted power by up to 10dB over CASs with the same coverage area [36].

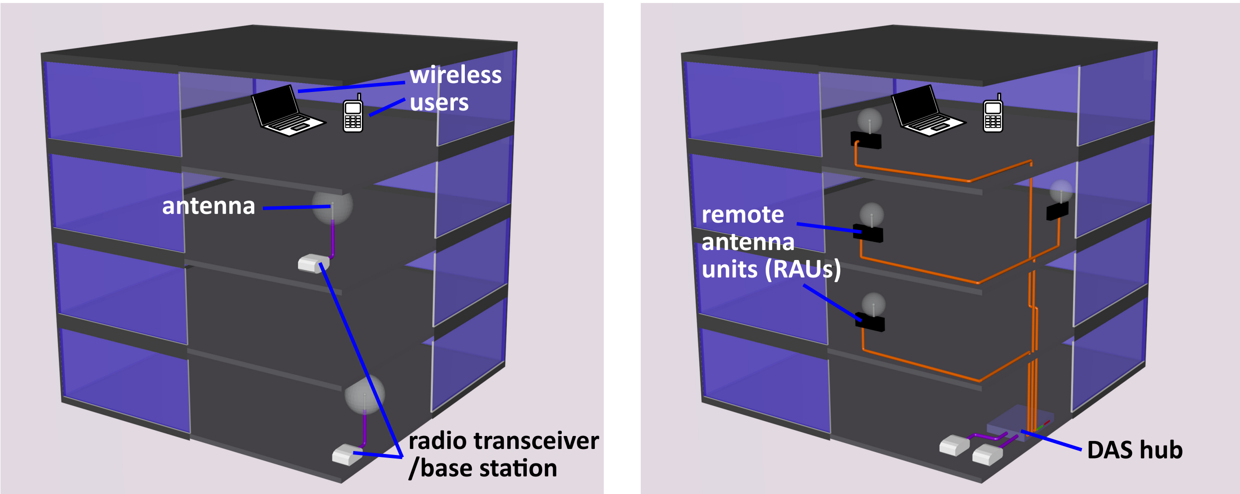

(a) (b)

Figure 1.8: Comparison of: (a) traditional collocated antenna system and (b) distributed antenna system.

DASs are often seen as an alternative to femtocell and wireless relay technology, though the technologies need not be mutually exclusive [37]. In recent years DASs have enjoyed significant popularity and it is estimated that in 2010 there were over 89,000 installations worldwide [38].

Many commercial DASs are narrowband by nature and are designed to operate only over a frequency range sufficient to support a single service, for example 2.05-2.15GHz to support 3G WCDMA. However, it also possible to build broadband DAS that can operate over a wide RF frequency range, for example ZinWave DAS that operate over a frequency range from 150MHz to 2.7GHz [39, 40]. Broadband DAS usually make use of radio-over-fibre (RoF) technology as discussed in Section 1.3.2. A major advantage of broadband DASs is that they can support any wireless service within a specified frequency range regardless of the exact protocol or modulation format. For this reason broadband DASs are referred to as being *multi-service*, *service agnostic* or *service independent*.

Previously, DAS have been demonstrated to improve wireless performance for a range of services including 802.11g WiFi and cellular CDMA services [41, 42]. Another burgeoning application for DAS is the ability to use it with *radio-frequency identification (RFID)* tag technology to allow improved coverage for error-free reading of passive UHF RFID tags within a large area [43]. By carefully controlling the phase shifts between the signals transmitted from each antenna, it is possible to adjust the position of dead zones caused by multipath interference such that tags can be read at every point in a room. More generally, this technique can be used to significantly mitigate the problem of multipath interference in wireless communication systems [44, 45].

Aside from improving network coverage, DAS can be used to facilitate the addition of capacity to a network. In order to fundamentally increase the available capacity of a network serving many users it is necessary to add more base stations to the network. DAS offers the potential to do this while keeping all equipment centrally located, thereby avoiding the need to install additional infrastructure. This is achieved by using a single network of antennas connected to multiple centrally located base stations in a *base station hotel* configuration. In the simplest case, multiple base stations would operate over the same broadband DAS infrastructure on different frequency channels, termed a *multichannel* DAS. In more advanced systems the capacity could be dynamically allocated to different remote antenna units based on demand from users. For example, if users were heavily concentrated in one area then each remote antenna in that area could be connected to a different base station. If users were more evenly distributed then groups of adjacent remote antennas could be allocated to each base station. Further, in times of low demand all but one base station could be turned off thereby saving energy. This ability to intelligently control DAS can also be used to mitigate interference [46, 47].

DAS thus provide an attractive solution to the problem of improving indoor wireless coverage and adding capacity to wireless networks. In order to enable effective realisation of such DASs it is important to carefully design the mechanism for distributing the analogue RF to the antennas. This is discussed in Section 1.3.

1.2.4 Other methods

There are a number of other methods commonly used to improve the performance of indoor wireless networks. Antennas can be tailored for indoor wireless applications by carefully controlling properties such as their placement height, polarisation, directivity and beam profile [48, 49]. Further, broadband antennas are available that can support multi-service operation over a broad range of frequencies [50, 51].

It is also possible to select optimum locations for wireless base stations to ensure that maximum quality coverage can be provided with the minimum number of base stations [52, 53]. However, this is building specific and a particular arrangement can become sub-optimal when the environment changes.

Cognitive radio promises to improve the performance of indoor wireless systems by increasing the available bandwidth. Under this system, devices and base stations have software-defined radio front-ends that are able to sense current RF spectrum usage in their local area and can communicate via any unused bands (though at present these are restricted to unlicensed bands) [54]. The main challenge cognitive radio faces is the huge complexity of spectrum sensing – that is, determining the usage characteristics of radio resources in terms of frequency, time, space and coding schemes [55]. This challenge adds significant computational overhead to cognitive radio networks.

1.3 Distributing analogue radio signals

The performance of a DAS is determined to large extent by the means used to transfer the analogue radio signal to the remote antennas. These can be divided into two main categories: passive and active methods. Passive methods make use only of passive electrical components such as cables, signal combiners, power splitters, diplexers and attenuators to distribute radio signals to the antennas. These often amount to little more than standard antenna systems with very long feeder cables. Active methods differ from passive methods in that in addition to passive components they contain active circuit elements such as amplifiers, repeaters or optical communication links [56].

1.3.1 Coaxial cable

The most common method of passive radio signal distribution is connecting remote antennas to the base station by long lengths of coaxial copper cable [56, 57]. Radio frequency splitters and combiners are then used to feed the signal to multiple antennas. This requires a minimum of additional equipment giving this method the advantage of simplicity. However, high quality coaxial cable has large capital and installation costs making such systems potentially expensive. Another major drawback is that electrical loss in copper increases with frequency due to the skin effect. This makes it unsuitable for providing a truly broadband and hence multiservice system [58].

This power loss is not always undesirable – in fact, the *leaky feeder* or *radiating cable* technique exploits the fact that radio signal will leak from feeder cables, effectively turning the cable into a very long antenna. This creates an almost continuous distributed antenna system and has been successfully deployed in confined environments such as tunnels [59, 60].

It also possible to construct active DASs that use coaxial or other copper cabling to connect to remote antennas. These systems differ from passive DASs in that they have amplifiers and other processing electronics located at the remote antennas, instead of just at the central DAS hub. Such systems are easier to design as the loss in the cabling can be compensated for electronically using automatic gain control. There is thus a reduced need to use carefully selected splitters and attenuators to ensure uniform power delivery to antennas [58]. However such systems still suffer from reduced SNR and limited bandwidth.

1.3.2 Radio over Fibre

Radio over fibre (RoF) is an active technique of distributing analogue radio signals that overcomes the bandwidth and cost limitations of coaxial cable [40]. This also enables DAS to make use of optical fibre already installed in buildings for Ethernet networks. It is common for large buildings to have significant amounts of pre-existing optical fibre - in fact in 2007 there was an estimated 17 million km of optical fibre installed in buildings worldwide [61]. This provides a significant reduction in RoF installation costs compared with coaxial cable.

The basic principle is illustrated in 1.9. In the downlink case radio signals transmitted from the base station are converted to optical signals in the RoF hub. These optical signals are then transmitted via optical fibres to one or more *remote antenna units (RAU)* where they are converted back to electrical signals before being transmitted via the antenna. The wavelength of the light used is usually 1310nm or 1550nm (due to silica fibre transmission windows at these wavelengths) but 850nm systems have been demonstrated due the availability of low-cost lasers at this wavelength [62].

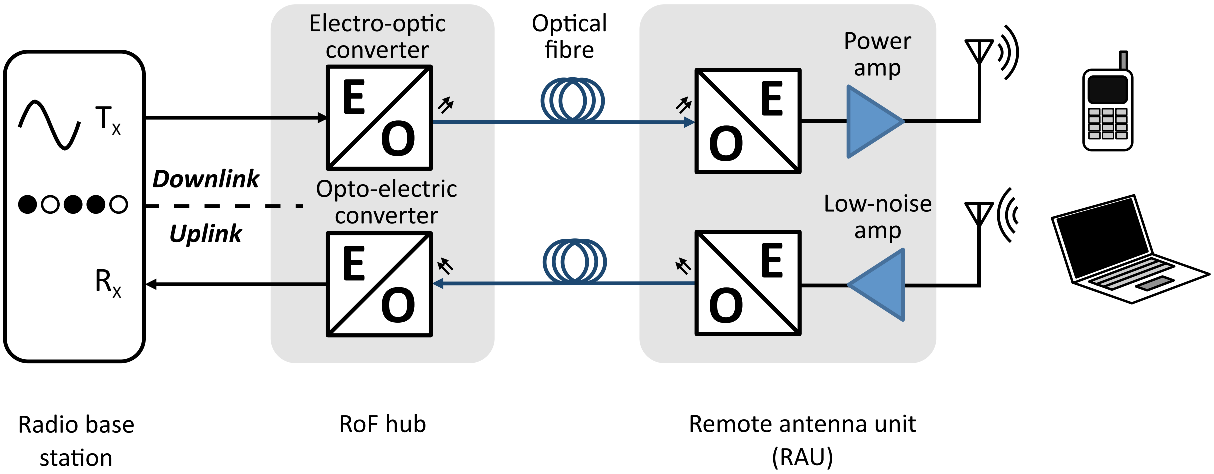

Figure 1.9: Schematic of a generic radio over fibre system.

At the transmitting end of a RoF link the simplest method of electrical-to-optical conversion is *intensity modulation (IM)*, whereby the radio signal controls the intensity of the output from the laser. In the simplest case, this is done by directly controlling the current flowing through the laser, a process called *direct modulation*. It also possible to perform intensity modulation by passing a *continuous wave (CW)* laser beam through an external modulator such as a Mach-Zehnder modulator or an electro-absorption modulator [63, 64]. These two process are illustrated in Figure 1.10.

External modulators can provide greater linearity and can operate at much higher frequencies, though this comes at the cost of a more complex and expensive system. However, future photonic integrated circuits manufactured on silicon could drive down costs significantly [66]. External modulators also avoid the problem of frequency chirp that occurs in direct modulation of semiconductor lasers, which can be problematic if using longer lengths of fibre [64]. However, perhaps the greatest advantage of external modulators is that they can be designed to introduce additional amplification into the signal path, as compared to direct modulation which can only provide attenuation. This could reduce the requirements of other amplifiers in the link and further improve noise performance.

In addition to intensity modulation, a number of other schemes have been suggested for RoF modulation. One simple variation is optical single side-band intensity modulation, used to send high frequency millimetre wave signals over fibre with minimal dispersion [67]. Frequency modulation and phase modulation have also been demonstrated and while they can provide significant SNR improvements, they require more complicated circuitry to operate including coherent optical detection [68].

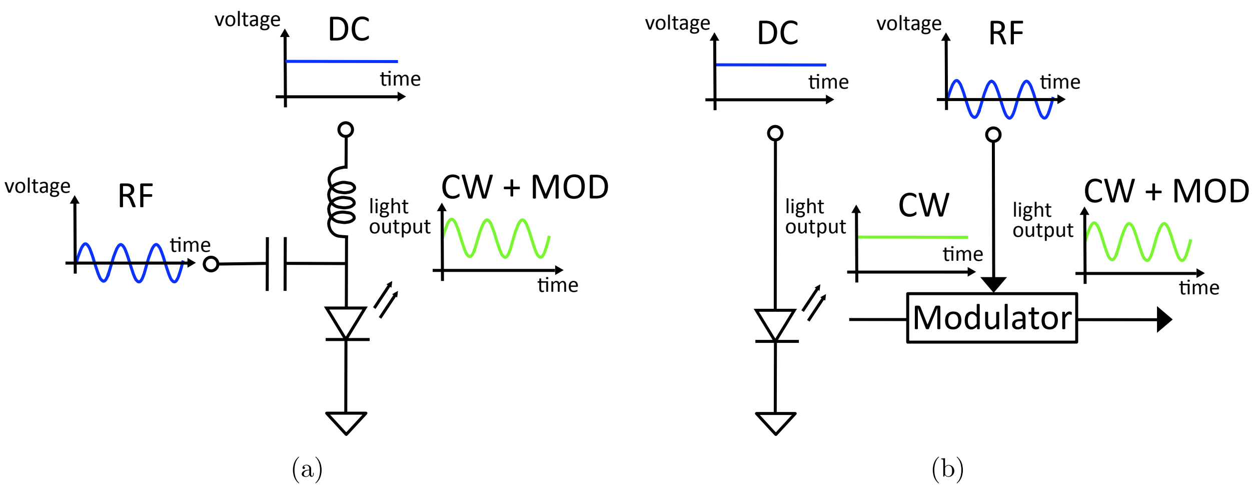

Figure 1.10: Intensity modulating a laser using (a) direct modulation and (b) external modulation. Green signals are optical and blue signals are electrical [65].

In some cases an intermediate frequency up-conversion of the radio signal is done before transmission. This technique, referred to as *sub-carrier multiplexing (SCM)* is often used to avoid interference between different services or to allow separate MIMO spatial channels at the same frequency to be multiplexed on a single fibre [69, 70]. SCM can also be used to prevent optical crosstalk between the uplink and downlink and to enable the transmission of baseband digital data alongside RoF traffic [71]. *Intermediate frequency over fibre (IF over fibre)* is a related technique used to down-convert the frequency of a radio signal so that it can be sent over lower bandwidth fibre, such as multimode fibre (MMF). This necessarily reduces available bandwidth and so is not a broadband solution.

There also exist digital RoF systems that are able to digitise a radio signal to varying degrees and send this to an RAU via low quality optical or electrical links [72, 73, 74]. These systems are often not as broadband as analogue systems as they rely on frequency down-conversion and many of them currently only provide a single service at a time.

At the receiving end of a RoF link the simplest method of optical-to-electrical conversion is *direct detection (DD)*, where a photodiode in the RAU detects the received light and generates a current proportional to it. This current is then amplified, often using a transimpedance amplifier (TIA).

Most analogue optical receivers operate on direct detection, ignoring optical phase and frequency information. By comparison, most analogue radio receivers make heavy use of phase and frequency information and so are referred to as *coherent*. Coherent detection analogue optical links have been studied extensively and have been shown to offer some performance improvement over direct detection. However, they tend to require more complex transmitters and receivers and have not found widespread use in RoF systems [75, 76]. Coherent receivers are necessary when using phase and frequency modulation schemes.

One of the key benefits of RoF compared with coaxial links is the very low loss. Optical fibre can have an equivalent electrical loss less than 0.5dB/km at 1310nm for a modulation frequency of 6GHz, whereas a standard half-inch coaxial cable could be expected to have a loss of 730dB/km in the same situation [65]. Another substantial advantage of using RoF systems is the immense bandwidth available. *Single mode fibre (SMF)* can in theory provide an RF bandwidth of up to 50THz from the combined bandwidth in the 850, 1310 and 1550nm bands, although existing commercial systems only use up to 1.6THz [77]. Even so, this bandwidth is several hundred times broader than entire spectrum used for wireless internet and mobile communications.

Multi-mode fibre (MMF) has a bandwidth-distance product of about 500MHz.km in over-filled launch conditions but this can be increased four fold to 2GHz.km by using offset launch techniques [78]. Using mode-selective launch techniques this can be increased even further, as discussed in Section 1.4.2. By comparison even the best coaxial cable on the market has a 3dB bandwidth of about 1GHz at 100m [79]. Broadband multiservice RoF DAS operating over MMF have been experimentally demonstrated [40].

For MMF links of a few hundred metres or less, the bandwidth is often limited by the laser, modulator or the photodiode. The bandwidth of the modulation scheme can vary from 3GHz for directly modulated low-cost Fabry-Perot Laser diodes to 100GHz for high performance external modulators. The bandwidth of photodiodes can be as high as 500GHz so these are not often the limiting factor [76].

The main factor limiting the performance of RoF systems is the dynamic range, defined as the range of RF signal powers that the system can handle. Because wireless users are generally located at a range of distances from any antenna, wireless systems must be able to deal with a very large range of received powers on the uplink and so wireless standards often set stringent dynamic range requirements. The lowest acceptable signal power is limited by noise, and the highest acceptable signal level is generally limited by distortion arising from nonlinearities in the system. Lasers and photodiodes are fundamentally nonlinear devices so distortion tends to be a much greater problem in RoF systems than in coaxial systems. Metrics to quantify these limits are discussed further in Section 2.3.4.

The dynamic range of RoF links can be improved by proper selection of lasers and photodiodes to reduce noise and distortion. Using distributed feedback (DFB) lasers instead of the cheaper Fabry-Perot or *vertical-cavity surface-emitting laser (VCSEL)* designs has been shown to improve dynamic range of a link by 10-20dB [71]. Similarly, avalanche photodiodes (APDs), which have a much greater sensitivity to weak signals due to avalanche multiplication of incident photons, can provide superior dynamic range over standard PIN photodiodes though they are generally slower and more expensive [80, 81]. There also exist systems designed to counteract nonlinearity by analogue predistortion of the signal [82, 83].

Although RoF systems do require more equipment than passive coaxial systems, when the much lower cost of optical fibre and the superior performance is considered it has been shown that for distances of over 100m it is more appropriate and economical to use optical fibre instead of coaxial cable for DAS [84]. Clearly, RoF DAS is a very powerful and effective technology that will play a key role in future wireless infrastructure for next generation networks.

1.3.3 Radio over Free-Space Optics

A key shortcoming of both coaxial and RoF DAS is the need to have an existing cabling infrastructure or to install new cabling, which can be expensive or impractical. Using a fixed cabling infrastructure also limits the possible positions of RAUs and base stations, hence limiting the flexibility of the network.

The alternative, then, is to wirelessly transfer the radio signal to remote antennas. Such wireless links would ideally be broadband and produce as little interference with other wireless services as possible. To achieve this at sufficiently low cost so as to offer an advantage over cabled systems the best option is to use point-to-point free-space optical links [85]. Case studies have found that using free-space optical links in place of wired links can provide savings on installation costs of around 85% for short-range ($\leq$200m) inter-building digital links [86].

Digital Free-Space Optical Links

There are many examples of digital FSO links over both short and long distances. Many of the short-range applications are in high speed optical interconnects between computer chips, for example with 256 channels running at 83Mbps each over a distance of 75mm [87]. There are also long-range applications, usually for transferring data between buildings, for example 16 channels running at 10 Gbps each over a distance of 2.16km [88]. Such long-range outdoor systems are vulnerable to outages caused by adverse weather such as heavy fog. Building-to-building digital FSO systems are commercially available, some of which are shown in Figure 1.11. Equipment costs for such systems can range in price from £3,500 to £30,000, and installation costs usually range from £1500 to £3500 [89, 90, 91]. Digital FSO links are also used to provide data links between satellites [92] and for short-range ($<$ 1m) transfer of data between computing devices via the IrDA protocol [93].

Another application of free-space optical links that has seen a re-emergence is their use in optical wireless. This entails the complete replacement of RF wireless links with high-bandwidth free-space optical links transporting data to users. Despite being proposed over 30 years ago [94], optical wireless has recently seen a resurgence in popularity due to new technologies offering capacities of up to 1 terabit/s [95]. Organisations such as the Visible Light Communication Consortium have been set up to promote the future development of optical wireless systems [96].

A major difficulty faced by all these systems is power loss, most of which is caused by misalignment or strategies designed to increase tolerance to misalignment. Free-space optical links are very sensitive to misalignment, which can arise from lack of precision in directing the beam at the receiver (termed *pointing error*), thermal drift of the terminals and building vibration [97]. This problem has been studied extensively because of its fundamental importance to the performance of FSO links [98, 99].

There are a number of ways that problems associated with misalignment can be reduced. The simplest is to use a beam that widens more quickly, i.e., a beam with large divergence [100]. Divergence is a measure of the increase in beam diameter with distance from the transmitter, and is usually specified as an angle in milliradians. A larger divergence will create a larger spot size at the receiver making it more likely that some part of the beam will reach the detector even

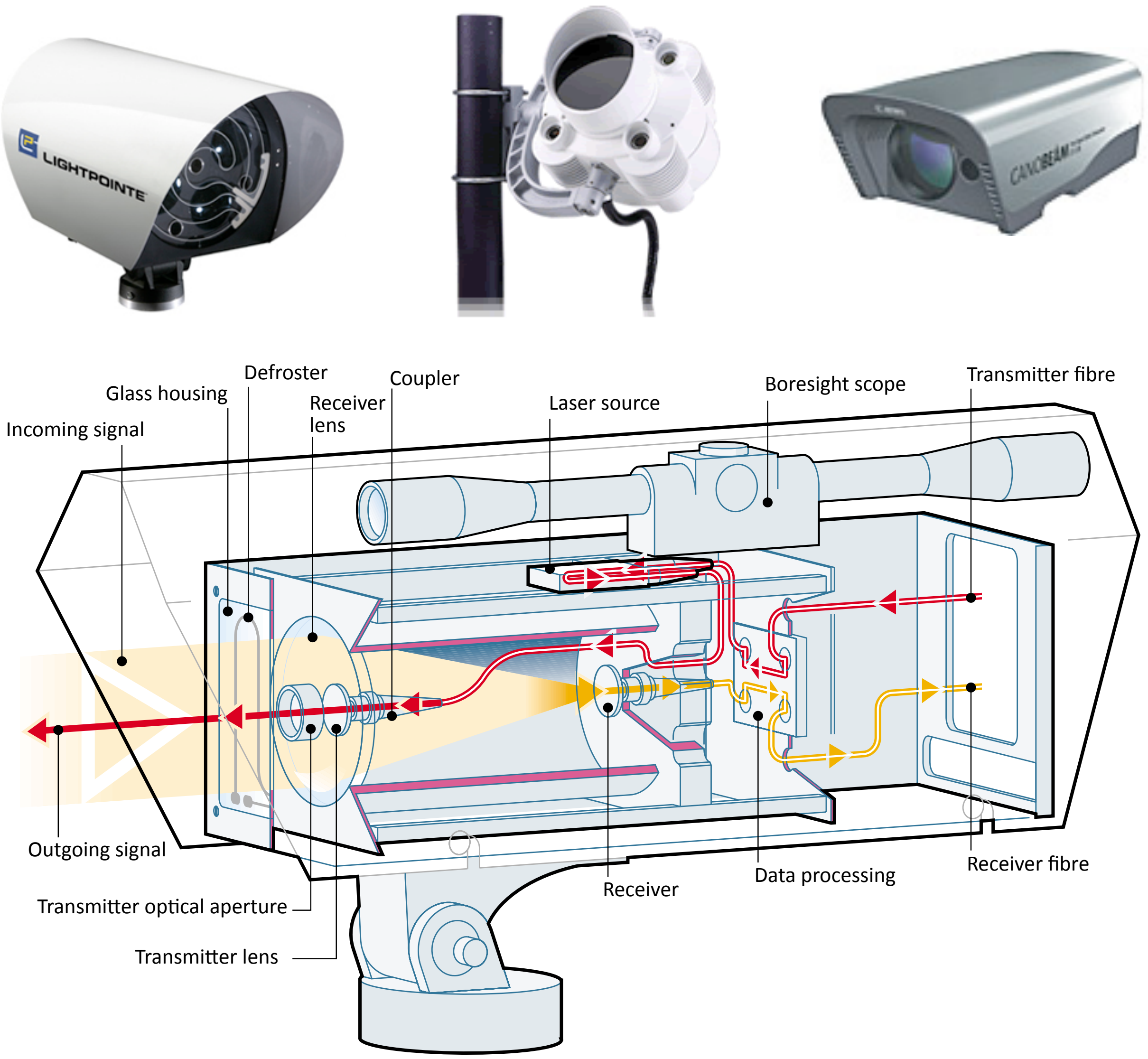

Figure 1.11: Typical commercial digital FSO transceivers. Clockwise from top left: LightPointe FlightStrata, fSONA SONAbeam, Canon Canobeam and a cut-away view inside a typical FSO head unit [86].

if it is misaligned. However, this necessarily causes power loss because only a small fraction of the transmitted power will be received as illustrated in Figure 1.12. This loss could be avoided by using a large optical receiver but these are often difficult to make. In order to compensate for this power loss, an obvious solution is to increase the power of the transmit beam. However, as with any system where lasers are used in free-space, there are limits restricting the maximum power of laser beams for eye safety reasons. To that end, infra-red wavelengths (1300-1600nm) are often preferred because of their higher eye-safe power limit [101].

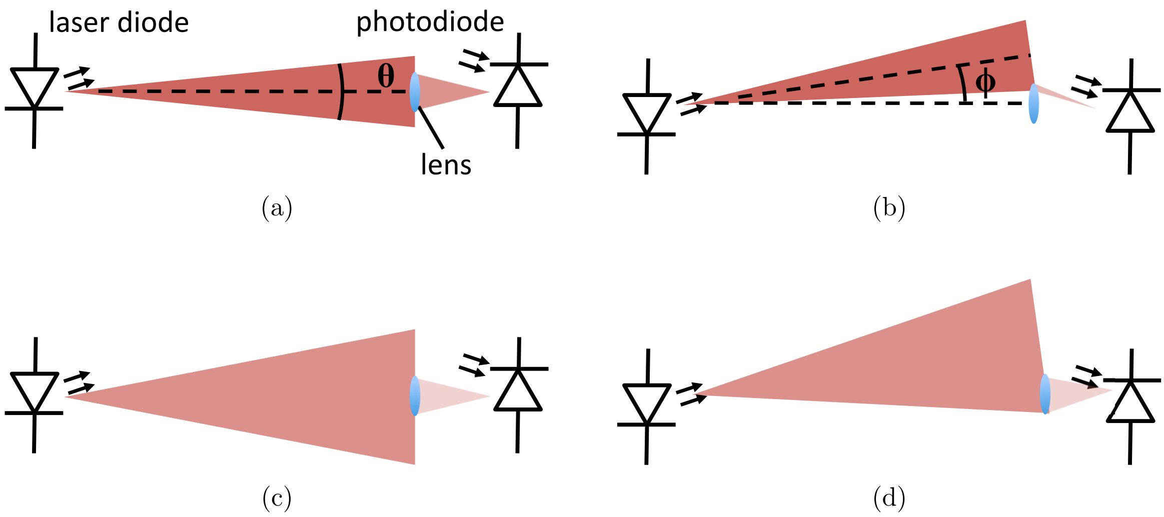

Figure 1.12: Illustration of the trade-off between beam divergence, power loss and ease of alignment in a FSO link: (a) a low divergence beam with no misalignment and divergence angle denoted by θ, (b) low divergence beam with angular misalignment of ϕ showing significant power loss, (c) large divergence beam showing increased power loss compared with (a), (d) misalignment with large divergence no longer significant change in power loss. Shading indicates the beam power density, where lighter shading means lower power.

It has been suggested that the full-angle beam divergence should be in the region of 2-5millirad to enable reliable manual alignment [102, 103, 104]. Systems using divergent beams as their only means of mitigating misalignment have been shown to maintain acceptable link quality for several years before needing realignment [90]. Customised passive optical devices that reduce coupling losses while still enabling manual alignment have also been designed, for example the optical antenna [105]. A practical implementation of a system using divergent beams for alignment over distances of 50m is presented in Section 2.4.2.

Another common method of reducing pointing error is automatic tracking, whereby a feedback loop between the transmitter and the receiver ensures the beam stays optimally aligned. This allows the beam to have a much smaller divergence increasing the received power. Electromechanically controlled lenses and mirrors are often used to steer the beam [106]. However, these are slow and bulky so more advanced tracking mechanisms have been proposed using all-optical beam steering and phased optical arrays [107, 108, 109]. Such tracking mechanisms require additional optical equipment and control circuitry so are generally not low-cost.

In outdoor FSO systems, there is also a need to consider the effect of adverse weather conditions. Particles suspended in the air such as moisture droplets in fog or aerosols can cause very large optical attenuations due to absorption and scattering. Spatial fluctuations in temperature and humidity can cause further scattering of light, referred to as *scintillation*, which further reduces performance [110]. However, these problems can largely be ignored for short distance indoor applications [111].

Analogue Free-Space Optical Links

Though digital FSO links are more common, analogue FSO links also exist and have been successfully used for transmitting radio signals over medium-long distances. The basic concept is similar to RoF but the transmission medium for the laser beam is free space rather than optical fibre. Consequently such links are referred to as *radio over free-space optics (RoFSO)* links. A generic RoFSO system is illustrated in Figure 1.13.

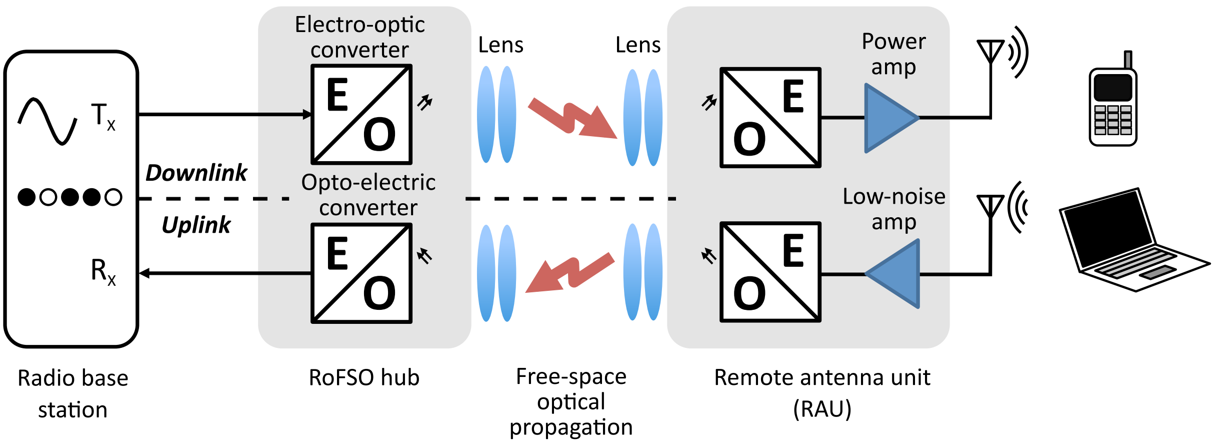

Figure 1.13: Schematic of a generic RoFSO system.

Katz and Arnon have demonstrated a RoFSO system providing specific cellular services (WCDMA and GSM) at up to 2GHz [81]. It is shown to work over a distance of 500m but requires use of relatively complex and expensive equipment including *erbium-doped fibre amplifiers (EDFAs)*, automatic gain control units and stabilising mechanisms to assist alignment. The system is not demonstrated to be truly broadband over the stated bandwidth and is not shown to support emerging 802.11n/ac or 3G/4G cellular services.

Refai et al. have also demonstrated a RoFSO system, targeted at CDMA antenna remoting applications, which operates at frequencies up to 1GHz [112]. The system was demonstrated to provide sufficient performance to support a single CDMA carrier but the work does not examine how dynamic range varies with frequency, a requirement to demonstrate potential for multiservice operation. The length of the link is only 3m, too short to be of practical use for DAS applications. Further, the system requires use of predistortion circuitry and external modulators adding cost and complexity to the set-up.

Bucholtz et al. have developed two experimental RoFSO systems [113, 114]. These systems are designed for longer range applications (500m-32km) and make use of external modulators. They have been tested up to 1GHz but do not support multiservice or broadband operation.

Kazaura et al. have demonstrated a RoFSO system that can provide multiple services up to and including 802.11g WiFi at 2.4GHz [115]. To achieve this it makes use of dense wavelength division multiplexing (DWDM) techniques requiring multiple lasers at significant additional cost. This system is designed to provide wireless coverage to remote areas over distances of >1km and so uses advanced telescopic receivers and automatic electromechanical tracking mechanisms, illustrated in Figure 1.14. This pushes the cost of the transmitter and receiver to over £6,500 each. This significant expense makes it unsuitable as a low-cost alternative to RoF. Further, adding another service requires adding another DWDM channel so the system cannot be considered intrinsically multiservice.

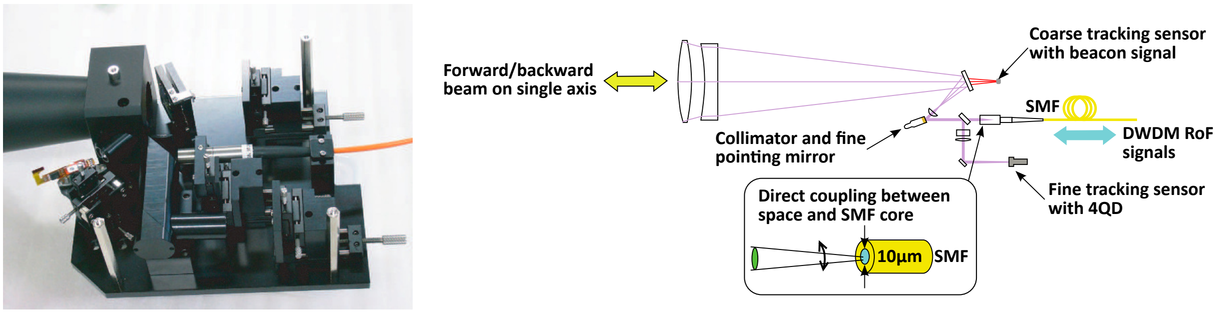

Figure 1.14: Tracking system used for the transmitter/receiver of the RoFSO system described in [116].

1.3.4 Comparison of methods

Taking into account all the information presented in the previous 3 sections, Table 1.1 summarises the different properties of DAS built with traditional coaxial cables, RoF and RoFSO.

1.4 Increasing backhaul capacity

Another critical aspect of redesigning wireless delivery infrastructure is increasing the data capacity of the backhaul network. The backhaul network comprises the links that connect together many neighbouring wireless cells into a single network. These links aggregate the data streams from many users at several wireless cells and so must have very high data capacities. Though traditionally these backhaul links were implemented using electrical or microwave links, increasingly they are relying on optical links such as synchronous digital hierarchy (SDH) [117].

With the exploding demand from users, as discussed previously, there is an associated increase in demand from backhaul networks, as illustrated in Figure 1.15. It can be seen that this demand is predicted to continue to grow, eventually leading to the creation of bottlenecks as existing fibre optic links reach their maximum capacity, particularly for the highest capacity sites.

Table 1.1: Performance comparison of coaxial cable, RoF using multimode optical fibre and RoFSO as DAS signal distribution mechanisms. Coaxial cable and RoF data taken from [84].

Parameter	**Coaxial cable**	**RoF**	**RoFSO**
Attenuation (electrical) over 50m	>40dB	0.1dB	20-40dB
3dB bandwidth over 50m	2GHz	10GHz possible (typical commercial system ∼3GHz)	10GHz (limited by laser)
Maximum range	∼100m	several km	50-100m
Estimate variable cable cost	∼£1/m	£0.68/m	nothing
Estimated capital equipment cost	£210	£420	£500 (target)
Estimated installation weight	>100kg/m	<20kg/m	nothing
Ease of installation	low	moderate	high
Layout flexibility	low	low	high

It is generally considered that perhaps the most major challenge facing the mobile industry is how to provide backhaul links with enough bandwidth for services such as 4G/LTE [118]. To avoid backhaul links becoming bottlenecks it is important to consider new ways of utilising the huge untapped data transmitting potential of optical fibres.

1.4.1 Optical fibres

Optical fibres were first developed in the 1960s and the first generation of commercial fibre optic communication systems were deployed in the 1970s. Today our global internet and communication networks rely critically upon fibre optic cable and it is estimated that there is over 1 million km of submarine fibre optic cable linking together all the nations of the world [120]. Further, there is an estimated 17 million km of optical fibre installed in buildings worldwide for local area networks (LAN) [61].

There are several types of optical fibre commonly in use. The two main categories are *single mode fibre (SMF)* and *multimode fibre (MMF)*, named because of the number of propagation modes of light that each type supports as illustrated in Figure 1.16. Submarine cables use single-mode fibre because of its ability to preserve pulse shapes over long distances due to low dispersion. Fibre installed in buildings is more often multimode fibre, most of which conforms to Telecommunications Industry Association standards, namely the OM1, OM2, OM3 and OM4 standards. OM1 is the oldest standard and specifies fibre with a graded refractive index profile with core diameter 62.5μm. OM2, OM3 and OM4 are more recent standards and use graded refractive index profiles with core diameter 50μm. Increasingly, fibres installed in buildings for data communications are OM2 or OM3 standard fibres in place of the older OM1 standard as

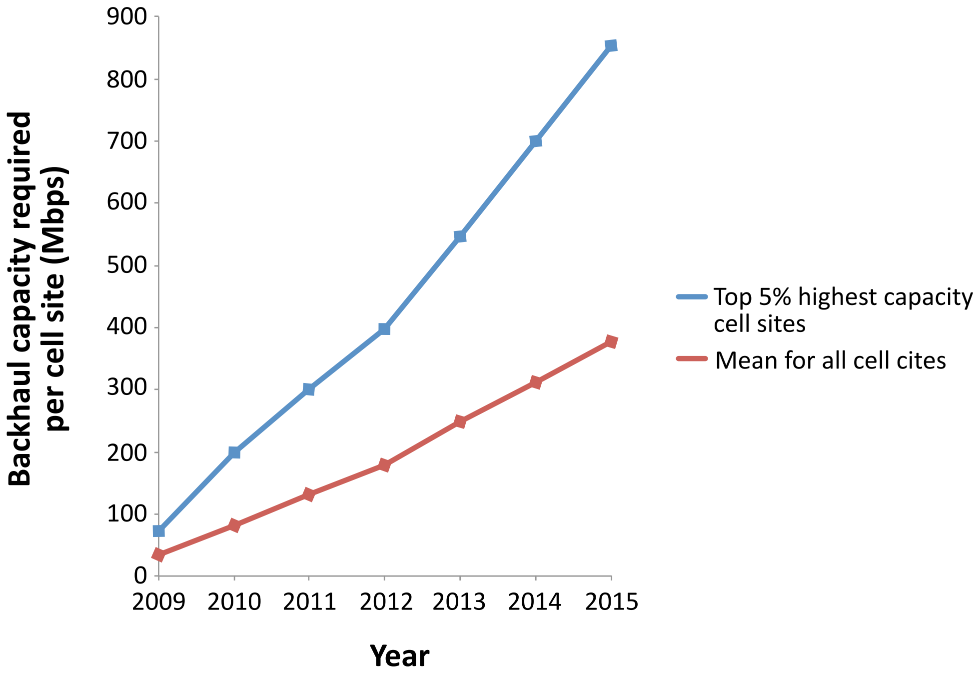

Figure 1.15: Graph showing measured and predicted increase in backhaul demand per cellular site accumulated from several 3G/LTE operators [119].

illustrated in Figure 1.17. There are other types fibre, such as *hard-clad silica (HCS)* or *plastic optical fibre (POF)* that have step-index refractive index profiles, but the bandwidth of these is generally reduced by increased modal dispersion.

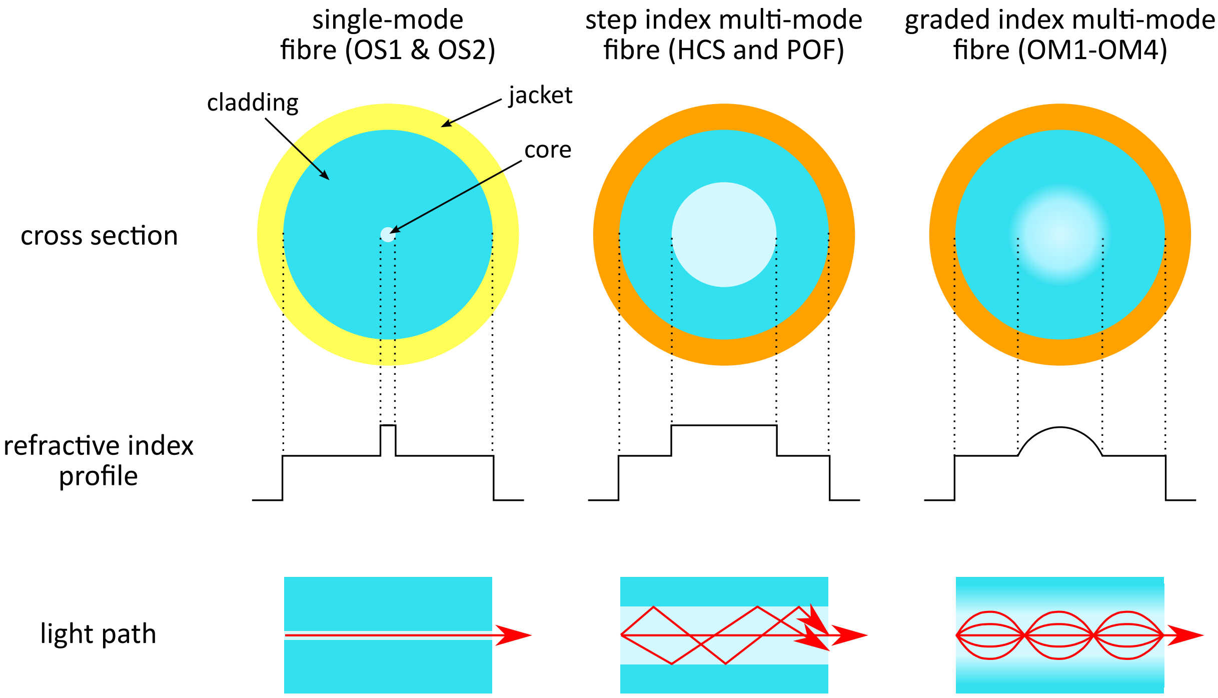

Figure 1.16: Refractive index profiles for different types of industry standard fibre. Also shown is the ray optics approximation of how light propagates in such fibres.

To date advances in optical fibre technology have kept ahead of growing demand for capacity as illustrated in Figure 1.18. However, we are now nearing the upper theoretical Shannon capacity of optical fibres using existing technology and it is predicted that in the next 10 years there will be so called "capacity crunch" where the demand placed on optical fibre will exceed available capacity [121]. This will have significant impact on the backhaul networks for wireless communication systems when these links become bottlenecks for data.

There have been many different technological approaches to improving fibre capacity. Perhaps the two most important advances in the last two decades have been the development of *wavelength division multiplexing (WDM)*, which uses multiple parallel communications channels operating on different wavelengths of light, and development of new highly-efficient encoding techniques for light such as polarisation multiplexing combined with QPSK [122].

Multimode fibre, which has traditionally had lower bandwidth due to modal dispersion, has seen significant improvements in bandwidth in recent years. Offset launch techniques, now widely adopted, have increased the bandwidth distance product by a factor of 4 by reducing the number of excited modes [78]. However, there are now emerging techniques that can actually exploit these different propagation modes to vastly increase the capacity of optical fibres, a

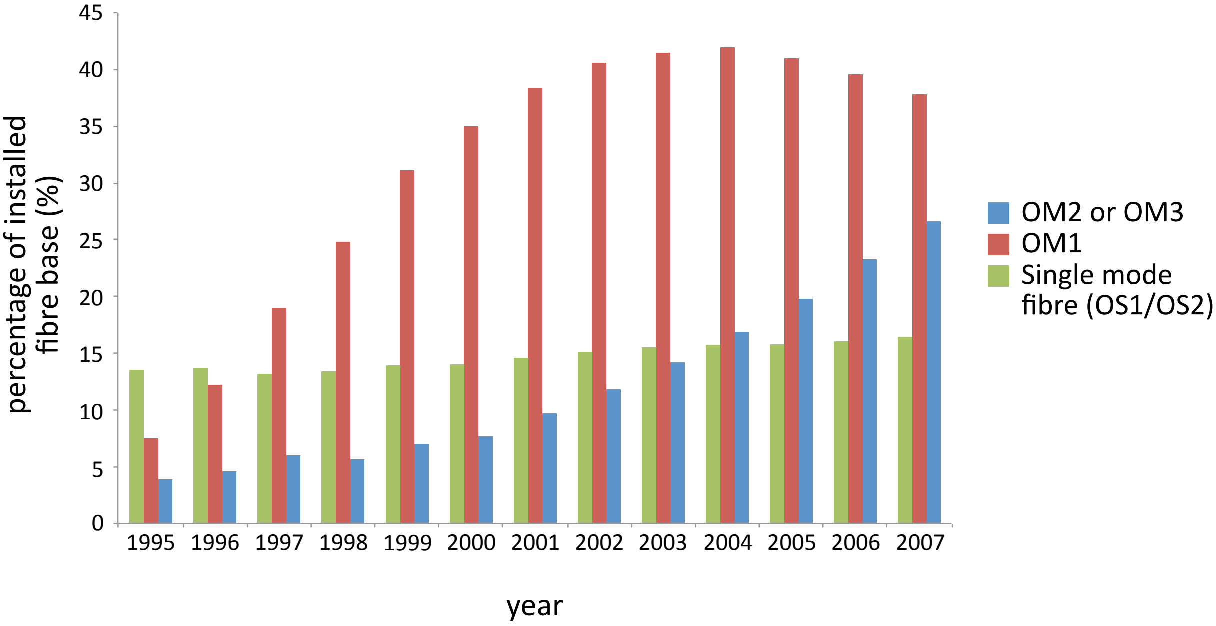

Figure 1.17: Graph showing percentage of installed fibre base in buildings by type of fibre. The increasing usage of OM2 and OM3 is clear [61]. Older fibre standards, such as FDDI, are not shown.

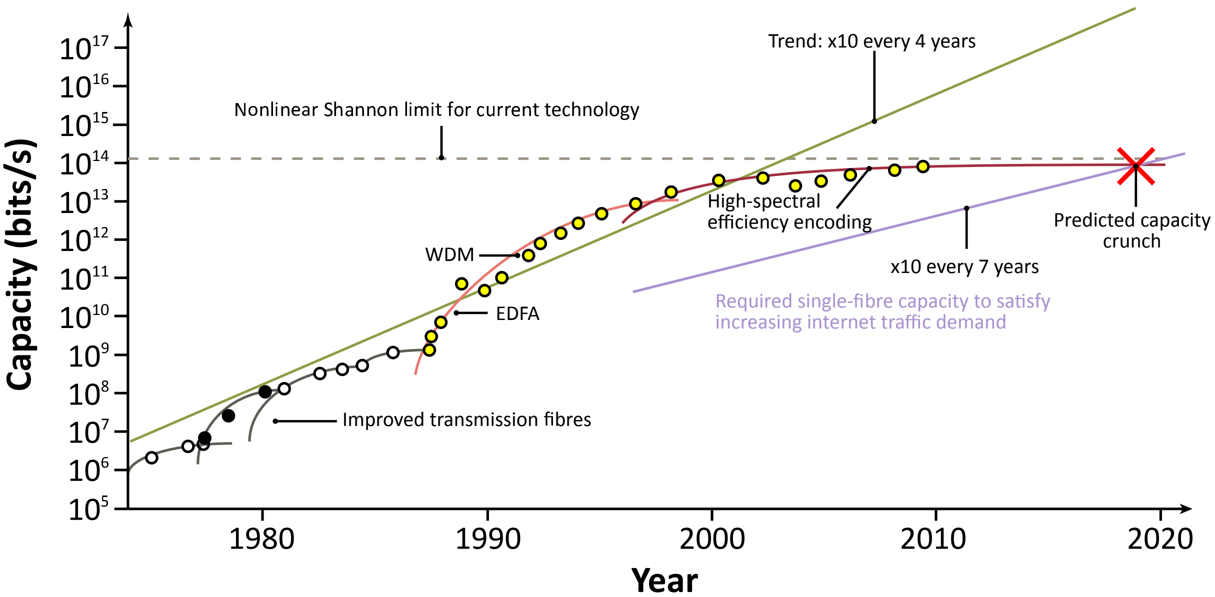

Figure 1.18: Graph showing the increase of record capacities for single-fibre communication systems as a function of year. Shown also are the technology trends as well as the demand trends [121].

technique called *mode-division multiplexing*

1.4.2 Mode-division multiplexing

Mode division multiplexing of multimode fibre is a technique that allows different propagation modes, or linear combinations thereof, to be individually excited. Generally, any arbitrary amplitude-phase distribution of light incident on the fibre will result in the propagation of some linear combination of the eigenmodes of the fibre, discussed in further detail in Section 5.2.1. By measuring several arbitrary functions of the amplitude-phase distribution at the output it is possible to use digital signal processing (DSP) algorithms to transform the channel so that it can be considered to be composed of multiple independent *eigenchannels*, each with a different SNR value, very similar to what is done for wireless MIMO as described in Section 4.2.1 [123]. This enables multiple data streams to be transmitted simultaneously via different eigenchannels. This transformation to an eigenchannel representation, achieved through the singular value decomposition (SVD) of the channel matrix, can be performed in real time to implement a coding scheme. This scheme is, in many cases, equivalent to other simpler detection algorithms such as *zero-forcing (ZF)* or *minimum mean square error (MMSE)*, which are more commonly used [124].

There are two aspects to any MDM system – the ability to launch modes selectively and the ability to detect modes selectively. In early work this was achieved by launching light onto only a small area of an MMF either by a centred SMF designed to launch fundamental modes [125], or a small spot of light offset from the centre designed to launch only higher order modes [78].

Another more recently developed method is to attempt to launch individual propagation modes directly into a fibre. As discussed in Section 5.2.1 light propagating in a multimode fibre can be decomposed into components with orthogonal cross-sectional intensity/phase profiles. In a perfect fibre these orthogonal components should not couple with one another, making for an ideal launch condition. This has been achieved by a number of methods, including using beam masks made from etched silica to launch Hermite-Gaussian modes as shown in Figure 1.19 [126], and more recently by using computer generated holograms to launch Laguerre-Gauss modes [127, 128]. The latter method is the preferred one used to implement the MDM system in Chapter 5.

At the receive end, MDM systems must also be able to detect modes, or combinations thereof, selectively through spatial filtering. Perhaps the simplest way of doing this is to use multimode fibre couplers, in which the cores of two input MMF are placed very close together such that high order modes couple between the fibres whereas low order modes do not [123]. Much like the technique of using offset beams at the transmitter, it is also possible to use offset masks at the receiver to detect only a small section of the received intensity profile and this has been successfully used to implement MDM [129]. Similarly, it is also possible to use phase masks, either fixed [130] or generated dynamically using computer generated holography [131, 132] to attempt to detect the orthogonal components of the received composite beam. One such example using fixed phase masks is shown in Figure 1.20.

Another technique that can significantly improve the performance of an MDM system is to use specialised fibre. Recent work has considered special types of fibre that only support a small number of guided modes (typically fewer than 10), termed *few-mode fibre (FMF)*. This is in

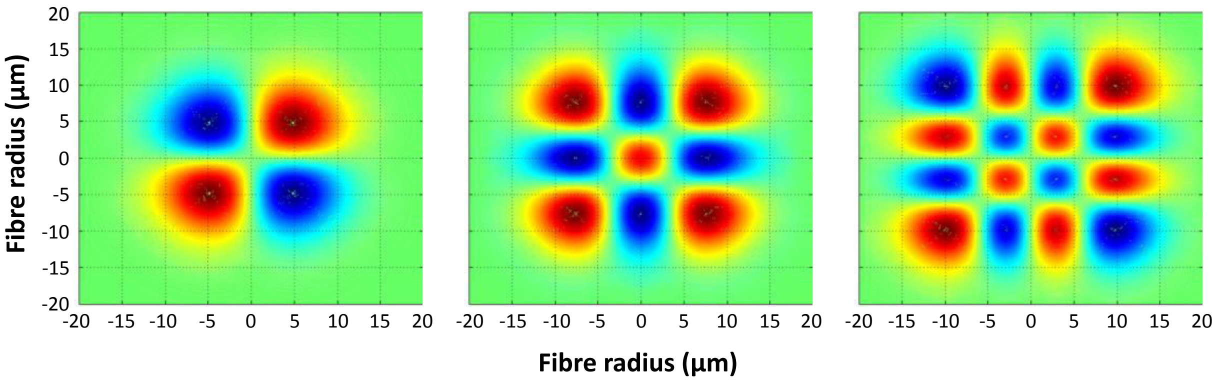

Figure 1.19: Cross-sectional profiles of the three lowest order square Hermite-Gaussian modes that can be used for selective mode excitation in MMF [126].

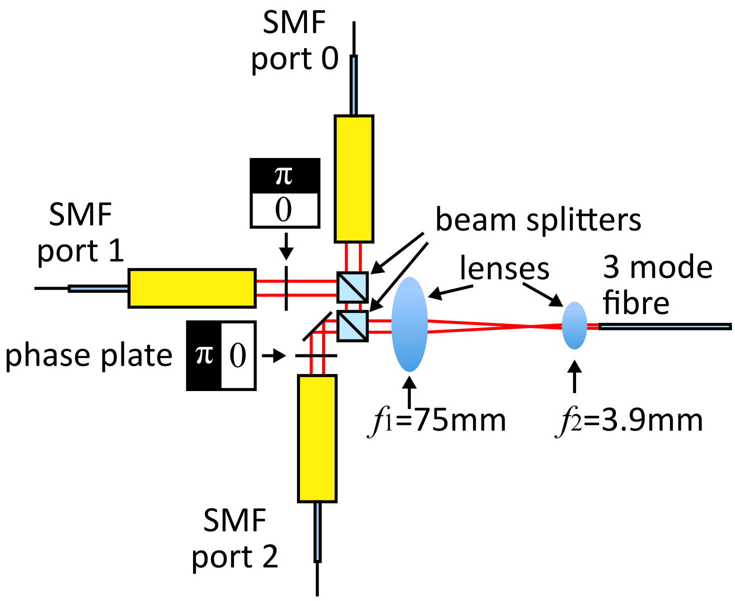

Figure 1.20: Schematic of a mode-multiplexer for 6 modes launched into few-mode fibre [131].

contrast to OM1, OM2 and OM3 MMF that typically supports ∼100 modes at 1550nm and ∼200 at 850nm. Such fibres generally have step-index profiles and can be designed such that the modes they support are easy to launch and there is very little coupling between them. For this reason they are well suited to longer distances (>10km) [133, 134].

Taking the idea of customised fibre to its extreme creates another effective way to implement spatial multiplexing: with multi-core fibres. Such fibres consist of a single cladding structure containing many cores, each of which is usually designed to behave as single mode fibre carrying data independently of the other cores. Technically, such fibres do not support multimode propagation, though the simultaneous excitation of parallel single-mode channels could be considered as a *supermode* of a structured fibre. This has been demonstrated for as many as 19 cores [135]. More recent research has explored *microstructured fibres*, with multiple cores so closely spaced that coupling between them cannot be ignored and they can be considered to support propagation of multiple *supermodes* propagating jointly across cores [136]. This represents a middle ground between multiple single mode propagation and multimode propagation.

The main shortcoming of FMF and multicore techniques is that they require new installation of fibre, a potentially costly and impractical undertaking. As discussed in the previous section, given the many millions of km of OM1,OM2 and OM3 fibre installed in buildings an MDM system used to increase backhaul capacity in such building would need to be able to operate using this. The MDM system used in this work, introduced in more detail in Chapter 5 is designed for and tested using OM2 and OM3 fibre.

1.5 Infrastructure for next generation wireless protocols

As new high speed wireless services such as 4G become widespread the design of the wireless delivery infrastructure will be of critical importance to meeting growing user demands for data. This includes both backhaul links as described in the previous section as well the technology to distribute wireless signal, such as DASs discussed in Section 1.2.3. DASs will have to support emerging new high speed protocols, whether through upgrades to existing single-service DASs or through use of service-independent broadband RoF DASs.

One of the most important technical challenges in this respect is how to combine the capacity benefits of MIMO with the coverage benefits of DAS. This is becoming increasingly important as more wireless services begin to offer MIMO functionality. It is also important that MIMO DASs be broadband so that they can support the full range of existing MIMO systems (800MHz − 5.2GHz for both LTE/4G and 802.11n support) as well as currently unspecified future services. The layout design of DAS installations is of particular importance in achieving this goal. It is important to consider different possible arrangements of antennas and base-stations as the number of users is increased.

In a generalised MIMO-enabled DAS, it is possible to replicate the M transmitted spatial streams at K RAUs, separated by much greater distances than the elements within each antenna array. This can be done in a number of different ways, two examples of which are shown in Figure 1.21. The key difference is the degree to which spatial streams of each service are replicated at separate RAUs. This can be quantified by introducing a term the *replication factor*, R, defined as:

$$R = A = \frac{T}{K} \tag{1.5}$$

where A is the number of antennas per RAU, T is the total number of antennas in the entire DAS and K is the number of RAUs.

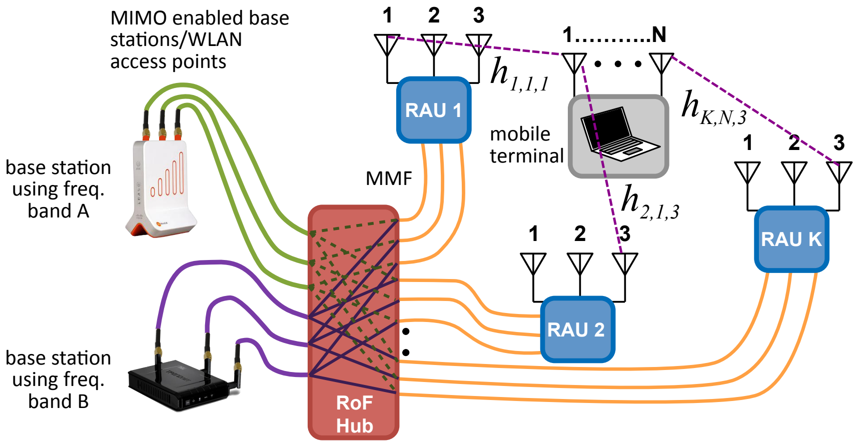

(a)

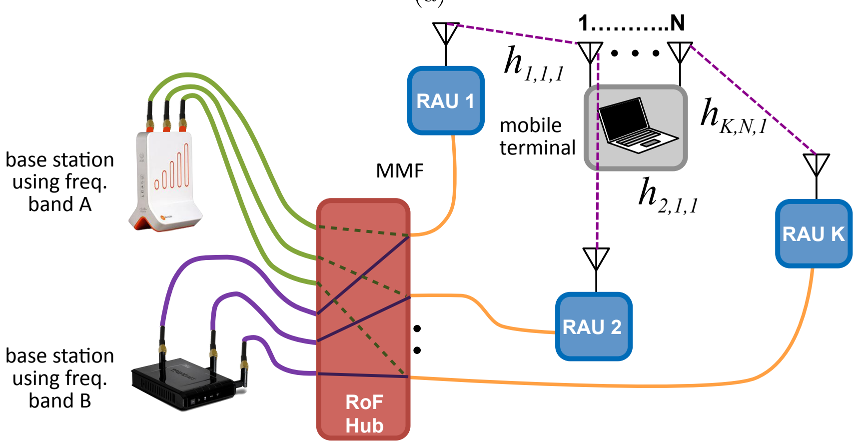

(b)

Figure 1.21: Example layouts for MIMO DAS with K RAUs supporting two base stations each with 3 spatial channels: (a) replicating all base station antennas at all RAUs – a $3 \times N$ MIMO DAS with a replication factor $R = 3$ and (b) using only one spatial stream at each RAU – a $3 \times N$ MIMO DAS with a replication factor $R = 1$.

Previous work has examined two approaches to designing such MIMO DAS. The first is to send all MIMO spatial streams to each RAU, i.e., an $M \times N$ MIMO DAS with replication factor of $R = M$ such as that of Figure 1.21a. This has been shown to provide improved performance over MIMO CAS [137]. A number of multiplexing schemes to provide this functionality over a single fibre have been proposed. Sub-carrier multiplexing and other RF frequency translation techniques have been experimentally proven to be effective [138]. However, these techniques necessarily use up additional sections of the available RF spectrum, which would be quickly exhausted for large numbers of MIMO streams (particularly if they are broadband). *Wavelength division multiplexing* (WDM) has also been proposed as a potential solution to support larger numbers of streams [139, 140]. However, each stream in a WDM system is limited to the bandwidth of the MMF, typically 2GHz.km using offset launch techniques [78]. To provide a 6GHz bandwidth per stream, sufficient to support most modern wireless services including 802.11n at 5.2GHz, the maximum fibre length is limited to ∼300m, which is still sufficient for many designs. The main shortcoming of the WDM approach is the complexity and potential cost of the system – a separate laser source is needed for each wavelength. In DWDM systems each laser must also be carefully temperature controlled to avoid wavelength drifting, incurring additional equipment costs, though uncooled DWDM systems have been proposed [141]. Coarse WDM (CWDM) also avoids the need for temperature control by using lasers with widely spaced wavelengths, though this approach still requires multiple lasers.

The second approach to implementing MIMO DAS is to have separate MIMO spatial streams sent to different RAUs, i.e., an $M \times N$ MIMO DAS with replication factor of $R = 1$ such as that of Figure 1.21b. This, too, has been shown to offer improved capacity over co-located MIMO [142, 143]. This approach has the advantage that it does not require additional fibres or multiplexing so can be implemented with minimal upgrades to existing DAS. Hybrids between these two approaches have also been investigated and shown to offer improved capacity for a 2×2 MIMO system [144].

Theoretical work comparing $M \times N$ MIMO DAS with $R = M$ to MIMO DAS with $R = 1$ has found that the former can offer improved capacity [145]. However, these analyses assume ideal composite fading conditions and are for lower receive SNR (∼10dB) than are found in many indoor DAS installations (typically $>$ 20dB). Once the receive SNR is above ∼20dB, channel capacity becomes increasingly more sensitive to increases in SNR than to reduced correlation between spatial channels [146]. Though systems can operate well with SNR much lower than 20dB, the maximum channel capacity is directly dependent on SNR so high SNR is desired to provide sufficient capacity to meet increasing user demand.

Simulations of a single service (LTE) DAS supporting 2×2 MIMO in a realistic DAS layout have found that both of the two approaches provide comparable results in terms of capacity [147]. However this has not been verified by experimental measurements nor done for a broadband case. Further, little experimental work has been done on indoor MIMO DAS with 3 or more spatial streams.

1.6 Overview of thesis

This dissertation outlines four important contributions to the design of wireless infrastructure design. In particular, these four contributions are related to distributed antenna systems deployed in buildings.

Chapter 2 looks at the design and implementation of a *radio over free-space optics (RoFSO)* link, in which the fibre of a RoF link is replaced with a free space link of up to 50m. This enables much easier and cheaper implementation and deployment of DAS. Further, this enables the creation of very high density DAS with greater flexibility – a key requirement for radical capacity improvement. *This is the first demonstration of a low-cost, broadband RoFSO system designed for operation over distances of ∼50m in indoor DAS environments.*

Chapter 3 then examines in detail the unusual nonlinear behaviour that arises in semiconductor lasers when operated under the conditions required for RoFSO links. The causes are examined and the effects are simulated and observed experimentally. It is found that the high-order nature of this nonlinear behaviour renders meaningless existing measures of link dynamic range, in particular spurious-free dynamic range (SFDR). As a result a new metric for dynamic range called *dynamic-distortion free dynamic range (DDFDR)* is proposed and experimentally validated. This new metric is of great importance to the design of such links as it accurately reflects actual performance in the presence of high-order nonlinearities and can thus be used to design RoFSO links for truly broadband, multi-service operation. *This is the first detailed analysis of high-order distortion effects in lossy analogue optical links and DDFDR is the first metric able to usefully quantify the performance impacts of such behaviour.*

Chapter 4 explores the interaction between DAS infrastructures and the emerging high-speed multiple-input multiple-output (MIMO) protocols they must support. MIMO uses multiple independent radio channels operating simultaneously and on the same frequency. This then changes the way DAS must be designed. It is found that for two representative indoor DAS scenarios, existing directly modulated radio-over-fibre (RoF) installations can enhance the capacity advantages of broadband 3×3 MIMO radio services while providing the coverage benefits of DAS without the requirement for additional fibres or multiplexing schemes. This is true for both the single user and multiple user cases when the possibility of having multiple base stations is considered. A theoretical analysis suggests that only for systems with large numbers of MIMO streams (> 4) is it beneficial to send multiple streams to a single destination. *This is the first experimental work that suggests that clustering of remote antennas in a MIMO DAS is not necessarily beneficial for small numbers of MIMO streams. It is also the first work to propose a basis for making decisions on the level of remote antenna clustering in a DAS based on the number of MIMO spatial channels in use.*

Chapter 5 then considers emerging wireless systems that require large numbers of MIMO channels (4-8) with each channel being broadband (up to 6GHz bandwidth) and how this will be supported on RoF DAS when it is desirable to send all such channels down a single fibre. This is achieved using an emerging method of multiplexing over optical fibre called *mode-division multiplexing (MDM)*. Computer-controlled holograms are used to launch and detect individual propagation modes in a multimode fibre. This is demonstrated to offer improved capacity for a 2×2 MIMO-enabled RoF DAS. Further, the system is characterised to show its potential to provide broadband, near-orthogonal channels up to at least a 4×4 MIMO case and is shown to be robust when the fibre is tightly bent. *This is the first demonstration and analysis of a RoF DAS multiplexing system for MIMO that makes use of MDM. It is the first MIMO over RoF DAS system shown to be capable of providing at least* 4×4 *capability for broadband MIMO channels (3GHz bandwidth).*

Chapter 2

Radio over Free-Space Optical Links

General overview

In order to increase the capacity of wireless networks to keep pace with user demand it is necessary to redesign wireless infrastructure. Distributed antenna systems have a major role to play in this as they enable the creation of dynamically controllable dense networks of signal sources, enabling improvements in coverage and very simple and low-cost addition of extra capacity. Using conventional techniques to connect small, densely-packed remote antennas in a DAS would require prohibitively expensive cabling infrastructure. As a result, this chapter details the development of a novel free-space optical link capable of directly transporting radio signals to remotely located antenna units without cables.

First, a design for a novel RoFSO system is proposed. The set-up is low-cost as it uses direct modulation and detection and does not require optical amplifiers, external modulators or automatic alignment tracking systems. This design is then modelled using a link budget and a spreadsheet simulation is developed. Next, an experimental link using two different lasers, operating at 1547nm and 1310nm, and using an optical attenuator as a free-space simulator is presented. With the 1550nm laser the link is shown to provide a third-order spurious-free dynamic range (SFDR) of >95dB/Hz$^{2/3}$ for an equivalent free-space distance of 50m in the 800MHz and 2.4GHz bands. With the 1310nm laser, which exhibits superior linearity, this same third-order SFDR performance is observed up to an equivalent free-space distance of 300m. Both systems are demonstrated to support 802.11g wireless services providing an EVM <5.6% over a dynamic range of >39dB.

The optical attenuator of the 1310nm experimental set-up is then replaced with a 16m free-space optical link. This enables an examination of the implementation practicalities of free-space optical links such as alignment, which are of critical practical importance. This link is demonstrated to provide a third-order SFDR of >100dB/Hz$^{2/3}$ over a frequency range from 300MHz–3.1GHz, demonstrating the broadband multiservice nature of the link. The performance at 16m is then extrapolated to 50m and is concluded that at this distance the link can provide a third-order SFDR of >109dB/Hz$^{2/3}$ and an 802.11g EVM dynamic range of 36dB. It is concluded that this experiment demonstrates a proof-of-principle broadband, low-cost RoFSO system capable of operating over a distance of 50m, making it suitable for multiservice indoor DAS applications.

This work is drawn partly from a paper presented at the 2010 Semiconductor and Integrated Opto-Electronics (SIOE) conference in Cardiff.

2.1 Introduction

As described in Chapter 1, distributed antenna systems (DAS) using radio-over-fibre (RoF) links provide a powerful means of redesigning indoor wireless delivery infrastructure to meet the increasing demands of users. However, one very important consideration in using RoF DAS is the cost and practicality of installation. In some buildings there may not be pre-existing fibre that can be used for RoF. Even if there is pre-existing fibre, it may not be accessible from the all the RAU locations required to deploy a DAS optimally. Laying large amounts of fibre can be costly or simply not practical so one attractive alternative is to replace some of the optical fibre links in a DAS with free-space optical links - that is, radio over free-space optics (RoFSO) links.

As discussed in Section 1.3.3, free-space optical links have typically been used for either very short-range (<100mm) digital links between chips or for long-range digital data transfer (500m to 2km) [87, 114]. RoFSO links have typically up to now been designed for long-range links [115]. However, for application in high-density indoor DASs, such RoFSO links need only operate over a distance of about 50m. This means that some of the design parameters may be relaxed, enabling designs that are comparable in cost to that of the fibre links they are intended to replace (considering both installation and operation costs). This is particularly important here because of the large number of RoFSO links require to implement a high-density DAS. To achieve this, such links must use as little additional equipment as possible – alignment should be possible using only low-cost lenses and without the use of advanced automatic tracking systems, optical amplifiers or external modulators.

Because of the need to replicate wireless signals faithfully over distance, such RoFSO links are placed under stringent requirements. In particular, the transmit power, optical loss and receiver noise floor must be controlled so that signals with large dynamic ranges are supported. This is required by most wireless systems because on the uplink they must cope with a large variation in power received from different users. It is therefore a significant design challenge to control the parameters of such a link using only simple components, namely directly-modulated lasers and low-cost lenses. Of particular importance is ensuring that the beam is large enough such that it is easily aligned to the receiver while ensuring that the power loss does not adversely affect dynamic range. Furthermore, in order to offer the same advantages as RoF DAS, such links must be demonstrated to be broadband, thereby enabling multiservice operation.

This chapter reports the design and construction of a novel, low-cost RoFSO link. The system supports broadband multiservice radio signals, which are directly modulated onto low-cost distributed feedback (DFB) laser diodes. The link is implemented using only lenses and does not use optical amplifiers but is able to be aligned manually. Selecting the design parameters to enable this is the key achievement of this work.

First, a theoretical model is developed and used to create a link budget simulator, which enables the testing and evaluation of different design parameters for the optical link. It enables the performance of the system to be predicted under a range of conditions. Next, an experimental link is set-up using a fibre link with an attenuator. Two different wavelength lasers are tested: 1547nm and 1310nm. These are chosen because of their compatibility with optical fibre and existing RoF links. This makes them easier to integrate and enables them to reuse modified

RoF equipment. Further, the eye safety limits allow larger transmit powers at these wavelengths than at other potential RoF wavelengths, e.g., 850nm. The 1310nm laser is found to offer better dynamic range performance due to higher modulation linearity, offering a 6.3dB improvement over the 1550nm laser at optical attenuations >20dBo. Similar low-cost highly-linear 1310nm lasers are readily available due to their use in CATV systems [148] and so 1310nm is the preferred wavelength for this RoFSO link. For both lasers, it is seen that the results match the theoretical link budget predictions, verifying the utility of the model as a design tool.

Finally, a 16m free-space link is demonstrated. Of particular importance here are the practical issues not clear from the previous modelling and fibre experiments, in particular the ability to align the system and the measured optical loss. This link is set up using direct modulation and detection only, with no optical amplifiers, and is shown to provide a third-order SFDR of >100dB/Hz$^{2/3}$ over a frequency range from 300MHz–3.1GHz, with only manual alignment. This is sufficient to support a range of wireless services, including 802.11g/n.

2.2 RoFSO System Description and Setup

A schematic of the proposed low-cost broadband RoFSO system is shown in Figure 2.1. At the optical transmitter direct modulation is used to control the intensity of the laser output. The resultant intensity-modulated beam is then transmitted down a length of fibre, collimated using a lens and finally transmitted via free space. At the optical receiver another lens is used to couple the light into a fibre at the end of which it is directly detected using a photodiode. This intensity-modulated direct-detection scheme is often referred to as an *IM-DD* system. It is also possible to remove the fibre on the receive side and have the light fall directly on the photodiode, but the fibre is included in the design to demonstrate compatibility with existing RoF systems on a physical level.

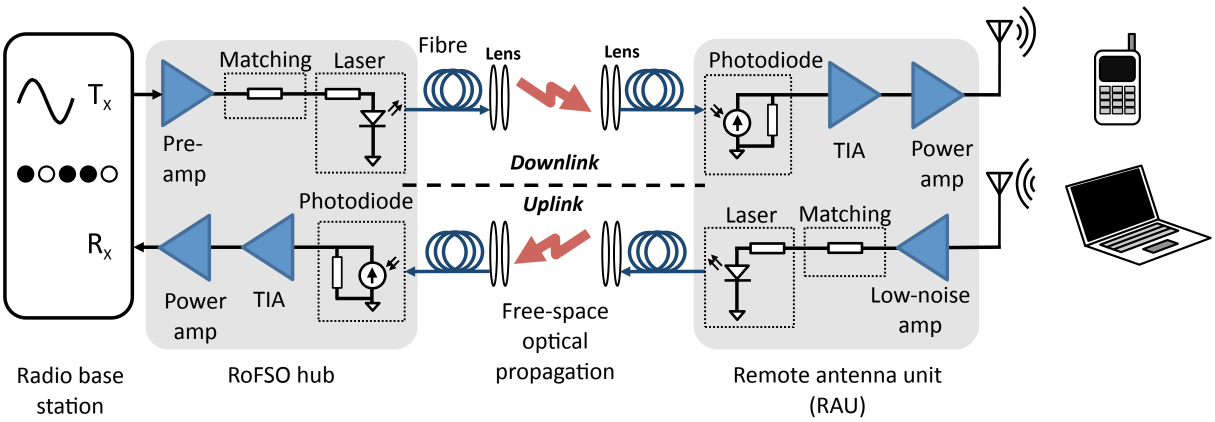

Figure 2.1: Schematic diagram of the proposed RoFSO system showing both the uplink and downlink. TIA stands for *transimpedance amplifier.*

Broadband operation is achieved by using lasers, photodiodes and RF amplifiers with high bandwidths of 3GHz or more, fairly common figures for such devices. The link is constructed entirely using low-cost components including commercially available laser diodes and standard photodiode receivers. It does not require any optical amplifiers, external modulators or advanced equipment required for DWDM.

Any practical RoFSO system must be full duplex so that users can both transmit and receive wireless signals. Accordingly, the system described in this chapter can be used to implement both an uplink and a downlink. However, the uplink has more stringent design requirements than the downlink in terms of dynamic range and noise, due to the wider range of signal powers it must handle.

2.3 Link budget modelling

In order to establish the feasibility of such a RoFSO link and quickly test design parameters, it is first necessary to analyse it theoretically by way of a *link budget*. A basic link budget takes into account all gains and losses, both electrical and optical, in a link including amplifiers, electro-optical and opto-electrical conversion, free-space loss and lens losses. For a given input signal to the link, the magnitude of the output signal can then be estimated. In more advanced link budgets, noise levels and nonlinear distortion throughout the system can also be predicted. This allows estimation of the overall system dynamic range, as discussed in Section 2.3.4.

In creating the link budget the ultimate concern is the end-to-end transformation of the radio signal. To simplify analysis of this the link is treated using small-signal approximations, ignoring bias circuitry. However, bias points are selected for optimum performance particularly with regard to the lasers because of their influence on nonlinear characteristics. Figure 2.2 shows the full small-signal circuit model developed for the RoFSO link presented here, along with the equations modelling gain and noise. It is generally assumed that the impedances of cascaded stages are matched to 50Ω, the most commonly used value in RF circuitry. However, there are some stages for which this is not assumed, such as at the input of the laser diode. Such cases are explicitly indicated in Figure 2.2 and the equations derived do not assume matching.

It can be seen that there is a strong interdependence between many of the elements surrounding the optical link, particularly if the impedances of components are not matched. For this reason, in much of the analysis it is convenient to consider the subsection of the link comprising the laser, the free-space optical link, and the photodiode separately from the overall link. This subsection of the link is referred to as the *optical link*, as indicated in Figure 2.2. This section covers the derivations of these equations in more detail, as well as considering the effects of third-order nonlinearity.

2.3.1 Gain

Optical link

From the small-signal model of the uplink of the optical link shown in Figure 2.2, it can be seen that the optical power output from the laser is given by:

$$P_{\mathrm{CW,out}} = \eta_{ld} \frac{v_s}{R_s + R_{\mathrm{match}} + R_{\mathrm{ld}}} \tag{2.1}$$

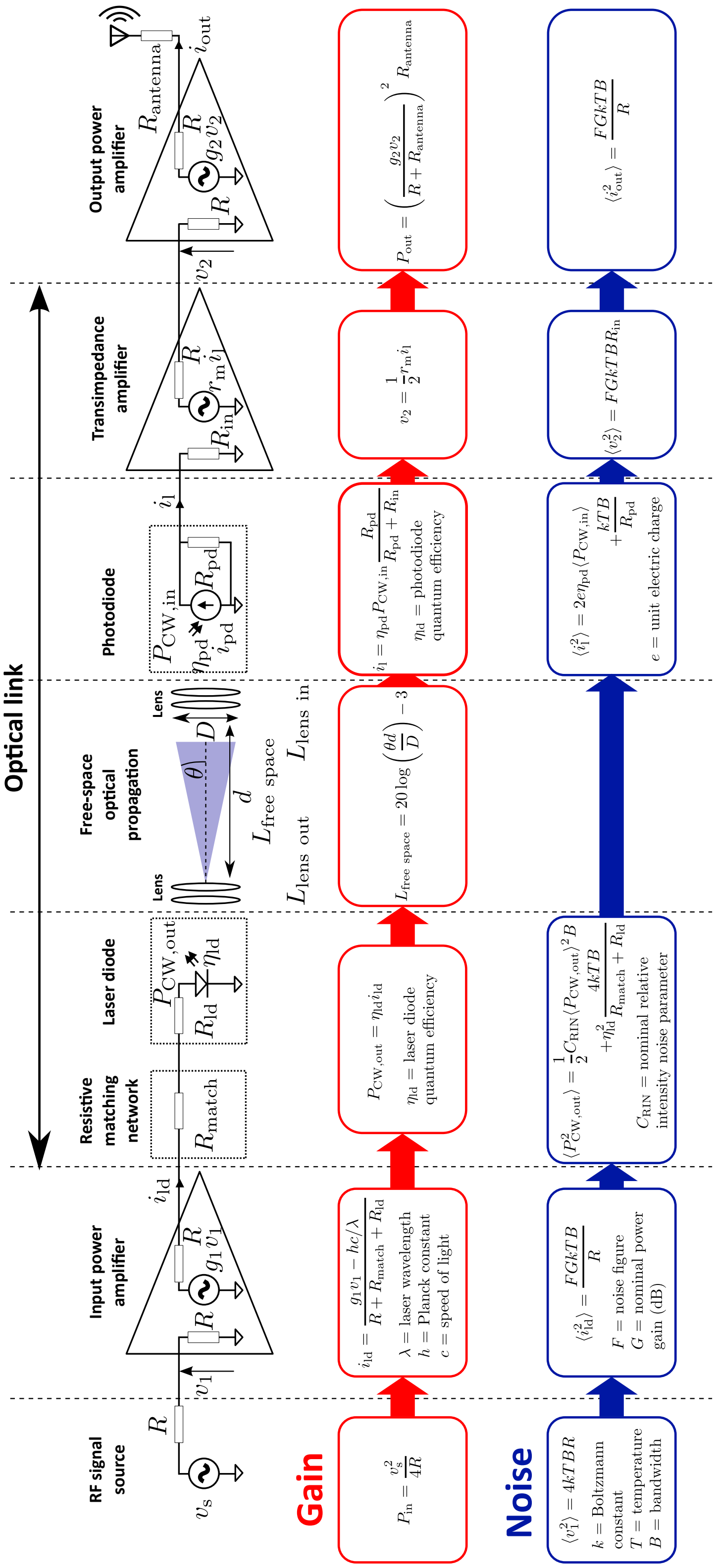

Figure 2.2: Flow chart showing equations used to model gain and noise for the full RoFSO link.

where η_{ld} is the quantum efficiency of the laser diode in W/A, v_s is the output voltage of the previous amplifier stage, R_s is the internal resistance of the previous stage, R_{match} is the matching resistor and R_{ld} is the internal resistance of the laser diode.

Due to unavoidable diffraction at the transmitting aperture, the diameter of any beam of light propagating in free-space will increase with distance. It is possible to focus beams to a minimum width known as the *beam waist*, but after this point the beam will diverge. For beam intensity profiles such as the common Gaussian profile, the beam width follows a well-defined curve as it approaches the beam waist. However, at a large distance from the beam waist it is possible to approximate the beam profile as a divergent cone, as illustrated in Figure 2.3.

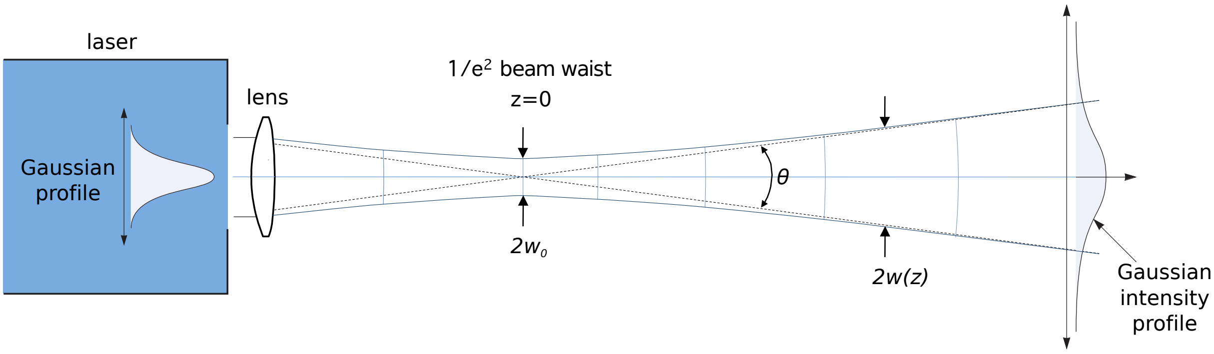

Figure 2.3: Gaussian profile beam converging to a beam waist. At a distance the beam can be approximated by a divergent cone.

The aperture of optical receivers is usually limited in size so with larger beams there can be significant power loss because only a fraction of the received beam will be detected. For a symmetric Gaussian profile beam, at a sufficiently large distance from the transmitter the received power and optical power loss are given by:

$$P_{\text{CW,in}} = \oiint_s \frac{2P_{\text{CW,out}}}{\pi w^2(z)} e^{-2r^2/w^2(z)} dA \tag{2.2}$$

$$L_{\text{free space}} = -10 \log \left(\frac{2}{\pi w^2(z)} \oiint_s e^{-2r^2/w^2(z)} dA \right) \text{ dBo} \tag{2.3}$$

$$\text{where } w(z) = w_0 \sqrt{1 + \left(\frac{z\lambda}{\pi w_0^2} \right)^2} \approx \frac{z\lambda}{\pi w_0} \quad (\text{for } z\lambda \gg w_0^2)$$

where s is the surface of the receiver, w_0 is the beam waist, λ is the wavelength of light, z is the distance from the beam waist, $w(z)$ is the $1/e^2$ beam width at z, and r is the distance from the centre of the beam. It should be noted that the term 'dBo' refers to a loss or gain in decibels occurring in an optical section of the link (hence the suffix 'o'). They are equivalent to 'dB' but are used here for convenience as an indicator of which section of the link is being referred to and as a reminder that end-to-end electrical power gain is related to the square of optical power loss.

If the incident beam is centred on a circular receiver of diameter D then the loss can be expressed as:

$$L_{\text{free space}} = -10\log\left(1 - e^{-D^2/2w^2(z)}\right) \text{ dBo} \tag{2.4}$$

As z becomes large, $w(z)$ tends to a straight line and can be written in terms of the beam divergence, θ. At the receiver, the distance from beam waist to the receiver, z, also approaches the total distance of the link, d, giving:

$$w_{\text{receiver}} \approx \frac{\lambda d}{\pi w_0} = d\tan\left(\frac{\theta}{2}\right) \approx \frac{\theta d}{2} \tag{2.5}$$

The free space loss can thus be approximated by:

$$L_{\text{free space}} = -10\log\left(1 - e^{-2D^2/(\theta d)^2}\right) \text{ dBo} \tag{2.6}$$

For comparing the relative effectiveness of different receivers, it is often useful to use the geometric loss approximation for small divergence angles, which assumes a uniform beam profile, as opposed to Gaussian profile [149]:

$$L_{\text{free space}} = 20\log\left(\frac{\theta d}{D}\right) \text{ dBo} \tag{2.7}$$

where θ is the divergence angle of the beam, d is the distance between the optical transmitter and receiver and D is the diameter of the circular receive aperture. If $d \gg D$, then a first-order Taylor series approximation can be applied to Equation 2.6, which makes it almost identical to Equation 2.7 save for a constant factor of -3dB. This 3dB difference accounts for the different beam profiles used in these two approximations - a uniform 'top hat' profile is assumed for the geometric case. In a Gaussian beam, more power is concentrated towards the centre and so the power detected there is greater. This Gaussian approximation is used to determine the free-space loss in the link budget.

In addition to free-space loss, the lenses may also cause some optical loss. The total received power at the photodiode can then be written:

$$P_{\text{CW,in}} = \frac{P_{\text{CW,out}}}{L_{\text{lens out}} L_{\text{lens in}} L_{\text{free space}}} \tag{2.8}$$

The current generated in the photodiode is then:

$$i_{\text{pd}} = \eta_{\text{pd}} P_{\text{CW,in}} \tag{2.9}$$

where η_{pd} is the responsivity of the photodiode in A/W. From figure 2.2 it can be seen that the current into the *transimpedance amplifier* (TIA) is:

$$i_l = i_{\text{pd}} \frac{R_{\text{pd}}}{R_{\text{pd}} + R_{\text{in}}} \tag{2.10}$$

and the output voltage delivered to the load is given by:

$$v_{\text{out}} = r_m i_l \frac{R_{\text{load}}}{R_{\text{out}} + R_{\text{load}}} \tag{2.11}$$

Therefore, the overall voltage gain is given by:

$$\begin{aligned} g_v = \frac{v_{\text{out}}}{v_{\text{in}}} &= r_m \frac{v_s}{R_s + R_{\text{match}} + R_{\text{ld}}} \frac{\eta_{\text{pd}}\eta_{\text{ld}}}{L_{\text{lens out}} L_{\text{lens in}} L_{\text{free space}}} \\ &\qquad \cdot \frac{R_{\text{pd}}}{R_{\text{pd}} + R_{\text{in}}} \frac{R_{\text{load}}}{R_{\text{out}} + R_{\text{load}}} \bigg/ v_s \frac{R_{\text{match}} + R_{\text{ld}}}{R_s + R_{\text{match}} + R_{\text{ld}}} \\ &= r_m \frac{\eta_{\text{pd}}\eta_{\text{ld}}}{L_{\text{lens out}} L_{\text{lens in}} L_{\text{free space}}} \frac{R_{\text{pd}}}{R_{\text{pd}} + R_{\text{in}}} \frac{R_{\text{load}}}{R_{\text{out}} + R_{\text{load}}} \frac{1}{R_{\text{match}} + R_{\text{ld}}} \end{aligned} \tag{2.12}$$

If we assume that the input and outputs are both impedance matched, the power gain becomes:

$$G_p = \frac{P_{\text{out}}}{P_{\text{in}}} = \frac{v_{\text{out}}^2}{R_{\text{load}}} \bigg/ \frac{v_{\text{in}}^2}{R_{\text{match}} + R_{\text{ld}}} \tag{2.13}$$

Overall

Once the gain of the optical link has been determined, it is considered a single element of the overall system. To determine the overall gain of the system, the power gains of the cascaded stages are simply multiplied (or added together if in dB).

2.3.2 Noise

Optical link

There are three main sources of noise in the optical link: thermal noise, shot noise and relative intensity noise (RIN). Nyquist showed that any resistive device produces random voltage fluctuations because of thermal excitation of charge carriers and that this effect can be modelled by a random voltage source [150]. The mean square of this voltage is modelled as:

$$\langle v_{\text{th}}^2 \rangle = 4kTBR \tag{2.14}$$

where k is the Boltzmann constant, T is the temperature of the resistor in kelvin, B is the bandwidth of the system and R is the value of the resistor in ohms. The angle brackets indicate the time average of a random process. In the optical link there are thermal noise sources associated with all resistors as well as with the transimpedance amplifier. The mean-square voltages of all the noise sources can be summed together to find the mean-square voltage of a single equivalent source. This is possible because the noise sources are modelled by independent, random variables of zero mean. Figure 2.4 shows an equivalent circuit using voltage sources to model the effect of thermal noise. Thermal noise created in this manner is assumed to be white noise (i.e. have a flat spectrum) over the range of frequencies used for most wireless services [76].

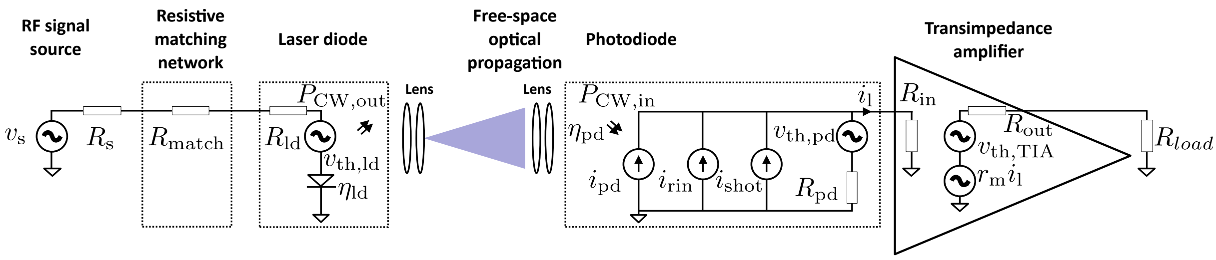

Figure 2.4: Schematic showing modelled noise sources in optical link.

There is also noise created as a result of the random nature of the excitation of charge carriers by photons in the receiver photodiode. This type of noise is called *shot noise* and it is a result of the quantum nature of electrical currents. For a given optical power, the rate of arrival of photons depends on the wavelength of the light and this influences the amount of shot noise. Similarly, the construction of the photodiode affects the way photons are converted to electrons and hence the shot noise level – for example avalanche multiplication devices can amplify shot noise. Here, it is assumed that a single wavelength is used and that a PIN photodiode is used at the receiver, with no avalanche effects. Assuming Poisson distributed arrival times for photons incident on the photodiode the mean-square shot noise current at the photodiode is given by:

$$\langle i_{\mathrm{shot}}^2 \rangle = 2eI_{\mathrm{pd}}B = 2e\left(I_{\mathrm{bias}} - I_{\mathrm{th}}\right)\frac{\eta_{\mathrm{pd}}\eta_{\mathrm{ld}}}{L_{\mathrm{lens\ out}}L_{\mathrm{lens\ in}}L_{\mathrm{free\ space}}}B \tag{2.15}$$

where e is the unit electrical charge, I_{bias} is the bias current of the laser, I_{th} is the threshold current and B is the bandwidth of the system. The effect of this noise can be modelled by a current source, i_{shot} at the receiver as shown in Figure 2.4. If the rate at which photons arrive at the photodiode is large relative to the system bandwidth, then this Poisson-distributed noise source is well-approximated by a Gaussian-distributed noise source [151]. In the free-space links used here, the system bandwidth is around 3GHz and the rate of arrival of photons is of the order of 10^{14} so this approximation is valid. The shot noise is then considered to be generated by a Gaussian source whose mean (and variance) is given by Equation 2.15.

The third type of noise, *relative intensity noise (RIN)*, arises from a combination of factors including the random nature of emission of photons from the laser cavity, fluctuation in the laser pump current and relaxation oscillation (i.e. resonance) of the laser cavity. This noise is produced entirely within the laser and manifests itself as random fluctuations in the laser output power. The average RIN power over a given bandwidth is defined as [152]:

$$\mathrm{RIN} = \frac{2\langle p_{\mathrm{RIN}}^2 \rangle}{\langle P_0 \rangle^2 B} \tag{2.16}$$

where p_{RIN} is the randomly fluctuating component of the laser output power, P_0 is the average intensity of the beam and B is the bandwidth of the system. Note that this formula represents an average and that in reality RIN is frequency-dependent and its spectrum will have a peak determined by the laser relaxation oscillation frequency. This peak moves as the bias current changes, so the bias current can be used to control the level of RIN. A consequence of this is that RIN is not white noise. However, in a band-limited system, if the RIN peak occurs at a frequency well outside the bandwidth it can be modelled as band-limited white Gaussian noise. Even if this is not the case, RIN can still be considered filtered white Gaussian noise and so can still display Gaussian statistics to a first-order approximation (though its higher order correlation properties may change). It is then reasonable to model RIN as being produced by a random Gaussian source as is done here.

By simple rearrangement and analysis of the circuit schematic, it can be shown that the resultant RIN current produced at the photodiode receiver can be modelled by a current source, i_{RIN}, as shown in Figure 2.4:

$$\begin{aligned}\langle i_{\mathrm{RIN}}^2\rangle &= \left(\frac{\eta_{\mathrm{pd}}\eta_{\mathrm{ld}}}{L_{\text{lens out}}L_{\text{lens in}}L_{\text{free space}}}\right)^2 \langle p_{\mathrm{RIN}}^2\rangle \\ &= \left(\frac{\eta_{\mathrm{pd}}\eta_{\mathrm{ld}}}{L_{\text{lens out}}L_{\text{lens in}}L_{\text{free space}}}\right)^2 \frac{B}{2}\left(I_{\mathrm{bias}} - I_{\mathrm{th}}\right)^2 \mathrm{RIN} \end{aligned} \tag{2.17}$$

Because all the noise sources used can be modelled as independent and Gaussian-distributed, when cascaded together as in Figure 2.4 the resultant combined noise is Gaussian-distributed with an expected noise power delivered to the load of:

$$\begin{aligned} N_{\mathrm{out}} = \Bigg[\Bigg(\langle v_{\mathrm{th,ld}}^2\rangle \frac{\langle v_{\mathrm{th,ld}}^2\rangle}{(R_s + R_{\mathrm{match}} + R_{\mathrm{ld}})^2} \left(\frac{\eta_{\mathrm{pd}}\eta_{\mathrm{ld}}}{L_{\text{lens out}}L_{\text{lens in}}L_{\text{free space}}}\right) \\ + \frac{\langle v_{\mathrm{th,pd}}^2\rangle}{R_{\mathrm{pd}}^2} \left(\frac{\eta_{\mathrm{pd}}\eta_{\mathrm{ld}}}{L_{\text{lens out}}L_{\text{lens in}}L_{\text{free space}}}\right) + \langle i_{\mathrm{RIN}}^2\rangle + \langle i_{\mathrm{shot}}^2\rangle \Bigg) \\ \cdot \left(\left(\frac{R_{\mathrm{pd}}}{R_{\mathrm{pd}} + R_{\mathrm{in}}}\right)^2 r_{\mathrm{in}}^2 + \langle v_{\mathrm{th,TIA}}^2\rangle \right) \Bigg] \frac{R_{\mathrm{load}}}{(R_{\mathrm{out}} + R_{\mathrm{load}})^2} \end{aligned} \tag{2.18}$$

where i_{shot} and i_{RIN} are as given in equations 2.15 and 2.17 respectively. It is noted that thermal noise produced in the photodiode is by far the dominant source of thermal noise because it is not affected by the optical loss. Shot noise is proportional to optical loss and RIN increases with the square of this loss. This provides a method of distinguishing between and measuring the different sources of noise in experiments.

Given the output noise power and the gain of a link, a convenient way to specify noise is through use of the *noise figure* defined as:

$$F = \frac{\mathrm{SNR_{in}}}{\mathrm{SNR_{out}}} = \frac{S_{\mathrm{in}}}{S_{\mathrm{out}}}\frac{N_{\mathrm{out}}}{N_{\mathrm{in}}} = \frac{N_{\mathrm{out}}}{G_p N_{\mathrm{in}}} \tag{2.19}$$

where G_p is the power gain of the system as defined in Section 2.3.1 and SNR stands for *signal to noise ratio*. The input noise is usually defined as the thermal noise power produced by a matched resistive load at the input. The equation for noise figure then simplifies to:

$$F = \frac{N_{\text{out}}}{G_p kTB} \tag{2.20}$$

This is a convenient metric because for an impedance-matched system with known gain, the output noise can be calculated by a simple rearrangement of this formula. The noise figure for the optical link can be found from inserting Equation 2.18 for output noise and Equation 2.13 for power gain into Equation 2.20.

Overall

If the noise figures of each component, including amplifiers and the optical link, the overall noise figure of the combined system is found by cascading the noise figures of the components:

$$F_{\text{total}} = F_1 + \frac{F_2 - 1}{G_1} + \frac{F_3 - 1}{G_1 G_2} + \cdots + \frac{F_n - 1}{G_1 G_2 \cdots G_n} \tag{2.21}$$

This is used in the link budget to determine the total resultant noise at the output. Noise figures for amplifiers are usually specified in the data sheets but can alternatively be determined empirically by measuring noise power at the amplifier output with a matched impedance on the input.

2.3.3 Nonlinearity

Distortion

As described in Section 2.3.2, the minimum allowable power for a radio signal on the RoFSO link is limited by noise – that is, the SNR must always be above a certain minimum threshold. Similarly, there are also limits on the how powerful the radio signal can become before the performance once again starts to decrease. The limiting factor here is distortion caused by nonlinearities in the system, particularly the laser.

The behaviour of semiconductor lasers can be modelled by a series of coupled differential equations, from which nonlinear behaviour can be seen to arise [153]. These equations, as well as a detailed discussion of the nature of nonlinear behaviour in semiconductor lasers are given in Section 3.3. For the purposes of developing a link budget it is sufficient to use a simplified high-level treatment of nonlinear behaviour.

The nonlinear nature of lasers is evident when plotting their output light power as drive current is increased, an example of which is shown in Figure 2.5.

From a high-level perspective the output power of a semiconductor laser is a function of the drive current, I, and time, t, expressed as $P(I, t)$. The dependence on time reflects the fact that the properties of the laser change dynamically with time, caused by phenomena such as spatial hole burning [154], resulting in additional time-dependent nonlinearity. In the link budget derived here only static (i.e. time-invariant) nonlinearity is considered for the sake of

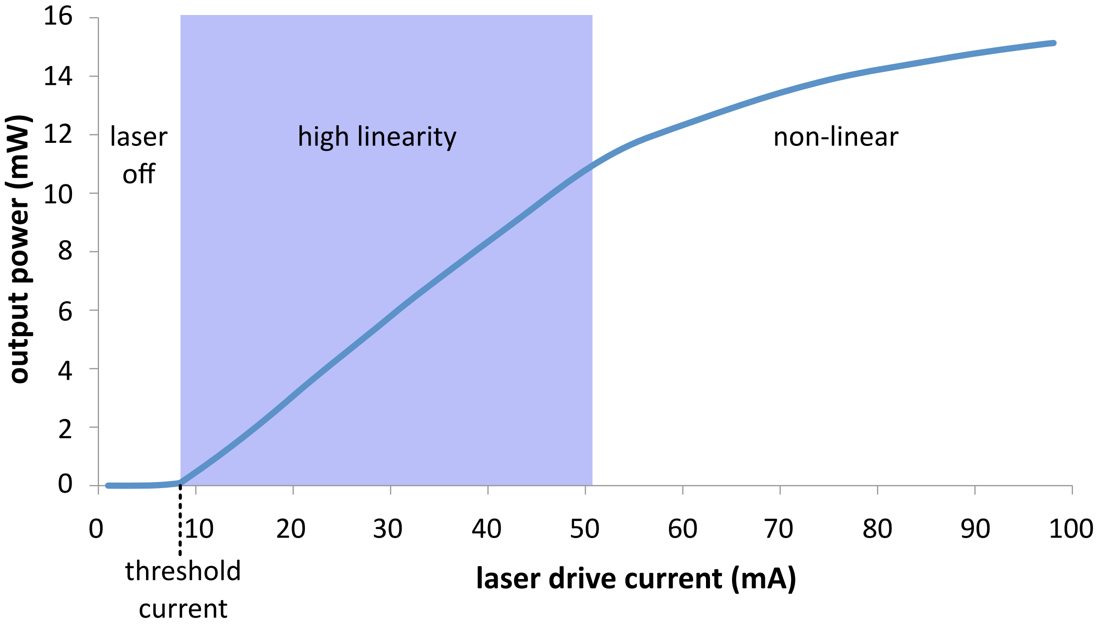

Figure 2.5: Measured light vs. current curve for a typical 1310nm laser diode showing the linear and nonlinear regions of operation.

simplicity in this initial approximation. The power transfer function is then assumed only to depend on I and can be expressed by its Taylor series expansion:

$$P(I) = P(I_0) + (I - I_0)\frac{\partial P}{\partial I} + \frac{1}{2}(I - I_0)^2\frac{\partial^2 P}{\partial I^2} + \cdots + \frac{1}{n!}(I - I_0)^n\frac{\partial^n P}{\partial I^n} + \cdots \tag{2.22}$$

where $P(I)$ is the transfer function of the laser and I_0 is the point around which the expansion is made.

Generally speaking, an information carrying signal can be represented as the sum of several sinusoids at different frequencies. The simplest possible case of this consists of just two sinusoids. With this as an input, the second order nonlinearity produces at the output:

$$\begin{aligned} g_2(x) &= b \cdot (\cos(f_1 x) + \cos(f_2 x))^2 \\ &= b\left(1 + \cos((f_1 - f_2)x) + \cos((f_1 + f_2)x) + \frac{1}{2}\cos(2f_1 x) + \frac{1}{2}\cos(2f_2 x)\right) \end{aligned} \tag{2.23}$$

Clearly, there are new frequency components being generated. Some of these are *harmonics*, whose frequencies are integer multiples of the input signals' frequencies (e.g., $2f_2$), and the rest are termed *intermodulation distortion (IMD) products* and have frequencies at linear combinations of the input signals' frequencies (e.g., $f_1 - f_2$). A third-order nonlinear system would produce the following distortion productions:

$$
\begin{aligned}
g_3 =& c \cdot (\cos(f_1 x) + \cos(f_2 x))^3 \\
=& \frac{c}{4}\big(9 \cdot \cos(f_1 x) + \cos(3 f_1 x) + 9 \cdot \cos(f_2 x) + \cos(3 f_2 x) + 3\cos((2 f_2 - f_1) x) \\
&+ 3\cos((2 f_1 - f_2) x) + 3\cos((2 f_1 + f_2) x) + 3\cos((2 f_2 + f_1) x)\big)
\end{aligned}
\tag{2.24}
$$

Pure harmonics (e.g. $2f_1$, $3f_2$) can often be filtered out because of their large frequency separation from the fundamental frequency. For the same reason even-order IMD products, such as the second-order products derived in Equation 2.23, can be filtered relatively easily are so are often ignored.

Odd-order IMD products, on the other hand, can fall very close in frequency to the original signals, particularly the products at frequencies $2f_1 - f_2$ and $2f_2 - f_1$ when f_1 and f_2 are close. In fact, these products almost always fall within the bandwidth of the original signal making them impossible to filter. This causes a reduction in signal quality and so these IMD products are often the main factor limiting the highest power signal the link can support. It is often assumed that nonlinear effects higher than third-order can be ignored but it is shown in the next chapter that for RoFSO links this is not always the case. Assuming third-order only behaviour results in inaccuracies when quantifying system performance. Ultimately, higher orders of distortion must also be considered. However, for the development of an initial link budget it is possible to obtain a very rough indicator of performance assuming only third-order distortion.

Under this third-order only assumption we consider a system with an input of two sinusoids of equal amplitude at frequencies f_1 and f_2. The spectrum and output power vs. input power plots look like those shown in Figure 2.6, with third-order IMD products at frequencies $2f_1 - f_2$ and $2f_2 - f_1$. The input power at which these third-order IMD products produce an output power equal to the fundamental harmonic power is called the *third-order input intercept point (IIP3)* and is commonly used as a measure of third-order only nonlinearity.

Optical Link

Again, assuming third-order only nonlinear behaviour that is time-invariant (i.e., ignoring dynamic effects) the laser diode, photodiode and TIA can each be assumed to have transfer function consisting of a linear term and a third-order term:

$$f(x) = ax + bx^3 \tag{2.25}$$

where a is either the quantum efficiency of the laser diode, the responsivity of the photodiode or the gain of the TIA. The second order term is ignored because it is assumed that second-order IMD products can easily be filtered. Using the circuit in Figure 2.2, the resultant voltage transfer function of the optical link can be written:

$$V_{\text{out}} = aV_{\text{in}} + bV_{\text{in}}^3 \tag{2.26}$$

where

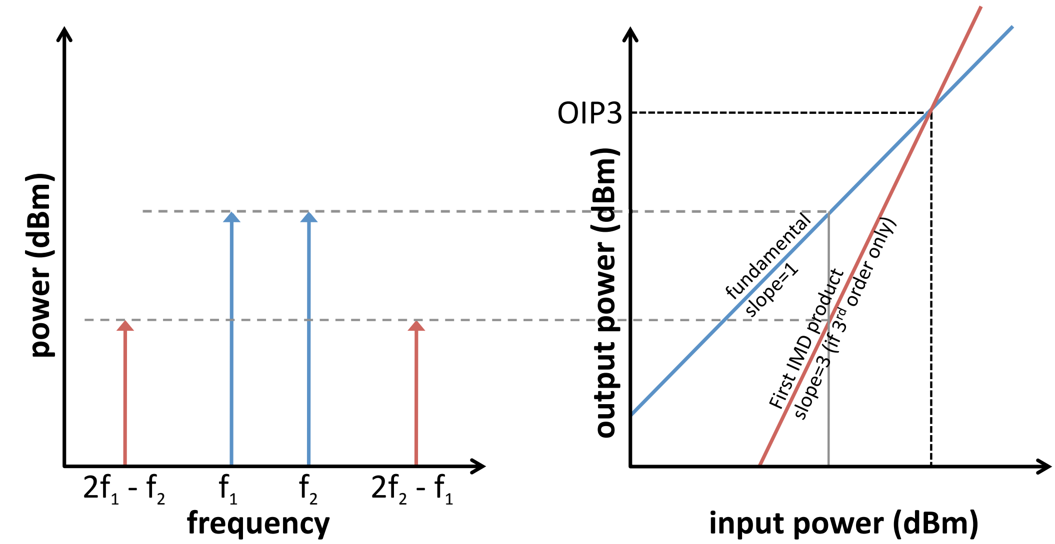

Figure 2.6: Power spectrum and input power vs. output power graphs showing third-order only IMD products.

$$a = \frac{R_{\text{load}}}{R_{\text{load}} + R_{\text{out}}} r_m \frac{R_{\text{pd}}}{R_{\text{pd}} + R_{\text{in}}} \frac{\eta_{\text{pd}}\eta_{\text{ld}}}{L} \frac{1}{R_{\text{match}} + R_{\text{ld}}} \tag{2.27}$$

and

$$\begin{aligned} b = \frac{R_{\text{load}}}{R_{\text{load}} + R_{\text{out}}} \Bigg(r_m \frac{R_{\text{pd}}}{R_{\text{pd}} + R_{\text{in}}} \left(\frac{\eta_{\text{pd}} b_{3\text{ld}}}{L_{\text{lens out}} L_{\text{lens in}} L_{\text{free space}}} + \frac{\eta_{\text{ld}}^3 b_{3\text{pd}}}{L^3} \right) \\ + b_{3\text{TIA}} \left(\frac{R_{\text{pd}}}{R_{\text{pd}} + R_{\text{in}}} \frac{\eta_{\text{pd}}\eta_{\text{ld}}}{L_{\text{lens out}} L_{\text{lens in}} L_{\text{free space}}} \right)^3 \Bigg) \frac{1}{(R_{\text{match}} + R_{\text{ld}})^3} \end{aligned} \tag{2.28}$$

where b_{3X} represents the third-order coefficient of the transfer function of device X. The IIP3 of the optical link is then:

$$\text{IIP3} = \frac{4}{3} \frac{a}{b} \frac{1}{R_{\text{match}} + R_{\text{ld}}} \tag{2.29}$$

Knowing this relationship, it is possible to experimentally determine the constituent third-order distortion coefficients based on the overall IIP3 of the optical link. This can be done by inserting attenuators at different parts of the link so that just one coefficient predominates. This can then be measured and used in the model. Other coefficients can be found in the same way or by fitting this model to experimental data.

Overall

When the IIP3s for each element in the system are known it is possible to cascade them together to determine the overall IIP3 of the system using the formula [155]:

$$X_{\text{total}} = \left(\frac{1}{X_1} + \frac{G_1}{X_2} + \frac{G_1 G_2}{X_3} + \cdots + \frac{G_1 G_2 \cdots G_{N-1}}{X_N} \right) \tag{2.30}$$

where X_n is the IIP3 of the n^{th} element in the system and G_n is the gain of that element.

2.3.4 Dynamic Range

Dynamic range is defined as the range of signal powers that a link can handle without significant performance degradation. The lower limit is determined by noise and the upper limit is determined by nonlinear distortion. Dynamic range is a very important measure and it is often specified in telecommunication standards. For a RoFSO system the primary consideration is the dynamic range of the section of the link extending from the terminals of the wireless base station to the input/output terminals of the antenna at the other end of the link. Provided this is greater than the requirements for the desired wireless services, the RoFSO link is effectively transparent to the radio transceiver.

Spurious Free Dynamic Range

One common way to quantify dynamic range is the *spurious-free dynamic range (SFDR)*. In its most general sense SFDR uses as its lower limit the input power at which the SNR is unity and as its upper limit the input power at which a nonlinear distortion product (a *spur*) becomes powerful enough to degrade performance of some system. The SFDR is simply the ratio of these two limits. This spur could be a harmonic creating out-of-band interference and degrading the performance of another service or, more commonly, it could be an IMD product creating in-band interference.

SFDR can be measured using a specific test whereby two sinusoids of the same amplitude at different frequencies are input to a system, termed a *two-tone test*. At the output appears an amplified version of the two sinusoids as well as distortion products due to nonlinearities as discussed in Section 2.3.3. This is illustrated in Figure 2.7.

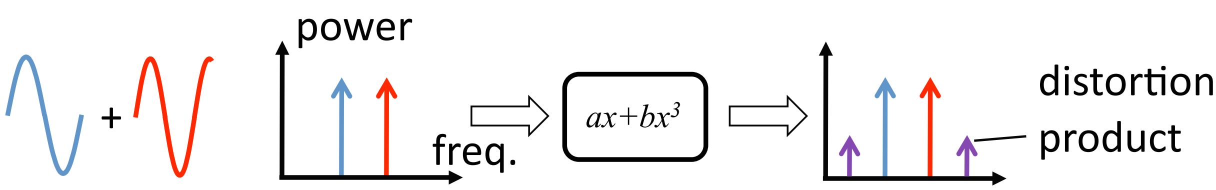

Figure 2.7: Illustration of the standard two-tone test to determine the SFDR showing how the IMD products are formed.

The most commonly used variant of SFDR uses as its reference spurs the IMD products created by third-order nonlinearities in this two-tone test, namely those at frequencies $2f_1 - f_2$

or $2f_2 - f_1$ for input tones at frequencies f_1 and f_2. This metric is hence termed *third-order SFDR*. The third-order SFDR is the ratio (or difference in dB) between the input power at which the $2f_1 - f_2$ (or $2f_2 - f_1$) IMD product rises above the noise floor and the input power at which the fundamental component rises above the noise floor. The noise floor used is normalised to a 1Hz measurement bandwidth to ensure that the third-order SFDRs for links of different bandwidths are directly comparable. The IMD products used here are assumed to arise purely from third-order effects, though this may not be the case in reality as discussed in the next chapter. The calculation of third-order SFDR is illustrated in Figure 2.8. From geometric considerations it can be seen that, assuming no distortion of order greater than 3 is present, the third-order SFDR is given by:

$$\mathrm{SFDR} = \frac{2}{3}\left(\mathrm{IIP3} - P_{\text{noise floor}} - G\right) \tag{2.31}$$

where $P_{\text{noise floor}}$ is the noise floor power measured at the output in dBm/Hz and G is the device gain in dB. The overall units are then dB/Hz$^{2/3}$. Though these may seem unusual units they simply reflect the fact that the noise floor is normalised to a 1Hz bandwidth (although this is done *before* conversion to dB and so the notation is misleading) and the fact that if a bandwidth other than 1Hz were to be used, then to denormalise the third-order SFDR in linear units it must be multiplied by the target bandwidth raised to the $^2/_3$ power.

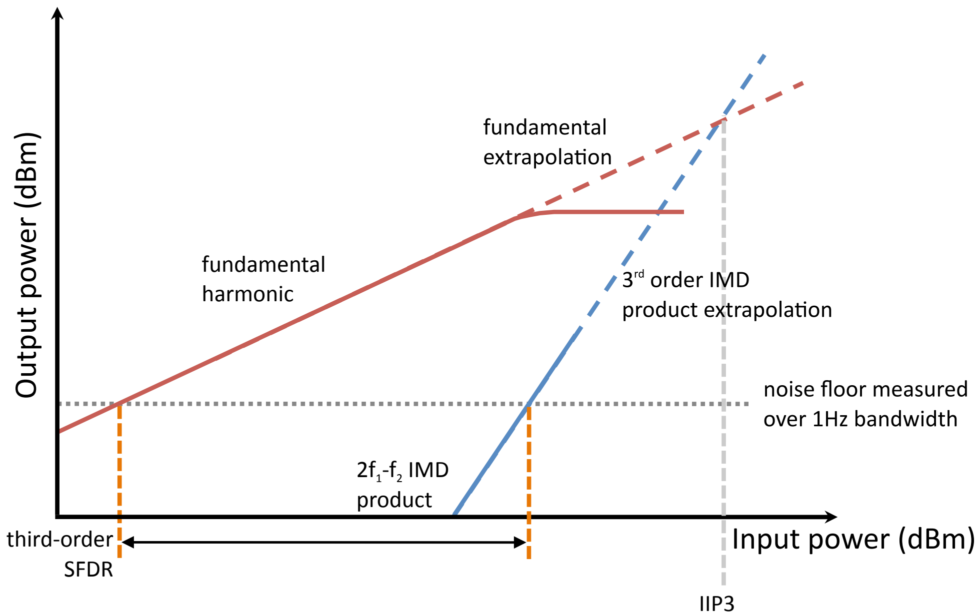

Figure 2.8: Graph of input power vs. output power for a system showing a geometric representation of third-order only SFDR.

By cascading noise figures and third-order intercepts for all stages in the link budget, it is possible to determine the overall system third-order SFDR. This is the most useful parameter predicted by the link budget as it indicates which services the link can realistically support.

However, if distortion of order higher than three is present, third-order SFDR becomes difficult to predict due to the changing slope of the $2f_1 - f_2$ IMD product and other measures must be used. This is discussed in detail in the next chapter.

While third-order SFDR is a useful metric, it is not fully representative of a system's dynamic range as it is only defined for a two-tone input, whereas real signals use a much broader range of frequencies. Estimated third-order SFDR values required to support a variety of wireless services are shown in Table 2.1.

Table 2.1: Common estimated third-order SFDR requirements for wireless services.

Service	**Required third-order SFDR (dB/Hz$^{2/3}$)**
WiFi (2.4GHz)	$\sim$95
GSM (900MHz) [156]	85-95
3G WCDMA (1.8-2.2GHz) [156]	<85

Error Vector Magnitude

Another method of quantifying system dynamic range is *error vector magnitude (EVM)*. This takes into account the modulation scheme of the data and provides a very realistic measure of end-to-end system performance.

Complex modulation schemes, such as 64-QAM OFDM used for 802.11g WiFi, create each transmitted symbol using a particular linear combination of sinusoids of different phase and amplitude. This can be expressed as the weighted sum of an *in-phase (I)* and a *quadrature (Q)* sinusoidal component with a relative phase difference of $\pi/2$ between them. Graphically, this is represented using a constellation diagram as in Figure 2.9.

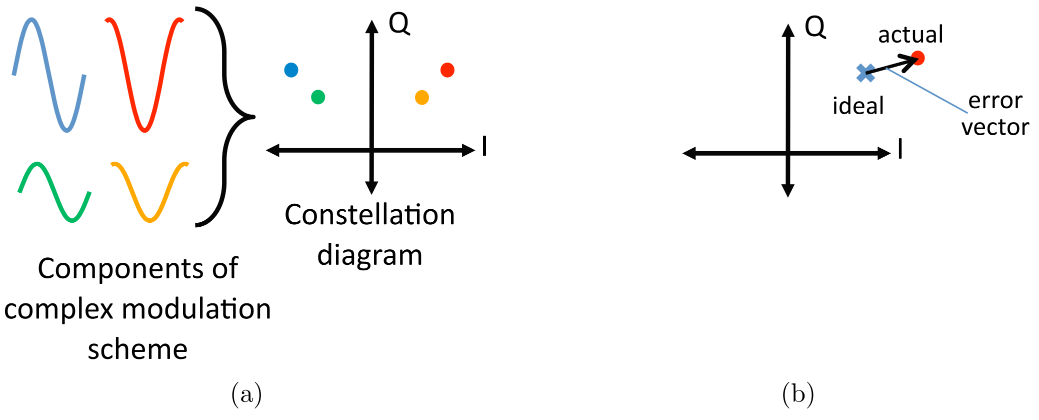

Figure 2.9: Illustration of the constellation diagram for a complex modulation scheme showing (a) the decomposition of a signal into constituent in-phase and quadrature components on a constellation diagram and (b) the error vector magnitude resulting from an actual received symbol with noise or distortion added.

Due to the effects of link noise and distortion a real received symbol will not fall exactly in the correct position on the constellation diagram. This offset from the ideal symbol vector is called the *error vector*. The magnitudes of all these error vectors can be averaged and quoted as a percentage of the magnitude of the maximum ideal symbol vector, giving the average EVM over a link:

$$\mathrm{EVM} = \sqrt{\frac{1}{N}\frac{\sum_{n=1}^{N}\left(\left|I_{\mathrm{meas}}\left[n\right]-I_{\mathrm{ref}}\left[n\right]\right|^2+\left|Q_{\mathrm{meas}}\left[n\right]-Q_{\mathrm{ref}}\left[n\right]\right|^2\right)}{\max_n\left(I_{\mathrm{ref}}\right)^2+\max_n\left(Q_{\mathrm{ref}}\right)^2}} \tag{2.32}$$

where $I_{\mathrm{meas}}[n]$ is the measured in-phase value for the n^{th} symbol, $Q_{\mathrm{ref}}[n]$ is the ideal quadrature value for the n^{th} symbol etc. The range of signal powers over which the EVM is less than a specified level is referred to as the *EVM dynamic range* and provides a very realistic measure of system performance. An example plot of EVM vs. transmitted signal power highlighting the dynamic range is shown in Figure 2.10. The 802.11g standard requires that for proper operation the EVM must be kept below 5.6% over a power range of 48dB for the uplink [157]. 3GPP WCDMA services require an EVM of only 17.5% for the uplink but over a dynamic range of 69dB [158]. If the cell size, i.e. the area served by a single wireless transceiver, is reduced then the dynamic range requirement can be lowered. In a DAS, the effective cell size is greatly reduced because of the more even distribution of radio signal and so a lower EVM dynamic range would still allow the same overall coverage area. Thus, these limits are not considered strict.

Typically, link budgets are calculated using spreadsheets that work on statistical average behaviour. The calculation of EVM requires simulated modulation of data, a task for which spreadsheets are not well suited as they cannot usually generate and process large data sets dynamically. As a result EVM is often not included in link budget models. However, it is easily measured experimentally, such as in Section 2.4, and provides a useful and practical measure of dynamic range. The main drawback of EVM dynamic range as a metric is that it depends on the modulation scheme used and so is a service specific measure. This is in contrast to third-order SFDR, which is service-independent and can be estimated using spreadsheet models.

2.3.5 Spreadsheet model

Spreadsheets are well suited to link budget calculations as they allow the examination of intermediaries for cascaded quantities such as gain and noise, and allow for quick adjustment of multiple parameters. Using the equations derived thus far, a spreadsheet model of a RoFSO link was constructed. All equations were simply translated into cell evaluation formulas, and the parameters of components, taken from data sheets or measured independently, serve as the inputs to the calculation. The gain, noise, IIP3 and third-order SFDR can be calculated directly from this spreadsheet. As discussed in Section 2.3.4, EVM dynamic range is not included due to the inability of spreadsheet models to process modulated data. A screenshot showing typical usage of the RoFSO link budget spreadsheet is shown in Figure 2.11.

The spreadsheet consists of 3 sheets. The main sheet, shown in Figure 2.11, models the

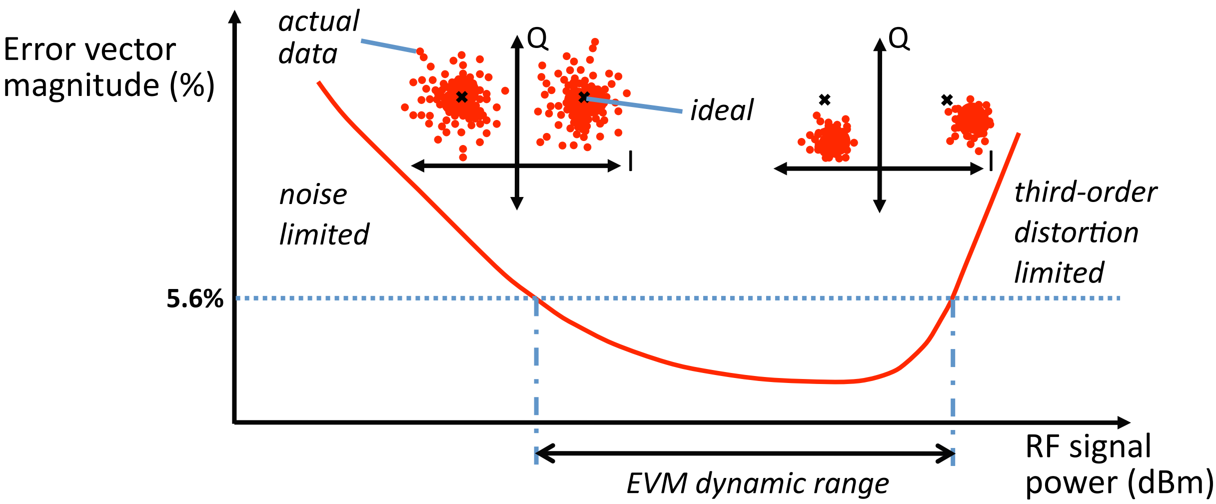

Figure 2.10: Example graph of EVM vs. received signal power for 802.11g showing a typical EVM curve shape and the dynamic range. The constellation diagrams indicate the causes of performance degradation.

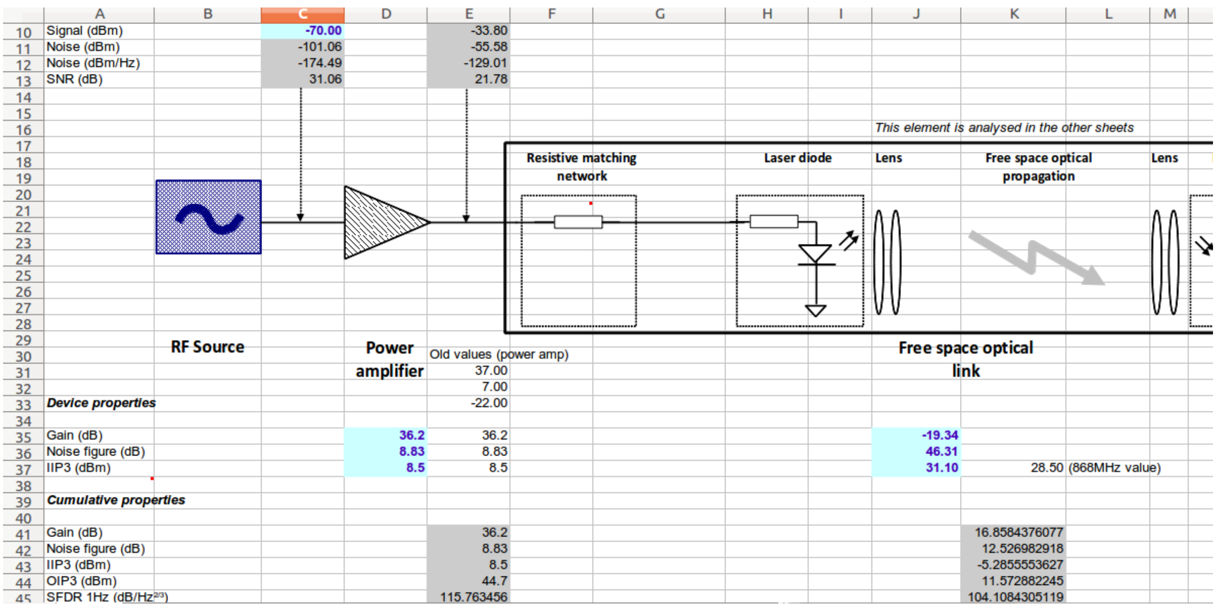

Figure 2.11: Sample screenshot of uplink RoFSO link budget spreadsheet showing device parameters and cascading of noise and gain.

performance of the entire link from RF transceiver to transmitting antenna. The second sheet models in detail just the optical link, taking into account laser and photodiode parameters. The final sheet models the free-space optical loss enabling difference beam divergences, lens sizes and misalignment scenarios to be tested.

Figure 2.12 shows a simulated graph of third-order SFDR vs. optical loss for a 1550nm laser operating using the simulation parameters listed in Table 2.2. These parameters represent realistic values taken from datasheets of available components. It is seen that the link is predicted to provide a third-order SFDR of $>95\text{dB/Hz}^{2/3}$ for an optical loss of up to 14dBo. To enable such a system to operate over a distance of 50m with a beam divergence angle of 2mrad, a typical value for practical FSO systems [103], a receiver of diameter 14mm would be required. This provides a positive initial indicator of feasibility for a low-cost manually aligned RoFSO link designed for indoor DAS. Further, this result demonstrates that the set of simulation parameters used produces a feasible result and so these can be used to form the starting point for building an experimental demonstrator link.

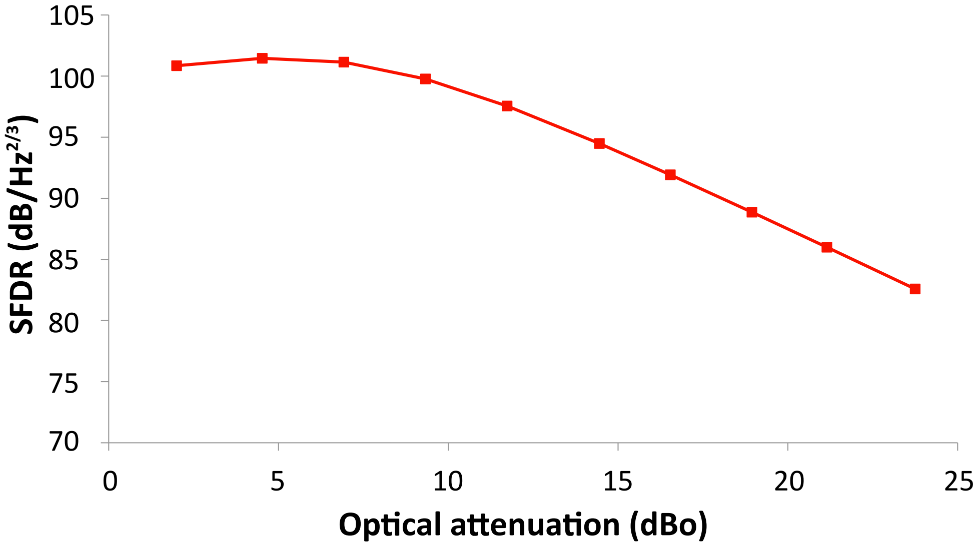

Figure 2.12: Graph showing simulated graph of third-order SFDR vs. optical loss for 1550nm laser.

2.4 Experimental Link

2.4.1 Fibre testing

Having developed and simulated a link budget model of the RoFSO uplink to verify its feasibility and test and determine design parameters, the next logical step is to build an experimental demonstrator. This enables a more thorough evaluation of design parameters beyond the limits of the simulation and with off-the-shelf components. Initially, a RoF system was built with

Table 2.2: Parameters for the link budget simulation of third-order SFDR using 1550nm laser.

Parameter	**Value**
Pre-amp gain	36.2dB
Pre-amp noise figure	8.9dB
Pre-amp amplifier IIP3	8.5dBm
Laser wavelength	1550nm
Laser threshold current	10mA
Laser bias current	76.7mA
Laser CW transmit power	10dBm
Laser external efficiency	0.15W/A
Laser RIN	-170dB/Hz at 76.7mA bias
Laser 3^{rd} *order intercept current*	168mA
Photodiode responsivity	0.31A/W
Photodiode output noise floor (matched)	-76.1dBm
Photodiode IIP3	30.1dBm
TIA transresistance	1074V/A
TIA equivalent noise input current	0.014nA/Hz
TIA 3^{rd} *order intercept current*	153.3mA
Post-amp gain	25dB
Post-amp noise figure	3.8dB
Post-amp IIP3	13dBm
Modulation frequencies	2.4GHz
Laser operating temperature	25°C

an additional variable optical attenuator to mimic the free-space loss. The ability to adjust attenuation manually enables a more thorough validation of the system against the theoretical model. It also enables operation of the link in a range of different loss regimes so that the effect on real modulated signals can be observed.

The experiment was run using two different set-ups – one using a 1547nm wavelength laser and the other using a 1310nm wavelength laser. There are 3 spectral bands typically used in silica fibres centred at 850nm, 1310nm and 1550nm. The first is used primarily due to the availability of cheap *vertical-cavity surface-emitting laser (VCSEL)* devices while the second two are used because of the favourable loss and dispersion (chromatic and waveguide) properties of silica fibres at these wavelengths. Only the latter two are tested here because devices at 850nm not well suited to free-space operation as their transmit power must be less than -4dBm for eye safety, compared with the >12dBm limits for the latter two [101]. It is desirable to select a wavelength compatible with silica fibres so that readily available RoF equipment can be modified to enable low-cost RoFSO links and furthermore, so that it would be possible to couple light directly to and from RoF links in a hybrid RoF-RoFSO DAS. 1310nm and 1550nm are both commonly used wavelengths that are well-suited to both silica fibre and free-space operation. As a result, both are tested here.

Experimental setup

The fibre demonstration of the RoFSO uplink was done using the set-up shown in Figure 2.13. The specifications for this set up are detailed in Table 2.3. The target output power of the lasers for link operation is 10dBm, just below the maximum eye safe limit at 1310nm [101]. This high power is used to compensate as far as possible the large optical loss.

It should be noted that for the 1547nm link, the laser power used for comparing experimental and simulated noise performance is lower than for comparing gain. This is because the RF spectrum of laser RIN is dependent on the laser bias current and at the bias required for 10dBm output power the RIN becomes too small to be distinguished from other noise sources. At lower bias current, however, the RIN increases to an observable level. The main reason it is desirable to be able to observe RIN in this case is so that the link budget modelling of RIN can be verified against experiments. For the actual implementation of a RoFSO link it is, of course, desirable to minimise all sources of noise.

The two modulation frequencies used, 868MHz and 2.4GHz, represent UHF RFID and 802.11g/n WLAN bands respectively. These are chosen because they are services that can be provided over a broadband RoF DAS at opposite ends of its typical frequency range.

Results

Figure 2.14 shows how the measured link noise varies with optical attenuation for both lasers. A good fit is seen with the simulated results indicating the validity of the model, with the predicted results lying within 2dB of measured results. The match is not perfect because of inaccuracies in the specification of component parameters as well as measurement errors. A few of the system parameters may also have a dependence on modulation frequency that is not accounted for in the link budget model.

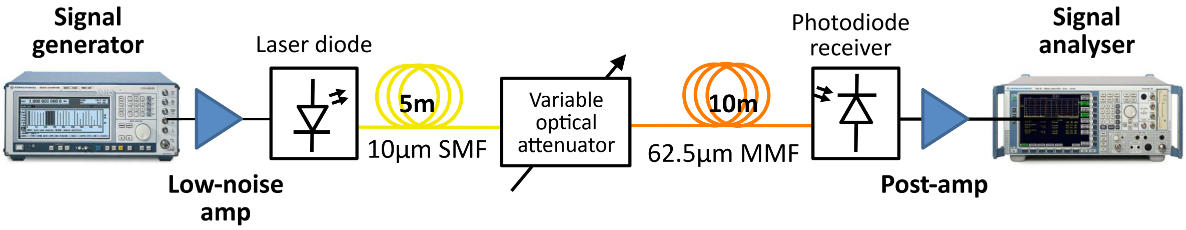

Figure 2.13: Experimental set-up used to verify and test RoFSO uplink in fibre.

Table 2.3: Parameters for the experiment using two different lasers

Parameter	**1547nm setup**	**1310nm setup**
Signal generator model	Rohde and Schwarz SMIQ 068	Rohde and Schwarz SMIQ 068
Low-noise amplifier gain	36.2dB	36.2dB
Laser model	Mitsubishi FU-68PDF DFB	Sumitomo SLV521A DFB
Wavelength	1547nm	1310nm
CW transmit power	-11.8dBm (noise test), 10dBm (gain & SFDR test)	10dBm
Laser bias current	24.3mA (noise test), 76.7mA (gain & SFDR test)	50mA
Optical attenuator loss range	2-35dBo	10-30dBo (to avoid damage to receiver)
Photodiode receiver model	Agilent 11982A Amplified Lightwave Converter	Picometrix PT-12B MM PIN/TIA receiver
Post-amp gain	25dB	36.2dB
Signal analyser model	Rohde and Schwarz FSQ26 Vector Signal Analyser	Rohde and Schwarz FSQ26 Vector Signal Analyser
Tested modulation frequencies	868MHz, 2.4GHz	2.4GHz
Laser operating temperature	25°C	25°C

It is worth noting that the noise levels found here (∼ -129dBm/Hz for the 1310nm laser) may be powerful enough to cause interference in other frequency bands. For example, 802.11n receivers must have a minimum sensitivity of -155dBm/Hz with an adjacent channel rejection ratio of 16dB [159]. If operating in an adjacent band to an 802.11n service this RoFSO link would produce an unacceptable level of interference and may therefore not meet regulatory requirements. This is a major area for improvement and could perhaps be achieved through use of optical amplification and very low-noise amplifiers.

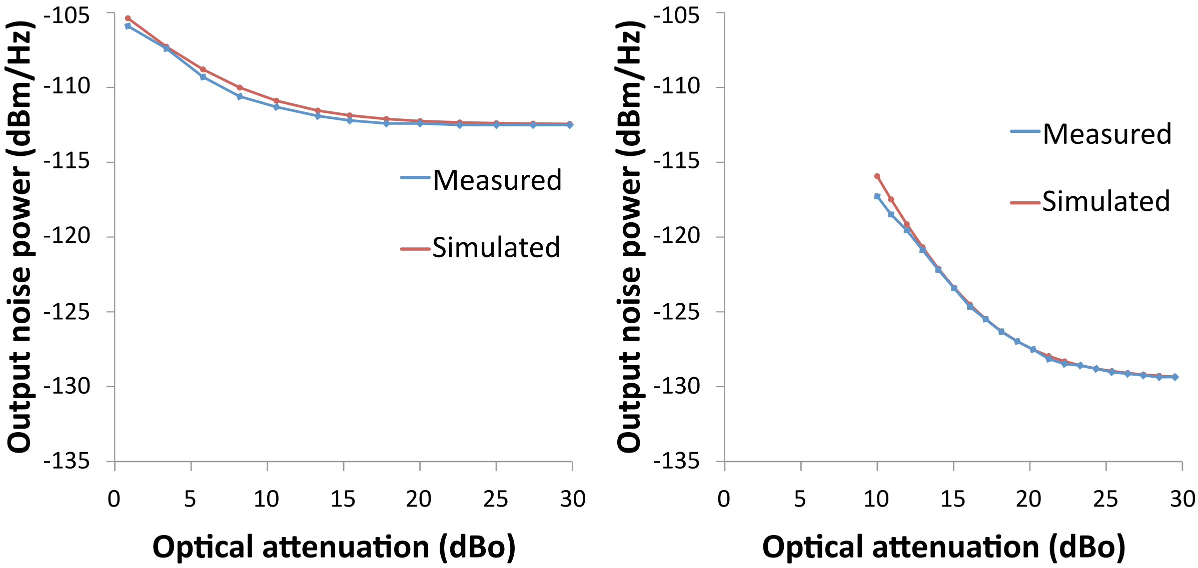

(a) (b)

Figure 2.14: Graph of measured noise vs. optical attenuation for RoFSO link for (a) 1547nm laser modulated at 868MHz with -11.8dBm CW output, and (b) 1310nm laser modulated at 2.4GHz with 10dBm CW output.

Next, the third-order SFDR is measured using a two-tone test as described in Section 2.3.4. The results of this test for the 1310nm laser are shown in Figure 2.15 and it is seen that the third-order SFDR cannot be predicted accurately due to the fact that the $2f_1 - f_2$ IMD product has a slope much greater than three, meaning that higher-order nonlinear effects, as opposed to third-order effects, are dominant. As a result it is not possible to fit a third-order line to this IMD product and so the third-order SFDR for a 1Hz bandwidth cannot be determined. In order to quantify dynamic range it is necessary to use another metric, which is developed in the next chapter.

However, it is still possible to determine a lower bound for the third-order SFDR from Figure 2.15 by taking a third-order extrapolation from the point where the $2f_1 - f_2$ IMD product intercepts the instrument noise floor. This will always give a third-order SFDR lower than the actual value, but it does allow some degree of comparison between systems. This method is used to estimate the third-order SFDR for the 1310nm set-up. This higher-order distortion was not observed for the 1550nm laser and so the third-order SFDR was calculated as described in

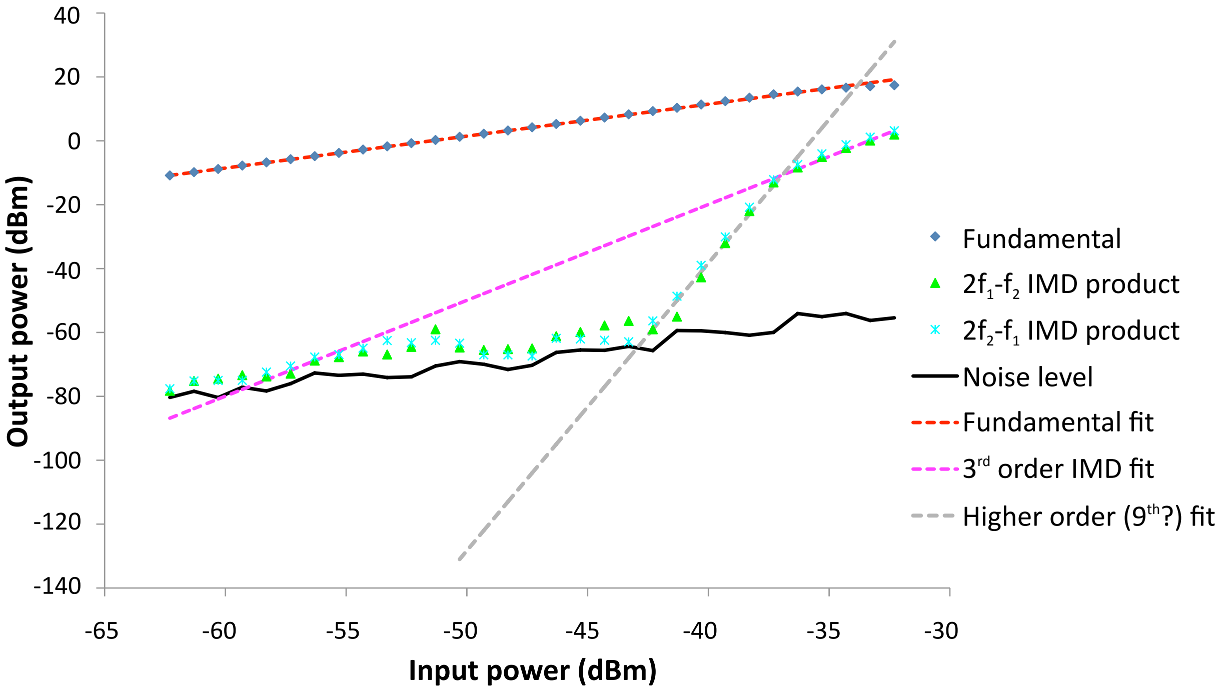

Figure 2.15: Graph of output power vs. input power for a two-tone test of the 1310nm link showing higher order distortion for 15.6dBo optical attenuation.

Section 2.3.4. Figure 2.16 shows the measured third-order SFDR for the 1550nm and 1310nm lasers, respectively. For the 1550nm case, a good match is observed between the measured results and the results simulated using the link budget model.

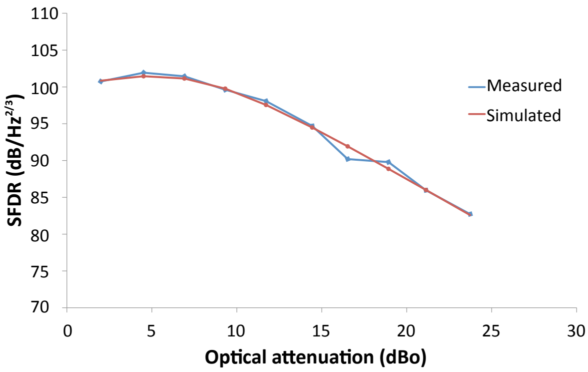

(a)

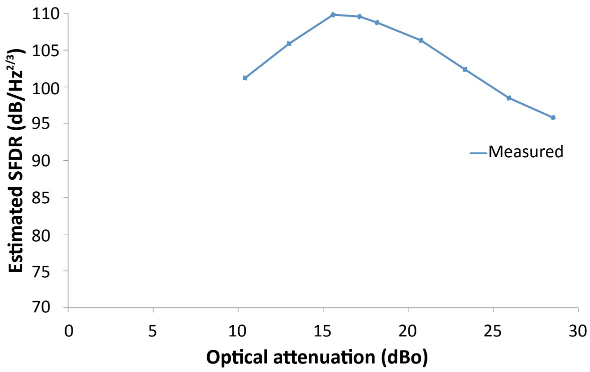

(b)

Figure 2.16: Graph of third-order SFDR vs. optical attenuation for (a) 1547nm link at 868MHz with 10dBm CW output and (b) 1310nm link at 2.4GHz with 10dBm CW output using the estimated lower bound of third-order SFDR.

It would appear from Figure 2.16 that even when using an underestimate of third-order SFDR the performance of the 1310nm laser is superior to that of the 1547nm laser in terms of dynamic range. This is because the 1310nm laser is highly linearised – that is, it has been designed to minimise nonlinear behaviour for small signals. This is common amongst 1310nm lasers as many of them were originally designed for use in cable television (CATV) applications, with strict linearity requirements [148]. The trade-off is that the onset of nonlinear effects for larger signals is much more abrupt, as evidenced by the sudden higher-order behaviour observed here. Even so, the overall third-order SFDR of this laser is very high, and is in the upper region expected of a commercial DFB laser diode [71].

For both lasers, when the optical attenuation is decreased sufficiently the third-order nonlinear behaviour of the photodiode increases and starts to dominate. This is because the received optical power begins to approach the maximum level allowed by the photodiode. It is possible to confirm this by changing the optical attenuation by a known amount and observing the corresponding decrease in IMD power. A 2dB/dBo change indicates the nonlinearity is caused mostly by the laser, but a larger change indicates the nonlinearity must be caused in the photodiode. In both cases here a change of 6dB/dBo is observed when the attenuation is set below ~5dBo for the 1547nm link and ~15dBo for the 1310nm, indicative of third-order nonlinear behaviour. As a result of this it is observed in Figure 2.16 that for lower optical attenuations the third-order SFDR tends to decrease. This decrease in third-order SFDR is further amplified by increased shot noise at the photodiode for low optical attenuations. The net result of this is that there exists an optimum operating point where the third-order SFDR is a maximum – ~5dBo for the 1547nm link and ~15dBo for the 1310nm link.

It is possible to convert the optical losses to equivalent free-space distances if the beam divergence and receiving lens diameter are known, as discussed in Section 2.3.1. In this case a beam divergence angle of 2mrad and a 20mm diameter receiving lens are assumed, both of which are well within the range commonly found in commercial FSO links. These parameters result in a free-space optical loss of 11dBo and using Equation 2.6, this is seen to be equivalent to a real free-space distance of 50m.

It can then be said that a third-order SFDR of greater than 95dB/Hz$^{2/3}$ is provided up to a distance of 50m for the 1547nm system and 300m for the 1310nm system. The superior performance of the 1310nm system is largely due to the laser's superior linearity performance. Over a distance of 50m, it would be possible to allow beam divergences up to 12.6mrad and still keep the lower-bound third-order SFDR above 95dB/Hz$^{2/3}$ for the 1310nm system.

For both wavelengths, the third-order SFDR up to at least 50m is sufficient to operate GSM cellular and UHF RFID in the 800-900MHz band and 802.11g services in the 2.4 GHz band. The measurements for the 1547nm system were also repeated at 2.4GHz and for an optical attenuation of 11dBo it was found that the third-order SFDR was 97dB/Hz$^{2/3}$, again sufficient to provide 802.11g services. This broadband behaviour is ensured by choosing broadband components at each stage of the link.

Next, the 802.11g EVM characteristics were then measured experimentally for a range of optical attenuations as shown in Figure 2.17. 802.11g is chosen because of its widespread use and very stringent EVM dynamic range requirements.

By measuring the dynamic range of each EVM curve, it is possible to produce a graph showing how this varies with optical loss, as shown in Figure 2.18. As expected the dynamic range decreases by 2dB for every 1dBo of optical loss, owing to the quadratic relationship between optical and electrical loss. When the loss gets less than ~10dBo for the 1547nm link or ~20dBo for the 1310nm link, the increasing effect of shot noise starts to cause a reduction in performance at lower signal powers. Similarly, the increasing effect of third-order distortion in the photodiode reduces performance at higher signal powers, meaning there is a roll-off in dynamic range at about 45dB for the 1547nm link and peak dynamic range of 39dB for the 1310nm link. These both fall just short of the 48dB dynamic range needed for 802.11g, but as discussed in Section 2.3.4 the smaller cell sizes enabled by DAS can compensate for this. Assuming a 2mrad beam divergence and a 20mm diameter receiver, the 1547nm link provides an EVM dynamic range of >45dB up to a distance of 50m and the 1310nm link provides an EVM dynamic range of ~39dB up to 70m (or 50m for a 2.8mrad beam divergence). Because EVM reflects actual performance using real data, this is an excellent verification of the system's ability to transfer wireless services over a distance of 50m.

It is noted from Figure 2.18 that at high optical attenuations (>20dBo) the EVM performance of the 1310nm link is significantly better than for the 1547nm laser, providing about 6.3dB extra dynamic range. However, at low attenuations this improvement reduces as photodiode nonlinearity begins to dominate and shot noise increases. If the photodiode were more linear, it is observed that a dynamic range in excess of 48dB could be achieved at 10dBo of loss for both laser diodes.

It should be noted that the maxima in EVM dynamic range and estimated third-order SFDR occur at different optical losses. This is because the EVM test signal is a much more complex mix of sinusoids than the two-tone third-order SFDR test signal and so the peak power is much higher than the average power and occurs only occasionally. This means the onset of

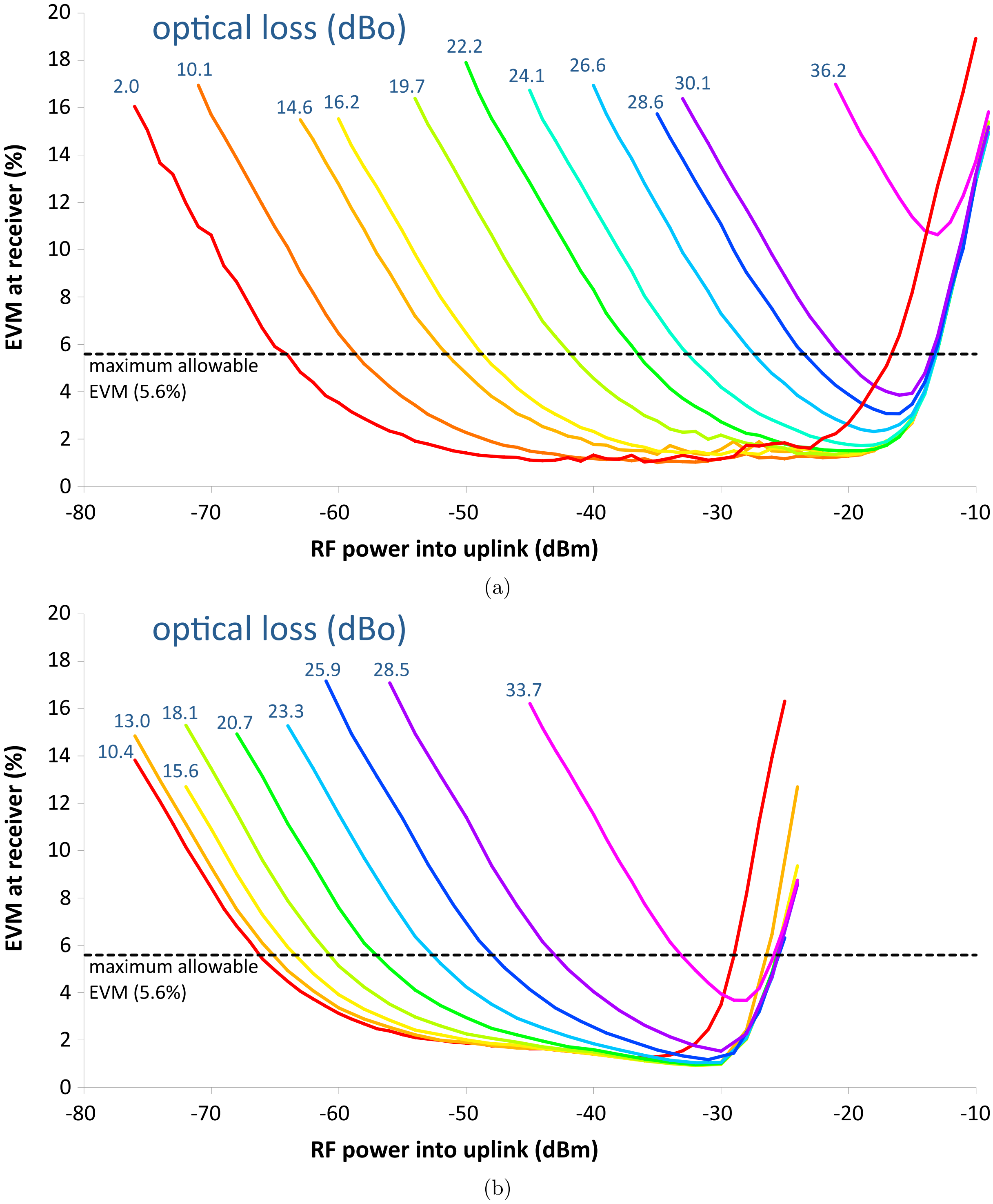

Figure 2.17: 802.11g EVM curves at 2.4GHz with different optical attenuations for (a) 1547nm link and (b) 1310nm link.

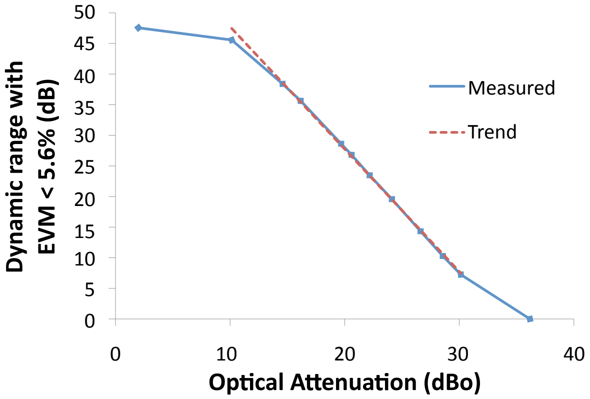

(a)

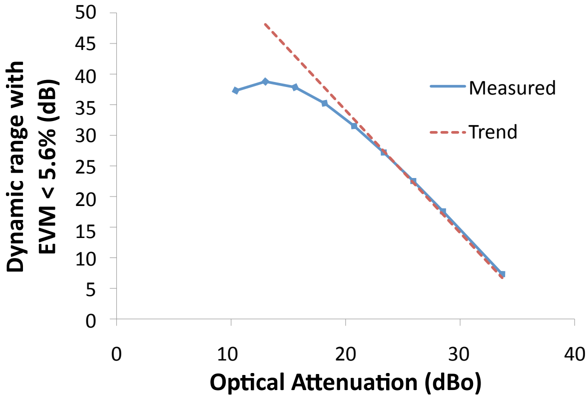

(b)

Figure 2.18: 802.11g EVM dynamic range vs. optical attenuation at 2.4GHz for (a) 1547nm link and (a) 1310nm link.

photodiode distortion is not as abrupt. This mismatch in peak powers is discussed further, along with compensation strategies to enable comparison in Section 3.2.1.

2.4.2 Free-space testing

Experimental setup

Following the fibre testing, the system was demonstrated over an actual free-space link. Up until this point the parameters of the free-space link, such as beam divergence and receiver diameter, have only been simulated. However, the free-space link is of great practical importance when designing a RoFSO link as this is what differentiates if from RoF and is the limiting factor determining many of the design constraints. Experimental testing over a real free-space optical link is then essential because it enables investigation of the practicalities of critical aspects of RoFSO design, namely alignment, stability and optical coupling losses. There are also important implications for eye safety when operating free-space optical links also and these, too, are discussed later in this section.

Having tested both 1547nm and 1310nm laser, it was decided to use a 1310nm laser for the actual free-space link. This was largely because of its superior dynamic range performance at high optical loss, a consequence of the availability of highly linearised lasers designed for CATV [148]. Further, in practical terms this is the wavelength most commonly used for existing RoF systems and high-speed Ethernet installations so it has a greater degree of compatibility with pre-existing equipment.

A diagram of the experimental set-up used is shown in Figure 2.19. The parameters of this set-up are listed in Table 2.4. Again, only the uplink was tested due to its more stringent design requirements. Owing to the dimensions of the room, the longest practical free-space distance was 4m and so mirrors were used to extend the total free-space distance to 16m. Lateral space constraints on the optical table made the use of additional mirrors difficult. However, 16m is sufficient for an indicative investigation of alignment, stability and coupling loss in free-space links and the results can readily be extrapolated to 50m links.

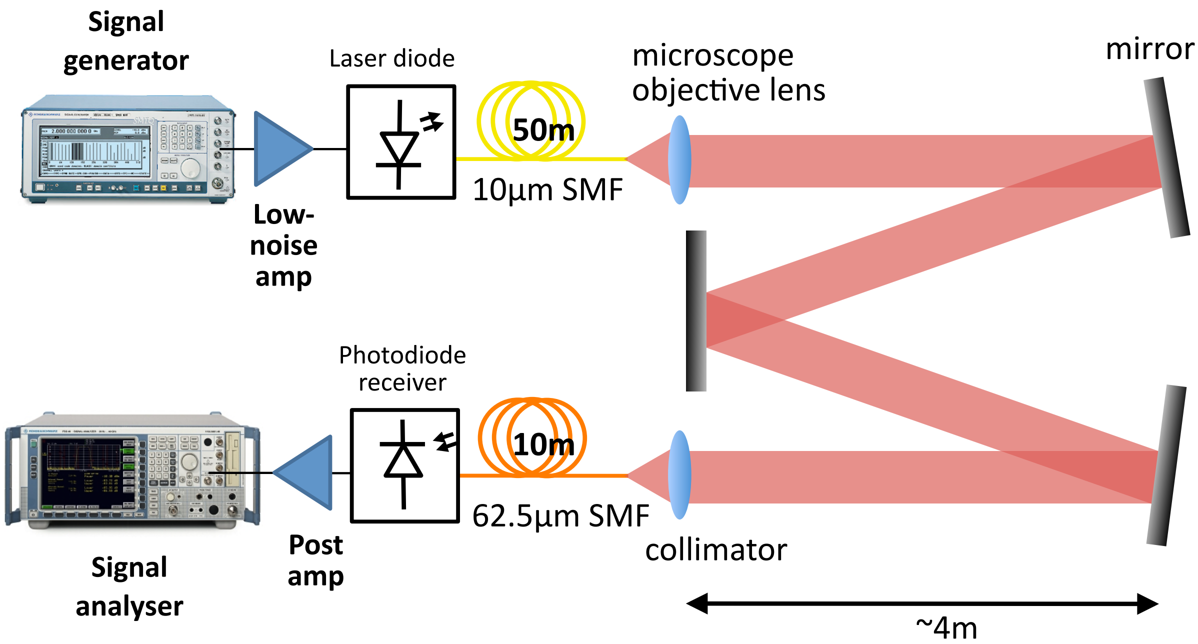

Figure 2.19: Experimental set-up for free-space testing of the RoFSO uplink at 1310nm.

On the transmit side of the link, a lens is used to collimate the beam exiting the single mode fibre. It is necessary to ensure that the *numerical aperture (NA)* of the lens is larger than that of the optical fibre to ensure that minimal light is lost when coupling. NA is a quantity that indicates how rapidly a beam exiting a fibre diverges and how rapidly collimated light entering a lens converges to a point, as illustrated in Figure 2.20. In order to collect as much light as possible from the fibre the NA of the lens and fibre must be matched.

For lenses NA is closely linked to the focal length by the equation:

$$\mathrm{NA} = n \sin\left(\arctan\left(\frac{D}{2f}\right)\right) \approx n\frac{D}{2f} \tag{2.33}$$

where n is the refractive index of the medium surrounding the lens (1 for air), D is the lens diameter and f is the focal length of the lens. To allow proper alignment of the fibre with the lens and control of the resultant beam diameter, the lens is placed on a translation stage allowing it to be moved in the X-Y-Z axes relative to the fibre. This cannot correct for angular misalignment between the lens and fibre, but this is assumed to be small due to good fixed alignment of the mounts.

At the receive end a collimator is used to collect the incident light. This is a precision manufactured component designed to couple the maximum possible power into the receive fibre and has an effective receiving diameter of 6.6mm (although the physical aperture diameter is 20mm). The fibre used at the receiver is OM1 62.5/125 MMF. This is because its large core diameter (62.5μm) and NA make it able to collect more light at a wider range of angles of

Table 2.4: Parameters for the 1310nm free-space experiment

Parameter	**Specification**
Signal generator model	Rohde and Schwarz SMIQ 068
Low-noise amplifier gain	36.2dB
Laser model	Sumitomo SLV521A DFB
Wavelength	1310nm
CW transmit power	10dBm
Laser bias current	50mA
Free-space link length	16m
Optical coupling loss into fibre	~8dBo
Geometric optical loss	~2dBo
Photodiode receiver model	Picometrix PT-12B MM PIN/TIA receiver
Post-amp gain	36.2dB
Signal analyser model	Rohde and Schwarz FSQ26 Vector Signal Analyser
Tested modulation frequencies	300MHz-3.1GHz (200MHz intervals)
Laser operating temperature	25°C

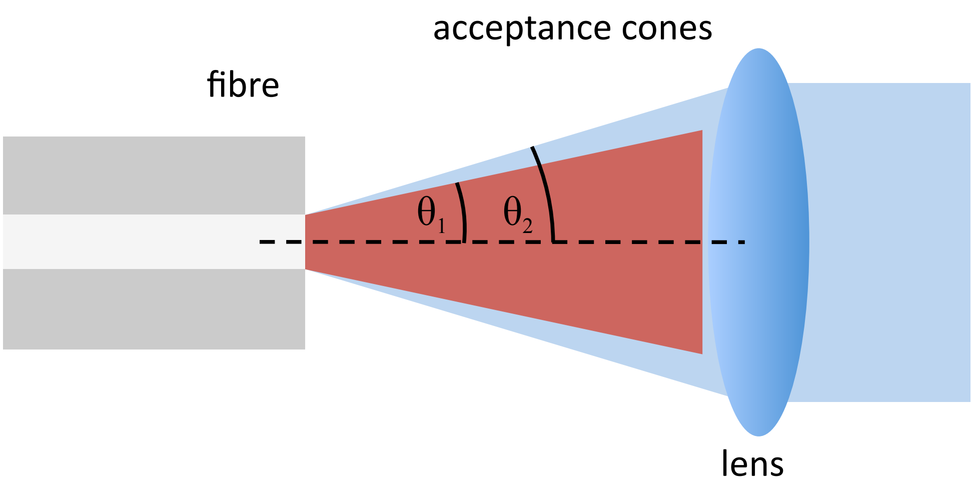

Figure 2.20: Illustration of matching of numerical apertures (NA). The NA of the fibre is defined as $\sin\theta_1$ and the NA of the lens is $\sin\theta_2$, where θ_1 and θ_2 are the respective maximum acceptance angles of the two elements. Clearly, in order to properly couple all light from the fibre into the lens the acceptance angle, and hence NA of the lens, must be greater than that of the fibre.

incidence than the more common 50μm diameter fibre. A photograph of the set-up is shown in Figure 2.21.

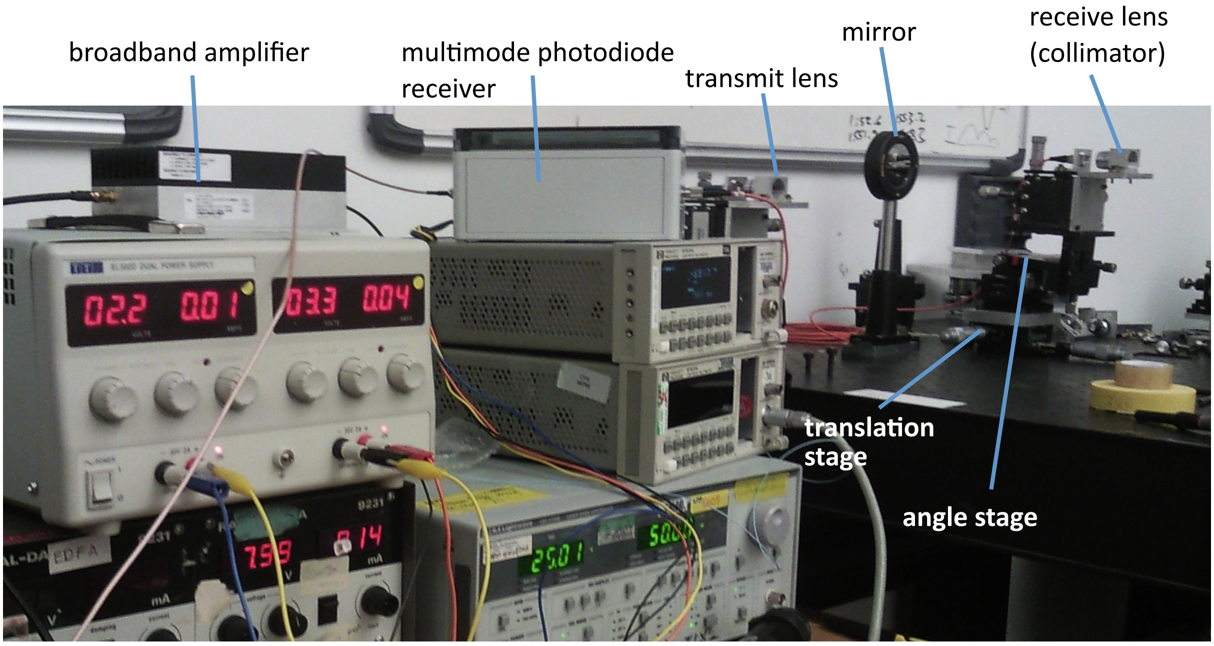

Figure 2.21: Photograph of experimental set-up of RoFSO system.

Alignment

One of the key problems faced in setting up the free-space link is alignment. It is desirable to have the transmitted beam aligned on the receive lens along the optical axis to minimise optical loss. First, alignment must be achieved in the X-Y plane, perpendicular to the beam. This is achieved by steering the beam using the translation stage at the transmit side, adjusting the mirrors and moving the translation stage holding the receive collimator. An infra-red detector card is used to attain rough alignment and then an optical power meter is used to fine-tune it. Alignment in this plane tends to shift with time as the aligned components (mirrors, translation stages) slowly move under the effect of building movements and gravity. This problem is mitigated by regular realignment of the beam, which was found to be required roughly every 2-3 hours for optimal performance. However, this effect is random and sometimes alignment is preserved for many days. Generally speaking realignment is done whenever optical loss increases by >3dB.

The second problem experienced is angular misalignment. This refers to the situation where a beam may be correctly aligned in the X-Y plane but the angle of incidence on the lens is such that the light is not focussed or centred properly on the fibre and as a result there is significant power loss. This problem illustrated in Figure 2.22. Angular adjustment is enabled by mounting the receive lens on an angle stage placed on top of the translation stage, as shown in Figure 2.21.

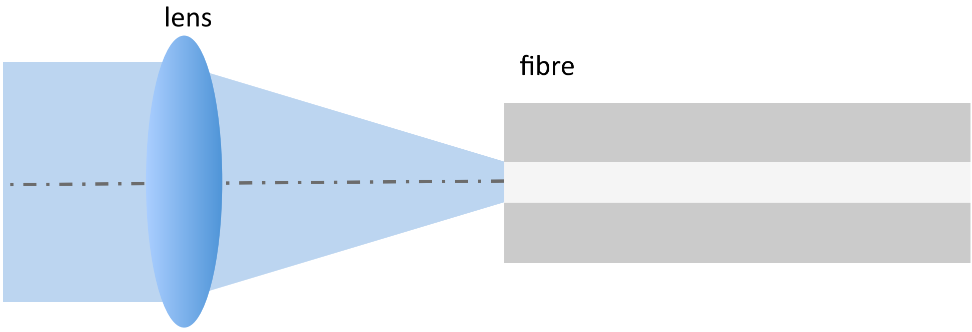

(a)

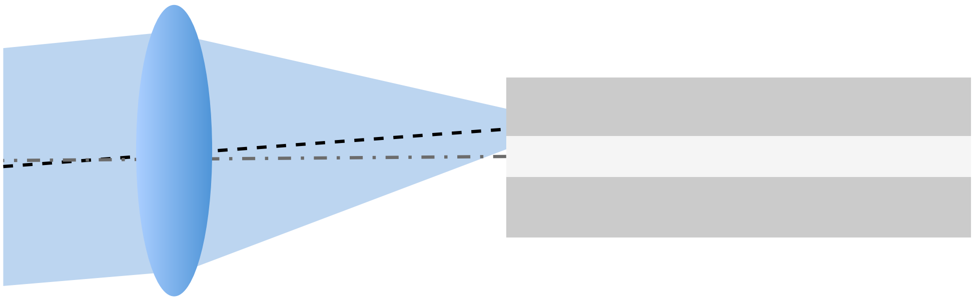

(b)

Figure 2.22: Illustration of how angular misalignment at the receiver causes power loss: (a) shows the ideal case with no angular misalignment while (b) shows how a small angular misalignment can cause the light to be focused off the fibre core causing very large loss.

Another way to analyse both angular and planar misalignment this is to consider the *field of view (FOV)* of the transmitter and the receiver. The FOV is effectively the cone of acceptance for light based on the acceptance angle for the receiver and the beam divergence for the transmitter. If the FOV of the transmitter completely contains the receiver and vice versa then there will be at least some power detected at the link. For a Gaussian profile beam the maximum power will be detected when both transmitter and receiver lie in the centre of each other's FOV. This is illustrated in Figure 2.23. Because the receiver is a collimator, it has an optimally small FOV and so this makes angular alignment challenging.

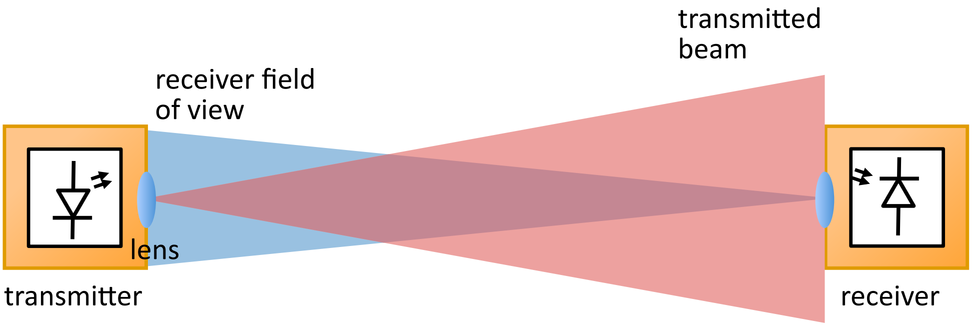

(a)

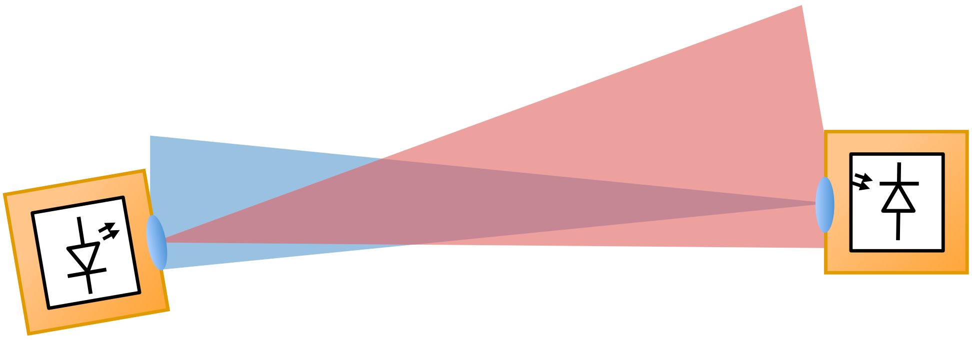

(b)

Figure 2.23: Illustration of field of view: (a) shows ideal alignment while (b) shows a sub-optimal but still acceptable alignment because the transmitter and receiver are still within each other's field of view.

The main detrimental effect of misalignment is optical power loss and so a simple mitigation strategy is to increase the laser power. However, there are limits on the maximum power in order to meet eye safety requirements. Laser distortion is also worse at higher transmit powers. The transmit power is thus limited to 10dBm. The beam divergence could be reduced to increase received power but this would increase the probability of misalignment and would increase the loss resulting from a small misalignment. The receiver size could also be increased to reduce optical loss but this would require non-standard and potentially costly optics. In theory it is also possible to use multiple beams so that at least one of them is always aligned on the receiver, where each beam contains 10dBm of optical power - a form of electronic tracking (or equivalently spatial diversity) [160]. In a full RoFSO communication architecture, *automatic gain control (ACG)* could be implemented to make adjustments to the gain of amplifiers to compensate for minor variations in optical loss over time, thus stabilising performance.

Eye safety

Because RoFSO systems are designed to be used in buildings where there will be large numbers of users, the laser links used must be eye safe. According to the IEC standard, at 1310nm the laser power must not exceed 11.9dBm in order to be classified as a class 1 eye safe laser [101]. This is the only class safe for operation in free-space without any additional safety measures.

The eye-safe limits are designed such that for a collimated beam entering a dilated pupil (a worst case scenario) the power is sufficiently low that it will not cause damage to the eye, even when incident for an extended period. In this case, however, the beams used are not usually collimated, a consequence of the need to enable easy manual alignment. It may then be possible to increase the transmit power beyond the nominal limit without compromising safety by determining limits specific to this set-up. This would potentially enable the lasers to be operated at higher power, thereby compensating for optical loss. However, in this case nonlinear effects in the laser and photodiode would come into play and so there would not be much improvement in dynamic range.

Reflections

When light is launched from a fibre into air, Fresnel reflection will occur at the glass-air interface due to the change in refractive index. This effectively creates an elongated laser cavity that can produce additional distortion in the link [161]. This problem initially caused spurious results when measuring 802.11g EVM, particularly at lower powers. To mitigate this problem, an optical isolator with 45dB isolation was introduced directly after the laser to prevent reflected light returning into the laser cavity.

However, the isolator alone was not entirely effective and so to further mitigate the problem a drop of index matching gel was placed on the end of the fibre. The refractive index of this gel is similar to that of glass to minimise reflections at the glass-gel interface. The gel forms a droplet shape on the end of the fibre and it is in fact this geometry that is the reason it works so well in this situation. The curved surface means that reflected light is not parallel to the fibre and so very little of it couples back into the SMF. This is illustrated in Figure 2.24. The use of angled fibres would have a similar effect but these are more difficult to align.

A comparison between the 802.11g EVM curves using the two approaches is shown in Figure 2.25. Clearly, index matching gel is a better performing solution than using an optical isolator. Further, it is cheaper and simpler to implement. Its performance is comparable to that achieved using fibre and an attenuator as measured in Section 2.4.1.

Coupling loss

Another issue encountered with the free-space link is optical coupling loss, also referred to as insertion loss. This is distinct from geometric loss as it is not related to distance. Rather, it

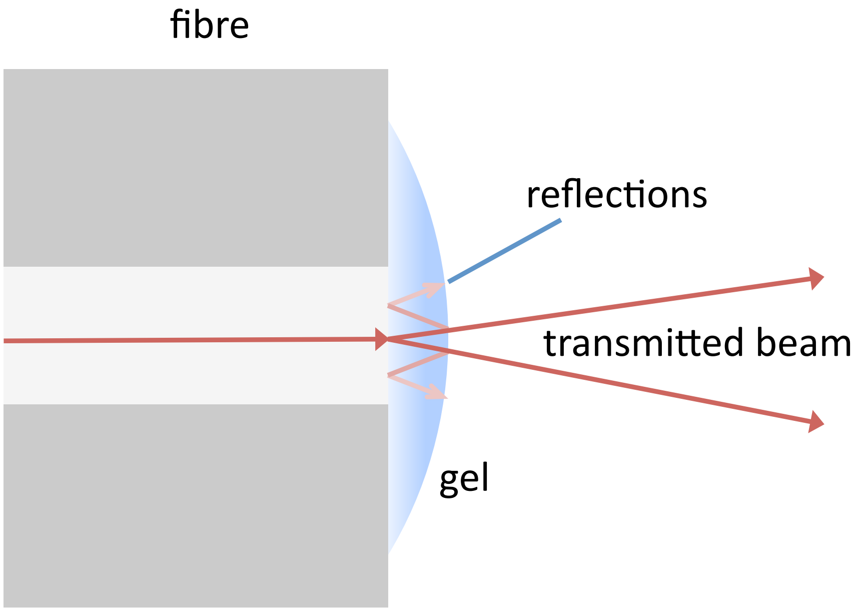

Figure 2.24: Illustration of how a drop of index matching gel prevents reflections back into the fibre.

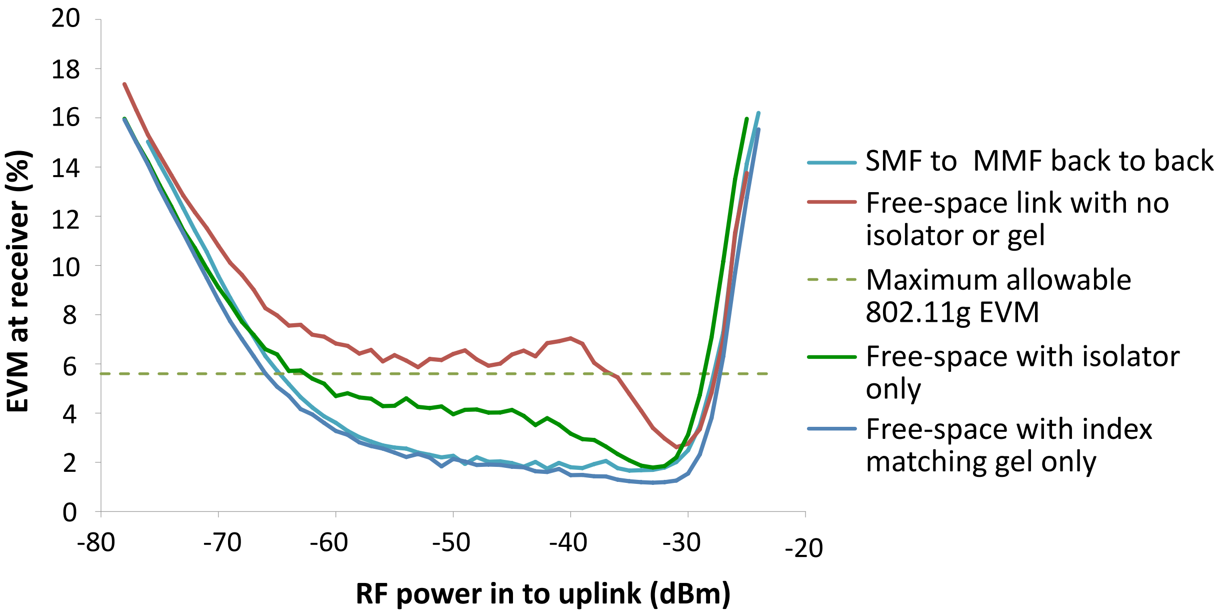

Figure 2.25: Comparison of two different methods of reducing fibre-air coupling reflections. The SMF to MMF curve represents the ideal case when a fibre and attenuator are used to simulate free-space.

is caused by effects in the receive optics, such as lens-fibre misalignment, losses in connectors, modal losses in fibre and poor coupling into the photodiode. It is defined by measuring the power received by the photodiode as a fraction of the power incident on the aperture of the receive lens.

Commercial FSO systems with automatic tracking generally have optical coupling losses of 4-5dBo [116] while for systems without tracking this range is generally 9-14dBo [103, 112]. There have been customised passive optical devices designed to reduce coupling losses while still enabling manual alignment. One such device, that works by focussing light from a large range of angles of incidence over a relatively large receive area, is the optical antenna [105].

In this experiment it is possible to get the overall loss down to around 10dBo for a 16m link, even though at this distance the geometric loss is only be expected to be about 2dBo. This suggests that there is approximately 8dBo of coupling loss, a relatively low amount for a non-tracking FSO system. Possible causes of this loss include inability to align the beam optimally given the limits on the precision of angular alignment, non-ideal position of the beam waist, connector losses and imperfections in optical equipment.

Results

After addressing these design issues, the performance of the free-space RoFSO demonstrator was measured. Firstly, the beam profile at the receive aperture was measured to determine its shape and size. The horizontal profile of the beam is shown in Figure 2.26 and is observed to be Gaussian in shape. Because the beam is coupled from SMF it is approximately symmetrical and so will have this same profile along any cross-sectional axis orthogonal to the optical axis. This was verified experimentally by moving a power meter in both axes and confirming that the half-power width was the same.

By using the approximations discussed in Section 2.3.1 the $1/e^2$ divergence angle of the beam is estimated to be 0.53mrad. This is significantly less than the 2mrad specified in Section 2.4.1. However, it was found that it is still relatively easy to align the link over a distance of 16m and that this alignment remains stable for at least several hours. Further, the effect of using a 2mrad divergence, as might be required in longer links or in environments with less mechanical stability, can be modelled simply by adding in an additional optical loss or reducing the transmit power. For this reason the 0.53mrad divergence is used for the experiments presented here.

Next, the link was aligned and the optical attenuation was measured to be $\sim$10dBo. This represents approximately the minimum loss attainable by manual alignment of this system over 16m. As seen in Section 2.4.1, in this region of optical attenuation when using this particular laser the photodiode distortion is the dominant nonlinear effect in the link. As a result third-order distortion is dominant rather than higher order effects arising in the laser. Higher order effects only start to dominate at higher optical attenuations. This makes it possible to measure the third-order SFDR of the link in this case. Consequently, the third-order SFDR was measured at 200MHz intervals across a frequency range of 300MHz-3.1GHz. The resultant graph is shown in Figure 2.27.

It can be seen that the third-order SFDR is above 100dB/Hz$^{2/3}$ over the entire frequency range. This demonstrates the system's broadband nature and its ability to support a wide range of wireless services. The 802.11g EVM was also measured for this system and the dynamic range

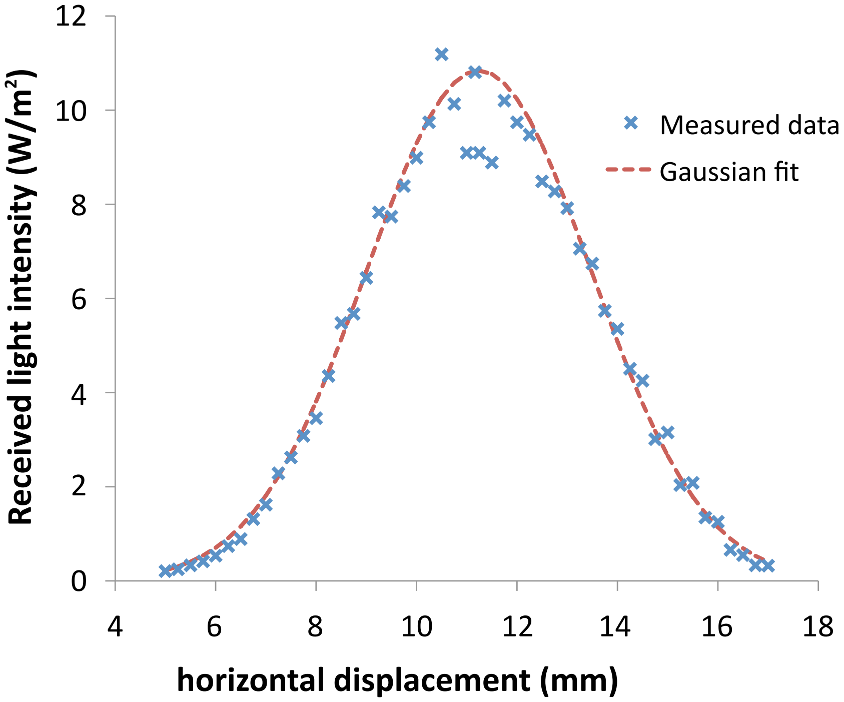

Figure 2.26: Cross-sectional profile of laser beam at 16m from the transmitter.

was found to be 38.7dB. The EVM curve was compared with that from a fibre test with the same loss and an almost identical result was achieved, as shown in Figure 2.28.

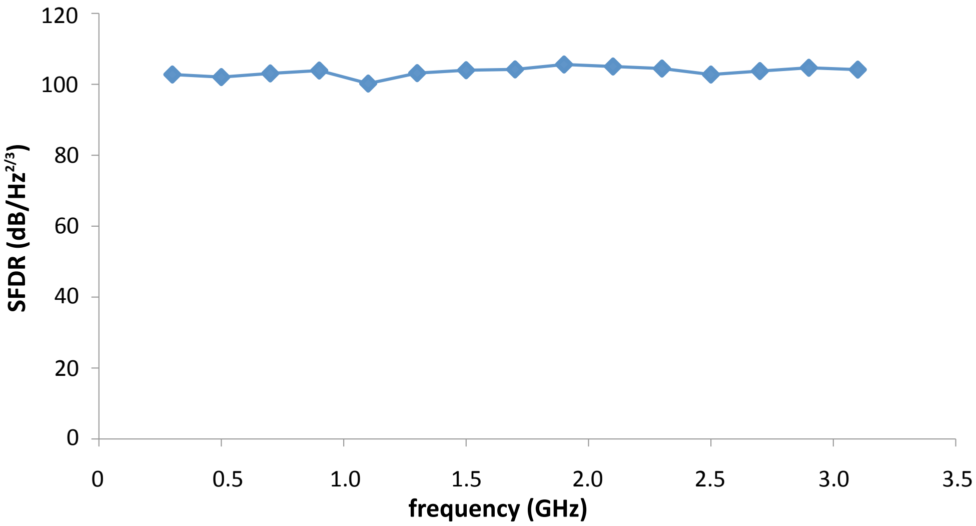

Figure 2.27: Graph showing third-order SFDR vs. frequency for RoFSO link of length 16m.

A beam with divergence of 0.53mrad will create a spot of diameter of 26.6mm at a distance of 50m. By using the equations in Section 2.3.1 and using the effective diameter of the receive collimator as 6.6mm it is estimated that the geometric loss at 50m is about 10dBo. Adding this to the 8dBo of coupling loss, the total loss over 50m would be 18dBo. It is predicted using the results in Section 2.4.1, determined using a fibre attenuator, that this 50m link would have an estimated third-order SFDR of 109dB/Hz$^{2/3}$ at 2.4GHz and the EVM dynamic range would be 36dB. It may seem counter-intuitive that a longer link could have an improved third-order SFDR but this is the case here due to the reduction in the effect of photodiode nonlinearity at higher optical loss. The EVM dynamic range does not experience this same effect at the same optical attenuation because of the difference in test signal peak power as discussed in Section 2.4.1. If a perfectly linear receiver were used, the EVM dynamic range would be 39.5dB. This falls just short of the 802.11g standard but the use of these links as part of a DAS compensates for this by significantly improving wireless signal strength over the same coverage area.

Further extrapolation shows that the link can provide a third-order SFDR of above 95dB/Hz$^{2/3}$ for an optical loss of up to 28dBo. When coupling loss is accounted for, this gives a theoretical maximum range of 175m. However, the EVM dynamic range at this distance would drop to less than 20dB. This discrepancy reflects the limitations of the third-order SFDR estimation technique, which is less accurate for higher bandwidth services.

2.5 Conclusions

Radio-over fibre distributed antenna systems are very important in the design of in-building wireless infrastructure to improve coverage and, increasingly, enable the deployment of ultra-

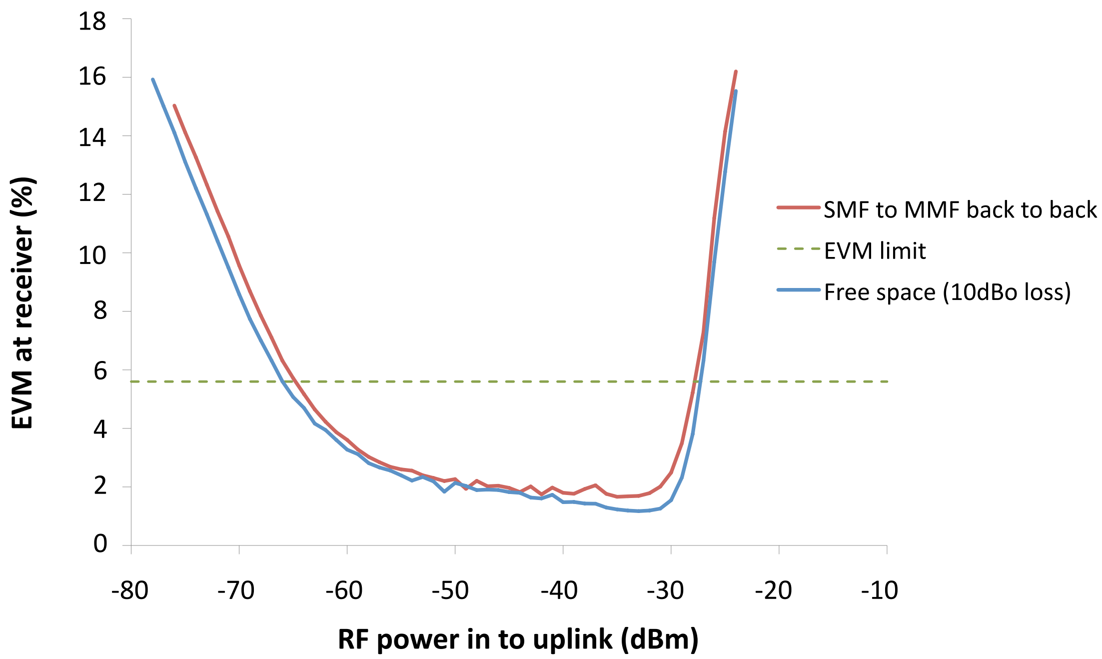

Figure 2.28: Graph showing 802.11g EVM of a 16m RoFSO link with an optical attenuation 10dBo. It can be seen that this matches very closely the ideal case when the free-space link is replaced with a fibre with a 10dBo attenuator.

high capacity wireless networks needed to avert an imminent shortfall between user demand and available capacity. However, the main drawback of existing DAS is the need to have a cabling infrastructure in place, whether it be coaxial or optical fibre. Radio-over free-space optical (RoFSO) links are a possible low-cost alternative to RoF links for feeding analogue wireless signals to remote antennas without the need for an extensive cabling infrastructure.

In this chapter, a novel RoFSO link is simulated and experimentally demonstrated. First, a link budget model is developed in order to simulate performance for different design parameters and in turn help to determine the optimal parameters. An experimental demonstration of the link using two different lasers operating at 1547nm and 1310nm over fibre with a variable attenuator is then presented. The measured results show that this link can provide an estimated third-order SFDR of greater than 95dB/Hz$^{2/3}$ in the 800MHz and 2.4GHz frequency bands at an optical attenuation of up to 11dBo and 27dBo for the two lasers respectively, corresponding to free-space distances of 50m and 300m. This is sufficient to support most wireless services in these bands. There is also good agreement between simulated and experimental results. The 802.11g EVM dynamic range is measured to reach a maximum of 45dB for the 1547nm system and 39dB for the 1310nm system, with both maxima occurring at an equivalent free space distance of $>$ 50m.

In order to examine some of the very important practicalities of free-space optical links, such as alignment and stability, the experiment is then extended to include a 16m free space link operating at 1310nm. This free-space link is measured to have a third-order SFDR of >100dB/Hz$^{2/3}$ over a frequency range from 300MHz to 3.1GHz with an optical attenuation of $\sim$10dBo. This is more than sufficient for operation of most wireless services and demonstrates the broadband nature of the link. The performance can be extrapolated to a 50m link and it is predicted that such a link would have an even higher third-order SFDR of 109dB/Hz$^{2/3}$ over the same frequency range due to reduced photodiode nonlinearity. The 802.11g EVM dynamic range at this distance is 36dB.

This chapter presents the successful demonstration of a low-cost RoFSO link capable of transporting multiservice wireless signals spanning a frequency range from 300MHz-3.1GHz over a distance of 50m. It is of a sufficiently high quality and simplicity that it can be used in place of RoF links in an indoor DAS. This ultimately enables new design possibilities for realising high-capacity wireless infrastructure without requiring prohibitive cabling infrastructure.

Chapter 3

High-Order Distortion in Directly-Modulated Semiconductor Lasers in High-Loss Analogue Optical Links

General overview

This chapter reports a theoretical and experimental investigation of the effects of high-order nonlinear distortion products produced by directly-modulated semiconductor lasers on the performance of high-loss analogue optical communication links requiring large RF dynamic range. In order to provide sufficient RF dynamic range to support radio services in links with high optical transmission loss, for example in radio over free-space optics (RoFSO), while keeping costs low, it is necessary to use directly-modulated lasers. However, in these applications the lasers must be driven to high modulation depths in order to maximise dynamic range without increasing the CW laser power. Simulations show that under these unique conditions the first detectable nonlinear distortion is often the result of dynamic distortion due to the laser being driven near threshold. It is shown that this type of distortion is characterised by a sharp increase in the contribution of high-order (fourth order or greater) nonlinear terms resulting from the influence of laser relaxation oscillations. As a consequence, the third-order spurious-free dynamic range (SFDR) metric no longer accurately reflects the performance of such links as it assumes that third order effects are dominant. An alternative measure of dynamic range termed *dynamic-distortion-free dynamic range (DDFDR)* is proposed. This differs in that the upper limit is defined as the modulating power at which the peak optical modulation index (OMI) reaches unity. At this point the error vector magnitude (EVM) measured for a range of different wireless services starts to increase rapidly due to high order distortion. This makes DDFDR a practical, service-independent metric of dynamic range. For two different wireless services it is observed experimentally that on average the DDFDR upper limit predicts the EVM knee point to within 1.1dB, while the third-order SFDR predicts it to within 6.2dB. The DDFDR is thus shown to be a more accurate indicator of real link performance when high-order distortion is dominant.

This chapter is drawn primarily from work published in the IEEE/OSA Journal of Lightwave Technology [162].

3.1 Introduction

As described in Chapter 1, wireless communications systems are an increasingly important and ubiquitous feature of modern society but we are faced with an imminent shortfall in available capacity that must be addressed with radical new approaches to wireless infrastructure design. Radio-over-fibre (RoF) has been shown to be a cost-effective and high-performance means of distributing broadband analogue radio signals to remote antennas in DAS [40]. The fibre infrastructure requirement of RoF links can be very expensive and so in some DAS installations it may be desirable to replace them with radio over free-space optics (RoFSO) links. In order to be an economically viable alternative to a broadband RoF link, any RoFSO link must be low-cost, broadband and provide comparable performance.

Because of optical alignment tolerances, free-space loss and coupling loss, RoFSO links must accommodate large optical losses. This loss will be time variant but over short periods of time can be considered to remain constant. The noise floor of these high-loss links is dominated by thermal noise in the receiver. The noise figure of the link, defined as the decrease in SNR in dB from input to output, increases with the optical loss and in doing so restricts the lower limit of the RF dynamic range. In order to provide large RF dynamic range it is then necessary to push operation closer to the upper limit of the optical link RF dynamic range, which is limited by nonlinearity in the transmitter. To do this without using costly optical amplifiers or high power lasers, it is necessary to operate lasers at the maximum optical modulation depth. To keep RoFSO links relatively low-cost compared with their RoF counterparts this should be done using directly-modulated semiconductor lasers as the source and a photodiode detector as the receiver.

These operating conditions make such links susceptible to high-order (i.e. greater than third order) nonlinear behaviour which is generated in directly-modulated semiconductor lasers as the peak OMI approaches unity, termed *dynamic distortion*. The effect of this behaviour on the link performance is examined both theoretically and experimentally. It is found that the usual figure of merit for analogue optical links, third-order SFDR, no longer accurately reflects the performance of such links as it assumes that third order effects are dominant. When dynamic distortion is dominant it is found that the dominant order of distortion at the input power that causes the first intermodulation distortion (IMD) product to be greater than the noise floor is high (greater than third-order) but not readily predictable. This is the first time that the practical implications of this high-order distortion on the performance of optical communication links have been investigated.

It is demonstrated that in such a regime a new metric called dynamic distortion free dynamic range (DDFDR), which is the RF dynamic range where the OMI of the laser output remains less than unity, can be a better indicator of link performance. Like third-order SFDR, DDFDR uses the noise floor as its lower limit but the upper limit uses the peak modulation power at which peak OMI reaches unity. This upper limit is bandwidth-independent and is the same regardless of the actual dominant order of distortion. At this upper limit the EVM performance of all real wireless services carried on the optical link starts to increase rapidly due to the very rapidly increasing distortion, regardless of service. The measure is thus service-independent. It is, however, only valid for systems where dynamic distortion is dominant.

An example high-RF-power high-loss optical link is used to confirm experimentally the presence of dynamic distortion and its effect on third-order SFDR, and to validate the proposed DDFDR metric. It is shown that when high-order dynamic distortion is dominant DDFDR is a better predictor of EVM performance at the onset of distortion than third-order SFDR.

3.2 High-RF-power high-loss optical links

Some optical links are required to operate under conditions of high optical loss (or losses which are time varying and can reach high levels) compared with standard fibre links, for example links using lossy polymer optical fibre or free-space optical (FSO) links. The noise figure of such links can be calculated from the link budget if the gain and noise figure of each device are known [76]. As the optical loss increases shot noise and then thermal noise at the receiver begin to dominate. The overall noise figure of the link also increases. This restricts the lower end of the RF dynamic range because the RF signals have insufficient SNR.

To provide a large RF dynamic range to transport radio services such links must allow operation up to higher RF power levels, where distortion caused by nonlinearity imposes an upper limit. This is achieved by increasing the power of the RF modulating signal, meaning that such links can be considered high-RF-power compared with standard fibre links. Many real radio services have a high tolerance to error (for example 3GPP allows 17% EVM [158]) so can provide acceptable performance when a significant amount of nonlinearity is present. Such links can be operated at high-RF-power levels as a practical means of providing large RF dynamic range.

3.2.1 Free-Space Optical Links

FSO links are constructed from an optical transmitter, typically a laser, and an optical receiver, a light detector usually consisting of a focussing element and a photodiode. Such links usually transmit digital modulated signals but have been designed to support direct transmission of analogue RF signals through analogue RF modulation [112]. This has been achieved using a simple intensity modulation (IM) scheme at the transmitter and a simple direct detection (DD) scheme at the receiver followed by an amplifier [163]. An example IM-DD RoFSO system was illustrated in Figure 2.1.

The modulation could be done using an external modulator integrated with a laser via photonic integrated circuit (PIC) technology. However, the use of external modulators is still considered to be impractical since it is more expensive than direct modulation [164]. Direct modulation of laser diodes has been shown to provide dynamic range performance comparable with externally modulated sources at lower cost [165].

Optical Loss in FSO Links

As discussed in Section 1.3.3 FSO links are prone to misalignment resulting in significant power loss. This has both a fixed component, a result of the divergent beams used as a cost-effective means of increasing alignment tolerance, and a variable component resulting from the changing environment (temperature, vibrations etc.). This variation has been shown to be relatively slow (a few kHz) compared with the bandwidths of many RF services (greater than 100MHz) and so the loss can be considered constant over the course of a single test measurement [106].

Using typical figures for the required beam divergence to allow for alignment error (1-5 mrad) and for the diameter of the optical receiver, the geometrical propagation loss is in the range 0.6-17dBo [103]. So-called optical decibels (dBo) are used to distinguish optical power loss from RF power loss for clarity, as discussed in Section 2.3.1. In addition, published experiments have found unavoidable optical coupling losses of 8-14dBo [106, 112]. The minimum total optical loss in a FSO link with optimum alignment is therefore 8.6dBo. By comparison, for fibre links of typical indoor DAS spans (50-100m) the optical loss is expected to be less than 0.5dBo in addition to laser coupling losses of 3-4dBo. FSO links can therefore be considered to be high-loss relative to fibre links.

RF Transmit Power in FSO links

Radio services must handle a large dynamic range of received powers on the uplink due to the so-called *near-far effect* which must be supported by the RoFSO link. The lower end of the RF dynamic range of the RoFSO link is limited by the attenuation of low power signals and the thermal noise floor of the receiver. This could be overcome by amplifying the optical signal but optical amplifiers are too expensive for such low-cost systems. A lower-cost strategy is to increase the output power of the laser and increase the power of the RF modulating signal.

One way to do this would be to increase the bias current and output power of the laser. However, there are limits to how much laser bias levels can be increased [76]. Using a higher-powered laser would be another option but low-cost semiconductor lasers suitable for high-power direct modulation in the gigahertz frequency range are not readily available. Also, for free-space applications such as RoFSO the output power of the laser may be limited due to eye-safety requirements. Therefore, as well as increasing the optical output power to overcome the high optical losses, a high modulation depth must be used.

Experimental RoFSO Link

To illustrate the issues which this chapter addresses, an experiment on an example of a RoFSO uplink is recorded here. The uplink as depicted in Figure 2.1 is set up in an experiment to evaluate the RF dynamic range. A 16m free-space optical link is created by coupling light to and from fibres using adjustable lenses. The laser used is a directly-modulated 1310nm Sumitomo SLV521A DFB operated at a bias current of 50mA with a 10mW CW output. This choice of wavelength allows the use of low-cost and readily available components. Index matching gel and optical isolators are used to prevent distortion arising from optical feedback into the laser cavity [166]. The optical loss is measured to be 10±1dBo over a 24-hour period with dynamic variations in loss being sufficiently slow that they have negligible short-term impact on performance, consistent with previous experiments [106]. The receiver used is polarisation insensitive so that changes in the orientation of the transmitter or receiver polarisation, or polarisation changes in the fibre do not affect the performance.

To measure the link performance, the laser is directly modulated with a 64QAM 802.11g wireless LAN signal at a carrier frequency 2.4GHz. The EVM vs. input power curve is shown in Figure 3.1. It can be seen that 38.7dB RF dynamic range is achieved with an EVM below the 5.6% limit specified by the IEEE 802.11g standard. This demonstrates the viability of such high-loss free-space links for transporting analogue RF signals as has been indicated in previous research [163].

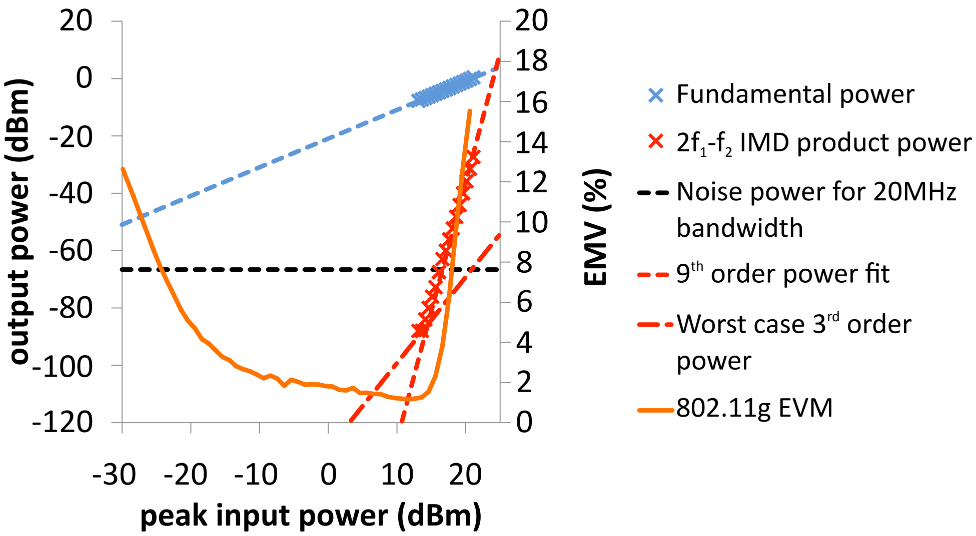

Figure 3.1: Graph showing output power and EVM vs. peak RF input power for a demonstration RoFSO uplink.

Overlaid on the EVM curve in Figure 3.1 is the power curve of the main intermodulation distortion (IMD) product arising from laser nonlinearities in a two-tone test. Due to the high peak-to-average power (PAPR) ratio of 802.11g signals the peak power of this input signal is a better indicator of the point at which distortion starts to occur. Therefore, peak power is used for all the input signals to allow a fair comparison of the onset of distortion.

It is observed that the IMD product rises above the noise floor for a 20MHz bandwidth, (the bandwidth of the 802.11g signal), 1dB above the peak power at which the 802.11g EVM starts to increase due to distortion, the knee point. This is expected because the power at which the first IMD product rises above the noise floor in a two-tone test (normalised to a service bandwidth) represents the first time distortion is large enough to cause the EVM to rise detectably above its noise-limited value.

In Figure 3.1 this IMD product does not follow a third-order trend. However, it is expected that at low powers third-order distortion would dominate. Therefore, a 'worst case' third-order fit, assuming third order behaviour ceases immediately below the instrument noise floor, is used. When this is extrapolated it is found that its intercept with the 20MHz bandwidth noise floor is 8dB above the EVM knee point. Evidently the common assumption of a third-order dominated IMD product, which can be extrapolated to predict the dynamic range at a particular bandwidth, is not accurate here.

The measured IMD products suggest that high-order (5^{th} and greater) nonlinearities are dominant. Consequently, third-order SFDR no longer accurately reflects performance under modulation with real signals because it assumes nonlinearity is third-order dominated. An alternative metric is needed to enable design and comparison of links.

3.3 Theory of nonlinear behaviour in lasers

As shown in the previous section, high-order nonlinear distortion can arise in RoFSO links as a result of the high optical loss and the high modulation depths used. In order to develop a new metric to quantify dynamic range when third-order SFDR fails it is necessary to understand theoretically the causes of this high order distortion at high modulation depths and to simulate this behaviour.

3.3.1 Causes of nonlinearity

Models for the behaviour of directly-modulated semiconductor lasers are well-established [167]. In order to investigate nonlinearity it is necessary observe how such a model behaves under extreme modulation conditions. Previous research into dynamic distortion has successfully used a simple rate equation model and so a similar approach is used here [168]:

$$\frac{dN}{dt} = \frac{I}{eV} - g_0 \left(N - N_{om}\right)\left(1 - \epsilon P\right) - \frac{N}{\tau_n} \tag{3.1}$$

$$\frac{dP}{dt} = \Gamma g_0 \left(N - N_{om}\right)\left(1 - \epsilon P\right) P - \frac{P}{\tau_p} + \Gamma\beta\frac{N}{\tau_n} \tag{3.2}$$

where N represents the carrier density, N_{om} the transparency carrier density, I the drive current of the laser, e the unit charge, V the volume of the active region, g_0 the optical gain, P the photon density, ϵ the gain compression factor, Γ the confinement factor, β the spontaneous emission coupling coefficient, τ_p the photon lifetime and τ_n the carrier lifetime.

A third equation representing the optical phase of the light inside the cavity is commonly used. However, the theoretical results derived here are for devices intended to be used in optical links using phase-insensitive photodiode-based envelope detectors. Similarly, the intended links for these devices are sufficiently short that dispersion can be neglected. Further, they do not use narrowband optical filtering so there is no mechanism for FM-IM conversion. As a result optical phase can be omitted from the simulation for simplicity. The simulated behaviour matches closely that observed experimentally in Section 3.4, indicating the validity of this assumption.

These rate equations are solved for a number of different drive currents using the following parameters, taken from related work on simulating nonlinear effects in semiconductor lasers [166]: $N_{om} = 4.6 \times 10^{24}\text{m}^{-3}$, $eV = 1.44 \times 10^{-35}\text{m}^3\text{C}$, $g_0 = 10^{-12}\text{s}^{-1}\text{m}^3$, $\epsilon = 3.8 \times 10^{-23}\text{m}^3$, $\Gamma = 0.646$, $\beta = 10^{-3}$, $\tau_p = 2\text{ps}$, $\tau_n = 3.72\text{ns}$, $I_{th} \sim 21\text{mA}$. Additional parameters used in the simulation are the effective refractive index of the laser cavity, $n_{\text{eff}} = 3.6$, wavelength of light, $\lambda = 1310\text{nm}$, reflectivity of the cavity ends, $R = 0.2985$, cavity length, $L = 300\mu\text{m}$, bias current, $I_{bias} = 110\text{mA}$, and conversion ratio of the photodiode receiver, $G = 450\text{V/W}$. Although changes in temperature can alter the threshold current, gain and wavelength of the laser, creating potential additional nonlinearity [154], the temperature is assumed to be constant.

The 1310nm wavelength is chosen to leverage the availability of low-cost lasers designed for 10-gigabit Ethernet (10GbE) and better system margins when compared with 850nm devices.

In directly-modulated lasers, nonlinear effects become more significant as the optical modulation index (OMI) increases. OMI can be quoted as an RMS quantity but in this chapter the terms OMI and peak OMI are used interchangeably to mean the maximum instantaneous OMI. Therefore, for a single tone input the OMI is defined as OMI $= I_{amp}/\left(I_{bias} - I_{th}\right)$. For other input signals the maximum instantaneous current replaces I_{amp}.

Consider the case of a laser biased well above the lasing threshold and modulated with single frequency sinusoid. If the OMI is less than unity, then a small amount of nonlinearity will arise from the gain compression factor ϵ. This gain compression is a result of a number of effects including gain saturation due to a finite number of carriers, spatial hole burning and leakage currents [154]. Nonlinearity in this regime that arises primarily from gain compression is termed static distortion, as illustrated in Figure 3.2, and is typically dominated by second-order and third-order effects.

As the OMI rises to unity the minimum drive current begins to drop just below the laser threshold current and a second type of nonlinearity caused by the turn-on delay begins to occur. This sudden turning on of the laser can be modelled accurately using fairly simple approximations [169]. However, the rate equation model is necessary to simulate additional nonlinear effects caused by relaxation oscillations. This is referred to as dynamic distortion, as illustrated in Figure 3.2.

As OMI increases even further gain compression starts to damp the relaxation oscillations caused by dynamic distortion thereby reducing its effect. This also limits the maximum output power. Thus the output power is effectively clamped at both upper and lower limits creating a clipped sine-wave. Nonlinearity in this regime is referred to as overmodulation distortion, as illustrated in Figure 3.2.

The frequency domain spectra for static, dynamic and overmodulation distortion scenarios are shown in Figure 3.2. It can be seen that high-order harmonics (fourth-order and above) are barely detectable in the static distortion regime, but become more prominent when dynamic distortion begins to occur. Previous work has shown significant spectral broadening due to FM effects under large OMI conditions but in this case only IM effects need to be considered [170].

The powers of the first 9 harmonics are recorded as the input power, or equivalently the OMI, is increased and are plotted in Figure 3.3. It can be seen that at the point where the OMI reaches unity, dynamic distortion begins to occur and the higher order harmonics increase rapidly in power. Prior to this point, in the static distortion regime, only the first four harmonics are significant. This shows that dynamic distortion is dominated by high-order nonlinear effects.

Previous research has shown that the relaxation oscillations occurring in this regime create increased levels of distortion, but this is the first time a link between this effect and increased high-order distortion has been drawn [168, 171]. Static distortion can be reduced through use of predistortion circuits but these are undesirable for RoFSO as they only cancel up to third-order distortion and have narrow operating bandwidths [82].

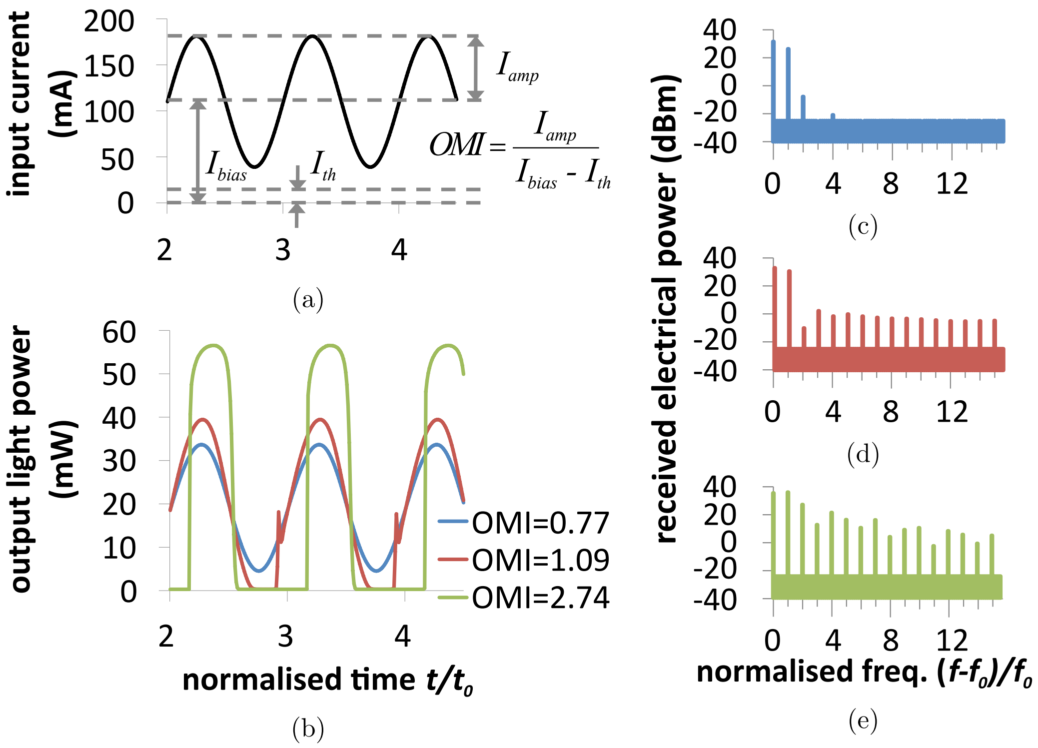

Figure 3.2: Simulation results illustrating different types of distortion: (a) input current consisting of a bias current, I_{bias}, of 110 mA and a modulating sinusoid at frequency $f_0 = 1$ GHz ($T_0 = 1$ns) with an amplitude, I_{amp}, of 72mA resulting in an OMI of 0.77 (b) laser output power vs. time showing the effects of static, dynamic and overmodulation distortion encountered for OMI $= 0.77$, 1.09 and 2.74 respectively, (c)-(e) power spectra of the received electrical signals for the static, dynamic and overmodulation distortion scenarios respectively.

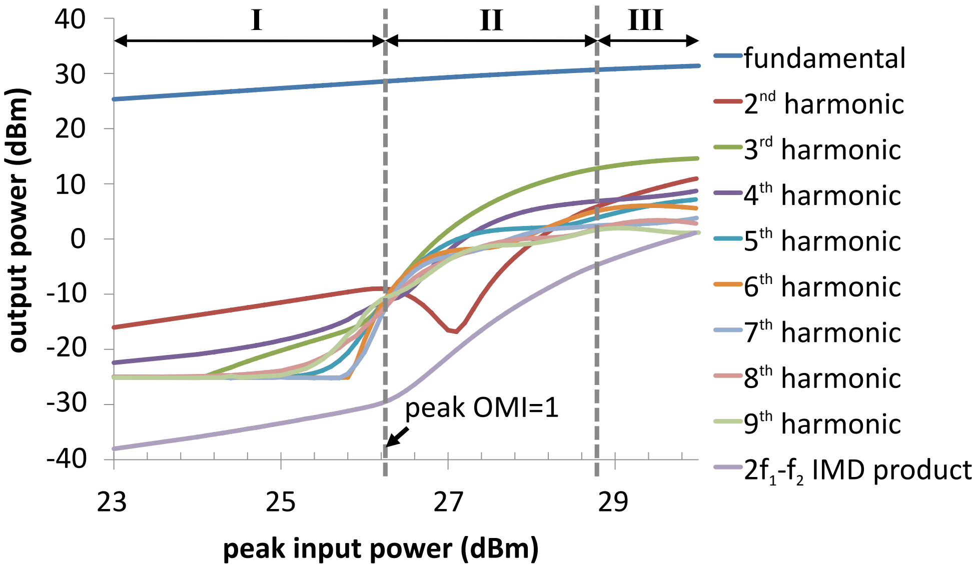

Figure 3.3: Graph showing how power of harmonics varies as peak input power (or equivalently OMI) is increased for a single-tone input. The three regimes of distortion are indicated on the graph: I – static distortion, II – dynamic distortion, III – overmodulation. Also shown is the power of the $2f_1 - f_2$ IMD resulting from a two-tone input.

3.3.2 Effects on third-order SFDR

In high-loss optical links it is often the case that dynamic distortion has already started to occur in the laser before the first IMD product becomes greater than the noise floor. In this case dynamic distortion is the dominant factor determining RF dynamic range.

Previous research has investigated the effects of third-order IMD products on the third-order SFDR of analogue optical links using a range of different lasers [172]. However, as will be shown, these methods of analysis become less meaningful when the laser is driven at high OMI as the dominant order of the distortion is not readily predictable. Work has also been conducted on DFB lasers as standalone devices and their performance under modulation in analogue applications, particularly CATV [148]. However, they only examine static distortion effects and do not consider the effects of high-order dynamic distortion on third-order SFDR or on performance metrics used for real services under high optical loss.

The nonlinear distortion in any of the three regimes can be considered to arise from a high-order polynomial transfer function. For a two-tone input, consisting of tones at frequencies f_1 and f_2, it can be shown that the $2f_1 - f_2$ IMD product is contributed to by all odd order polynomial terms as follows:

$$P_{2f_1-2f_2} = a_3\frac{3}{4}A^3 + a_5\frac{25}{8}A^5 + a_7\frac{735}{64}A^7 + a_9\frac{1323}{32}A^9 + K \tag{3.3}$$

where $P_{2f_1-f_2}$ is the power of the first IMD product, A is the amplitude of the current of a single input tone and a_n is the Taylor series coefficient for the n^{th} order term of the polynomial light-current transfer function of the laser. In many systems third-order distortion dominates and so the fifth and higher order terms are neglected. When dynamic distortion is dominant, however, the high-order terms contribute significantly to the first IMD product. Using the same parameters described in the previous section, the power of the first IMD product with increasing input drive power is simulated. The result is shown in Figure 3.4.

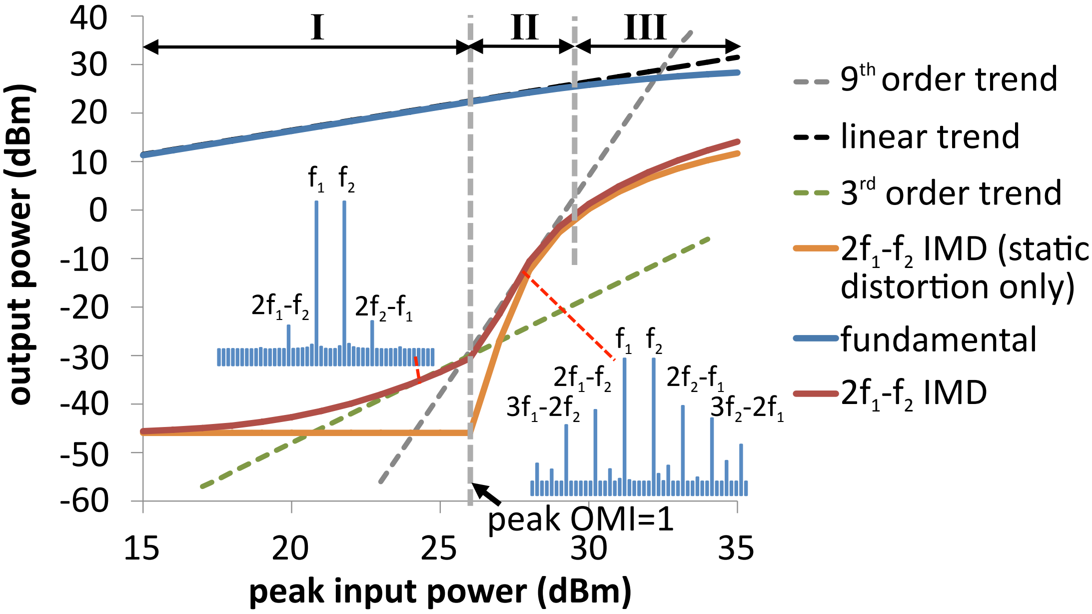

Figure 3.4: Graph of output power vs. peak input power for a two-tone input with tones at 950MHz and 1.05GHz. The three regimes of distortion are indicated on the graph: I - static distortion, II - dynamic distortion, III - overmodulation distortion. The curve labelled 'linear' shows the case when the gain compression factor is zero. Overlaid are the spectra of the received electrical power showing the magnitudes of the various IMD products, including higher order products such as $3f_1 - 2f_2$.

It can be seen that the first IMD product begins to rise above the noise floor with a slope of 3, indicating the initial dominance of third-order nonlinearity. When the peak OMI reaches unity the curve for the first IMD product undergoes a sharp increase in slope. This point coincides with the sharp increase in power of high-order harmonics as was shown in Figure 3.3. This change in slope of the IMD product power curve can then be seen to be due to increased levels of high-order distortion created by dynamic distortion. The slope observed is much greater than 3 but is not constant or predictable (in Figure 3.4. it reaches a maximum value of 9). The dominant order of distortion at any power level is unpredictable without precise knowledge of the laser parameters, which are not often available. As the input power is further increased overmodulation distortion starts to dominate and the IMD product power begins to roll off.

For any nonlinear system it is expected that as power is increased higher order effects will become noticeable at some point. However, previous research has clearly identified a link between the presence of relaxation oscillations and a sudden change in nonlinear behaviour as the OMI approaches unity [171]. These relaxation oscillations cause nonlinear behaviour of a higher order than would be expected in the case of a clipped sinusoid exhibiting no high-frequency oscillatory behaviour, which is often the assumed behaviour for systems operating in a clipping regime. This high-order behaviour will occur even for a theoretical perfectly linear laser that does not exhibit any gain compression as shown in Figure 3.4.

The third-order SFDR is measured in a two-tone test where the input power of the tones is increased until a third-order trend line can be established. This third-order trend is then extrapolated to lower powers to find the intercept with the 1Hz noise floor as shown in Figure 3.5, giving the 1Hz normalised third-order SFDR. This can then be used to estimate the useful dynamic range of a service with a particular bandwidth by extrapolating the third-order trend to higher powers and finding the intercept of the trend with the noise floor at that bandwidth assuming that the dominant distortion will remain as third-order. However, this assumption is invalid in the systems described here because under dynamic distortion higher order effects dominate. It is therefore not possible to perform the usual linear extrapolation and so the 1Hz normalised SFDR figure is no longer a useful indicator of the dynamic range at a given bandwidth.

If this is ignored and the standard third-order extrapolation from the 1Hz noise floor is used anyway it will tend to overestimate the distortion-free dynamic range at higher bandwidths (with their associated higher noise floors). For example the third-order SFDR overestimation for a 20MHz bandwidth noise floor, as used for 802.11g wireless services, is shown in Figure 3.5.

However, third-order SFDR is still an attractive figure of merit because it is determined using a simple test that can be run independently of any particular service and at any frequency, or can be calculated from measurable device parameters. It is also a commonly used metric and so is important for comparison purposes. However, since the dominant order of the distortion under deep modulation with a high noise figure cannot be predicted another service-independent measure of the performance limits for directly-modulated high-RF-power high-loss optical links that retains the desirable properties of third-order SFDR is needed.

When dynamic distortion is dominant, there is a very steep increase in the power of the first IMD product just after the peak OMI reaches unity. The slope of the IMD product curve at this point is unknown and constantly changing but is large (usually above 7^{th} order). This is sufficiently steep that it can be modelled by a vertical line at the input power for which OMI=1. This sets an upper limit on the peak RF modulating power that is independent of bandwidth and the exact order of distortion.

It is predicted that this sharp rise in distortion causes a sharp increase in EVM for a radio service sent over the link when the RF modulating power is such that the peak OMI reaches unity. This should cause the knee point of any EVM vs. power curve to occur at the same peak power regardless of service. RF services can continue to operate beyond the knee point as they are designed to cope with some third-order distortion. However, when high-order distortion is dominant EVM increases more rapidly so the knee point becomes a good indicator of a practical upper limit for the RF modulating power. The RF power where peak OMI is unity is therefore a realistic and practical measure of the highest modulating power that can be used when dynamic

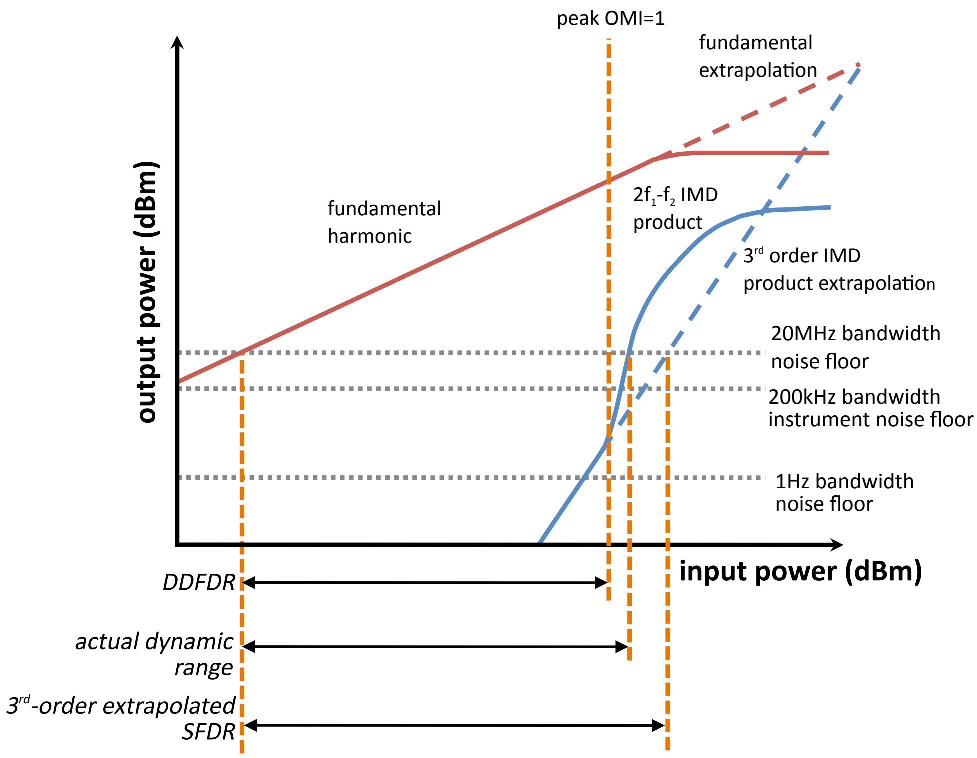

Figure 3.5: Graph showing received electrical output power vs. input power of a single tone for a two-tone test illustrating some of the inaccuracies of conventional SFDR and highlighting the improvement offered by use of DDFDR. 20MHz is the bandwidth of 802.11g wireless.

distortion is dominant.

Aside from increasing EVM due to in-band interference, distortion also causes out-of-band interference. However, due to the availability of robust means to deal with this interference, EVM is almost always the first metric to deviate from the required standard as signal power is increased [173].

It is proposed that a new measure of dynamic range called dynamic distortion free dynamic range (DDFDR) be used as a measure of dynamic range under dynamic distortion dominated conditions. The upper limit of this is defined as the RF modulating power at which the peak OMI=1 and the lower limit is defined as the RF modulating power at which the SNR=1 for a given bandwidth. This is illustrated in Figure 3.5. The point where peak OMI=1 can easily be calculated from readily available device parameters of the laser (namely threshold current), which is simpler than measuring the third-order intercept required to calculate third-order SFDR. The noise can be calculated for a link using device parameters of all the components, as is done for third-order SFDR. Like third-order SFDR, DDFDR can be normalised to the noise power measured in a 1Hz bandwidth. In most situations, normalised DDFDR would not reflect the actual performance of system with a bandwidth of 1Hz and third-order SFDR would be a more suitable metric due to dominant third-order behaviour in this regime. However, normalisation allows the DDFDR to be calculated for a service of any bandwidth and for comparison between links. The units of normalised DDFDR are dB/Hz although as mentioned in section 2.3.4, this is not strictly correct but is intended to indicate that the noise floor power is measured in a 1Hz bandwidth. To find the DDFDR for a particular bandwidth, B, it is necessary to add $10\log_{10}(B)$ to the normalised DDFDR.

DDFDR is only accurate if the link noise figure is sufficiently high that the first IMD product intercepts the noise floor after the peak OMI of the modulating signal reaches unity and if high-order dynamic distortion is dominant at this point. In the case of RoFSO links this high noise figure can be due to high optical loss or high receiver bandwidth. For noise figures lower than this third-order static distortion is usually dominant and third-order SFDR can be used accurately.

DDFDR has a tendency to underestimate actual dynamic range as the upper limit is less than the actual IMD product power. However this is desirable when designing systems as it represents the worst case scenario.

3.4 Experimental investigation

To verify the theoretical results presented in the previous section it is shown that high-order distortion effects are experimentally reproducible in directly-modulated lasers with high modulation depths and that in high-loss optical links this reduces the utility of third-order SFDR. Further, the DDFDR of the laser used is shown to be a better predictor of link EVM performance under such conditions.

3.4.1 Setup

For this experimental investigation a high-RF-power high-loss IM-DD RoF test link is used, as shown in figure 3.6. The parameters for this set-up are listed in Table 3.1.

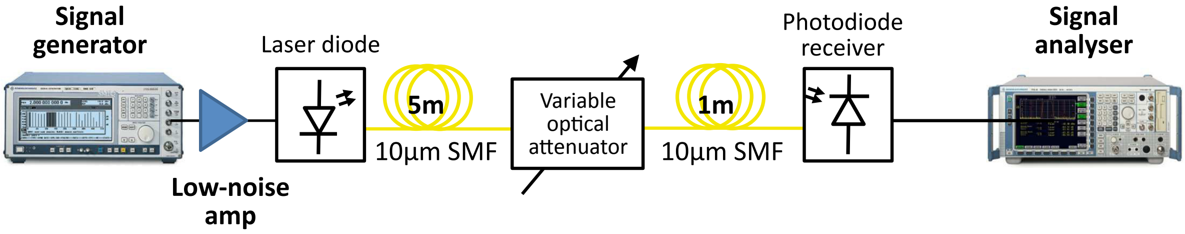

Figure 3.6: Experimental set-up used for testing of RoF link.

An optical attenuator is used to allow a variable broadband optical loss, mimicking that found in free-space optical links. The results in the next section using this attenuator show a good match with the results in Section 3.2.1 using an actual free-space link. For the photodiode used, the maximum allowable optical input power is 2dBm and so the attenuation is set to ensure that the received optical power is far enough below this to avoid causing further nonlinear distortion.

Table 3.1: Parameters for experimental set-up

Parameter	**Specification**
laser part number	Sumitomo SLV521A DFB
wavelength	1310nm
CW transmit power	10dBm
laser bias current	50mA
optical attenuator loss	11.9dBo
photodiode receiver	Agilent 11982A Amplified Lightwave Converter
tested modulation frequencies	2.4GHz
laser operating temperature	25°C
noise measurement bandwidth	200kHz
peak OMI range	0.1-3.5

The temperature is held at 25°C using a *thermoelectric cooler (TEC)*. Dynamic temperature effects only become important at modulation frequencies less than 100MHz and so do not affect temperature stability here [154].

3.4.2 High-Order Dynamic Distortion

For the experimental setup described previously the power of the first IMD product in a two-tone test is measured and is plotted against input power as shown in Figure 3.7.

It can be seen that the first IMD product does not exhibit third-order behaviour – a ninth-order slope provides a better fit. Because of the high optical loss of this link even for an RF bandwidth as low as 200kHz, the first effect to appear above the noise floor is high-order distortion. Using the third-order extrapolation technique discussed in Section 3.3, for a bandwidth of 20MHz (used in 802.11g) the calculated third-order SFDR is at least 6dB larger than the actual

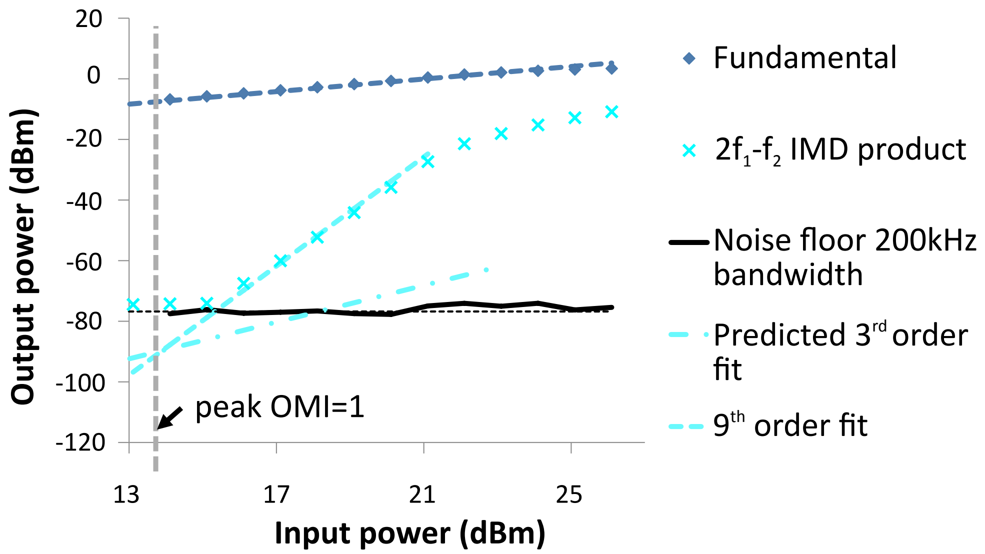

Figure 3.7: Graph showing output power vs. peak input power for a two-tone SFDR test with the 1310nm Sumitomo SLV521A DFB.

IMD product free dynamic range.

When the spectrum is analysed, as shown in Figure 3.8, IMD products created exclusively by fifth and higher order distortion products are seen to be present. Clearly, high-order nonlinearities are dominant in this case and their appearance is consistent with the onset of dynamic distortion as predicted in Section 3.3. With this particular link it is not possible to observe third-order distortion by reducing optical loss because any further decrease in optical loss begins to cause nonlinear behaviour in the photodiode.

The measured time domain response of the link with a single tone input at 500MHz is shown in Figure 3.9. It can be seen that for this particular modulation level the laser drive current drops below the threshold and when it turns on again there is a delay followed by relaxation oscillations. This is the behaviour predicted in Section 3.3 and is the cause of dynamic distortion.

Two other lasers are also tested under similar conditions. Optical losses are kept the same but transmit powers and bias currents are adjusted in order to run the lasers at their optimum operating points. The test conditions are still representative of RoFSO systems. The plots for the two-tone SFDR tests are shown in figures 3.10a and 3.10b.

For both of these lasers, the first nonlinear behaviour to be observed is third-order. However, in both cases the noise floor appears very close to the onset of high-order distortion meaning that if higher optical loss or higher RF bandwidth are used the high-order distortion will dominate. For example, in both cases high-order distortion would become dominant with 5dBo additional optical loss and a 2MHz signal bandwidth. It can be seen that this dominance of dynamic distortion is not a consequence of the particular laser used. Rather, the operating conditions of high-RF-power, high-loss, RoFSO links, make them very susceptible to it.

It is also noted that the dominant order of distortion varies between the lasers – 7^{th} order is a

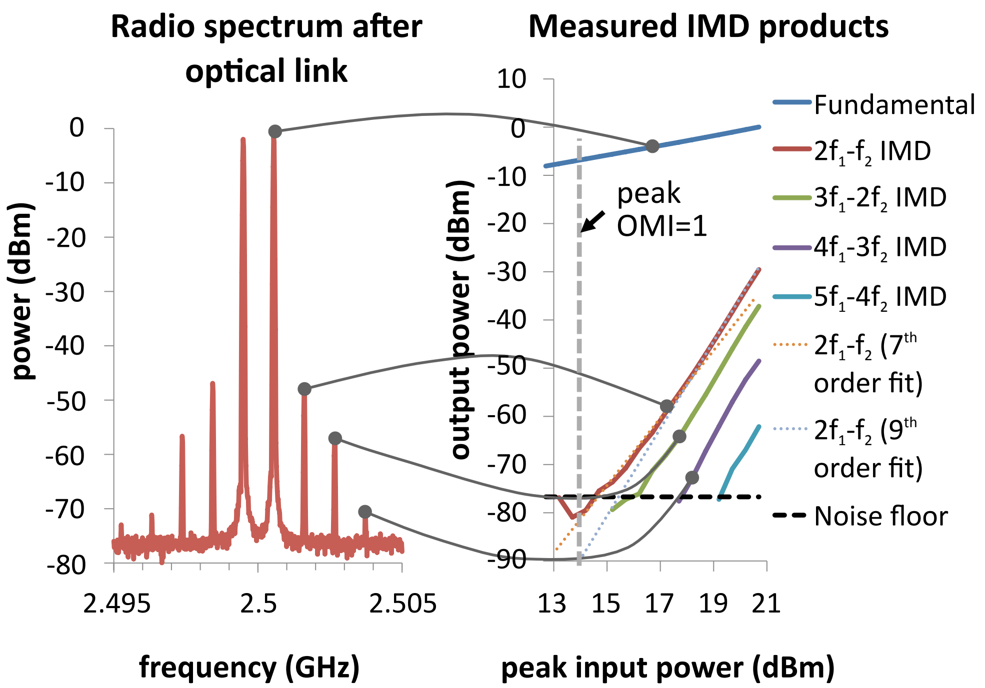

Figure 3.8: Graph showing high-order IMD products at output of test link under a two-tone test. The plot on the left is the spectrum and the plot on the right shows how the different components increase with input power.

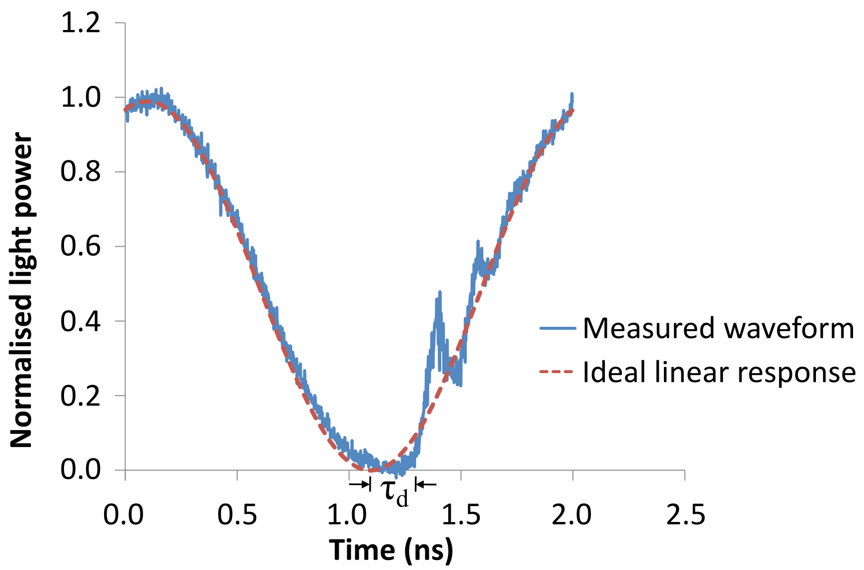

Figure 3.9: Measured graph of light power vs. time showing turn-on delay, τ_d, followed by relaxation oscillations, both hallmarks of dynamic distortion.

good fit for the 1547nm laser while 9$^{\text{th}}$ order is better for the 1310nm device. This demonstrates the dependence on measurement conditions of the order of distortion in these high-order cases. This agrees with the theory proposed in Section 3.3.

From a practical perspective it is undesirable to drive the laser sufficiently hard that dynamic distortion is encountered. However, in order to use the maximum RF dynamic range it is necessary to be able to establish limits for linear operation. Third-order SFDR is not suitable for this task in cases where high-order effects are dominant so DDFDR provides a more accurate and realistic alternative.

It is worth nothing that high-order dynamic distortion caused by relaxation oscillations can also be minimised through careful laser design. By increasing the cavity length, reducing facet reflectivity or reducing the bias current it is possible to reduce the frequency of and/or dampen the relaxation oscillations, thereby reducing their impact on linearity. Reducing the bias current has the downside of reducing output power, and so adjusting doping levels may be necessary in such a case to avoid sacrificing power. Long-cavity lasers designed to significantly reduce relaxation oscillations (often termed *class A lasers*) have been proposed for analogue RF applications, though they generally suffer from reduced RF bandwidths [174].

This is the first practical situation in which dynamic distortion effects have been found to be important and the first time their impact on third-order SFDR and modulation performance has been investigated.

3.4.3 DDFDR Performance

To examine the performance of the DDFDR a two-tone test is performed using the same link set-up with the 1310nm laser described in Table 3.1. EVM curves for 802.11g and 3GPP services over the same link are also recorded and the results overlaid in Figure 3.11.

Both tests use a 2.4GHz carrier frequency. The 3GPP service is tested in QPSK modulation mode. The 802.11g service is tested in 54Mbps 64QAM mode. When comparing EVM for different modulation schemes the peak OMI is defined using statistical measures of the peak to average power ratio (PAPR). Measurements have shown that for 802.11g instantaneous power is less than 10dB above the average 99.9% of the time [173]. Similar statistical values can be obtained for a two-tone SFDR test signal and 3GPP [175, 176]. This allows for a fair comparison between services.

It is observed that both the services tested reach their knee points and experience an increase in EVM at the same peak input power of 14dBm. This is the point at which the peak OMI of these services reaches unity. The overlay of the IMD product indicates that high-order dynamic distortion is the dominant nonlinear effect in this setup. This is consistent with the theory that the high-order behaviour of the IMD product curve is linked to this abrupt increase in EVM across all the services as proposed in Section 3.3.

For each service, the knee point of the EVM curve is compared with the DDFDR upper limit and the third-order SFDR upper limit for the service bandwidth (20MHz for 802.11g and 5MHz for 3GPP). The offset of the DDFDR and SFDR upper limits from the EVM knee points are shown in Table 3.2.

It can be seen that the DDFDR upper limit gives a more accurate estimate of the EVM knee point than SFDR. Across the two services the average magnitude of the offset of the DDFDR

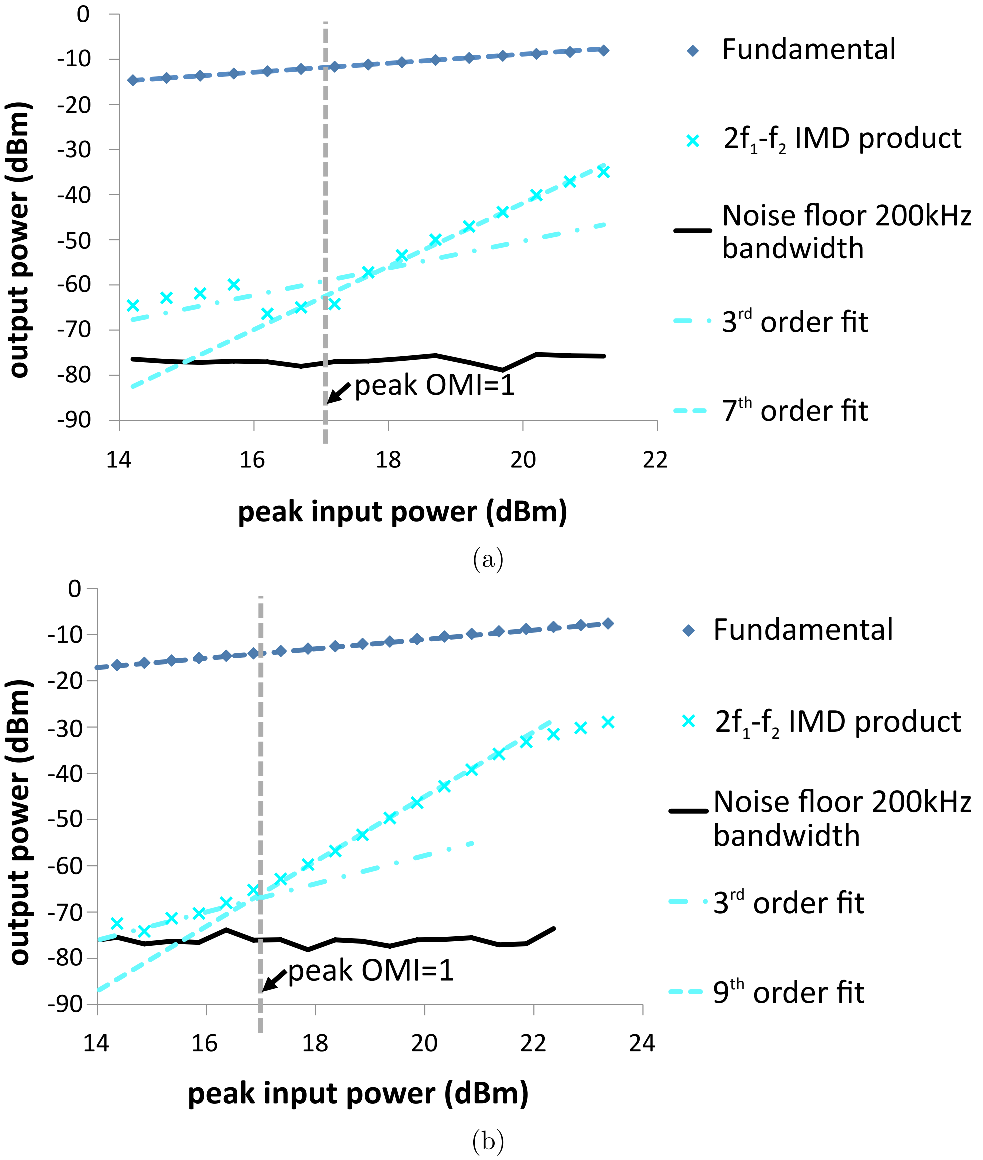

Figure 3.10: Graph showing output power vs. input power for two-tone SFDR test using: (a) a 1547nm Mitsubishi FU-68PDF DFB at 9.45dBm output power and 50mA bias current, and (b) a 1310nm Sumitomo SLW4260 DFB at 4.94dBm output power and 40mA bias current.

Table 3.2: Offsets of third-order SFDR and DDFDR upper limits from EVM knee points

Service	**Offset of knee point from SFDR upper limit**	**Offset of knee point from DDFDR upper limit**
802.11g	-8.4dB	-1.5dB
3GPP	-4.1dB	0.7dB

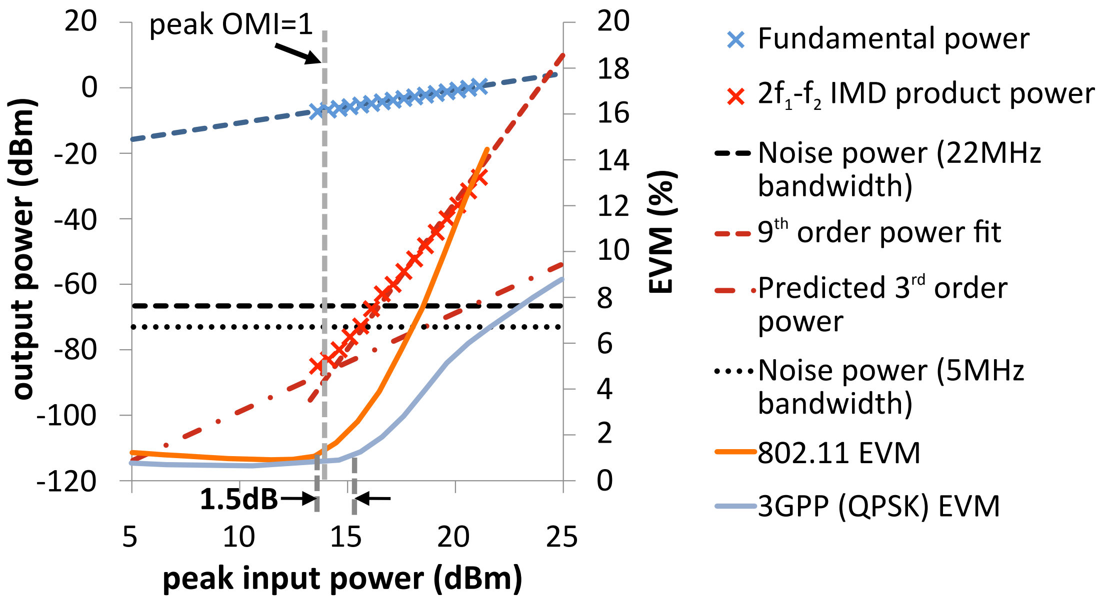

Figure 3.11: Graph showing comparison of two-tone SFDR power curve and EVM curves for several modulation schemes at 2.4GHz. Solid curves represent EVM values while dashed curves represent output power levels for a two-tone test.

upper limit from the knee point is 1dB while for third-order SFDR it is 6dB. This result suggests that DDFDR provides a more accurate and realistic estimate of RF dynamic range than third-order SFDR for real services under conditions where high-order dynamic distortion of unknown order is dominant.

The knee points of the services have a spread of 1.5dB. Because DDFDR aims to predict this knee point this clearly places a limitation on the accuracy of DDFDR. However, it is seen that DDFDR tends to occur at the lower end of this spread suggesting that it represents an upper limit beyond which high-order distortion starts to significantly degrade EVM performance for at least one service. This is in contrast to extrapolated SFDR which tends to overestimate this upper limit, meaning that systems designed using it may inadvertently be driven into a regime of high-order nonlinear behaviour. In this sense, DDFDR is a safer measure of this upper limit as it enables links to avoid this regime. Further, despite this fundamental limit on its accuracy, DDFDR is still significantly more accurate in predicting performance than SFDR when high-order dynamic distortion is present.

3.5 Conclusion

It is shown theoretically and experimentally that dynamic distortion tends to be the dominant factor limiting performance in high-RF-power high-loss analogue optical links using directly-modulated semiconductor lasers, such as low-cost RoFSO links. Dynamic distortion is caused by relaxation oscillations and hence characterised by high-order nonlinear effects. It is shown that due to their operating conditions, high loss links are susceptible to this dynamic distortion.

In order to demonstrate a link's ability to support radio services it is necessary to use a service- and bandwidth-independent measure of dynamic range. Usually this is achieved using third-order SFDR but this fails in these situations due to the presence of dominant high-order distortion. It is not possible to use a specific higher-order equivalent of SFDR because the exact order of the distortion is unknown. A new measure of dynamic range, dynamic distortion free dynamic range (DDFDR) is proposed, the upper power limit of which is the RF power at which the peak instantaneous OMI reaches unity. The lower limit is the noise floor power, similar to third-order SFDR. DDFDR can be bandwidth normalised, like third-order SFDR, but is only valid under conditions where high-order distortion is dominant. DDFDR can be evaluated at a range of different frequencies to demonstrate the broadband and service-independent operation of a system. It can also be used to compare between different lasers in the same link.

It is observed that when the peak OMI reaches unity in high-RF-power high-loss optical links the EVM of a number of services increases at the same peak power level, independent of bandwidth or modulation scheme. This causes an effective compression of the knee points for the EVM curves across different services. It is found experimentally that when EVM curves for different services are compared the knee points all fall within a 1.5dB range of one another irrespective of the RF service. Further, it is shown experimentally that in dynamic distortion limited systems the upper limit of the DDFDR can on average predict the EVM knee point to within 1dB, compared with third-order SFDR which only predicts it to within 6dB. This indicates that under conditions of dominant dynamic distortion the DDFDR provides a better service-independent indicator of the limits within which a link can be operated without experiencing increased EVM than third-order SFDR.

The DDFDR metric will play an important role in the design of low-cost, high-density wireless infrastructure needed to meet exploding capacity demands.

Chapter 4

Evaluation of Layout Designs for 3×3 MIMO-Enabled Radio-over-Fibre Distributed Antenna Systems

General overview

This chapter demonstrates experimentally that for two representative indoor distributed antenna system (DAS) scenarios, existing radio-over-fibre (RoF) DAS installations can enhance the capacity advantages of broadband 3×3 multiple-input multiple-output (MIMO) radio services without the requirement for additional fibres or multiplexing schemes. This is true for both the single user and multiple user cases with single and multiple base stations.

First, a theoretical example is used to illustrate that there is negligible SNR improvement when using a MIMO DAS with all N spatial streams replicated at N remote antenna units compared with a MIMO DAS with only one of the N streams at each remote antenna unit for $N \leq 4$.

It is then confirmed experimentally that a 3×3 MIMO DAS offers improved capacity and throughput compared with a 3×3 MIMO collocated antenna system (CAS) for the single-user case in two typical indoor DAS scenarios – one with significant line-of-sight (LOS) propagation and the other entirely non-line-of-sight (NLOS). The improvement in capacity is 3.2% and 4.1% respectively.

Next, experimental channel measurements confirm there is negligible capacity increase of the 3×3 configuration with 3 spatial streams per antenna unit over the 3×3 configuration with a single spatial stream per antenna unit. The former layout is observed to provide an increase of $\sim$1% in the median channel capacity in both the single and multiple user scenarios. With 20 users and 3 base stations a multichannel MIMO DAS using the latter layout offers median aggregate capacities of 259 bit/s/Hz and 233 bit/s/Hz for the LOS and NLOS scenarios respectively.

It is concluded that DAS installations can further enhance the capacity offered to multiple users by multiple 3×3 MIMO-enabled base stations. Further, designing future DAS systems to support broadband 3×3 MIMO transmission may not require significant upgrades to existing installations for small numbers of spatial streams.

This chapter is drawn primarily from work published in IEEE Transactions on Vehicular Technology [177].

4.1 Introduction

As discussed in Chapter 1 there is an imminent need to increase the capacity offered by wireless networks. Further, as introduced in Section 1.5 a key aspect of this is finding the best way to combine the coverage benefits of DAS with the capacity benefits offered by MIMO transmission.

In a generalised MIMO-enabled DAS, it is possible to replicate the M transmitted spatial streams at K remote antenna units (RAUs), separated by much greater distances than the elements within each antenna array. This can be done in a number of different ways, two examples of which were shown in Figure 1.21. The key difference is the degree to which spatial streams of each service are replicated at separate RAUs. This can be quantified by introducing a term the *replication factor*, R, defined as:

$$R = A = \frac{T}{K} \tag{4.1}$$

where A is the number of antennas per RAU, T is the total number of antennas in the entire DAS and K is the number of RAUs.

There are two main approaches to designing MIMO DASs. The first is to send all MIMO spatial streams to each RAU i.e. an $M \times N$ MIMO DAS with replication factor of $R = M$ such as that of Figure 1.21a. This approach has been shown to provide improved performance over MIMO CAS [137], and a number of multiplexing schemes to provide this functionality over a single fibre have been proposed [138, 140, 178]. The second approach is to have separate MIMO spatial streams sent to different RAUs, i.e. an $M \times N$ MIMO DAS with replication factor of $R = 1$ such as that of Figure 1.21b. This, too, has been shown to offer improved capacity over co-located MIMO [142, 143]. This approach has the advantage that it does not require additional fibres or multiplexing so can be implemented with minimal upgrades to existing DAS.

Previous work on these two approaches has been largely theoretical and has not reflected a range of realistic indoor DAS scenarios [144, 145, 147]. Further, little experimental work has been done on indoor MIMO DASs with 3 or more spatial streams. This is of critical importance as emerging wireless services offer anywhere from 4 (4G/LTE) to 8 (802.11ac) spatial streams. Consequently, this chapter investigates the performance of different designs for 3×3 MIMO DAS from an experimental perspective. Because the experiments are conducted using a commercially available RoF DAS compatible with standard OM1-OM4 multimode optical fibre and the locations of RAUs in the experiments are typical for an indoor DAS installation, the results are immediately applicable to many existing DAS installations.

To conduct a full analysis of a MIMO system it is necessary to consider the performance in a number of cases: a single user accessing a single base station (SU-SB), a single user accessing multiple base stations (SU-MB), multiple users accessing a single base station (MU-SB) and multiple users accessing multiple base stations (MU-MB). Together, these cover all possible access scenarios for broadband MIMO DASs [37].

SU-SB scenarios form a good starting point for identifying underlying behaviour and are the most commonly investigated. However, in future MIMO DAS, MU-MB scenarios will be of the greatest practical importance and so it is necessary to consider how the sum-rate capacity for multiple users (or equivalently the capacity per user) varies as more base stations are added to the network [179]. It has been shown theoretically that in the case of multiple users, DAS provides significant capacity improvements over CAS [180, 181]. However, such work has been largely theoretical and has relied on advanced techniques that are not currently practical to implement.

There are a number of different ways in which additional base stations are added to a system. In a CAS, these additional base stations are simply installed at other locations in a building and serve a small area around them. In a DAS, the additional base stations are installed at the same location as the existing base station and make use of the same DAS infrastructure. As was discussed in Section 1.2.3, one way of achieving this is by ensuring base stations operate on different frequency channels. For example in 802.11n, multiple base stations could be set to operate on different frequency channels over the same DAS. The downside of this approach is that it reduces frequencies available to neighbouring DAS installations and creates greater potential for intercell interference.

As an alternative to sharing frequencies in this manner, the DAS controller can partition the DAS such that each base station makes use of a its own subset of RAUs. Each base station then serves users within range of its allocated RAUs. This approach also enables dynamic reconfiguration – for example if only one user were present, all but one of the base stations could be switched off thereby saving energy. This is another key advantage of DASs [37].

The performance of MIMO systems depends heavily on the propagation environment. In order to achieve spatial multiplexing gain, and thus maximise the capacity gain over non-MIMO systems, there must be a degree of decorrelation between the transfer coefficients of different transmit-receive antenna pairs over a range of fading environments. This ensures that the complex weighted sum of transmitted signals detected at each receive antenna is sufficiently different that the resultant channel matrix is invertible. Linear methods can be used to extract each transmitted signal offering a capacity gain. These conditions are not met, for example, in purely line-of-sight (LOS) propagation scenarios as the signals at each receive antenna will, in general, be identical [124].

For MIMO to work there must be at least some degree of multipath propagation, usually modelled as random fading, that ensures decorrelation between receive antennas. However, within this constraint there are two important extreme cases: predominantly line-of-sight (LOS), i.e. propagation is governed by Rician fading with only a small multipath propagation component, and non-line-of-sight (NLOS), i.e. propagation is governed by Rayleigh fading and consists only of multipath propagation [182]. LOS scenarios usually result in high correlation between spatial streams due to the reduced impact of multipath fading. MIMO DASs can still experience improved performance in LOS environments due to increased SNR [183].

The aim of this chapter, therefore, is to combine all possible scenarios for number of users and base stations with two very different propagation scenarios to offer a comprehensive experimental insight into the impact of layout design for MIMO DASs.

First, a theoretical justification of metrics used to evaluate the performance of MIMO systems is presented. Next, it is shown theoretically, using an illustrative example, that an $N \times N$ MIMO DAS with $R = N$ offers negligible SNR benefit over an $N \times N$ MIMO DAS with $R = 1$ for small N (≤ 4). Because of the strong correlation between SNR and channel capacity in many MIMO scenarios it is reasoned that the two systems should exhibit similar channel capacities.

Next, it is shown experimentally for the SU-SB case that a broadband 3×3 MIMO DAS provides improved capacity over CASs. Experiments are conducted in both LOS and NLOS scenarios. The observed improvement is seen to be due to increased SNR in the LOS case, and both increased SNR and reduced spatial correlation in the NLOS case. In both cases DASs offer an improvement in both coverage and capacity. This result is then corroborated with throughput measurements using a 3×3 MIMO DAS and an IEEE 802.11n access point. A 3×3 MIMO DAS with $R = 3$ and a 3×3 MIMO DAS with $R = 1$, both with the same total transmit power, are then experimentally characterised and compared and it is shown that for the two typical indoor DAS scenarios, the $R = 1$ system offers comparable capacity to the $R = 3$ system, consistent with the theoretical findings.

Following this, a multi-user analysis is conducted and the total aggregate capacity of the network is investigated. It is first shown that it is necessary to incorporate multiple base stations to offer significant capacity improvement for multiple users. In a CAS this is achieved by installing additional base stations at new locations, whereas in a DAS this is achieved by operating several base stations simultaneously over a single DAS infrastructure. This is only possible if each base station operates on a unique frequency channel. The 802.11n standard defines 3 non-overlapping 20MHz channels in the 2.4GHz band and 21-27 non-overlapping 20MHz channels in the 5GHz band (depending on local regulations), so there is much scope for implementing such a system. If too many channels are used in one DAS, however, it could create problems with interference from adjacent cells.

For the same two indoor environments a number of multiple-user scenarios are compared – a 3×3 MIMO DAS with $R = 3$ and multiple base stations, a 3×3 MIMO DAS with $R = 1$ and multiple base stations, and the case with 3 separate 3×3 MIMO CAS base stations. It is found that using multiple base-stations over a single DAS provides superior performance to having the same base stations placed at separate locations. Further, using a 3×3 MIMO DAS with $R = 3$ offers negligible performance advantage over a 3×3 MIMO DAS with $R = 1$.

It is concluded that in realistic DAS installations the existing infrastructure may be capable of supporting the capacity gains of 3×3 MIMO without requiring additional fibers or multiplexing schemes. Further, this holds true for multiple-user systems, provided the DAS can support simultaneous operation of multiple base stations.

4.2 Theory of MIMO wireless systems

4.2.1 Single-user MIMO systems

The performance of a MIMO system can be evaluated by calculating the Shannon capacity of the wireless channel it uses. To do this, it is necessary to measure the complex channel transfer coefficients $h_{k,n,m}$ for every possible pair of transmit and receive antennas on the RAU and mobile terminal respectively, as was shown in Figure 1.21. In many real propagation environments the transfer coefficients $h_{k,n,m}$ exhibit a dependency on frequency within the system bandwidth and so the channel is said to be *frequency selective*. However, in this work it is assumed that because the propagation environments tested are very small, the multipath delay spread is relatively small (of the order of 10-30ns) and so the coherence bandwidth is on the order of 10-50MHz. This is comparable to the channel bandwidth of 802.11g/n of 20MHz and so the channel is assumed to have a relatively flat frequency response, i.e., to be a *flat fading* channel [184]. Minor deviations from spectral flatness are assumed to be compensated to a degree using frequency equalisation, commonly available in services such as 802.11g/n that implement OFDM.

For each RAU, k, with M antennas transmitting to N receive antennas on the mobile terminal, these coefficients can be combined into an $N \times M$ flat-fading channel matrix $\mathbf{H}_k$:

$$\mathbf{H}_k = \begin{pmatrix} h_{k,1,1} & h_{k,1,2} & \cdots & h_{k,1,M} \\ h_{k,2,1} & h_{k,2,2} & \cdots & h_{k,2,M} \\ \vdots & \vdots & \ddots & \vdots \\ h_{k,N,1} & h_{k,N,2} & \cdots & h_{k,N,M} \end{pmatrix} \tag{4.2}$$

The signal received by the mobile terminal from the k^{th} RAU is then given by:

$$\mathbf{y} = \mathbf{H}_k \mathbf{x} + \mathbf{n} \tag{4.3}$$

where $\mathbf{x}$ is the input signal vector from the base station, $\mathbf{y}$ is the signal vector received by the user and $\mathbf{n}$ is a complex Gaussian random noise vector. In general, the entries of $\mathbf{H}_k$ are governed by random fading processes and in theoretical work these are often modelled as independent (or partially correlated) complex Gaussian variables – that is, Rayleigh fading (or Rician fading if correlated) if a multipath environment is assumed [22]. This results in a matrix of random variables, H_k (with the sans-serif typeface denoting a matrix of random variables), of which the rank is $\min(M, N)$.

There are many ways in which the presence of multiple transmit and receive antennas can be exploited to improve system performance. In general, this is achieved by transforming the data streams in order to spread them amongst the transmitting antennas and combine them again after the receiving antennas. This transformation is termed *coding* where *pre-coding* is implemented at the transmitter and *post-coding* at the receiver. One well-known example of this is the Alamouti pre-coding scheme, which spreads each symbol in a data stream across both space (i.e. different transmit antennas) and time. This significantly improves the probability the symbol will be received error-free by offering both spatial and temporal diversity, termed *space-time diversity coding* [185]. The optimal coding scheme for improving performance by way of diversity for a single data stream is *maximal ratio combining (MRC)*. MRC provides the maximum possible SNR at the receiver when the signals from each of the receive antennas are added [186]. There are also other commonly used sub-optimal combining schemes such as equal gain combining and selection combining [124]. The latter, which selects the most powerful signal from all the receive antennas, is often used due to its greater simplicity of implementation.

However, the maximum capacity in multiple antenna systems is actually achieved using *spatial multiplexing (SM)* coding schemes, in which multiple data streams are simultaneously sent via the transmit antennas. Because SM schemes are so widely used for to their high data rates, the term 'MIMO' is often taken to mean 'MIMO using SM coding' even though strictly speaking the term 'MIMO' refers only to the number of transmit and receive antennas. This convention is used here for consistency and convenience.

The optimal SM coding scheme is implemented by taking the singular value decomposition of the channel matrix, H_k:

$$\mathbf{H}_k = \mathbf{U}_k \mathbf{\Sigma}_k \mathbf{V}_k^H \tag{4.4}$$

where $\mathbf{U}_k$ and $\mathbf{V}_k^H$ are unitary $M \times M$ and $N \times N$ matrices respectively, $\mathbf{A}^H$ denotes the Hermitian transpose of $\mathbf{A}$ and $\mathbf{\Sigma}_k$ is given by:

$$\mathbf{\Sigma}_k = \begin{pmatrix} \sigma_{k,1} & 0 & \cdots & 0 \\ 0 & \sigma_{k,2} & \cdots & 0 \\ \vdots & \vdots & \ddots & \vdots \\ 0 & \cdots & 0 & \sigma_{k,\min(M,N)} \end{pmatrix} \tag{4.5}$$

where $\sigma_{k,p}$ is the p^{th} largest magnitude singular value of $\mathbf{H}_k$.

The squares of the singular values are in fact the eigenvalues of $\mathbf{H}_k$. It is seen that there are then S eigenvalues and corresponding eigenvectors, where $S = \min(M, N)$ is the rank of $\mathbf{H}_k$. In the optimal SM coding scheme, these eigenvectors collectively form a basis that can be used to decompose the channel into S equivalent *eigenmodes* or *eigenchannels*. These eigenchannels are orthogonal communication channels with an SNR scaling factor equal to the corresponding eigenvalue. Using eigenchannels or eigenmodes in this way is in fact an SM coding scheme termed *multiple eigenmode transmission* [124]. This scheme can be implemented by using $\mathbf{V}_k$ as a pre-coding matrix, requiring that full *channel state information (CSI)* be available at the transmitter, and $\mathbf{U}_k^H$ as a post-coding matrix. Then, by combining equations 4.3 and 4.4 an equivalent channel can be formed as:

$$\mathbf{y} = \mathbf{U}_k^H \mathbf{H}_k \mathbf{V}_k \mathbf{x} + \mathbf{U}_k^H \mathbf{n} \tag{4.6}$$

$$\mathbf{y} = \mathbf{U}_k^H \mathbf{U}_k \mathbf{\Sigma}_k \mathbf{V}_k^H \mathbf{V}_k \mathbf{x} + \mathbf{U}_k^H \mathbf{n} \tag{4.7}$$

$$\mathbf{y} = \mathbf{\Sigma}_k \mathbf{x} + \hat{\mathbf{n}} \tag{4.8}$$

where $\hat{\mathbf{n}} = \mathbf{U}_k^H \mathbf{n}$ is an adjusted noise term. Because $\mathbf{\Sigma}_k$ is diagonal the channel is now represented as several orthogonal eigenchannels of the original channel scaled by the singular values of $\mathbf{H}_k$. By precoding the input vector $\mathbf{x}$ with a diagonal weighting matrix $\mathbf{Q}_k$, it is possible to allocate a different power to each eigenchannel. It has been shown that if the input signal $\mathbf{x}$ is Gaussian distributed then the optimal values for $\mathbf{Q}_k$ are determined from $\mathbf{H}_k$ using the well-known water filling algorithm [187]. Multiple eigenmode transmission with water filling power allocation is in fact the optimal spatial multiplexing coding scheme in this case. In reality, however, $\mathbf{x}$ is drawn from a non-Gaussian discrete constellations, e.g., 64-QAM, and so water filling is no longer the optimal allocation strategy [188].

Implementation of a multiple eigenmode transmission scheme is only possible if $\mathbf{H}_k$ (i.e. the current CSI of the randomly varying channel) as measured at the receiver is fed back to the transmitter periodically, which can incur significant overhead and increase system complexity. As a result, in many practical MIMO systems $\mathbf{H}_k$ is not known at the transmitter. However, it has been shown that by estimating the channel matrix at the receiver using *successive interference cancellation (SIC)*, *zero forcing (ZF)* or *minimum mean square error (MMSE)*, it is still possible to implement high-performance spatial multiplexing. In fact, the V-BLAST architecture and associated algorithm, developed by Bell Labs, is a post-coding system that is able to achieve the same performance as multiple eigenmode transmission with uniform transmit power allocation [189, 190]. For this reason, V-BLAST has enjoyed significant popularity and is now commonly in use in many real MIMO protocols, such as 802.11n. Because V-BLAST systems do not have CSI available at the transmitter, water filling or other adaptive pre-coding schemes cannot be implemented and uniform power allocation is used for the spatial streams (i.e. $\mathbf{Q}_k = \mathbf{I}_M$). Further, at sufficiently high transmit SNR, such as found in many indoor DASs, the uniform power and water filling capacities converge [124]. Consequently, the multiple eigenmode transmission channel capacity with uniform power allocation is used in this chapter as the channel capacity for all MIMO systems unless stated otherwise. Capacities for water filling power allocation schemes are included for reference.

It was mentioned previously that here the channel fading is assumed to be flat within the bandwidth of interest. Furthermore, it is also assumed that the channel experiences *fast fading*, as opposed to *slow fading*. This means that the channel fading properties, and hence channel coefficients, change quickly relative to the length of codewords, i.e., the time taken to transmit each encoded symbol. In the slow fading case, the channel conditions remain constant for the transmission of a codeword and so if the conditions are poor there can be no guarantee that that symbol will be received error-free for any coding scheme. The performance in this case is usually then indicated by the probability that the channel will not be able to support a certain transmission rate, termed the *outage probability*. In the fast-fading case, however, by coding over an increasingly large time period it is possible to guarantee a maximum capacity of the link for which the probability of bit error is arbitrarily small [184].

For a linear, statistically time-invariant channel subject to *additive white Gaussian noise (AWGN)*, with flat, fast fading defined by a random channel matrix H_k and assuming uniform power allocation (due to no CSI available at the transmitter), the total Shannon capacity of the channel using a multiple-eigenmode transmission scheme (or equivalent) is simply the sum of the Shannon capacities of all the eigenchannels [124]:

$$\mathsf{C}_k = B \sum_{p=1}^{S} \log_2 \left(1 + \frac{\rho}{M} \sigma_{k,p}^2\right) \tag{4.9}$$

where B is the bandwidth of the channel, ρ is the total signal to noise ratio of the system and $\sigma_{k,p}$ is the p^{th} largest magnitude singular value of H_k. This Shannon capacity represents the maximum rate at which data can be transmitted down the channel with arbitrarily low error rate. Note that because H_k is a random variable matrix, the channel capacity, C_k, is a random variable governed by a probability density function. Often, the expected value of this quantity is quoted and is termed the *ergodic channel capacity*.

If perfect Rayleigh fading exists in the channel then all the singular values (and hence eigenvalues) of H_k have the same magnitudes and so the eigenchannels have equal capacity. In such a case there is a linear increase in channel capacity with the number of spatial streams giving a high *spatial multiplexing gain* over non-MIMO systems. In reality, there is often correlation between the entries of H_k and so some of the eigenchannels will necessarily have lower equivalent

SNR. As a result the spatial multiplexing gain is reduced. The spread of singular values (or equivalently eigenvalues), and hence degree of possible spatial multiplexing, can be quantified by the condition number, K, of the channel matrix $\mathbf{H}_k$. This number is often expressed in dB as:

$$\mathsf{K}_k = 20\log_{10}\left(\frac{\max\limits_p(\sigma_{k,p})}{\min\limits_p(\sigma_{k,p})}\right) \tag{4.10}$$

where K_k is the condition number in dB, $\sigma_{k,p}$ represents the p^{th} singular value of the channel matrix $\mathbf{H}_k$, $\max\limits_p(\sigma_{k,p})$ represents the maximum $\sigma_{k,p}$ across all p, and $\min\limits_p(\sigma_{k,p})$ represents the minimum $\sigma_{k,p}$ across all p.

The level of spatial correlation is intimately linked to the angular distribution of power at the transmitter and receiver – the more uniform (non-directional) this distribution is the lower the spatial correlation and the higher the spatial multiplexing gain [124, 191]. This follows from the scattering nature of multipath fading – radiation arriving at all angles must have been scattered heavily by a rich multipath environment and so will exhibit a highly random distribution. By contrast, in the case where there is strong line-of-sight from the transmitter to the receiver the distribution of power will consist of a large directional and deterministic component and a smaller random component, resulting in higher spatial correlation and a higher condition number.

In the case where multiple RAUs are transmitting the same spatial streams, the $\mathbf{H}_k$ matrices from each RAU are added to get the total channel response, $\mathbf{H}$, which can be used in place of $\mathbf{H}_k$ to find the capacity in equation 4.9. This method does not require any additional pre-coding so does not require feedback of the channel state information to the transmitter. Further, this ensures compatibility with SM algorithms such as V-BLAST.

If such information were available, however, it would be possible to use the additional antennas as part of a larger distributed array. An additional level of pre-coding could be applied to this array to implement *transmit beamforming*, which has been shown theoretically to increase capacity in systems operating MIMO over large scale transmit antenna arrays [192]. A full beamforming system requires the ability to send any arbitrary linear combination of spatial streams to any transmit antenna. This is difficult to implement without significantly upgrading transmission equipment and is incompatible with popular post-coding only SM algorithms, such as V-BLAST, which require symmetry in number of transmit and receive antennas.

A simplified version of transmit beamforming could be implemented by enabling each spatial stream at each RAU to undergo a variable phase shift, termed *phase-only transmit beamforming*. This could be implemented using electronically variable delays in the DAS hub. An even simpler solution is *antenna selection*, which selects only the optimal subset of antennas for use. For example, in a 3×3 MIMO DAS with replication $R = 3$ and 2 RAUs, an antenna selection algorithm would decide for each spatial stream which of the 2 RAUs to transmit that stream from in order to maximise available capacity. In practice this can be implemented by using RF switching to test different combinations in quick succession [193]. Here, antenna selection channel capacities are included to enable comparison with the performance that could be achieved with a simple pre-coding scheme if channel information were available at the transmitter.

Further, to provide an indication of the additional benefit that spatial multiplexing offers in a DAS it is necessary to compare the performance of MIMO DAS with that of a DAS using an optimal diversity scheme with no spatial multiplexing. Both MRC and selection combining are examined here to ensure a fair comparison between MIMO and non-MIMO schemes.

In order to determine channel capacity, experimental MIMO work either measures realisations of H_k directly under a range of fading conditions or else extracts parameters of the underlying statistical behaviour, such as the correlation between the fading of different elements of H_k , and then uses these to simulate different fading conditions [194]. In either case, it is desirable to test a range of multipath fading scenarios, or realisations of H_k. These are then used to calculate the capacity of a fast-fading channel using Equation 4.9. This allows a more generalised overview of performance that is less dependent on the nuances of a particular fading environment and reflects higher-level design features such as whether LOS or NLOS propagation is more dominant. Quantities such as Shannon capacity or condition number are then represented by probability distributions that can be compared for different cases. In this chapter, the cumulative distribution functions (CDFs) of such quantities are used for this purpose.

It should be noted that it is an unavoidable reality of MIMO propagation experiments that the results are to a degree specific to the propagation environment tested. It is simply not practical to take measurements in every possible propagation scenario. However, this problem is minimised by measuring the channel from many locations within the propagation environment for a wide range of fading scenarios, ensuring a good degree of statistical variation. This approach is used in the work presented here. Further, in this work two quite different but typical propagation environments are tested and compared in order to enable more general observations.

4.2.2 Multi-user MIMO systems

A basic multiuser MIMO system consists of a base station serving multiple users on the downlink, termed the *MIMO broadcast channel*, and multiple users sending data to a single base station on the uplink, termed the *MIMO multiple access channel*. This chapter centres on the design of wireless access systems rather than mobile terminals and so only the MIMO broadcast channel is considered. However, the performance of this is intimately related to that of the multiple access channel [195].

It is well known that *dirty paper coding*, which makes use of successive interference cancellation, is the optimal method of sharing a MIMO broadcast channel amongst many users [196]. In theory, separate base stations can be operated cooperatively using a DAS to reduce intercell interference and further improve available capacity [197]. However, such advanced multiuser MIMO techniques are complex to implement and are not yet used in real MIMO services such as 802.11n, although basic implementations are planned for future systems such as 802.11ac. It has also been shown for $M \times N$ MIMO systems where $M/N \approx 1$ that as the SNR increases the performance of DPC offers little improvement over simply sharing time slots between users, i.e. *time division multiple access* (TDMA) [198]. Because the systems examined here have relatively large SNR ($>$ 20dB) and have similar numbers of antennas on the transmit side as on each mobile receiver (e.g. 3×3 MIMO), only TDMA is considered in multi-user capacity analyses.

A TDMA system can be considered to behave as the sum of several single user systems. For a TDMA system with a base station, q, serving P users, the aggregate capacity, i.e. the total sum of the capacities for all the users, is a random variable given by:

$$C_{q\ \text{agg}} = \sum_{p=1}^{P} w_p C_p \tag{4.11}$$

where

$$\sum_{p=1}^{P} w_p = 1 \tag{4.12}$$

and C_p is a random variable representing the capacity available to the p^{th} user, determined from equation 4.9, and w_p is the weighting allocated to this user. In the case examined here with equal resource allocation, $w_p = \frac{1}{P}$. The resultant probability density function of $C_{q\ \text{agg}}$ can be computed from the probability density functions for C_1 through C_P using random variable analysis.

If there are Q separate base stations each serving different sets of users due to different spatial locations or different frequency resources, the total aggregate capacity of the network is:

$$C_{\text{agg}} = \sum_{q=1}^{Q} C_{q\ \text{agg}} \tag{4.13}$$

where C_{agg} is the aggregate capacity for the q^{th} base station as defined in equation 4.11. Again, the resultant probability density function for C_{agg} can be computed from the probability density functions of $C_{q\ \text{agg}}$ for $q = 1 \ldots Q$. In the case of a multichannel DAS where multiple base stations are run simultaneously over a single DAS, it is assumed that both time and frequency resources are shared between users with each user adopting the frequency channel of a particular base station and then time sharing with other users on that same channel.

4.3 Simulated comparison of $N \times N$ DAS layouts

It is first necessary to compare theoretically the performance of different design options for MIMO DASs. In particular, it is of interest to compare $N \times N$ with replication $R = 1$ configurations to $N \times N$ with replication $R = N$ configurations as both are currently being explored as potential options.

Full simulation of MIMO systems is difficult because it requires modelling of complex fading environments. Using a simple illustrative example, however, it can be seen that for small numbers of spatial streams the SNR performance of an $N \times N$ with $R = 1$ configuration approaches that of a $N \times N$ with $R = N$ configuration. Consider the two systems shown in Figure 4.1 representing a 4×4 MIMO DAS with $R = 1$ and a 4×4 MIMO DAS with $R = 4$ respectively. It is assumed that the average power transferred is the same across all possible pairs of transmit and receive antennas for a particular RAU and mobile terminal. This is because the antenna spacings within each RAU are much less than spacings between RAUs. The effects of fading are not included and instead the propagation loss over a distance is a used as an indicator of the mean statistical SNR.

The 802.11n standard specifies that receivers should be able to detect signals with powers

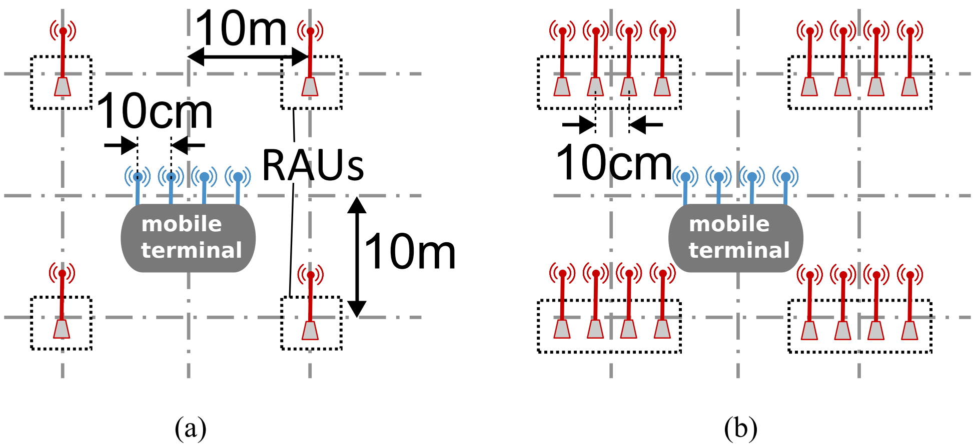

Figure 4.1: Layout of two theoretical MIMO DAS scenarios: a) 4×4 system with replication $R = 1$ and b) 4×4 system with replication $R = 4$.

as low as -82dBm over a 20MHz bandwidth channel [159]. Given this, a typical 802.11n receiver would be expected to have a noise floor less than -90dBm over this bandwidth. Transmit power for 802.11n access points is usually 10-20dBm and so in a typical scenario there might be a transmit power of 15dBm per RAU, with this power being uniformly distributed between the multiple transmit antennas. These test values are then used here and throughout rest of this chapter.

The spacing between antennas at each RAU and on the mobile terminal is 10cm, corresponding to about 0.8 wavelengths at 2.4GHz. This spacing creates sufficient antenna decorrelation in fading environments for MIMO to operate effectively. It is assumed for this simulation that the 3dB bandwidth of each antenna is much greater than 100MHz, enough to support any 802.11n channel in the 2.4GHz band.

The SNRs at all receive antennas for both the 4×4 MIMO DAS with $R = 1$ and 4×4 MIMO DAS with $R = 4$ cases are calculated at every point on a grid of 0.5m spacings. The free-space propagation loss used for this is calculated using the Friis transmission equation. Of course, a more realistic loss could be determined using the ITU propagation model as listed in Equation 1.2, which essentially amounts to increasing the loss exponent from 2 to 2.8-3.0. However, given the relatively small distances being considered it is not expected that this would change the overall trend observed, which is consistent with experimental results presented later.

Next, the ratio of the SNRs for the $R = 4$ MIMO DAS and the $R = 1$ MIMO DAS, termed the *SNR gain*, is calculated at each location. The SNR gains at every receive antenna at every point in the room are collated to produce a CDF. This CDF shows the proportion of points in the room that experience an SNR gain from the 4×4 with the $R = 4$ configuration.

This process is repeated for larger systems (9×9, 16×16 etc). The spacing between RAUs is kept constant to simulate realistic DAS installations in which it is impractical and expensive to place RAUs too closely. The transmit power per RAU is kept constant as N is increased to ensure a fair comparison. The resultant CDFs are plotted in Figure 4.2. It is seen that the SNR gain of $N \times N$ MIMO DASs with $R = N$ over $N \times N$ MIMO DASs with $R = 1$ increases with N. For example the median SNR gain increases from 0.9dB in the 4×4 MIMO DAS configuration to 2.2dB in the 9×9 MIMO DAS configuration. As N decreases, the median SNR gain tends towards 0dB indicating that there is minimal overall SNR improvement of $N \times N$ MIMO DAS with $R = N$ over $N \times N$ MIMO DAS with $R = 1$ for small N.

It should be noted that systems with larger N have the added disadvantage that they require N separate RF chains comprising mixers and analog-to-digital converters. Their complexity, cost and energy usage thus scales linearly with N [199]. Moreover, systems with $R = N$ require N separate RF amplifiers at each RAU, meaning they require on average N times as many amplifiers as $R = 1$ systems. An increase in N from 4 to 9 (i.e. 3.5dB) only offers a 1.3dB increase in SNR gain, a sublinear improvement. This suggests diminishing returns in terms of SNR of the $R = N$ configuration as N is increased.

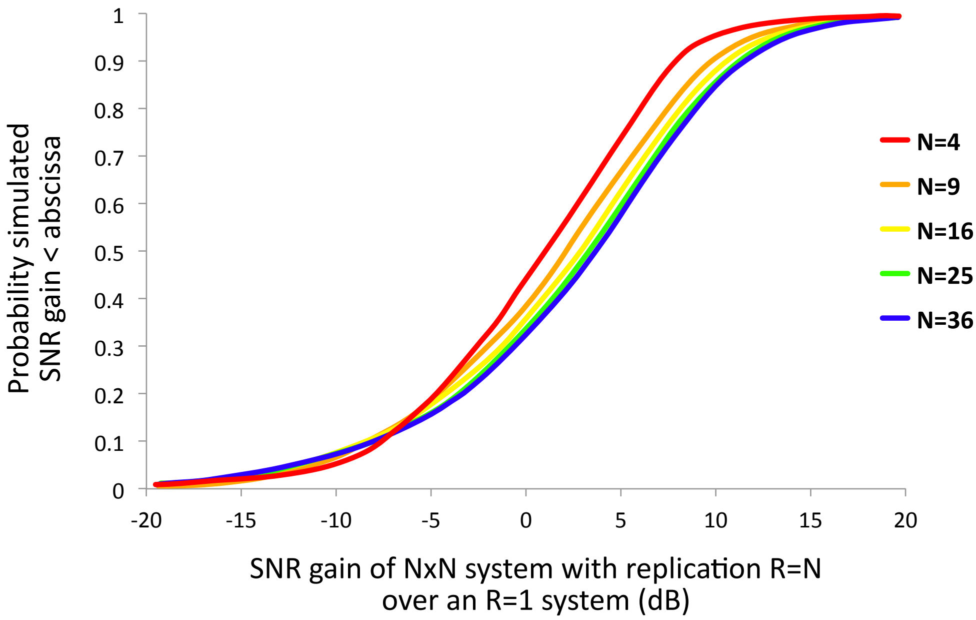

Figure 4.2: Graph showing the SNR gain for an $N \times N$ MIMO DAS with replication $R = N$ as N is increased.

The reason for this increase in SNR gain can be understood by considering the distance from each antenna on the mobile terminal to the nearest transmitting antenna for each spatial stream. For the $R = N$ case this distance is the same for every spatial stream because every RAU transmits every spatial stream. In the $R = 1$ case, however, some spatial streams are much further away from the mobile terminal than others. Because the distance between RAUs is kept constant, in this configuration the distance of the furthest spatial streams from the mobile terminal increases with N. This results in increased propagation loss of these spatial streams lowering their SNR. For small N this SNR reduction is counteracted by the greater transmit power per spatial stream at each RAU in the $R = 1$ configuration. This is why the two configurations offer similar performance for small N.

As mentioned previously, in MIMO systems with relatively high receive SNR (>20dB) increases in channel capacity are strongly linked to SNR and are less affected by changes in spatial correlation properties of the channel [146]. This link is particularly strong in environments with high spatial correlation, for example due to significant line-of-sight propagation as in this case [200]. Since for small values of N (2,3 or 4) the $N \times N$ MIMO DAS with $R = N$ and $N \times N$ MIMO DAS with $R = 1$ configurations exhibit similar SNR properties, it can then be said that they will have similar channel capacities. However, in future MIMO systems that have many more spatial streams, such as 802.11ac, this similarity no longer holds and it may be necessary to use $N \times N$ MIMO DAS with $R = N$ configurations to fully exploit the capacity gains of MIMO transmission. This will require multiplexing techniques, as described in Chapter 5.

4.4 Experimental set-up

4.4.1 Layout comparison tests

The first experiment sought to compare measured channel capacities for the two possible layout designs, i.e. with replication factors $R = 3$ and $R = 1$ respectively. This was done by measuring the 3×3 MIMO channel matrix in two typical indoor DAS scenarios under a wide range of multipath fading conditions.

Figure 4.3 shows the experimental system used to measure the 3×3 MIMO channel. A vector network analyser (VNA) is used to take measurements at 1600 channels over a frequency range of 1.7GHz to 2.7GHz. This range is sufficient to create many different multipath interference scenarios and is limited due to the frequency response of the antennas.

Careful measurements of the frequency responses of the RoF links and the antennas in isolation are taken. In this case, as there was no anechoic chamber available, this was achieved by measuring the loss between a single pair of transmit and receive antennas in an open outdoor environment (a field) to minimise multipath reflections. The loss was measured over a broad frequency range as the antenna separation was increased. The loss with distance was found to fit a square-law model very well. By compensating for this square-law loss, as well as for the reduction in effective area of the antenna with the square of frequency, the product of the transmit and receive antenna gains over a wide frequency range was extracted. The antennas used are monopoles that are omnidirectional in the azimuth plane so this gain is considered to be independent of azimuthal orientation.

The antennas used here were measured to have a 3dB bandwidth of 390MHz centred at 2.497GHz. Over the 1GHz frequency range used for these experiments the gain of the antennas varies by 25dB due to reduced efficiency but because the VNA uses a narrowband filter when taking measurements, the noise at the receiver is sufficiently low that even with such high attenuation the received SNR is >30dB. This means that the channel coefficients can still be measured accurately with these antennas and can be equalised using the antenna response measurements taken in isolation.

The measured antenna gains and measured RoF link responses are used along with the Friis transmission equation to calibrate the measurements so as to remove frequency-dependent effects, including compensating for antenna effective area. This is so that each measurement can be treated as a random channel sample from a fast-fading environment, without any inherent bias due to the actual frequency at which the measurement was taken [201]. However, this normalisation fully compensates for the loss of these elements, which could increase system SNR significantly beyond what would be expected in a real system. To account for this, the gain of the full link (excluding propagation loss) is measured at a frequency of 2.497GHz - the frequency at which the antenna gains are maximum. This gain is measured to be -12dB, which is then added to each calibrated channel measurement to give realistic values for system loss.

A PC driving an ARM microcontroller switches the transmit and receive arrays via two RF switches to allow measurement of one channel coefficient at a time. As discussed in Section 4.3, a typical 802.11n system operates using a 20MHz bandwidth channel with a transmit power of 15dBm and a receiver noise floor of -90dBm [159]. In the measurements taken here, the channel is sampled using a much narrower bandwidth (100kHz), but because approximately flat fading is assumed for up to a 20MHz bandwidth, it is considered that this transmit power is evenly distributed across this bandwidth. In reality, OFDM can equalise across different frequency sub-channels and so provided the channel is approximately flat anyway, this can be considered to have the effect of 'flattening' the channel. Therefore, these values for power and noise, normalised to a 1Hz bandwidth, are used for channel capacity calculations.

This set-up takes measurements that enable the calculation of the Shannon capacity limit of the channel, an indicator of the highest theoretically achievable data rate. Because these are taken for a large range of possible multipath fading scenarios, the result is a probability distribution of possible Shannon channel capacities.

Such measurements can be corroborated by measuring *throughput*, which provides an indication of the actual data rates achievable using existing technology, for example 802.11n. The throughput of the channel is tested using the setup shown in Figure 4.4 with parameters as listed in Table 4.1. The access point used is a TrendNET 690AP 802.11n capable of utilising up to 3 independent spatial streams. The receiver is a laptop with an Intel Centrino 6300 Ultimate-N wireless card installed, also capable of utilising up to 3 spatial streams. Throughput testing is done with the *Iperf* package. UDP packets are sent down the link at 100 Mbps and the packet loss rate is used to determine the achievable throughput of the link. It should be noted that this is *not* the same as measuring the Shannon capacity of the link, although it still serves as a relative indicator of performance enabling the comparison of different layout designs. The jitter, i.e. the variance of packet arrival times, can also be analysed.

The IEEE 802.11n standard defines 77 different possible *modulation and coding schemes (MCS)* that can be used to adjust the data rate on each spatial channel. For example, MCS 0 represents a single spatial stream using BPSK at a coding rate of 1/2, while MCS 50 represents 3 spatial streams with one using 64-QAM and the other two using 16-QAM [159]. In a realistic situation the MCS would be allowed to change dynamically to adjust to the channel conditions. For example if there were very high attenuation in one spatial channel, lower packet loss and hence better capacity could be achieved by using a slower modulation scheme in that channel. However for the throughput experiment presented here the access point is forced to use MCS 17. This uses 3 equal-rate QPSK streams with coding rates of 1/2. The reason for fixing the MCS is so that 3 equal-rate spatial streams are always being used, thereby fully testing 3×3

MIMO functionality for all the different antenna configurations.

If used naively, this method would produce the same throughput rate at every point in the room because this is fixed for a given MCS as defined in the standard. To enable comparison of throughput performance at different locations in the room without changing the MCS, UDP traffic is sent down the link at a much greater rate than the channel can support. The receiver can then determine the proportion of packets that were received error free to give an indication of the maximum achievable data rate of the link. This is seen to work by observing that in the back-to-back case with a simulated ideal MIMO propagation channel created using wired connections between the transmit and receive RF feeds, the achievable data rate approaches that of the selected MCS as set in the standard. UDP is used to avoid the additional retransmission overhead and delays inherent to TCP.

The DAS used in both cases is a Zinwave 2700, which provides 30m RoF links over OM1 MMF. As mentioned previously, the antennas used are monopoles that are omnidirectional in the azimuth plane.

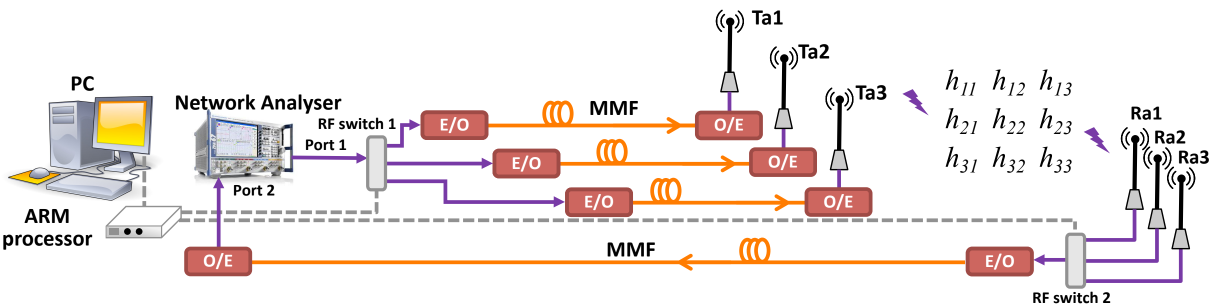

Figure 4.3: Experimental set-up of 3 × 3 MIMO channel measurement system.

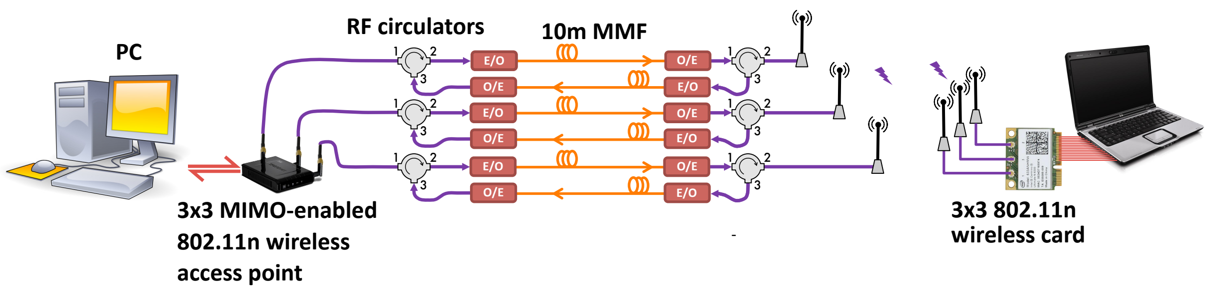

Figure 4.4: Experimental set-up of 3 × 3 MIMO 802.11n throughput testing system.

Measurements are taken for a range of different DAS configurations in two typical indoor DAS scenarios as shown in Figure 4.5. One of the test environments has a significant LOS between each RAU and the receiver while the other is entirely reliant on NLOS propagation. Because the room used contains many items, such as metal equipment racks and tables, there is sufficient multipath fading that spatial multiplexing can be achieved even for the LOS case

Table 4.1: Parameters of throughput testing setup

Parameter		Value
Frequency		2.4 GHz
MCS index	17	QPSK, coding rate 1/2
		3 spatial streams
		Max data rate: 43.3 Mbps
Channel bandwidth		20 MHz
A/P Transmit power		15 dBm
RoF link gain		-30 dB

as discussed in Section 4.1. These then represent two quite different but realistic scenarios. Measurements are taken at multiple points in both environments to evaluate the performance over a coverage area. In both cases the transmit and receive antennas at each RAU are spaced 10cm apart. The 3×3 MIMO DAS with $R = 3$ configuration is tested by measuring the 3×3 MIMO CAS response 3 times with the transmit antennas at different RAU locations each time. It is ensured that the room is kept static between these measurements. The 3×3 MIMO DAS with $R = 1$ configuration is tested by using the centre antenna of each group of 3 transmit antennas tested in the 3×3 MIMO DAS with $R = 3$ configuration.

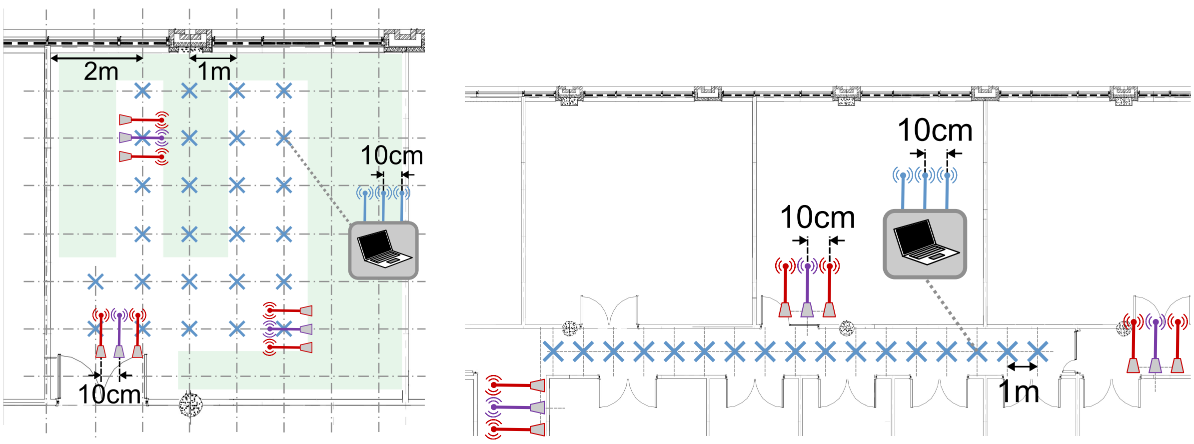

(a) (b)

Figure 4.5: Test propagation environments showing location of transmit antennas and receiver test points: (a) line-of-sight scenario (b) non line-of-sight scenario.

4.4.2 Tri-polarised antennas

Previous work has examined the use of tri-polarised antennas to improve MIMO performance by reducing the correlation between spatial channels and has shown improved performance for 3×3 MIMO systems [202, 203]. The reduction in correlation is a result of reduced cross-coupling between spatial channels using orthogonal polarisations. This works particularly well in LOS environments as it introduces orthogonality between spatial channels, which can usually only be produced as a result of strong multipath fading in NLOS environments. The purpose of this experiment is to test whether the use of tri-polarised antennas at the transmitter and receiver, a relatively simple modification, can provide additional performance improvement in a MIMO-enabled DAS.

The effect of using tri-polarised antennas in a 3×3 MIMO DAS with $R = 1$ is examined using the same experimental set-up as shown in Figure 4.3. The only difference is that the linearly polarised antennas are now rotated to produce three orthogonally polarised antennas, as illustrated in Figure 4.6. This is done for the LOS propagation scenario using the 3×3 MIMO DAS with $R = 1$ and a spacing of 4m between the RAUs as shown in Figure 4.6a and is compared with a MIMO CAS set-up in which all three transmit antennas are placed at a single position in the room separated by 0.1m, as shown in Figure 4.6b.

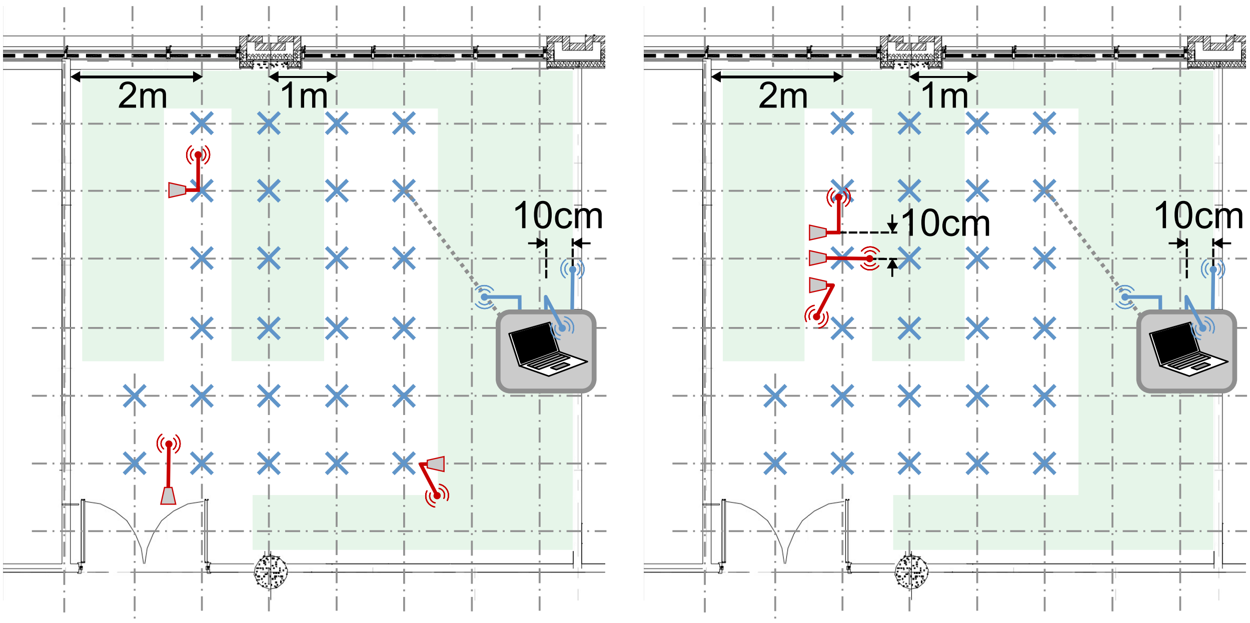

(a) (b)

Figure 4.6: Tested propagation environments showing location of transmit antennas and receiver test points for examing the effect of tri-polarisation antennas: (a) 3×3 with $R = 1$ MIMO DAS and (b) 3×3 MIMO CAS.

4.5 Single user results

4.5.1 Capacity

Figure 4.7 shows the ergodic channel capacity for the LOS propagation scenario as transmit power is increased relative to the receiver noise floor. It can be seen that once the transmit power is about 20dB above the receiver noise floor, the capacity becomes strongly linearly dependent on SNR in agreement with previous findings as discussed in Section 4.1. This is further evident from the fact that the water filling power allocation and uniform power allocation schemes begin to converge after this point. This region with high (>20dB) margin between transmit power and receiver noise floor is where many indoor wireless systems operate and so is of particular interest.

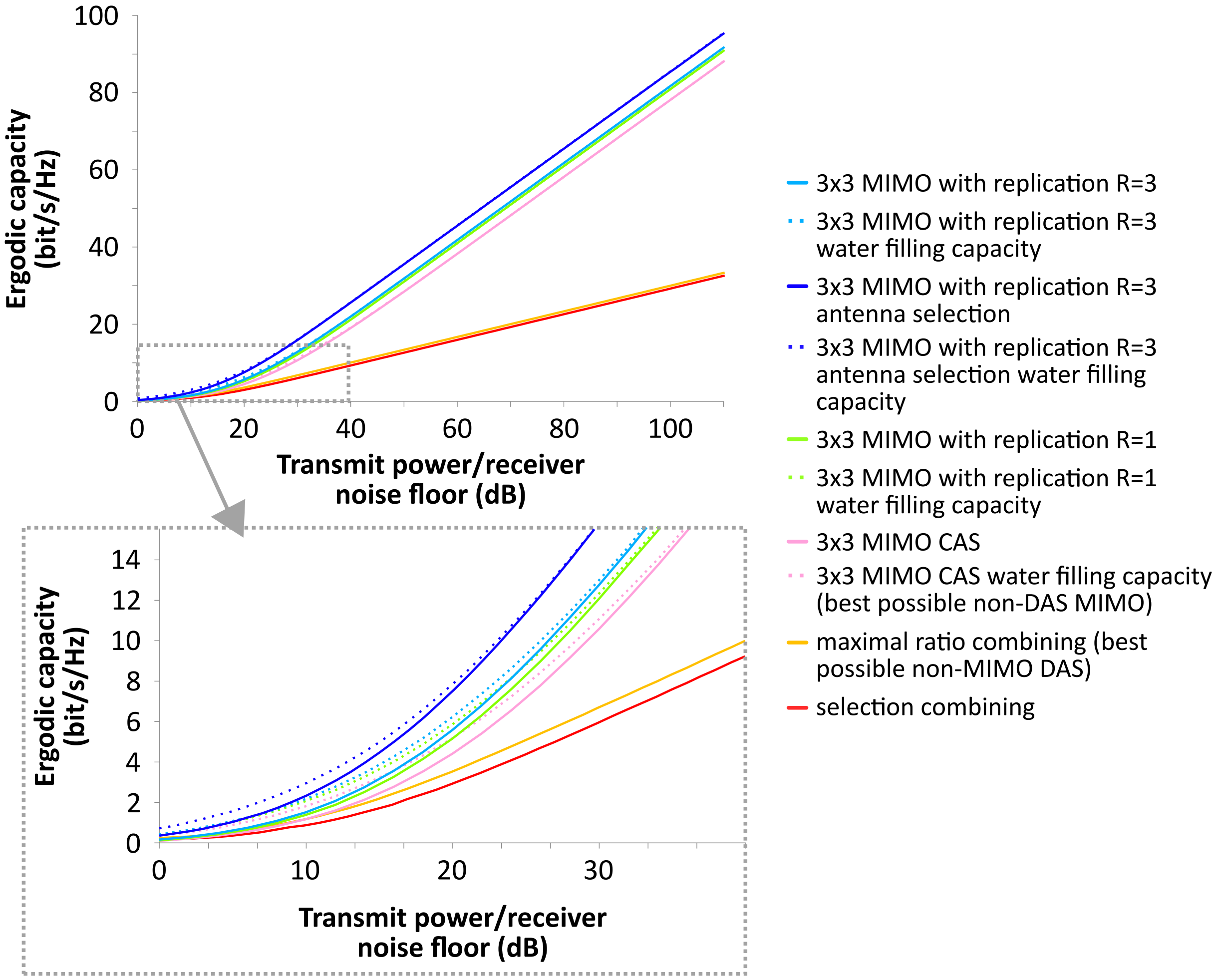

Figure 4.7: Ergodic channel capacity, as calculated from channel measurements, plotted as a function of transmit power relative to the receiver noise floor. This represents an average of measurements taken across many fading scenarios and measurement locations in the LOS propagation scenario.

The advantage of MIMO over diversity schemes such as maximal ratio combining and selection combining is clear from Figure 4.7. However, of greatest interest to the design of MIMO-enabled DAS is the difference between alternative DAS layout schemes. First, it is seen that all

MIMO DAS schemes outperform MIMO CAS in terms of capacity by at least 3.1 bit/s/Hz in the region of interest. The highest capacity is achieved with the 3×3 MIMO DAS with $R = 3$ using optimal antenna selection. However, just as with water filling this scheme requires channel knowledge at the transmitter to implement so is not currently compatible with popular MIMO protocols that make use of the V-BLAST algorithm. The most significant observation is there is very little improvement of the 3×3 MIMO DAS with $R = 3$ layout over the 3×3 MIMO DAS with $R = 1$ layout, the former offering only a 1.0 bit/s/Hz advantage in the region of interest. When the transmit power is 20dB above the receiver noise floor, i.e. a 20dB *transmit power margin*, the $R = 3$ scheme offers an 8% capacity increase. However, for a more typical transmit power margin of 90-120dB this improvement reduces to 1%.

As discussed earlier, the capacity calculations used here assume that the input symbols are Gaussian-distributed. For real modulation schemes with a sufficiently large symbol constellation (e.g., 64-QAM) and appropriate coding schemes it may be possible to produce a reasonable discrete approximate to this distribution and hence come close to achieving Shannon channel capacity. However, in channel scenarios where there is very low SNR at the receiver, real systems often revert to modulation schemes such as QPSK or BPSK. As a result, the distribution of transmitted symbols is highly quantised and very unlike a Gaussian. Consequently, for the lower channel capacities (at lower transmit powers or under worse channel conditions), the capacities achieved in a real system are expected to be significantly less than the Shannon capacity.

Next, the statistical fading behaviour is examined for a fixed transmit power of 15dBm and receiver noise floor of -90dBm. The measured CDF of channel capacities for the LOS and NLOS scenarios, showing the difference between the 3×3 with $R = 3$ and 3×3 with $R = 1$ MIMO DAS configurations are presented in Figure 4.8a and Figure 4.8b respectively. The CDFs are taken over all measured multipath fading scenarios and at all measurement locations so that they represent the probability of achieving a certain channel capacity over all possible fading environments and locations. Again, the improvement of MIMO DAS over MIMO CAS and diversity schemes is evident. As before, an antenna selection scheme is included as a reference because it represents the simplest possible scheme that could be implemented in a 3×3 with $R = 3$ system if channel knowledge were fed back to the transmitter.

It can be seen that for the LOS case in Figure 4.8a that 3×3 MIMO DAS schemes offer a significant performance improvement over 3×3 MIMO CAS or diversity schemes. Further, the 3×3 MIMO DAS with $R = 1$ offers capacity comparable to the 3×3 MIMO DAS with $R = 3$. The 3×3 MIMO DAS with $R = 1$ median capacity of 86 bit/s/Hz is just 0.8% short of the capacity offered by a 3×3 MIMO DAS with $R = 3$. This compares to the 3.2% capacity shortfall when using a 3×3 MIMO CAS.

The same is true of the NLOS case shown in Figure 4.8b and it is seen that the median capacity of the 3×3 MIMO DAS with $R = 1$ is 77 bit/s/Hz, 1.4% short of the 3×3 MIMO DAS with $R = 3$ case. This compares to the 4.1% capacity shortfall when using a 3×3 MIMO CAS in the NLOS case.

Further insight is gained from observing the condition number for the LOS and NLOS cases as shown in Figure 4.9. It is seen for both the LOS and NLOS cases that the condition number for the 3×3 MIMO DAS with $R = 3$ is only marginally better than the condition number for the 3×3 MIMO DAS with $R = 3$ (1.2dB and 1.3dB less respectively). This suggests that there

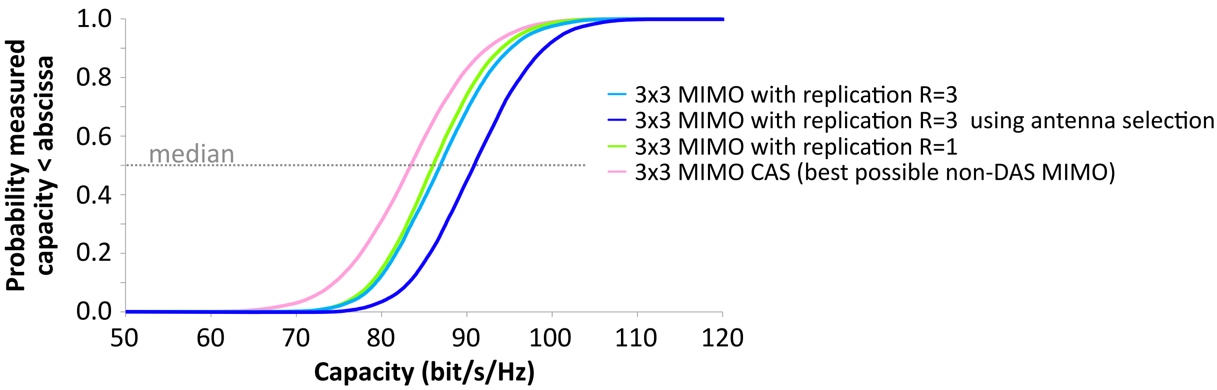

(a)

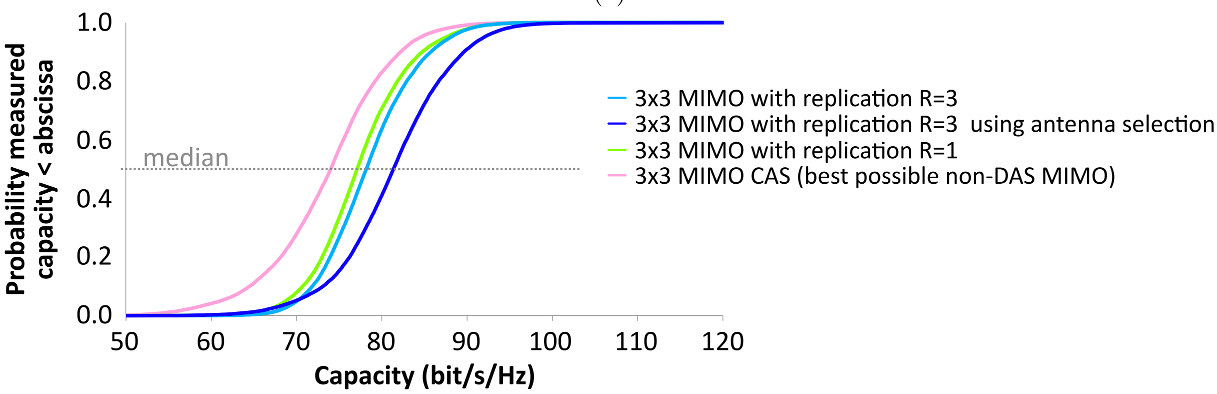

(b)

Figure 4.8: CDF of aggregate network capacity for a single user for two propagation scenarios: (a) LOS case and (b) NLOS case. A transmit power of 15dBm and a receiver noise floor of -90dBm in a 20MHz bandwidth are assumed. The median of each curve in the LOS plot then corresponds to a single point at a transmit power/receive noise ratio of 105dB on Figure 4.7. Diversity-only schemes are excluded for clarity.

is only a fairly small change in multiplexing gain between the two configurations.

However, there is a more significant improvement in condition number between the MIMO DAS configuration and the MIMO CAS, indicating that the former enables improved spatial multiplexing. This difference is particularly pronounced for the NLOS case. This is to be expected because the strong line-of-sight propagation component creates an uneven angular spread of power at the receiver resulting in high spatial correlation as discussed in Section 4.2.1. This should not change, regardless of the location of the transmit antennas. For the NLOS case though the only propagation method is multipath propagation, ensuring a more uniform angular spread of power at the receive antennas. When the antennas are distributed it can be seen from Figure 4.9 that the median condition number reduces by 5.4dB for the NLOS case suggesting that this act further improves the uniformity of the angular spread of received powers. This compares to the LOS case in which the median condition number reduces by only 1.5dB when the antennas are distributed.

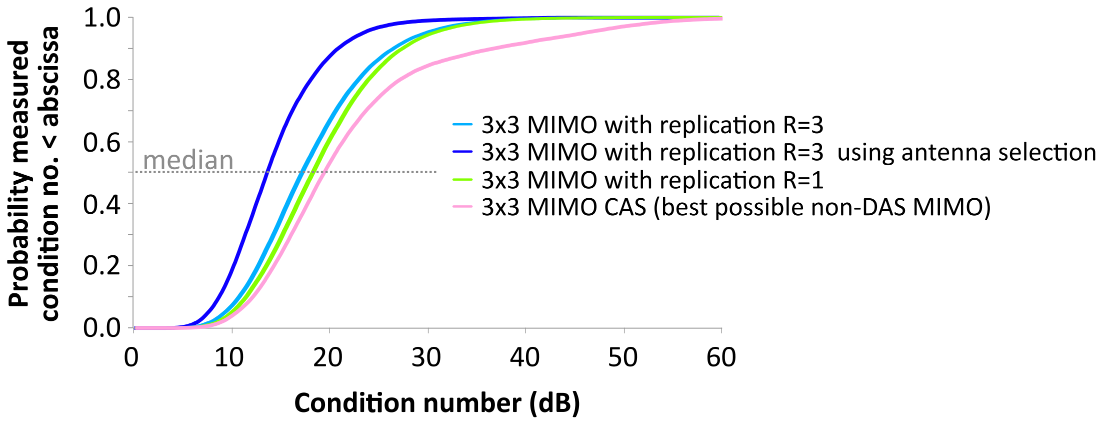

(a)

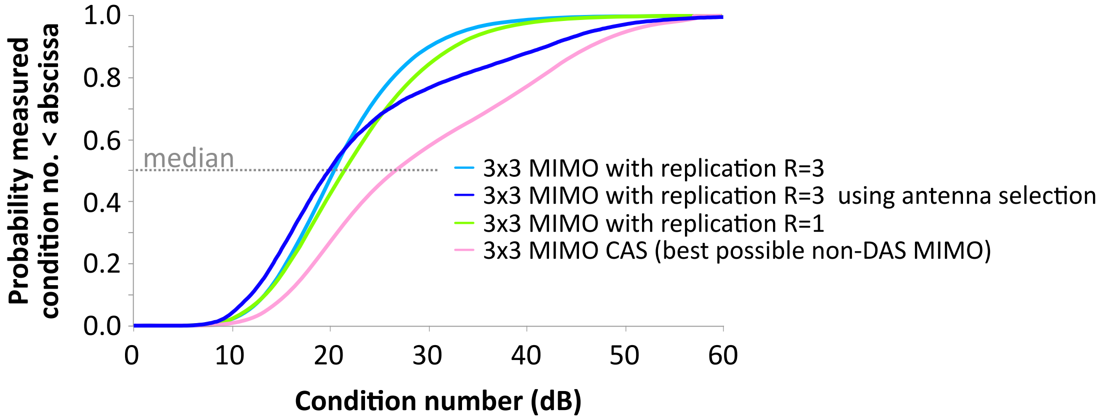

(b)

Figure 4.9: CDF of condition number for a single user with in two scenarios: (a) LOS case and (b) NLOS case

These results first show that in both LOS and NLOS cases, 3×3 MIMO DAS with $R = 1$ offers improved capacity over CAS and diversity-only DAS. In predominantly LOS environments the gain is largely due to increased SNR as the condition number is not significantly affected. However in predominantly NLOS cases, both an SNR and condition number improvement are obtained allowing a higher degree of spatial multiplexing.

Furthermore, they show that 3×3 MIMO DAS with $R = 3$ offers only minimal capacity improvement over 3×3 MIMO DAS with $R = 1$, typically of the order of 1%. This is a particularly relevant fact as the former designs have the significant disadvantage of requiring additional cabling or broadband multiplexing schemes to operate when compared with the latter, which can be implemented using pre-existing DAS installations. On balance then, it seems that the 3×3 MIMO DAS with $R = 1$ offers a lower-cost solution with comparable performance.

4.5.2 Throughput

Previous throughput measurements have shown MIMO DAS to offer an improvement over MIMO CAS for a 2×2 MIMO system [204]. However, throughput for a 3×3 MIMO DAS configuration has not been investigated nor has it been compared with the case of having additional base stations in place of a DAS.

Figure 4.10 shows the measured throughput for a 3×3 MIMO DAS with $R = 1$ compared with MIMO CAS in the LOS scenario, for both a single base station and the case with separate 3×3 MIMO CAS base stations in place of each RAU. For low values of throughput, there is shown to be little difference in the CDF curves. However, at higher throughputs it is seen that the MIMO DAS offers improved performance over the CAS case. A smaller improvement over the case with separate base stations is also observed. This suggests that under realistic MIMO test conditions, a 3×3 MIMO DAS with $R = 1$ offers improved throughput performance over a CAS. This is consistent with the results for Shannon capacity presented in Section 4.5.1.

Jitter

Throughput testing also enables the measurement of *jitter*, or more precisely *packet delay variation (PDV)*. Jitter is the standard deviation of the end-to-end transmission delays of sent UDP packets. One potential shortcoming of $N \times N$ MIMO DAS with $R = 1$ is that the different delays in the different spatial streams may inhibit performance if the spacing between transmit antennas is too large.

Figure 4.11 shows the measured jitter values for the 3×3 MIMO DAS with $R = 1$ and compares this with two possible MIMO CAS systems. The first CAS system has 3 base stations (located at the RAU positions as per Figure 4.5a) and allows the user to connect to the nearest one. The second has only one base station located at one of the RAU positions.

It can be seen that the MIMO DAS jitter is either less than or comparable to the jitter for the two CAS scenarios for over 80% of sample points. However, the worst 20% of measurements experience an average increase in jitter of about 70% for the DAS case. This is not likely due to differences in time-of-flight between the transmit and receive antennas because in such a small DAS, with propagation distances on the order of 10m, the time-of-flight for signals is of the

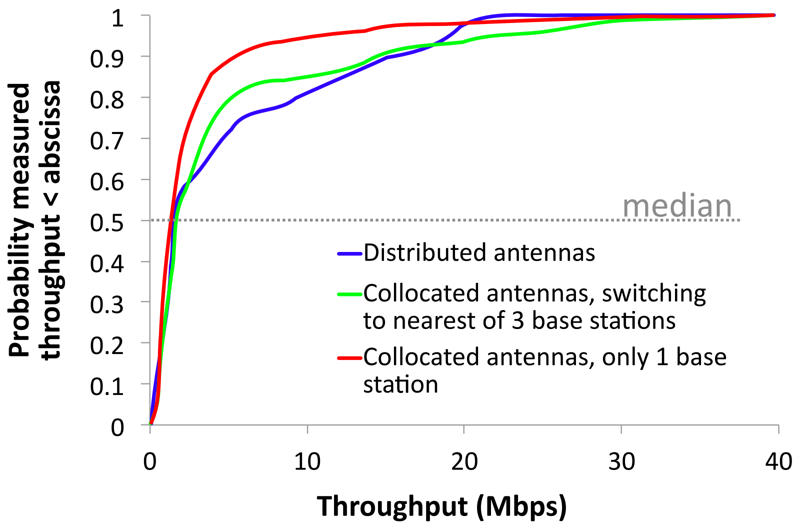

Figure 4.10: CDF showing improvement in throughput of using MIMO DAS with 3×3 802.11n compared with CAS

order of tens of nanoseconds. This is a mere fraction of the variation in jitter seen here, which is of the order of milliseconds.

A more likely explanation is that it is due to the difference in propagation losses for the different spatial streams in a DAS. This might result in different patterns of data loss - for example, data may be lost in large chunks (*bursty* loss) instead of slower and more continuously. Bursty packet loss would result in high UDP jitter. Overall, the difference in jitter performance is not substantial enough to be of concern, particularly considering that the measured throughput is improved in the DAS case and throughput is ultimately is the most important and realistic test of performance.

4.5.3 Effects of antenna polarisation

A graph of measured ergodic channel capacity vs. transmit SNR for the tri-polarised antenna test is shown in Figure 4.12 and a capacity CDF, taken over many fading environments at a transmit power of 15dBm and a receiver noise floor of -90dBm is shown in Figure 4.13. It is first noted that there is a reduction in capacity when using tri-polarised antennas as opposed to using only a single polarisation. This is true for both the DAS and CAS scenarios. In the DAS case for typical transmit powers (>0dBm), it is observed that there is a power penalty of 3.8dB when using tri-polarised antennas. That is, achieving the same ergodic channel capacity requires 3.8dB additional gain. The reason for this is that the power incident on the receive array is contained in a wider diversity of polarisations and each receive antenna is only capable of detecting some subset of these. This means that on average the power collected per antenna is $1/3$ of that collected in the single polarisation case. This corresponds to a theoretical power penalty of 4.7dB, comparable to the 3.8dB penalty observed here as shown in Figure 4.12. This difference

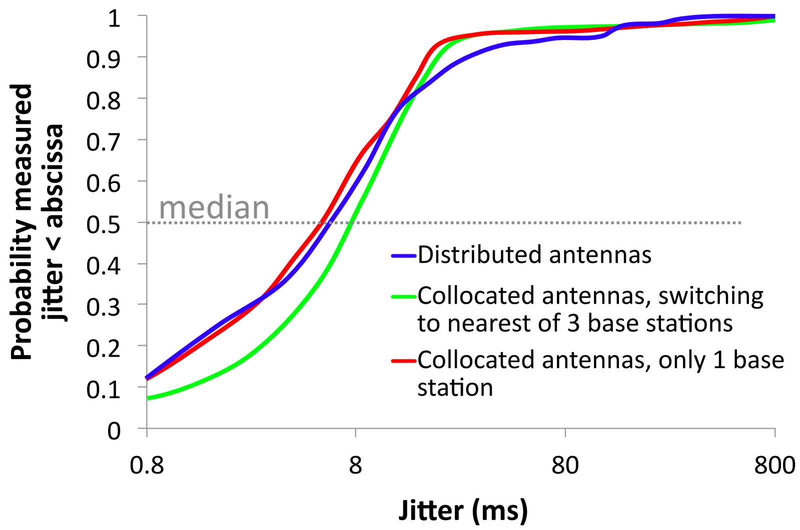

Figure 4.11: Graph showing the jitter, i.e. the standard deviation of packet arrival times, for 802.11n throughput testing using 3×3 MIMO DAS with $R = 1$ and 3×3 MIMO CAS.

reduces to 2.0dB in the MIMO CAS case, which could be due to increased coupling between polarisations at the transmitter, a consequence of the much closer spacing of the antennas.

Previous work has accounted for this power difference by normalising channel matrices [202]. However, this does not allow for a comparison that accounts for both channel decorrelation and SNR effects. SNR is a very important factor in MIMO performance and so here the effect of reduced SNR due to reduced power collection at the receiver is considered.

Another interesting observation is that using a tri-polarisation system seems to reduce the advantage of MIMO DAS over MIMO CAS. In the single polarisation case MIMO DAS offers a 1.8 bit/s/Hz improvement over MIMO CAS at high SNR. However, this reduces to just 0.6 bit/s/Hz in the tri-polarisation case, a 66% decrease. This can be examined in further detail by observing the condition numbers as shown in Figure 4.14.

It is also seen that, as expected, tri-polarised antennas enable lower condition numbers due to reduced spatial correlation. In the single polarisation case there is negligible change in condition number when going from a CAS to a DAS. However, in the tri-polarisation case the DAS has a median condition 3dB more than the CAS case, suggesting that some of the advantage offered by reduced correlation is in lost in the DAS case. This could be explained by the fact that the different polarisations experience significantly different propagation effects when the transmit antennas are highly separated in a DAS. This means it is less likely that all the transmitted polarisations will be orthogonal when they arrive at the receiver. In a CAS, however, because the propagation paths from each of the transmit antennas to the receiver are more similar, the polarisations incident on the receiver are more likely to be orthogonal.

This reduction in polarisation orthogonality and hence increase in condition number provides an effect that counters the SNR improvement gained from a DAS. It can then be said that there is reduced advantage when using a DAS in a system with tri-polarised antennas. Further, when

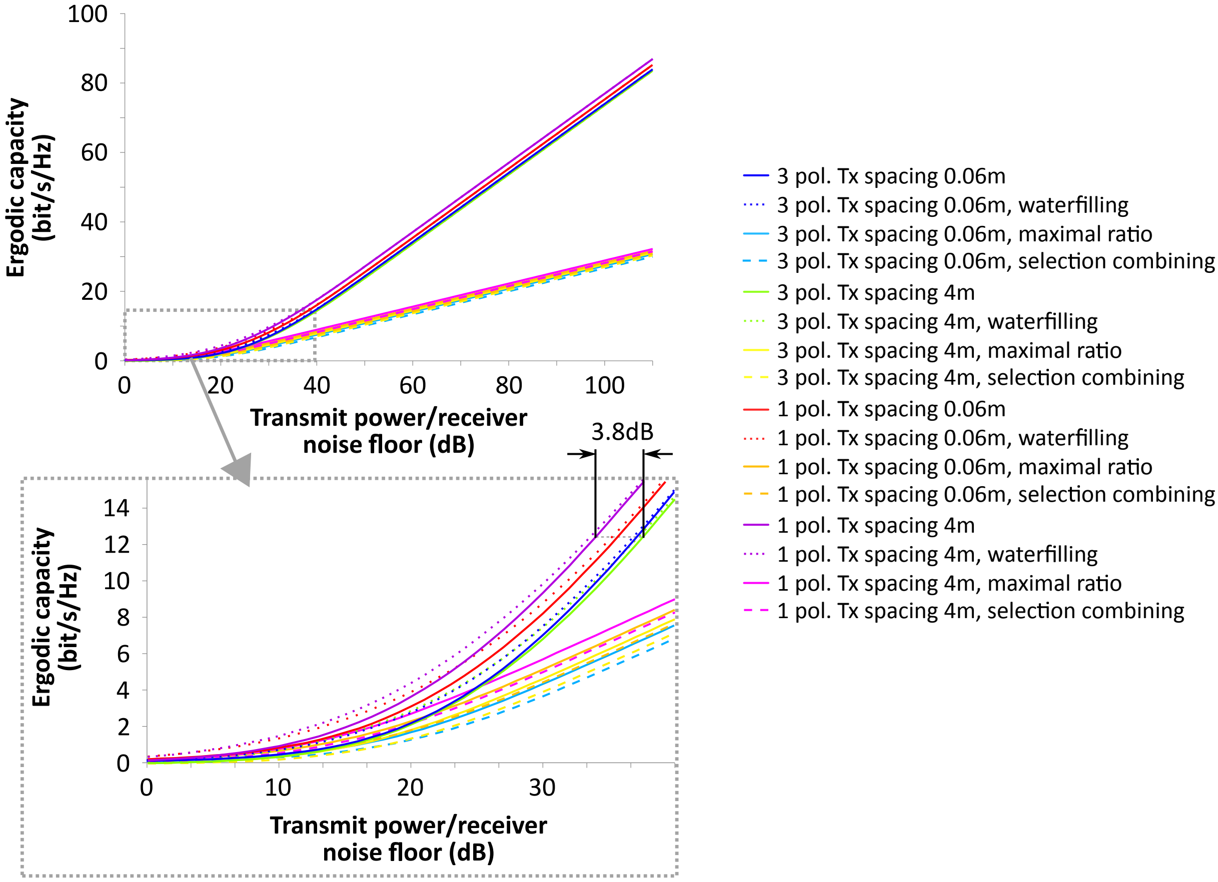

Figure 4.12: Ergodic channel capacity, as calculated from channel measurements, plotted as a function of transmit power relative to the receiver noise floor comparing different antenna polarisation configurations. This represents an average of measurements taken across many fading scenarios and measurement locations in the LOS propagation scenario.

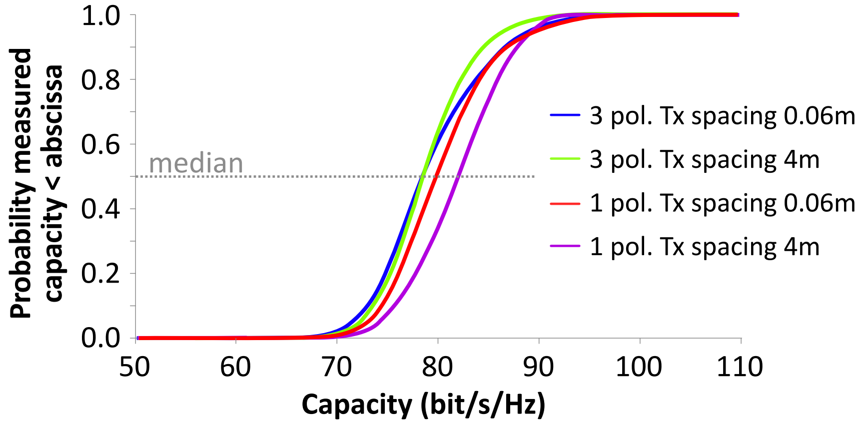

Figure 4.13: CDF of channel capacity for a single user showing the effect of single and tri-polarised antenna configurations in MIMO DAS and CAS systems.

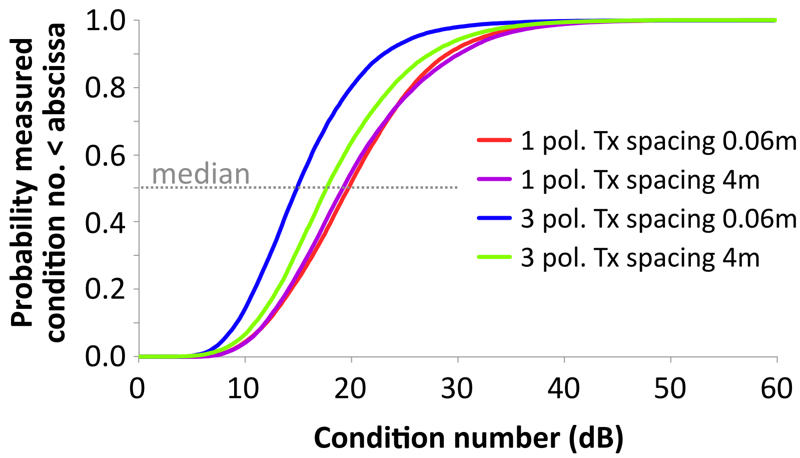

Figure 4.14: CDF of condition number for a single user showing the effect of single and tri-polarised antenna configurations in MIMO DAS and CAS systems.

both power and channel correlation are considered, for an indoor DAS a single polarisation system may provide better MIMO performance than a tri-polarised system, despite having less favourable correlation properties.

4.6 Multiple user results

4.6.1 Single base station

The capacity of a DAS where there are multiple users served by a single base station is now examined. Figure 4.15 shows the total aggregate capacity of a system as the number of users is increased for two cases: the first with a single base station and the second with 3 base stations. This is done for two different system configurations – a CAS with separately located base stations and a DAS with collocated base stations operating on separate frequency channels, an example of which was shown in Figure 1.21. The results are shown in Figure 4.15a and Figure 4.15b respectively.

It can be seen that in both cases if only a single base station is used there is an upper limit on the aggregate capacity as the number of users is increased. This upper limit shifts significantly higher when additional base stations are added. In fact, this upper limit is simply N times the median capacity for a single base station, provided that the number of users is $\gg N$. This indicates that additional base stations are a necessary requirement for adding capacity to a system.

If the number of base stations is increased for a fixed number of users the capacity will also approach a limit, as shown in Figure 4.15. In fact, it is seen that the two-user limit coincides with observed step-like changes in the CDF. This is because the two-user limit represents the capacity limit when two users are being served by two separate base stations. In CAS scenarios, there is a possibility that even if only two users are present, they will be located in such a way that they are both served by the same base station even if there are other unused base stations. This results in regions of reduced aggregate capacity, indicated by the step-like behaviour observed in Figure 4.15a. These steps are not observed in Figure 4.15b because capacity can always be shared between base stations when they are centrally located as in a multichannel DAS.

4.6.2 Multiple base stations

Finally, it is necessary to examine the scenario where multiple users are served by multiple base stations. This is the scenario of greatest practical importance for future wireless systems. As discussed in Section 4.1, this is achieved in a CAS by installing additional base stations at new locations or in a DAS by connecting additional base stations to the same DAS infrastructure and operating them on unique non-overlapping frequency channels, as is possible in 802.11n. Each user still uses a 20MHz bandwidth channel and may only connect to a base station operating on that same channel. Users accessing the same base station share time slots, as discussed in Section 4.2.2.

The aggregate capacity for multiple users accessing multiple base stations is shown in figures 4.16a and 4.16b for the LOS and NLOS cases respectively. A multichannel DAS running several

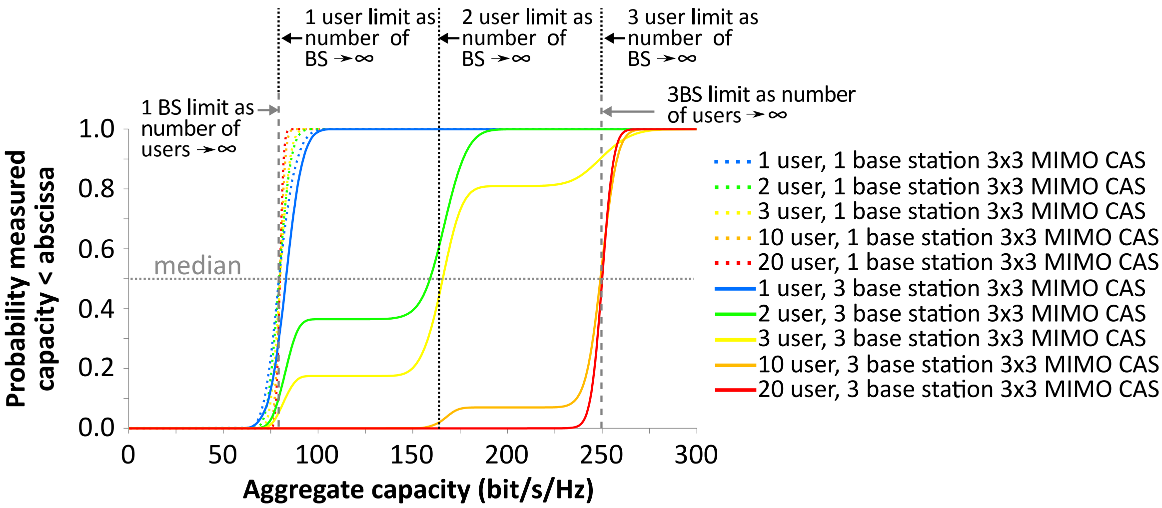

(a)

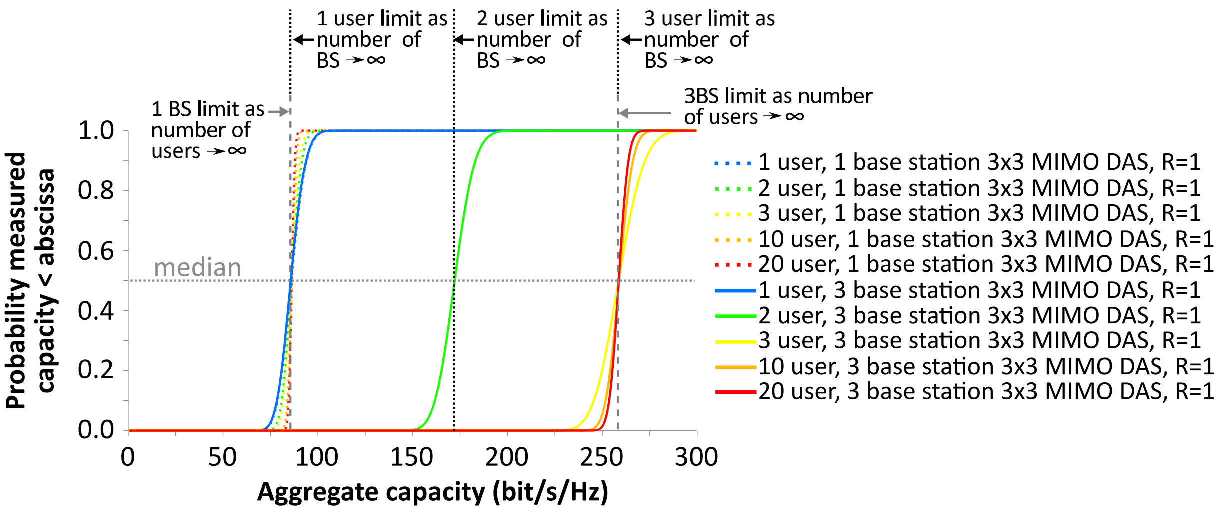

(b)

Figure 4.15: CDF of aggregate network capacity comparing capacity for a single base station with multiple base stations in the LOS scenario for two cases: (a) collocated antenna system and (b) distributed antenna system.

base stations simultaneously is compared with the case of installing separate CAS MIMO base stations at each of the DAS RAU positions.

It is seen that both configurations are able to significantly increase aggregate capacity. However, the multichannel DAS provides more uniform coverage than the separate CAS base station configuration as it avoids the step-like behaviour in the CAS curves in Figure 4.16a. As discussed in Section 4.6.1 this step-like behaviour arises because in a CAS, performance is more dependent on the distribution of users in the coverage area. For example, a multichannel DAS would cope just as well if all users were located very close to one RAU whereas in a CAS the capacity would be limited to the multiple-user single base station case

As discussed in Section 4.6.1, when the number of users is much larger than the number of base stations an upper limit on the aggregate capacity is approached. In the LOS scenario, this limit is 259 bit/s/Hz for the 3×3 MIMO DAS with $R = 1$ case, 0.8% less than the limit for the 3×3 MIMO DAS with $R = 3$ case at 261 bit/s/Hz. Similarly for the NLOS scenario this limit is 233 bit/s/Hz for the 3×3 MIMO DAS with $R = 1$ case, 1.3% less than the limit for the 3×3 MIMO DAS with $R = 3$ case at 236 bit/s/Hz. The separate base station CAS configuration provides the lowest of the upper capacity limits with 250 bit/s/Hz and 217 bit/s/Hz for the LOS and NLOS scenarios respectively.

It can also be seen that a 3×3 MIMO DAS with $R = 1$ multichannel DAS can offer multi-user median aggregate capacities 3.4% and 7.3% greater than having separate MIMO CAS base stations for LOS and NLOS scenarios respectively. Clearly, DAS has an important role to play in delivering capacity for multi-user multiple base stations scenarios. Further, a 3×3 MIMO multichannel DAS with $R = 1$ is sufficient to offer this additional support as it offers comparable median aggregate capacity to a 3×3 MIMO multichannel DAS with $R = 3$.

It should be noted that the different configurations each have their own drawbacks. Multichannel DAS can create problems with inter-cell interference as they use many frequency channels over the same spatial region. For advanced DAS features, such as dynamic capacity allocation, additional hardware is needed to be able to sense and process the user environment, increasing system cost. 3×3 MIMO DASs with $R = 3$ have the disadvantage of requiring additional multiplexing infrastructure or additional fibres to transport multiple MIMO streams to single RAUs. Because 3×3 MIMO DASs with $R = 1$ can be deployed using pre-existing non-MIMO DAS infrastructure this makes them a more cost-effective option than 3×3 multichannel DAS with $R = 3$. However, as discussed in Section 4.3 the difference in capacities between the two designs may increase with higher numbers of spatial streams making $N \times M$ DAS with $R = N$ a more attractive option if high capacity is required.

4.7 Conclusions

This chapter compares different design configurations of MIMO DAS and examines their effect on capacity and throughput performance. First, it is shown theoretically that in terms of SNR, $N \times N$ MIMO DAS with antenna replication $R = N$ only offers significant improvement over $N \times N$ MIMO DAS with antenna replication $R = 1$ for larger values of N (≥ 4).

Next, it is confirmed experimentally that a 3×3 MIMO DAS offers improvement in capacity and throughput compared with a MIMO CAS for a 3×3 system in two typical indoor DAS

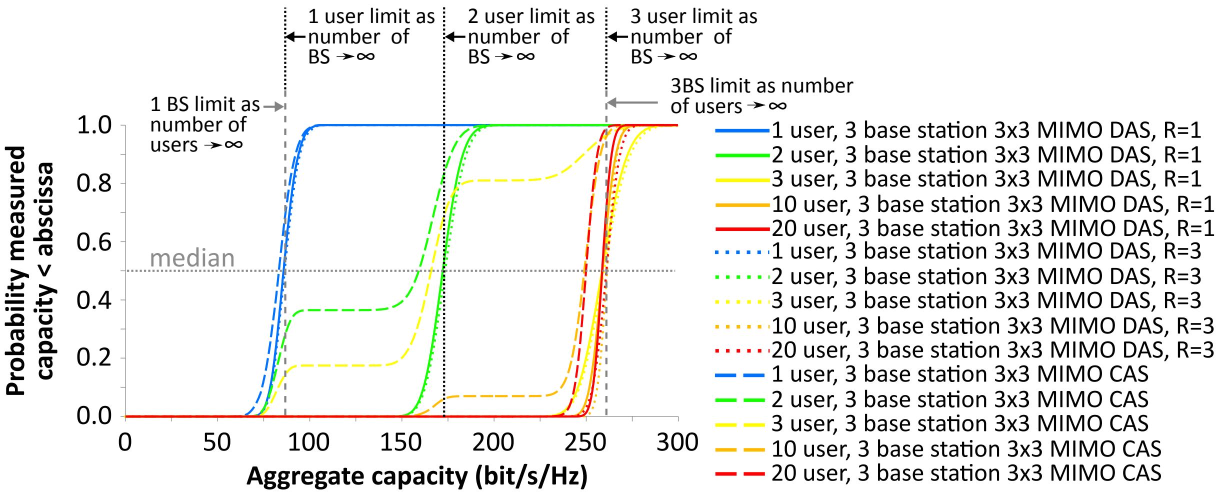

(a)

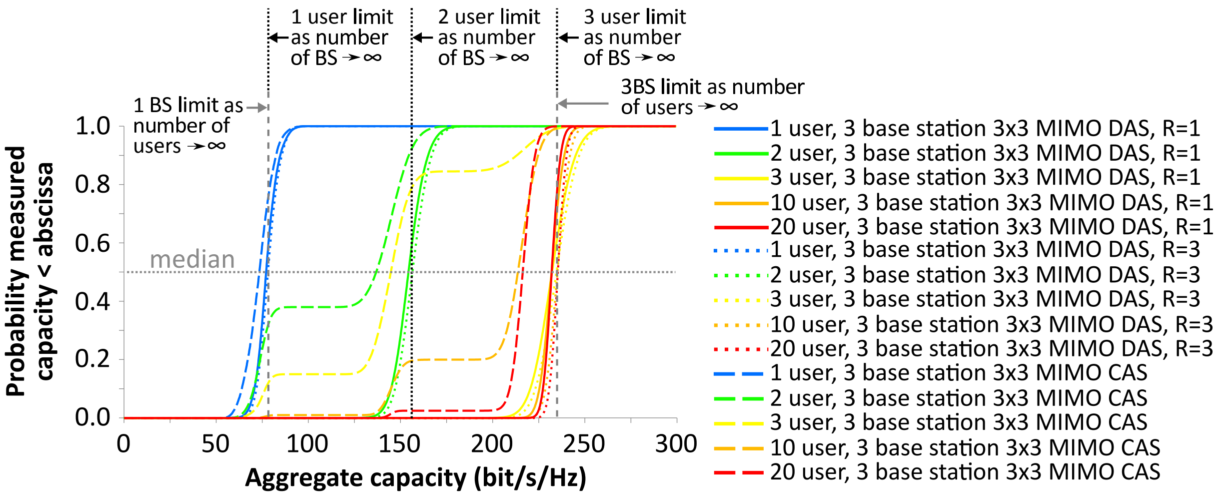

(b)

Figure 4.16: CDF of aggregate network capacity for multiple users with multiple base stations for two scenarios: (a) LOS and (b) NLOS.

scenarios offering 3.2% and 4.1% improvement in capacity respectively. It is then shown for both single user and multiple user scenarios using single and multiple base stations that a 3×3 MIMO DAS with antenna replication $R = 1$ can achieve similar performance to a 3×3 MIMO DAS with antenna replication $R = 3$. For the multichannel 3×3 MIMO DAS with antenna replication $R = 1$ and 20 users, median aggregate capacities of 259 bit/s/Hz and 233 bit/s/Hz are achieved for the two typical propagation scenarios respectively. These are only 0.9% and 1.4% short of the aggregate capacities for the multichannel 3×3 MIMO DAS with antenna replication $R = 3$ respectively.

This suggests that existing DAS infrastructure could be used to deploy 3×3 MIMO DAS with antenna replication $R = 1$ incurring minimal capacity penalty and without the need for additional fibres or multiplexing schemes.

To meet the demands of tomorrow's communication networks with high densities of users demanding high data rates it will be necessary to install more base stations per unit area to enable increased aggregate capacity. These results show that DASs have an important role to play because they are able to further improve on the performance of separately located base stations while offering additional flexibility. It is concluded that existing DAS installations can provide enhanced capacity to multiple users requiring 3×3 MIMO services without requiring additional infrastructure.

Chapter 5

Broadband Radio-over-Fibre Transmission of Wireless MIMO using Mode-Division Multiplexing

General overview

This chapter proposes a novel method for sending MIMO wireless signals to remote antenna units over a single multimode fibre (MMF). MIMO streams are sent via different propagation modes of a multimode fibre using mode division multiplexing (MDM). Individual modes are launched into the fibre using computer controlled spatial light modulators (SLM). Initially, two modes are separated using a multimode coupler. Then, in a second experiment, another SLM is used to extract individual modes, thereby acting as a mode-selective switch.

Combined channel measurements over 2km of mode-multiplexed MMF and a typical indoor radio environment show in principle a 2×2 MIMO link providing capacities of 10bit/s/Hz over a bandwidth of 6GHz. A 50% improvement in average wireless capacity is achieved compared with a case with no isolation between propagation modes. Using a second experimental set-up a full mode-transfer matrix for the first 9 mode groups is measured. The orthogonality of the transfer functions between different mode groups is examined using the condition number of the transfer matrix. The condition number is found to be $\leq$15dB over a bandwidth of 3GHz up to the 4×4 MIMO case over 2km of MMF, meaning it is able to support 4×4 MIMO protocols. This is an initial indicator of the system's performance and with further refinement it should be possible to achieve 5×5 MIMO or even 6×6 MIMO.

Finally, it is shown experimentally that mode-groups 1-6 exhibit modal power dissipation and inter-mode-group coupling properties sufficient to enable mode-multiplexing even when the fibre contains sharp bends (radius between 20mm and 7.2mm). These mode groups can therefore be used reliably for mode-multiplexing in bent OM2 and OM3 fibre.

Some of the work in this chapter is drawn from [178]. The early 2×2 experimental results presented in this chapter were partly collected by Joel Carpenter as part of a collaboration. However, the later experimental results were collected entirely by myself and the ideas and analysis expressed in this chapter are entirely my own.

5.1 Introduction

As discussed in chapter 1 there is an urgent need to develop new designs for wireless infrastructure to meet user demand. These new designs will need make use of both DAS and MIMO technologies. MIMO is rapidly being adopted by emerging protocols with wireless LAN standard IEEE 802.11n and cellular standard 4G/LTE supporting up to 4 separate MIMO RF spatial streams, termed a 4×4 MIMO system. Wireless LAN protocols presently in development, such as IEEE 802.11ac, allow for up to 8×8 MIMO.

It was shown in chapter 4 that for *low-order* MIMO installations (i.e. up to 4×4) that the coverage and flexibility benefits of DAS can be combined with the capacity improvements offered by MIMO simply by physically separating the antennas. This means that existing DAS infrastructures and layout designs can be effectively re-used if there are only a small numbers of spatial streams. However, when combining a DAS with *high-order* MIMO protocols that make use of many wireless spatial streams (e.g. 8×8), it is necessary to send several MIMO wireless spatial streams to each remote antenna unit (RAU) to attain optimum performance. This does not necessarily mean that all streams must be sent to every RAU as it may be sufficient to duplicate some subset of the streams at each RAU as a compromise between the two extreme design options. In either case a method of sending multiple streams to a single RAU is required.

The simplest way to implement this would be to use multiple fibres – one for each wireless spatial stream – but this is likely to be too costly, particularly if as many as 8 streams are required, as illustrated in Figure 5.1. Ideally, each RAU would be fed by just a single fibre. Since all MIMO spatial streams occupy the same frequency space, in order to send them over a single fibre a form of multiplexing is required. In order that the DAS can support multiple services the multiplexing scheme should support several (up to 8) channels. These channels should have at least a 6GHz bandwidth to support MIMO standards such as 802.11ac.

Further, any such multiplexing system must work over multimode fibre since around 85% of all pre-existing fibre installed in buildings is of this variety. Much of this was originally installed for LAN applications – in fact, between 1990 and 2007 over 14 million km of graded-index multimode fibre was installed in buildings globally [61]. Hence, a MIMO RoF multiplexing system that is able to make use of this pre-installed MMF would significantly reduce installation costs.

In many applications MMF is considered to perform worse than SMF because of its lower bandwidth arising from modal dispersion with an overfilled launch condition. However, in this chapter a *mode division multiplexing* system that actually exploits the multimode nature of pre-installed building fibre and transmits multiple broadband RoF channels via different fibre propagation modes is presented. The channels of this multiplexing system are broadband and only one wavelength of light is required. Further, this system is readily scalable to large numbers of MIMO wireless streams and the precise modal control it offers allows it to work over distances of up to 2km.

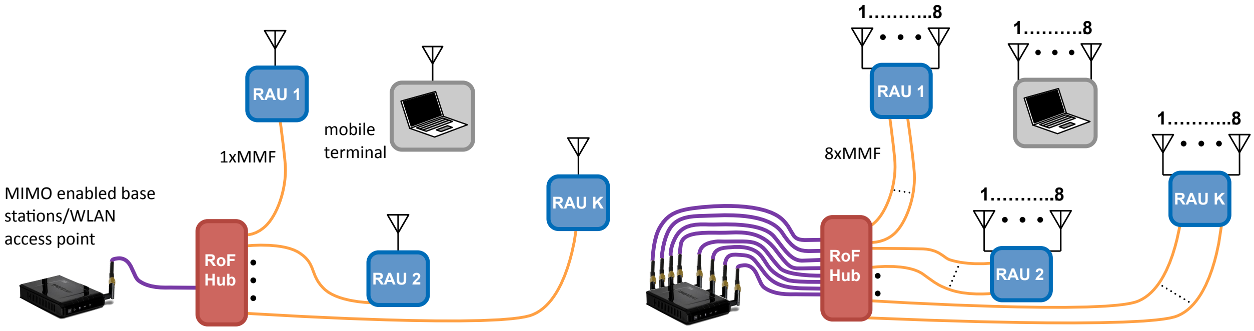

Figure 5.1: Illustration of multiple fibre solution for implementing MIMO DAS for: (a) a non-MIMO DAS and (b) an 8×8 MIMO DAS. The latter case requires an additional 7 fibres to be installed.

5.2 Theory

5.2.1 Mode division multiplexing

The propagation of light in an optical fibre can be accurately described using Maxwell's equations with the appropriate boundary conditions, which are determined by the radial refractive index profile of the fibre. Because of the increasing prevalence of OM2 and OM3 in buildings it is of particular interest to consider the case of these graded refractive index profile fibres.

The full set of solutions for a particular wavelength of light can contain either one or many solutions, each of which represents a different propagation mode of light in the fibre. Generally, propagation modes are composed of transverse electro-magnetic field (TEM), transverse electric (TE) and transverse magnetic field (TM) waves. However, it is convenient to introduce a common approximation called the *weak-guidance approximation* that ignores the TE and TM components. This is a reasonably accurate assumption because the refractive indices of the core and cladding of optical fibres are very similar (typically within 2%) [205]. In this way it is possible to simplify the full 3D vector solutions resulting from Maxwell's equations to an approximate set of solutions that satisfy a scalar wave equation. The solution for the electric field is of the form:

$$\mathbf{E}(x, y, z) = \mathbf{e}_{\mathrm{t}}(x, y) \exp\left\{j\tilde{\beta}z\right\} \tag{5.1}$$

where $\tilde{\beta}$ is the propagation constant for the particular mode of interest. Solutions for $\mathbf{e}_{\mathrm{t}}$ can be shown to combinations of following equations, parameterised in terms of radial distance from the centre of fibre, r, and azimuthal angle, ϕ [206]:

$$\mathbf{e}_{\mathrm{t}1} = F_{\ell}(r)\left\{\cos(\ell\phi)\,\hat{\mathbf{x}} - \sin(\ell\phi)\,\hat{\mathbf{y}}\right\} \tag{5.2}$$

$$\mathbf{e}_{\mathrm{t}2} = F_{\ell}(r)\left\{\cos(\ell\phi)\,\hat{\mathbf{x}} + \sin(\ell\phi)\,\hat{\mathbf{y}}\right\} \tag{5.3}$$

$$\mathbf{e}_{t3} = F_\ell(r)\{\sin(\ell\phi)\,\hat{\mathbf{x}} + \cos(\ell\phi)\,\hat{\mathbf{y}}\} \tag{5.4}$$

$$\mathbf{e}_{t4} = F_\ell(r)\{\sin(\ell\phi)\,\hat{\mathbf{x}} - \cos(\ell\phi)\,\hat{\mathbf{y}}\} \tag{5.5}$$

where ℓ is termed the *azimuthal index*, and $\hat{\mathbf{x}}$ and $\hat{\mathbf{y}}$ are orthogonal unit vectors on a plane normal to the direction of wave propagation. Under the weak-guidance approximation, equation 5.1 satisfies a scalar wave equation and so it is found that the radial profiles for each mode, $F_\ell(r)$, can be found by the solutions to:

$$\left\{\frac{\mathrm{d}}{\mathrm{d}r^2} + \frac{1}{r}\frac{\mathrm{d}}{\mathrm{d}r} + k^2 n^2(r) - \frac{\ell^2}{r^2} - \tilde{\beta}^2\right\} F_\ell(r) = 0 \tag{5.6}$$

where $n(r)$ is the radial refractive index profile and $k = 2\pi/\lambda$ is the free-space wavenumber. This can be seen to be a scalar wave equation eigenproblem, where $F_\ell(r)$ represents the eigenfunction for a particular mode and $\tilde{\beta}$ the eigenvalue. Generally, the solutions to this eigenproblem are found numerically. However, there do exist analytical solutions for certain refractive index profiles. For step-index profile fibres equation 5.6 becomes a form of Bessel's differential equation and so the solutions for $F_\ell(r)$ are given by Bessel functions. However, OM1, OM2 and OM3 fibres have graded refractive index profiles of the form:

$$n(r) = \begin{cases} n_{co}\sqrt{\left\{1 - 2\Delta\left(\frac{r}{R}\right)^\alpha\right\}}, & 0 \le r < R \\ n_{cl}, & r \ge R \end{cases} \tag{5.7}$$

where

$$\Delta = \frac{n_{co}^2 - n_{cl}^2}{2n_{co}^2} \tag{5.8}$$

and n_{co} is the refractive index at the centre of the core, n_{cl} is the refractive index of the cladding, R is the effective radius of the core and α is termed the profile parameter. OM1, OM2 and OM3 fibres use parabolic graded index profiles with $\alpha \approx 2$ (fine-adjusted to reduce modal dispersion at the target wavelength).

Assuming that the modal power is concentrated towards the centre of the fibre, a good assumption under the weak-guidance approximation, equation 5.7 can be approximated by a parabolic refractive profile infinite in extent. Though not physically realisable, this provides very close approximate solutions when solving equation 5.6. The solutions of this equation are [206]:

$$F_\ell(r) = \left(\frac{r}{R}\right)^\ell L_{m-1}^{(\ell)}\left(V\frac{r^2}{R^2}\right)\exp\left(-\frac{1}{2}V\frac{r^2}{R^2}\right) \tag{5.9}$$

where

$$V = \left(\frac{2\pi}{\lambda}\right) R n_{co} (2\Delta)^{1/2} \tag{5.10}$$

and $L_{m-1}^{(\ell)}(x)$ is a generalised Laguerre polynomial, ℓ is the azimuthal index and m is a positive non-zero integer termed the *radial index*.

These solutions form a set of linearly polarised (LP) eigenmodes that can be used as an orthogonal basis for producing all possible propagation solutions. They are commonly indexed using ℓ and m and are thus written $LP_{\ell,m}$. These are also sometimes referred to as Laguerre-Gauss modes. Figure 5.2 shows the cross-sectional intensity-phase profiles of the first few LP modes for a fibre with an infinite parabolic refractive index profile.

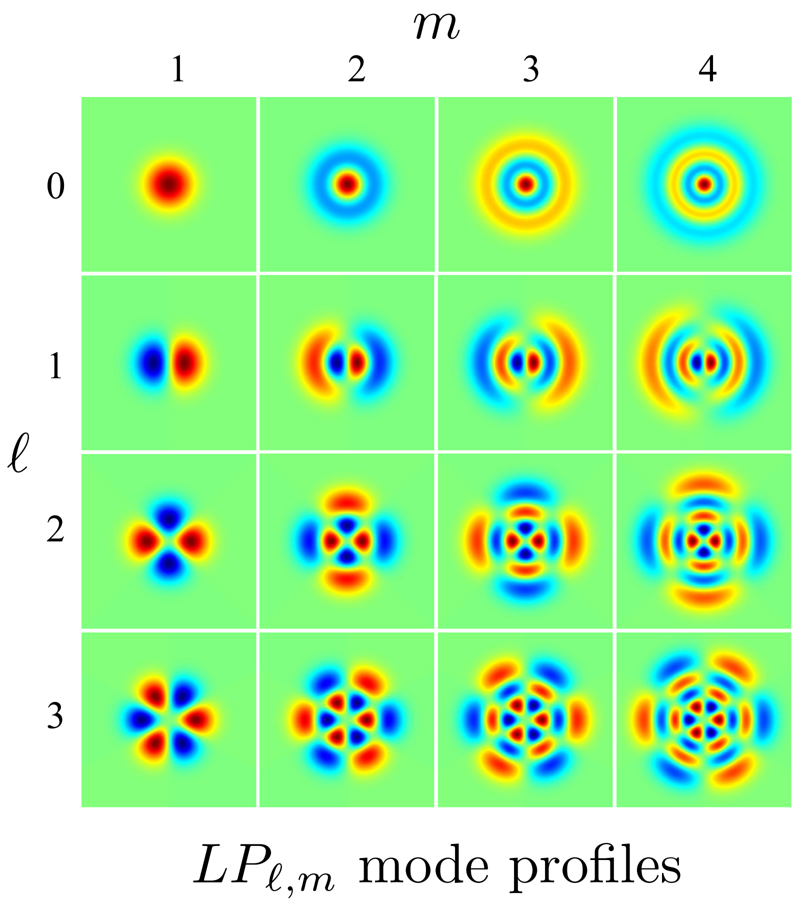

Figure 5.2: Cross-sectional intensity profiles of possible LP propagation modes for a multimode fibre with a parabolic refractive index profile.

There do exist other sets of modes (of the same cardinality as the $LP_{\ell,m}$ set) that can be used as orthogonal bases for all propagation solutions. These can always be formed from linear combinations of LP modes and two commonly used examples are Hermite-Gaussian modes and optical vortex modes [126, 207]. In reality the true set of eigenmodes for a fibre is unique to that fibre due to imperfections in shape and refractive index profile, material defects, bends, twists and other physical effects. The true eigenmodes of a particular fibre are termed its *principal modes*. For OM1, OM2 and OM3 fibre the infinite parabolic approximate solutions fairly closely resemble these principal modes [208].

Under the infinite parabolic refractive index profile assumption the propagation constant for each mode is [206]:

$$\tilde{\beta} = \frac{V}{R\,(2\Delta)^{1/2}} \left\{1 - \frac{4\Delta}{V}\,(2m+\ell-1)\right\}^{1/2} \tag{5.11}$$

It can be seen that modes that share a value of $2m+\ell$ have the same propagation constant β. Given this, there will be significant power coupling between such modes as they propagate along a fibre with minor imperfections, a phenomenon termed *degeneracy*. Modes with common values of $2m+\ell$ are grouped together for analysis purposes to form a *degenerate mode-group* or just *mode-group*. While minor imperfections over long length scales cause significant coupling within mode-groups, coupling between mode-groups is typically much lower and requires significant short length scale fibre imperfections [209]. This creates 'islands' of mode coupling that can be exploited for mode multiplexing [132, 206]. Because $\ell \geq 0$ and $m \geq 1$, the quantity $2m+\ell-1$ is often used to index degenerate mode-groups so that the lowest order, or fundamental, degenerate mode-group has an index of 1. This is the convention used in this chapter. At 1550nm there are typically about 10 such mode-groups that exist in OM2 and OM3 graded index fibres and as many as 19 when operating at 850nm [132, 210]. However, the highest order mode-groups (order 10 at 1550nm and orders 18 and 19 at 850nm), tend to be *leaky modes* where the power is slowly leaked as the mode propagates, as opposed to lower-order *bound modes* where the power can be transferred over long distances [211]. For this reason the leaky mode-groups are avoided for mode multiplexing systems.

It is worth mentioning that the eigenmode decomposition of an optical fibre channel can be considered a special case of the eigenmode decomposition of a generalised propagation channel, for example the highly random multipath propagation channels encountered in wireless MIMO as described in Section 4.2.1. However, given the more deterministic nature of the propagation environment inside an optical fibre it is possible to accurately approximate these eigenmodes based on *a priori* assumptions about the fibre. Radio propagation channels are generally very random so stochastic methods must be used.

The MDM system used in this work directly excites eigenmodes of the fibre based on the infinite parabolic graded index fibre approximation. In most cases these closely approximate the principal modes. By exciting modes in different mode-groups, it is possible to transmit multiple data streams in parallel using a single fibre with very little coupling between them, thereby avoiding the need for DSP algorithms [211, 212].

Using this technique in the context of a DAS transforms the RF MIMO streams of different antennas into different optical spatial channels propagating on different LP modes or combinations thereof. This is an interesting transformation in its own right, but is of practical benefit as the principles of modal selectivity upon which MDM relies for operation also heavily suppress the effect of modal dispersion, increasing the bandwidth-distance product of the fibre for each channel. This overcomes a major shortcoming of WDM solutions for MIMO DAS and allow greater lengths of fibre to be used.

5.2.2 Fibre dependent effects

In an ideal OM1,OM2 or OM3 fibre with a parabolic graded refractive index profile fibre light propagates in a linear combination of the LP modes and there is negligible coupling between modes along the fibre. In reality, however, there are many imperfections that degrade this ideal performance. Fibres are never perfectly manufactured so there are random variations in the refractive index profile along the fibre as well as material defects. The cross-sectional profiles of real fibres are often not rotationally symmetric and display some eccentricity or ellipticity [213]. The temperature of the fibre affects the dimensions, material properties and stress, which in turn affects the way light propagates. Often fibres must be joined together either by splicing or with connectors and any misalignment between the fibres or trapped dirt can significantly change the modal propagation properties. One of the most significant factors limiting performance when mode multiplexing over fibres inside buildings is the bending and twisting of fibres as they are laid inside walls and around sharp corners.

Bending and twisting of fibres has long been known to degrade performance due to coupling between spatial modes, particularly into higher-order modes, and between polarisations [214, 215]. Spatial-mode coupling arises from the fact that the tendency of light is to travel in straight lines so when it reaches a sufficiently sharp bend in the fibre the propagating modes are offset slightly from the central axis causing coupling of light into other modes once propagation has stabilised again [216]. In this situation high-order modes are often coupled into leaky modes propagating largely in the cladding and so their power drops off very quickly.

When fibre is placed under mechanical stress from being twisted or bent this sets up a birefringence condition whereby orthogonal polarisations of light experience different propagation constants. For example, for a fused-silica fibre operating at 1550nm the phase difference between orthogonal polarisations at the output of a fibre caused by birefringence is given by [217]:

$$\beta_b = -3.2 \times 10^7 \left(\frac{r}{R}\right)^2 \text{degrees/m} \tag{5.12}$$

where r is the radius of the fibre core in m and R is the radius of curvature of the bend in m.

Twisting of the fibre during manufacturing and during installation causes the axes of polarisation to rotate along the length of the fibre. For an otherwise ideal fibre this simply means that for a linearly polarised input the angle of polarisation at the output is not predictable. However, birefringence in the fibre is generally independent of the rotation of the polarisation axis. Consequently, regardless of the input polarisation, some of the light is coupled into an orthogonal polarisation where it experiences a different propagation constant. In single mode fibres large birefringence can be exploited to create polarisation maintaining fibres [218]. However the situation is more complex in multimode fibre because the varying material propagation constant results in a varying set of fundamental propagation modes. These slightly different but overlapping modal profiles produce additional coupling between modes.

In order to minimise the performance-degrading effects of bending there are minimum allowable bend radii specified in industry standards for particular kinds of fibre. For example the Telecommunications Industry Association states that the minimum bend radius of a fibre should be no less than 10 times the cable diameter, about 32mm for standard OM1-OM4 cables. Mechanically, fibres can withstand much smaller bend radii – a loop of radius 5mm has a breakage probability of less than 10^{-5} [219]. Using equation 5.12 it can be seen that a bend radius of 30mm produces a phase shift between polarisations of -22 degrees/m so it is expected that there is significant polarisation mode coupling in this case. If significant polarisation mode coupling occurs it is expected that there should a broader range of output polarisation orientation angles. Aside from polarisation mode coupling, birefringence also creates significant *polarisation mode dispersion (PMD)*, which causes pulse broadening due to the delayed arrival of orthogonal polarisations. This causes an associated reduction in fibre bandwidth-distance product and hence capacity.

Recently, there has been theoretical work on the implications on the effects of bending on mode propagation in a fibre [213, 220]. However, it remains as yet largely unknown to what degree coupling between modes arising from bending affects practical mode multiplexing systems. Further, no work has been done to experimentally measure the losses and coupling between modes in realistic situations. This is particularly important in systems where the aim is to launch predetermined approximations of the principal modes of a fibre to avoid the use of DSP algorithms and will place important limitations on design of such system.

5.2.3 Holographic excitation of modes

An MDM system capable of directly exciting any arbitrary eigenmode of the fibre must be able to launch any of these modes individually into the fibre. The simplest way to do this is to shine light on the end of the fibre with the exact phase and amplitude profile of the desired mode. This can be done dynamically, so that the pattern can be changed arbitrarily at any time, using a *spatial light modulator (SLM)*. There are two technologies typically used to implement SLM devices – *liquid-crystal on silicon (LCOS)* and *digital micromirror devices (DMD)*.

LCOS SLMs consist of a 2-dimensional array of pixels made from liquid crystals. In this research two main types of liquid crystals are used in the SLMs: *nematic* and *ferroelectric*. Nematic liquid crystals are named as such because the crystals used are in the nematic phase, meaning the molecules have only long-range directional alignment but no longitudinal alignment. By application of an alternating electric field of appropriate magnitude the direction of alignment for the molecules can be rotated to any arbitrary angle. The molecular structure of nematic liquid crystals exhibits optical anisotropy and so this rotation of the optical axis can be used in conjunction with polarising optics to create variable phase retarders. In a sufficiently thick liquid crystal cell, it is possible to alter the phase of light passing through a pixel by any amount from 0-2π. Because of this construction, nematic liquid crystal SLMs enable spatial phase modulation of light but cannot modulate amplitude. Further, incident light must be in the correct polarisation in order for the device to function. The ability to arbitrarily modulate phase enables a wide range of holograms to be displayed but typically means slow response times.

Ferroelectric liquid crystals, on the other hand, consist of crystals in the *smectic C chiral phase (SmC*)*. SmC* phase has a more ordered structure than nematic phase and as a result the movement of crystals under an applied electric field is more constrained. Typically, in an SmC* phase liquid crystal an applied field changes the orientation of the molecules between one of two bistable states, representing two different rotations of the optical axis. Again, because of the anisotropy of the structure, this can be used in conjunction with polarising optics to create either binary-phase modulation or binary amplitude modulation. In this research, only binary-phase modulation is used meaning that each pixel of the SLM is able to adjust the phase of incident light by either $-\pi$ or $+\pi$ radians. This effectively makes each pixel a switchable half-wave plate. Binary-phase SLMs are more limited in the range of possible holograms that can be displayed and hence far-field patterns that can be produced. One major limitation in this respect is that the far-field pattern must exhibit rotational symmetry. This is because the pixels can only take real values (+1 or -1) and thus the Fourier transform must have conjugate symmetry as shown in Figure 5.3. However, the fact that there are only two possible states for each pixel enables much faster switching, meaning that ferroelectric liquid crystals have a much faster response time. It is this property that has generally made ferroelectric LCOS SLMs an attractive option for telecommunication applications [221, 222]. As with nematic LCOS SLMs, the use of polarising optics generally makes ferroelectric LCOS SLMs polarisation sensitive.

Because ferroelectric liquid crystals are switched with a static electric field, the polarity of this field must be periodically reversed to avoid irreversible degradation of the liquid crystal, a technique known as *DC balancing*. This can result in periods of downtime during which the SLM cannot be used, although algorithms that switch single pixels at a time with minimal effect on the far-field have been proposed [223]. Nematic SLMs are intrinsically DC balanced as their state is set by applying an alternating electric field with no DC component.

It is also worth noting that although *transmissive* LCOS SLMs are in theory possible, most practical devices have a reflective backing behind each pixel making them *reflective* devices. This means that incident light passes through each pixel twice so only half the thickness of liquid crystal is required to achieve the desired phase shift. Devices such as polarising beam splitters (PBS) are then used to separate the reflected light from the incident light.

DMDs, by contrast, use microscopic moveable mirrors as pixels to create SLMs. These have a fast response and are polarisation insensitive. However, they can only modulate amplitude and cannot control the phase of light [224].

A truly full featured SLM would allow the adjustment of the phase and amplitude of every pixel. However, such devices do not currently exist and so in this work, the SLMs used modulate phase only. In this case, the SLM acts as a customisable diffraction grating such that the far-field interference pattern, termed the *replay field* can be precisely controlled. This is true even with only binary-phase capability. A phase-only SLM can then be considered a way of implementing a computer controlled hologram or phase mask.

The *far field* of a hologram is the diffraction pattern arising from it incident on a plane located a significant distance away from the hologram, or equivalently on a plane located at the focal point of a positive (convex) lens [225]. In general terms a hologram and its far field diffraction pattern are related by the Fourier transform. For an SLM made up of $N_p \times N_q$ pixels the replay field, $R(x, y)$, is given by:

$$R(x, y) = \frac{1}{N_x N_y} \sum_{p=0}^{N_p-1} \sum_{q=0}^{N_q-1} H(p, q) \exp\left[2\pi j \left(\frac{px}{N_x} + \frac{qy}{N_y}\right)\right] \tag{5.13}$$

where N_x and N_y are the x and y dimensions of the replay field and $H(p, q)$ represents the transfer function of a single hologram pixel at location (p, q). It is possible using this equation to apply an optimisation algorithm, such as the Gerchberg-Saxton algorithm, direct binary search, simulated annealing or a genetic algorithm, to find appropriate pixel values of H to generate an arbitrary desired replay field [226]. Appropriate constraints can be applied to H depending on the type of SLM being used, for example binary-phase. Some example binary-phase holograms and their replay fields are shown in Figure 5.3. It can be seen that it is possible to create patterns of the correct size, amplitude and phase profile to launch particular modes into a fibre using this method.

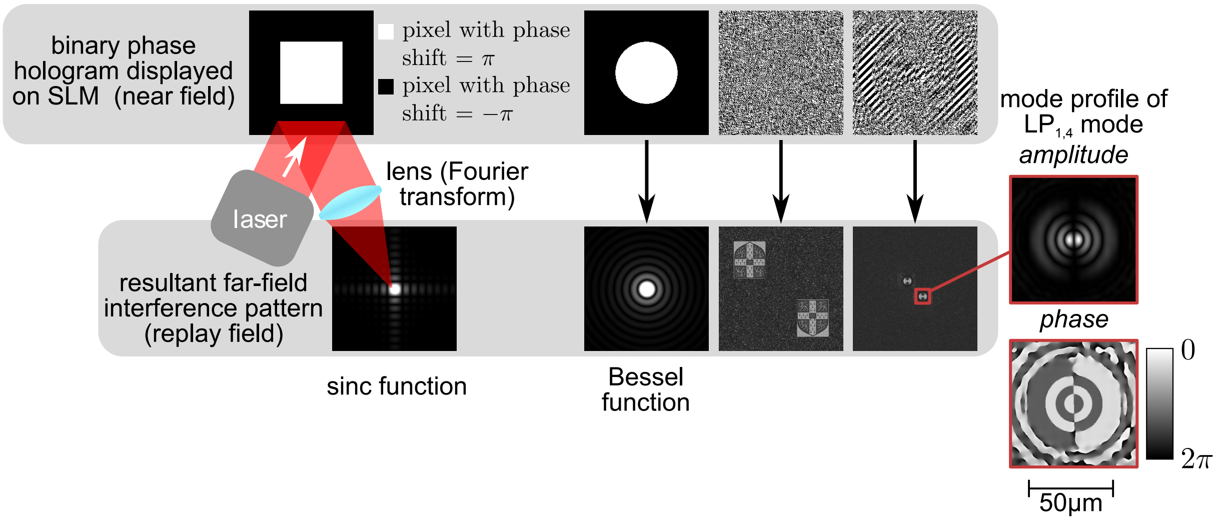

Figure 5.3: Illustration of far-field or replay-field patterns produced by various binary-phase holograms. The lens performs a Fourier transform on the near-field pattern from the hologram to produce the far-field pattern at its focal point. Because the holograms are binary-phase the Fourier transforms must be symmetric as shown in last two examples. The final example shows how an SLM displaying such a binary-phase hologram can be used to launch specific modes into MMF.

The work in this chapter makes use of a mode multiplexing system that uses holograms generated using LCOS SLMs used to launch and receive modes. It has previously been shown to be able to transmit two separate 12.5Gbps data streams over 2km of OM2 fibre [211]. In this set-up there are 9 non-degenerate mode-groups, each containing between 1 and 9 modes that can be individually excited using separate phase masks and that have 3dB bandwidths of greater than 6GHz. To provide 8 independent streams at 1550nm it would only be necessary to populate a single mode from each mode group, meaning low optical coupling between modes can be achieved. Previous MDM systems have been unable to provide more than 2-4 independent channels because of high coupling between modes at the transmitter and receiver resulting from, for example, the need to accommodate connector tolerances and fibre imperfections [123]. However, precise dynamically adjustable holograms make it possible to independently excite a much greater variety of modes. This has the potential to transmit large numbers of broadband MIMO streams, which will be essential for future MIMO systems.

It is noted that time-dependent variations in the holographic launch and detect systems and the fibre channel are of a relatively slow nature (several Hz) compared to those typically found in a fast-fading wireless environment (100s of Hz) [184]. Therefore, it is assumed that the MIMO DSP algorithms are able to re-estimate the channel regularly enough to compensate for such variations. The holograms do not then need to be adapted periodically for this purpose. However, in more advanced systems this may become an attractive option because there is plenty of spare bandwidth in optical fibres that could be used to feed back detailed channel state information from receiver to transmitter. This would enable the provision of optimal performance of the fibre channel over time.

In this chapter a 2-channel MDM system is combined with MIMO RF channel measurements of a typical indoor DAS scenario to create a proof-of-principle demonstration of a broadband 2×2 MIMO-enabled DAS RAU fed by a single fibre. The system is shown to offer improved MIMO capacity over the test area for 2 MIMO streams up to 6GHz over 2km of OM2 MMF. The MDM system is then extended to enable examination of the feasibility of transporting a 4×4 MIMO protocol over 2km of OM2 MMF. This is observed to provide excellent performance up to a frequency of 10GHz. The system is also observed to work when the fibre is tightly bent.

5.3 Experimental set-up

5.3.1 2×2 MIMO set-up

The capacity of a wireless MIMO link is determined by measuring the complex channel transfer coefficients $h_{k,m,n}$ as shown in Figure 1.21. As discussed in Section 4.2.1, in order to test the capacity of a fast-fading environment, these channel coefficient are measured for many random fading environments and are combined and represented by a random channel matrix, $\mathbf{H}_k$, for a particular RAU, k. For a linear, statistically time-invariant channel subject to *additive white Gaussian noise (AWGN)*, with flat, fast fading defined $\mathbf{H}_k$ and assuming uniform power allocation (due to no CSI available at the transmitter), the total Shannon capacity of the channel can be calculated using Equation 4.9, repeated here for convenience:

$$\mathcal{C}_k = B \sum_{p=1}^{S} \log_2 \left(1 + \frac{\rho}{M} \sigma_{k,p}^2\right)$$

where B is the bandwidth of the channel, ρ is the total signal to noise ratio of the system and $\sigma_{k,p}$ is the p^{th} largest magnitude singular value of $\mathbf{H}_k$. This Shannon capacity represents the maximum rate at which data can be transmitted down the channel with arbitrarily low error rate. Note that because $\mathbf{H}_k$ is a random variable matrix, the channel capacity, $\mathcal{C}_k$, is a random variable governed by a probability density function. The expected value of this is the ergodic capacity.

The entries of $\mathbf{H}_k$ vary randomly in different environments due to multipath interference. As discussed in Section 4.2.1, in order to find the capacity of a fast-fading environment (and obtain a more generalised result) a wide range of multipath interference realisations are measured. In this experiment, this is achieved by measuring the radio propagation environment over a frequency range from 1.7GHz to 2.7GHz (using the set-up shown in Figure 5.4a), and normalising for frequency effects as discussed previously. Measurements are repeated at 26 positions in the room, as shown in Figure 5.4, to demonstrate the system performance over a coverage area in a typical indoor DAS situation.

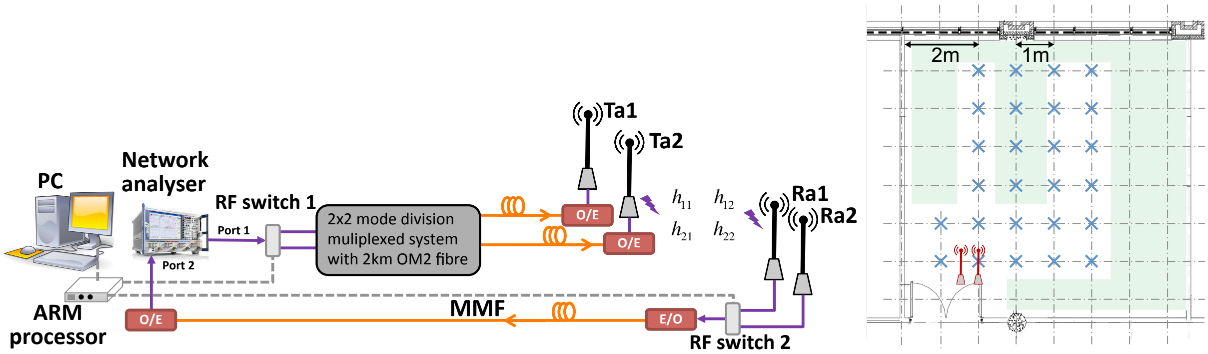

(a) (b)

Figure 5.4: (a) Experimental set-up of 2 × 2 MIMO RF system (b) DAS RF test environment showing test points.

The MDM system used is shown in Figure 5.5. A single 1550nm tunable laser source is used to produce two separate optical streams, each of which is externally modulated with a Mach-Zehnder Modulator (MZM). This system uses lenses to excite the fundamental mode ($LP_{0,1}$) of the fibre and an LCOS SLM to excite a programmable choice of higher order mode, for transmission of two spatial channels. A ferroelectric binary-phase 256 × 256 SLM with a pixel pitch of 15μm is used to generate phase masks that allow the light to be launched into the fibre with a particular mode profile. This set-up can launch any mode of the fibre, or super-positions of these modes.

As with any optical system, imperfections in components, termed *aberrations*, can limit performance and introduce additional noise. Aberrations can arise in almost every component in the system. The most basic aberration encountered in this research arises from misalignments where beams are not parallel to the optical axis, termed *tilt* (although this is not technically an aberration as it does not distort the image). Higher order aberrations include *defocus*, usually due to errors in distances between elements, *spherical aberrations* due to undesired effects occurring towards the edge of spherical lenses, and *coma* due to non-perpendicular propagation of light through a lens. There are also significant random variations in the wavefronts of light reflected off the SLMs caused by the non-flatness of their surfaces, an effect that appears as spatial optical noise in the far-field.

Because the SLMs are programmable, it is possible to correct for these aberrations to a degree by applying an appropriate calibration phase mask to the SLM, which is superimposed on the desired phase mask. In this research, the aberated wavefront is modelled using Zernike polynomials, a convenient choice as different order polynomials correspond directly to the commonly encountered aberrations described above [227]. The coefficients for the Zernike polynomials up to the 10$^{\text{th}}$ order are determined empirically by inputting a reference Gaussian beam from a single-mode fibre through the system and then running a steepest-descent search algorithm to maximise the detected power. This is then used to create the calibration phase mask to compensate for aberrations [228]. The algorithm does not always converge to the desired solution and so for much for much of this work aberration correction is not used. Future refinement of this method, perhaps even using it only to make fine adjustments from pre-calculated coefficients, should result in improved performance, particularly for high-order modes.

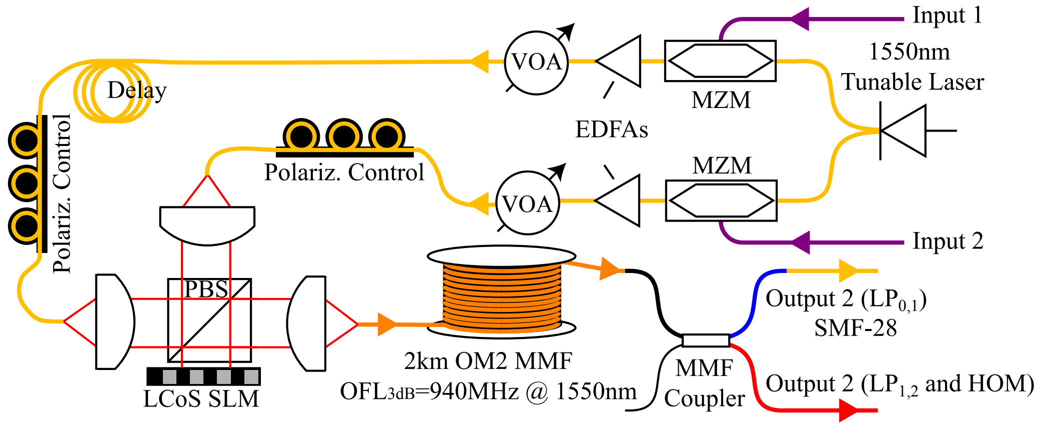

Figure 5.5: Set-up of mode division multiplexing system [211].

For the experiment a 2km reel of OM2 fibre is used. This has a nominal 3dB bandwidth of 940MHz for an overfilled launch condition. This bandwidth is greatly increased by the use of mode-multiplexing because this almost completely eliminates modal dispersion. Because OM2 fibre is manufactured to a higher degree of precision than its predecessor, OM1 fibre, the variation in performance between fibres is small and there are generally only minor defects in refractive index profile [229]. By contrast, OM1 fibres often suffer from significant defects such as unintended depression of the refractive index profile towards the centre of the fibre [78]. This particularly common defect causes significant degradation in the quality of modes that have power concentrated towards the centre of the fibre, such as $LP_{0,1}$. As a result, if OM1 fibre was to be used higher-order modes with more power in the fibre cladding could offer better performance. Further, it might be favourable to use an alternative mode basis such as Hermite-Gaussian, which has been shown to exhibit good modal propagation characteristics in such fibres [230].

At the receive end an MMF coupler is used to separate the low and high order modes. This method works because such devices are usually constructed simply by placing the cores of two fibres sufficiently close that light propagating in the high-order modes of one fibre (i.e. having more power in the cladding) will be forced to overlap into the core of the second fibre. In this way, power is coupled into the second fibre. The degree of modal overlap, controlled by the separation of the cores, determines the how much power is coupled to the second fibre.

For this experiment, 3 MMF couplers made by Go4Fiber were considered, each of which had different nominal splitting ratios for an overfilled modal propagation: 90/10, 70/30 and 50/50.

Previous modal characterisations of these couplers (see [211]) showed that the 90/10 has too high a modal cut-off, meaning only very high order modes are directed to the second output. It is undesirable to use such modes for the second channel in this MDM system because they were measured to have low bandwidth and high launch and propagation loss. Conversely, the 50/50 coupler has too low a modal cut-off, meaning that a significant portion of the fundamental mode is coupled between outputs of the coupler, resulting in poor modal isolation. The 70/30 coupler has the best compromise between modal isolation and bandwidth and so is used in this experiment.

Based on prior measurements of the 70/30 coupler, the fourth mode-group is known to offer the optimal combination of modal isolation relative to the first mode-group (~25dB) and bandwidth (>15GHz). Within this mode-group, the $LP_{1,2}$ mode is chosen for the high-order mode launch due to its slightly better observed stability over a 24-hour time period compared with the other possibility, the $LP_{3,1}$ mode [211]. This experiment then uses the fundamental mode, $LP_{0,1}$, for one channel and the $LP_{1,2}$ mode for the second channel. After the MMF coupler, a standard single mode fibre (SMF-28) is used to strip modes other than $LP_{0,1}$ from the first output.

If more than two modes were to be multiplexed, one possible solution would be to use another SLM at the output of the fibre to enable detection of arbitrarily selected modes. Alternatively, it is also possible to design couplers using asymmetric y-junctions that can transmit selected group of modes via different output arms [231]. This would enable multiplexing and demultiplexing of more than two modes using only fibre couplers. However, such devices have not yet been experimentally realised.

The complex transfer coefficients between each input (taken as the input to the Mach-Zehnder modulators) and the photodiode receivers placed at the optical outputs are measured using a network analyser and power meter. These are then used to produce additional transfer matrices, $\mathbf{H_{mux}}$, at 30 test frequencies from 40MHz to 6GHz. To obtain the response matrix of the combined system shown in Figure 5.4, each matrix $\mathbf{H_{mux}}$ is multiplied by each normalised $\mathbf{H}_k$ representing a different fading scenario (i.e., a particular realisation of the random matrix $\mathbf{H}_k$). Equation 4.9 is then used to calculate the capacity of the combined system for each fading realisation and frequency. These fading realisations are comprised of random variables the capacity calculated from them is also a random variable with a defined statistical distribution.

This multiplication process accounts for the effects of mixing between modes in the fibre as well as between spatial streams in free-space. MIMO systems periodically send pilot signals to determine the total channel matrix, in this case $\mathbf{H_{sys}}$, and in doing so detect the level of such mixing. Because of this, no additional DSP is required in the MDM system - the amplitude and phase of mixing between modes will be detected by the wireless MIMO protocol and used to extract the separate spatial streams. High levels of mixing between modes will result in reduced performance.

5.3.2 Higher order MIMO set-up

Following the successful demonstration of the MDM shown in Figure 5.5, another more advanced MDM system was built as shown in Figure 5.6. Again, this system multiplexes two separate optical streams generated from a single 1550nm tunable laser. One of the streams is coupled from an SMF directly into the MMF thereby exciting the fundamental $LP_{0,1}$ propagation mode in the fibre. The other stream is reflected off an SLM to excite a programmable choice of higher order mode in the MMF. A binary-phase 256×256 SLM with a pixel pitch of 15μm is used to generate phase masks that allow the light to be launched into the fibre with a particular mode profile.

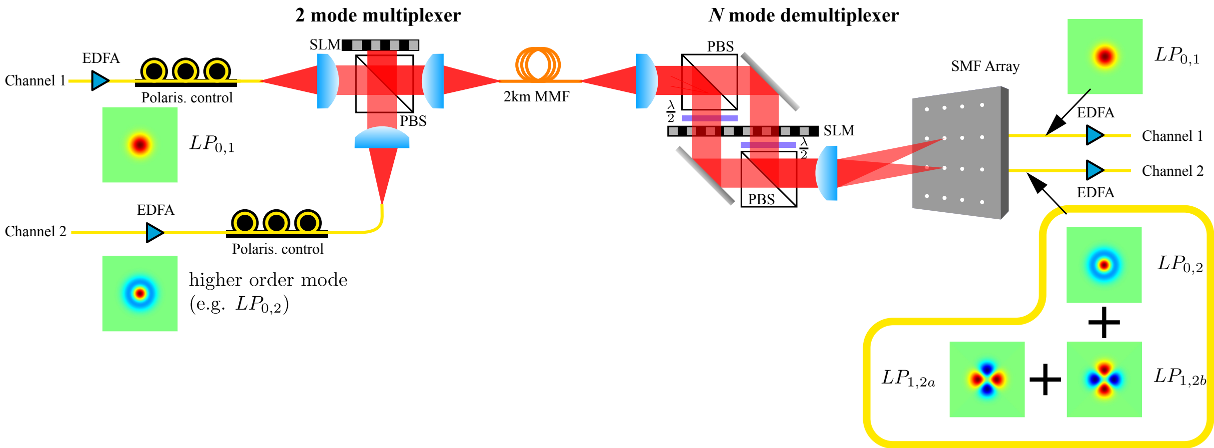

Figure 5.6: Set-up of advanced mode division multiplexing system with mode selective output (based on [132]).

The key difference in this set-up is at the receiver where the multimode coupler is replaced with a custom built *mode-selective switch*. This works as follows: the polarising binary splitter (PBS) splits the incident light beam into two beams of orthogonal polarisation. A half-wave plate then rotates one of these polarised beams to ensure that all light incident on the SLM is of the same polarisation. This is necessary as the SLM is polarisation sensitive. The two beams of light are then incident on the SLM, which in this case is a 256-phase nematic LCOS device with a resolution of 1920×1080. The receive area of the SLM is split into two halves with each half used to detect one polarisation of the original incident beam. After the SLM, a further half-wave plate restores the original polarisations and the two beams are recombined.

By programming an appropriate phase mask onto this receive SLM it is possible to detect individual modes exiting the fibre. For example, applying the $LP_{1,2}$ phase mask at the receiver will ensure that light leaving the fibre in the $LP_{1,2}$ mode, and only this light, is transformed into a Gaussian beam after the SLM. By superimposing a grating on this phase mask, the output Gaussian beam can be electronically tilted onto any one of 16 fibres in the output fibre array. Further, by superimposing the phase masks for detecting modes it is possible to direct power from modes to different fibres. This offers the potential for multiplexing between as many as 16 different modes.

Currently, this fibre array system only exists at the receiver although a similar system at the transmitter designed to enable large number of modes to be simultaneously launched is under construction. However, it is possible to gain an indication of the performance of this future system by launching each individual mode into the fibre and then seeing how it couples to every possible phase mask at the receiver. In this way a mode-transfer matrix can be produced. This mode transfer matrix can be represented graphically as shown in 5.7. Because of the large and unavoidable coupling between modes in each mode group the output is often aggregated by mode group for the purposes of gauging system performance from such graphs. This matrix should be similar to that produced using the future system because factors such the phase mask quality and misalignment that reduce performance will be the same in either case and because most of the observed degradation arises from unavoidable mode mixing within the fibre itself. Therefore, this mode transfer matrix is measured for the system and is used to indicate performance.

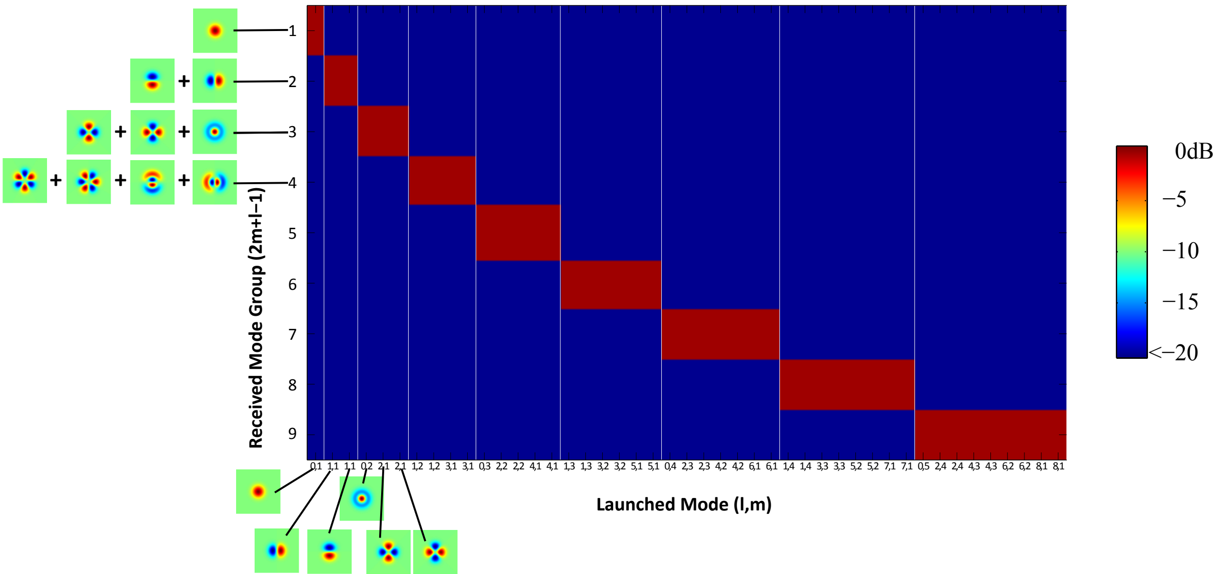

Figure 5.7: Graphical representation of an ideal mode transfer matrix with no mixing between mode groups. For ease of analysis, the output modes are aggregated across mode groups.

Because coupling between individual modes within mode-groups is very high compared with the coupling between modes in different mode groups, as described in Section 5.2.1, the mode transfer matrix is often aggregated over entire mode groups. If there are N mode groups this then results in an $N \times N$ *mode-group transfer matrix* as shown in Figure 5.8. In practice, this aggregation is achieved by setting the phase mask to be a super-position of the phase masks for all the modes within a group.

It should be noted that there are issues that must be addressed to make such a set-up more practical and economically feasible in future developments. Firstly, it is necessary to reduce the optical loss of the system. While the present de-multiplexer can have optical coupling losses as low as 4-5dBo, the multiplexer introduces optical losses up to ∼15dBo because it uses an SLM not optimised for use at a wavelength of 1550nm. This is easily corrected by replacing this SLM with one designed for operation at the desired wavelength. Further, the cost of SLMs can be significant, though in a production environment could be produced at much lower cost, comparable to that of liquid crystal displays. Because of the DSP capabilities of wireless MIMO

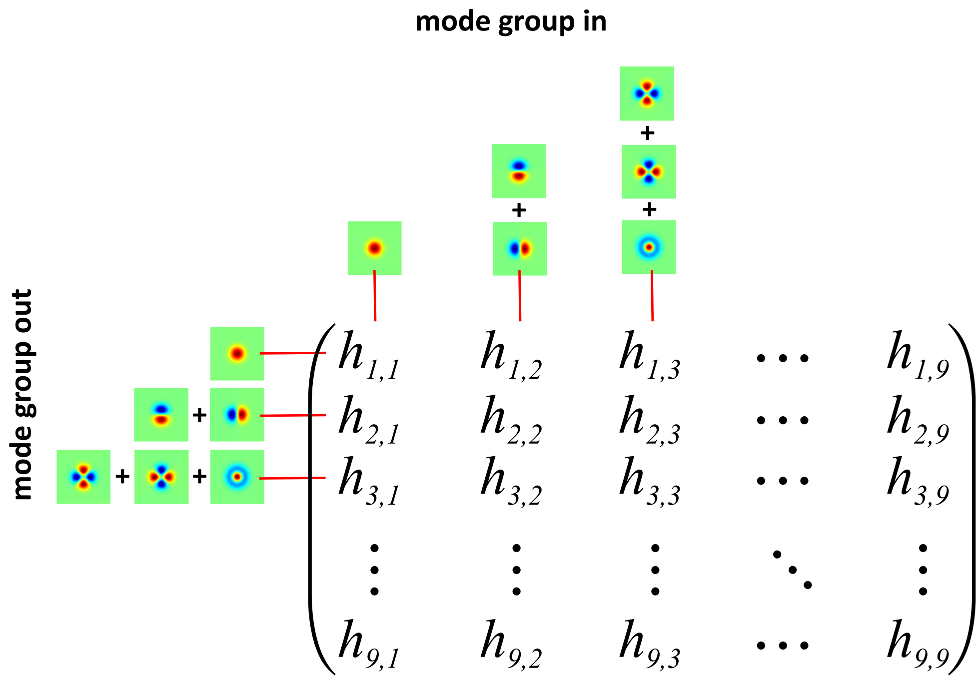

Figure 5.8: Illustration of how LP modes are aggregated to form a mode-group transfer matrix.

transceivers, coherent optical receivers and DSP circuits are not required in this application, which substantially reduces cost and energy usage.

5.3.3 Fibre bend radius test setup

Next, it was desired to gain experimental insight into the impact of fibre bending on modal propagation in mode multiplexing systems. In order to achieve this several makeshift mandrels were constructed using pieces of dowel of different radius, as listed in Table 5.1. Also listed is the curvature, κ, defined as $1/r$ where r is the bend radius of the fibre. This is a useful quantity for plotting as it makes it possible to plot data points for an unbent fibre of infinite radius.

A section of a 10 metre OM3 multimode fibre patchcord is wrapped around each of these pieces of dowel in turn. The total length of the bent section is kept constant at 690mm for each different bend radii. The patchcord was measured to have a radius of 3.2mm and this was accounted for when calculating the actual bend radius.

The system introduced in Section 5.3.2 is again used to measure the mode-transfer matrix. The mode-transfer matrix is also aggregated to create a mode-group transfer matrix in order to more easily observe general behaviour. For this initial investigation only power was measured but in future it is intended to enable the optical phase estimation capability of the system to observe the full complex mode-transfer matrix. However, the power matrix alone still provides useful insight and such a measurement has never before been published.

Linearly polarised light is launched into the fibre in a single, fixed orientation and then

Table 5.1: Radii of dowel used for testing fibre under different bend conditions. Radius measurements have an error of ±0.3mm due to nonuniformity of the dowel radii.

Dowel radius (mm)	**Fibre bend radius (mm)**	**Curvature κ ($\mathbf{m}^{-1}$)**
(straight fibre)	∞	0.0000
19.2	20.8	0.048
12.9	14.5	0.069
9.9	11.5	0.087
7.5	9.1	0.111
5.6	7.2	0.139

the received power is measured in both vertical and horizontal polarisations. This enables an initial examination of the impact on polarisation. Specifically, a histogram is produced of the absolute values of the polarisation orientation angles over every received mode for each launched mode-group. Because the phase angle of each received polarisation is not measured the output light is assumed to be linearly polarised at the orientation angle calculated from the power measurements. Modes with power less than or equal to the power meter noise floor are excluded from this analysis. Statistical quantities such as mean and variance are used to examine the degree to which polarisation mode coupling occurs. If the variance is seen to increase this consistent with the conclusion that polarisation effects are playing a part in mode coupling as discussed in Section 5.2.2.

5.4 Results

5.4.1 2×2 MIMO

Figure 5.9 shows a measurement of the coupling between the different inputs and outputs of the system shown in Figure 5.5 indicating the mode-multiplexing system loss as well as the coupling between modes. It can be seen that for the fundamental and $LP_{1,2}$ modes the electrical link loss is about 20dB, mostly due to the insertion loss of the SLM which is not designed for operation at 1550nm. From Figure 5.9 it is seen that the isolation between different modes as seen from the electrical inputs/outputs is more than 24dB over a frequency range of 18GHz. The standard deviations of the mode isolations over a 24-hour period are also shown. This indicates that the MDM link is well suited to sending separate MIMO streams with minimal cross-talk and is relatively stable over time. It should be noted that this system is built without requiring the use of fibre patchcords, but if they were to be used then additional mode coupling would likely be introduced at the connectors due to mismatches in fibre shape, concentricity and alignment. Some of this may be reversible by DSP, i.e., be characterised by unitary mode-coupling matrices, but would result in a different set of fundamental modes for the fibre.

Figure 5.10 shows the 2×2 MIMO channel capacity measurements, each normalised to a 1Hz bandwidth, over a 6GHz frequency range. In 802.11n systems a 20MHz bandwidth is used with a typical transmit power of -5dBm and receiver noise floor of -60dBm. These values are

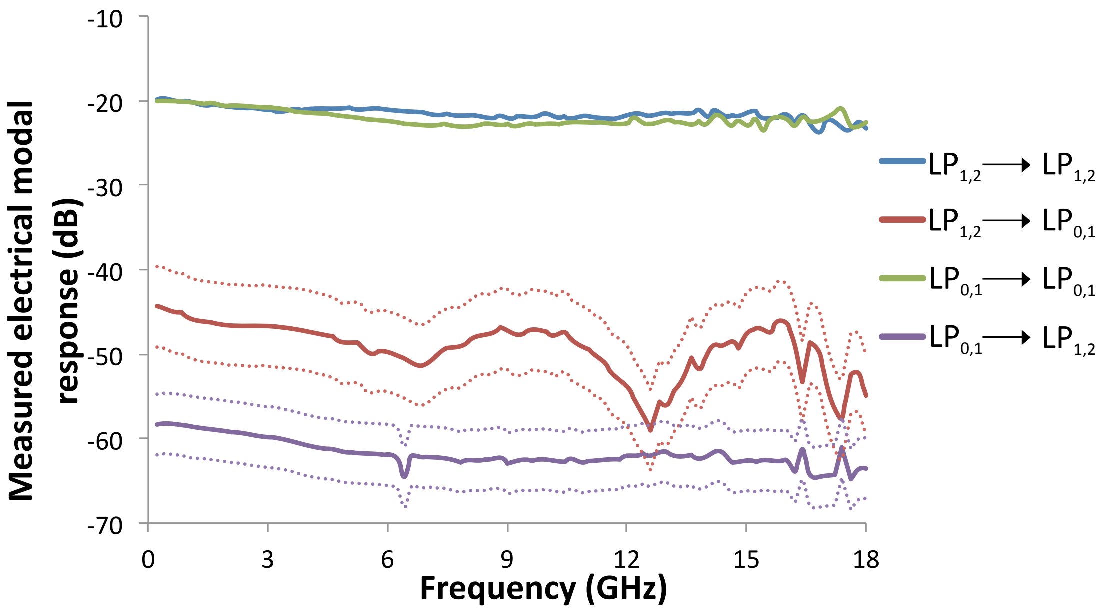

Figure 5.9: Graph showing coupling between multiplexed modes at the output of the fibre vs frequency. Dashed lines represent the standard deviation over a 24-hour period.

used here to give a representative SNR for a 1Hz bandwidth. Shown for comparison is the case where there is 0dB cross-coupling between the fibre modes, i.e. multiplexing is not possible due to high coupling between modes. The results are produced by inserting the many realisations of the full channel matrix (including both fast fading and the 2×2 mode-multiplexed link) into Equation 4.9 to produce a distribution of possible channel capacities. From this distribution, the median capacity can be estimated. As a measure of spread, it is possible to determine a rate such that any randomly positioned user in a fast-fading environment wishing to transfer data at that rate will experience an outage with a certain probability, in this case 10%. Here, this is termed the *10% outage capacity*. Both quantities are plotted in Figure 5.10.

Even with an electrical loss of 20dB from the mode-multiplexed link and an additional 12dB of electrical loss in other DAS components (antennas, electro-optic converters) the mode-multiplexed 2×2 MIMO link offers a 50% improvement in median capacity over the case where there is 0dB isolation between modes in the fibre for the same total transmit power.

5.4.2 Higher-order MIMO

To predict the performance of the system for higher numbers of MIMO streams, the mode transfer matrix was measured as described in Section 5.3.2. To ensure proper alignment of the mode launcher and detector the mode matrix was first measured using a 1m MMF patch cord that should exhibit very low coupling between mode groups. The resultant mode transfer matrix is shown in Figure 5.11. It is seen that the cross-coupling between mode groups is less than about 10dB for the first 4 mode groups. It is also seen that the higher order mode groups are

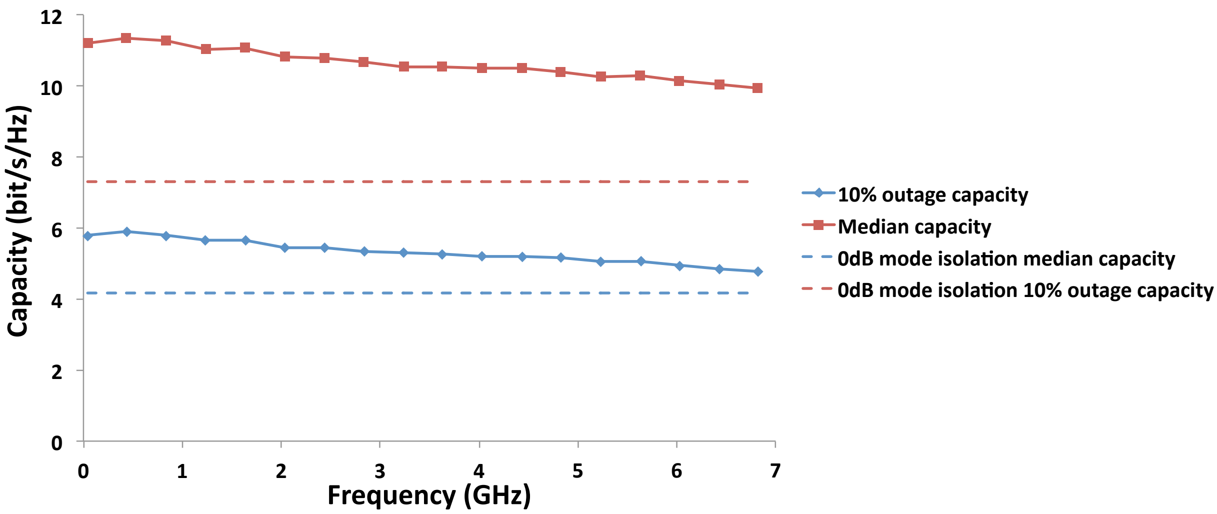

Figure 5.10: Graph showing channel capacity of the 2×2 MIMO system (detailed in Figures 5.4 and 5.5) vs frequency. Shown for reference is the case where there is 0dB of cross-coupling between modes in the fibre so that no multiplexing occurs.

more prone to cross-coupling with other mode-groups.

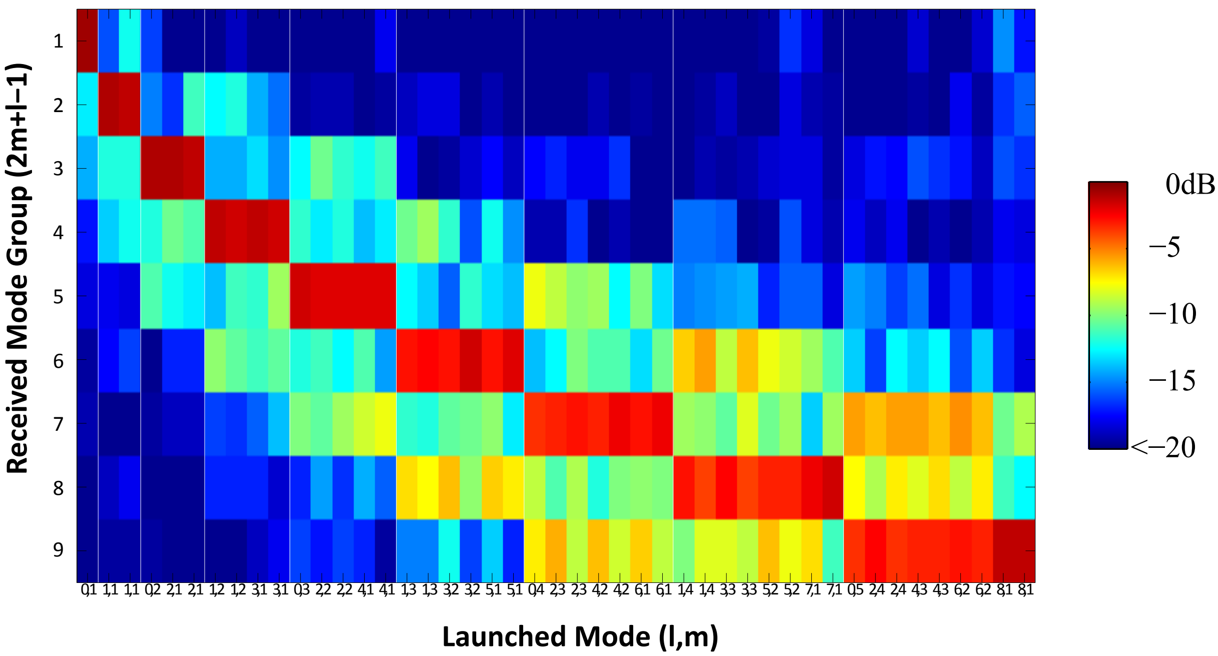

Figure 5.11: Graph depicting the mode transfer matrix for a 1m MMF patch cord. Modes at the output are aggregated into mode groups.

Following this the 2km of OM2 MMF was connected to the system and the mode-transfer matrix was measured again, as shown in Figure 5.12. It is seen that coupling between mode groups increases due to gradual interactions over the length of the fibre. However, there is still sufficient isolation between many mode groups, e.g. 1 and 2, 2 and 4, that the link is still well suited for mode multiplexing.

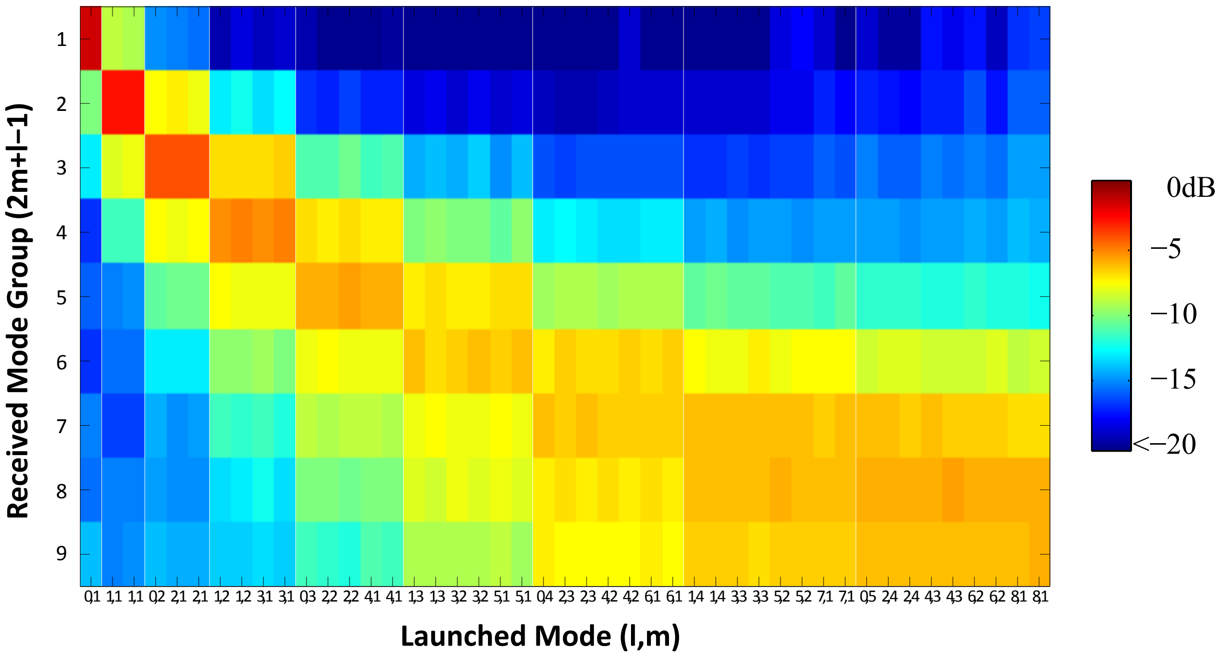

Figure 5.12: Graph depicting the mode transfer matrix for 2km of OM2 MMF. Because of the longer length it is seen that there is now substantial coupling between mode groups.

In order to establish the potential for the system to provide parallel wireless MIMO streams it is necessary to consider the radio spectrum frequency response of each possible mode-group coupling as in Section 5.4.1. This includes the radio frequency behaviour of all components used, including modulators, amplifiers, detectors and any effects caused by the slight broadening of the optical spectrum. The results represent the channel seen by a real wireless system connected to this system and so give a realistic measure of performance. Further, the phase of each different modal path is measured - an important quantity because real wireless MIMO systems measure both amplitude and phase of the propagation channel.

Using a vector network analyser to drive the modulator a 45×45 matrix of complex transfer coefficients between the first 45 modes was obtained at 1601 sample frequencies over a range of 40MHz-10GHz. Each 45×45 matrix was then further reduced to a 9×9 matrix by summing the responses for modes in the same mode group as described in Section 5.3.2. This is equivalent to using a phase mask that is a super-position of these modes. From this data, specific mode groups were selected to investigate their potential for use in a high-order mode multiplexing system. Mathematically speaking, a submatrix of the full mode-group transfer matrix is selected.

First, mode groups 1,2 and 3 are used to simulate a 3×3 MIMO link. The magnitude of coupling coefficients vs. frequency is shown in Figure 5.13. It is seen that there is a significant separation between desired mode coupling and unwanted cross-coupling between mode-groups. This indicates that the isolation properties are fairly good across a large frequency range for a 3×3 wireless MIMO system.

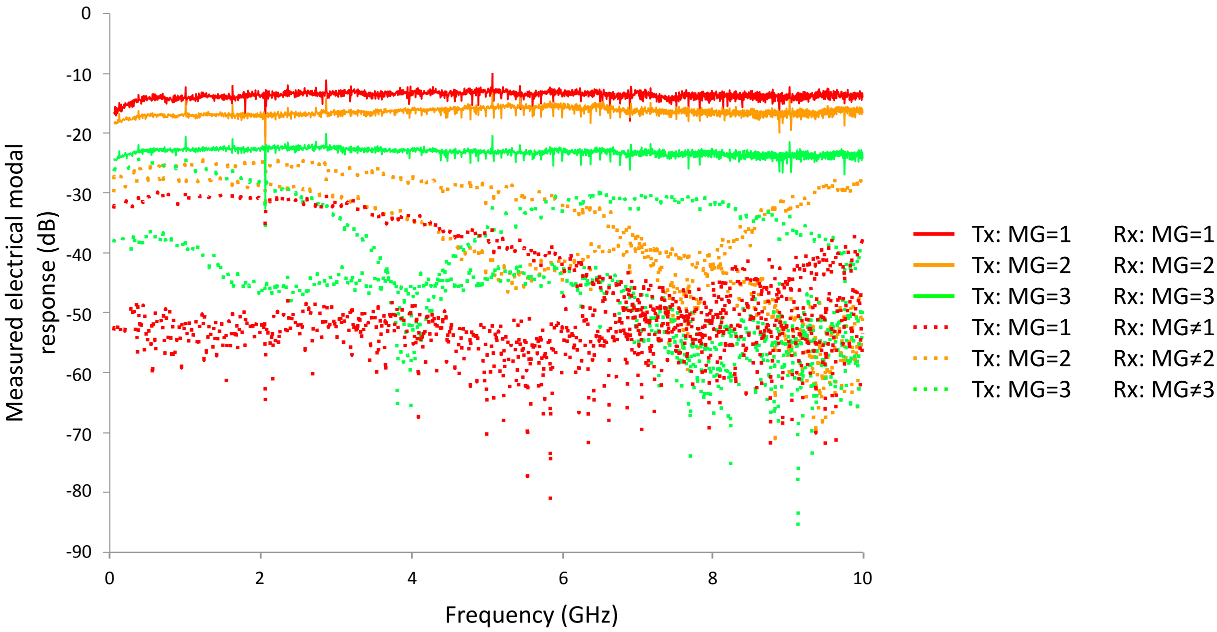

Figure 5.13: Graph showing the magnitudes of the mode-group coupling coefficients vs. frequency for a 3×3 mode-group division multiplexing system using mode-groups 1, 2 and 3.

Following this, mode groups 1, 2, 3, 4 and 5 are used to simulate a 5×5 MIMO link. The magnitudes of the coupling coefficients vs. frequency are shown in Figure 5.14. In this case, there is seen to be significantly more overlap in terms of coefficient magnitudes of the desired mode-coupling and the cross-coupling between mode-groups. This indicates reduced performance compared with the 3×3 case.

Despite the increase in cross-coupling between mode groups in the 5×5 case, this does necessarily mean the system is not suited for carrying 5×5 MIMO signals. Because wireless MIMO has built in digital signal processing capability, the most important factor determining performance is the orthogonality of the complex transfer matrices. This orthogonality can be quantified using the condition number of these matrices as discussed in Section 4.2.1. A low condition number ($<$ 10dB) indicates that the different channels are highly orthogonal and so can be very effectively separated by the digital signal processing algorithms of the wireless transceiver, thereby offering high theoretical link capacities.

The condition numbers for several of selected submatrices of the mode-group transfer matrix are plotted in Figure 5.15. It can be seen that up to the 4×4 case, the condition number generally is fairly low, staying mostly in the range of 15-19dB from 0-10GHz. This indicates that the

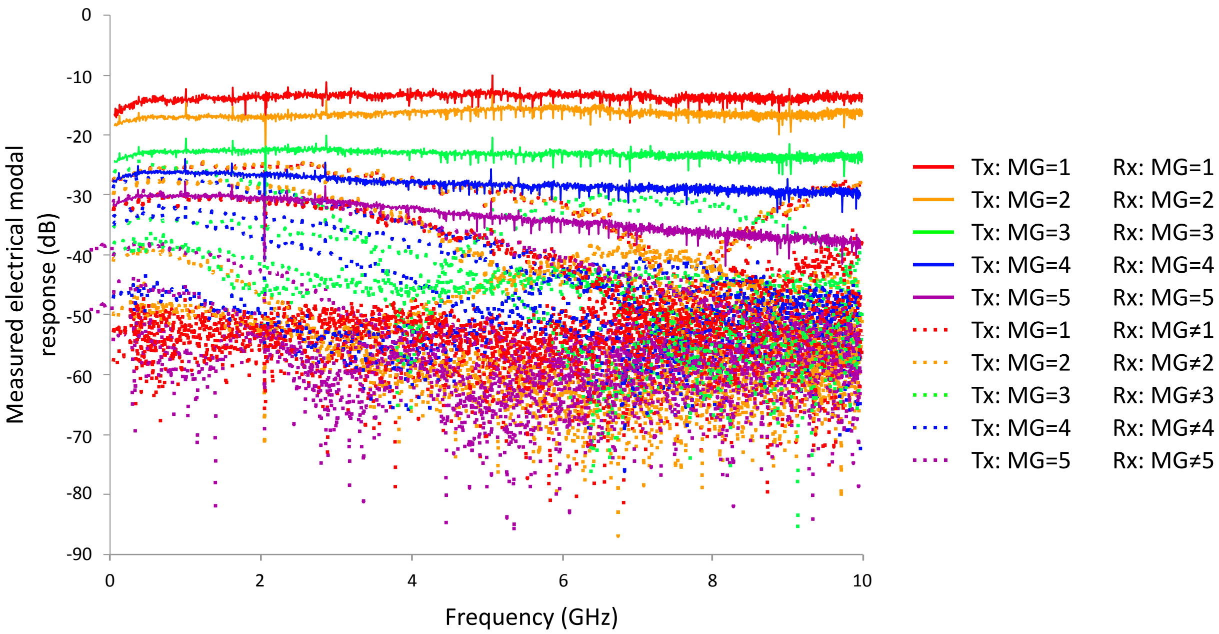

Figure 5.14: Graph showing the magnitudes of the mode-group coupling coefficients vs. frequency for a 5×5 mode-group division multiplexing system using mode-groups 1, 2, 3, 4 and 5.

mode multiplexing system offers high orthogonality for as many as 4 MIMO channels over the frequency range required by most MIMO services. Orthogonality is seen to deteriorate more noticeably for the 5×5 case and above, mainly due to the strong coupling between neighbouring higher-order mode groups that must necessarily be used. This is evidenced in Figure 5.12. This performance could be improved by better aligning the system. It is also possible to correct for lens aberrations, in particular coma, spherical and astigmatism, by superimposing appropriate Zernike polynomial phase masks, as discussed in Section 5.3.1. This correction was not used to measure these results but when applied should further reduce the mode-group coupling at higher orders.

These results clearly indicate the potential of the MDM system to enable the transmission of up to 4 streams of broadband RF MIMO over a single piece of fibre up to a distance of 2km. This is unprecedented in terms of both number of channels supported and distance, indicating the potential of this system.

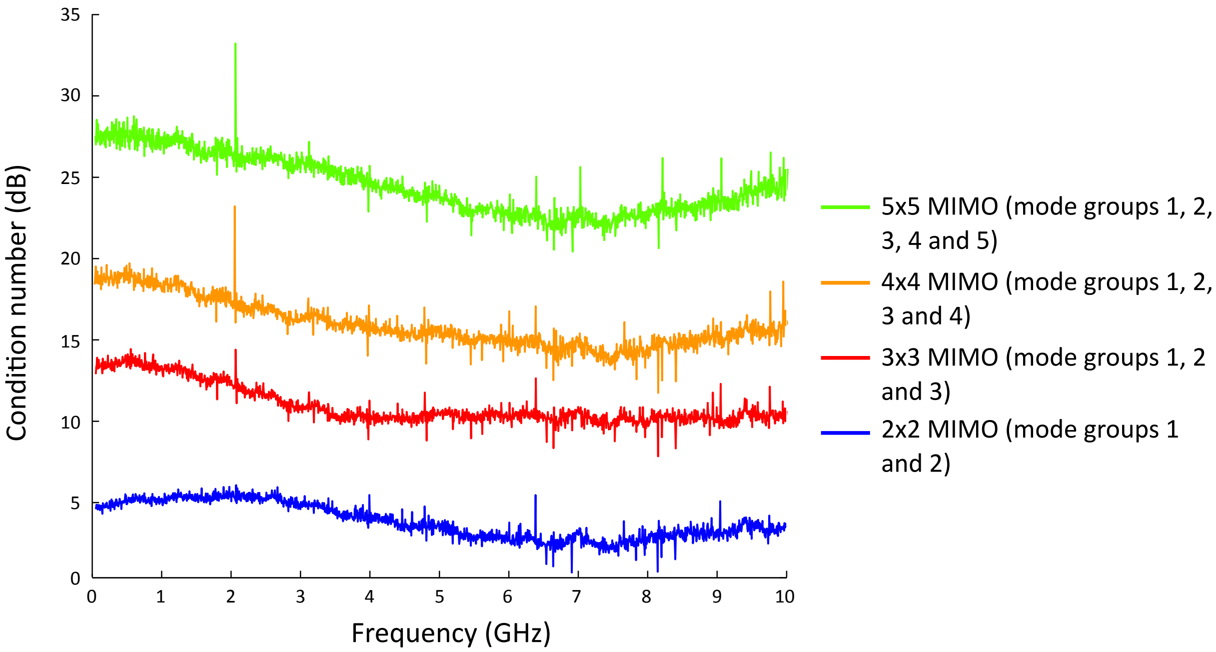

Figure 5.15: Graph showing the condition number of particular submatrices of the mode-group transfer matrix as the number of MIMO channels is increased.

5.4.3 Effects of fibre bend radius

First the unbent OM3 fibre was aligned and the mode-group matrix measured to provide a reference point as shown in Figure 5.16.

Figure 5.17 shows the total received power aggregated across all modes for power transmitted in a single mode group. It can be seen that for mode-groups 1-5 even at the highest curvature the total power stays constant to within 1dB. However, for mode-groups 6 and above it can be

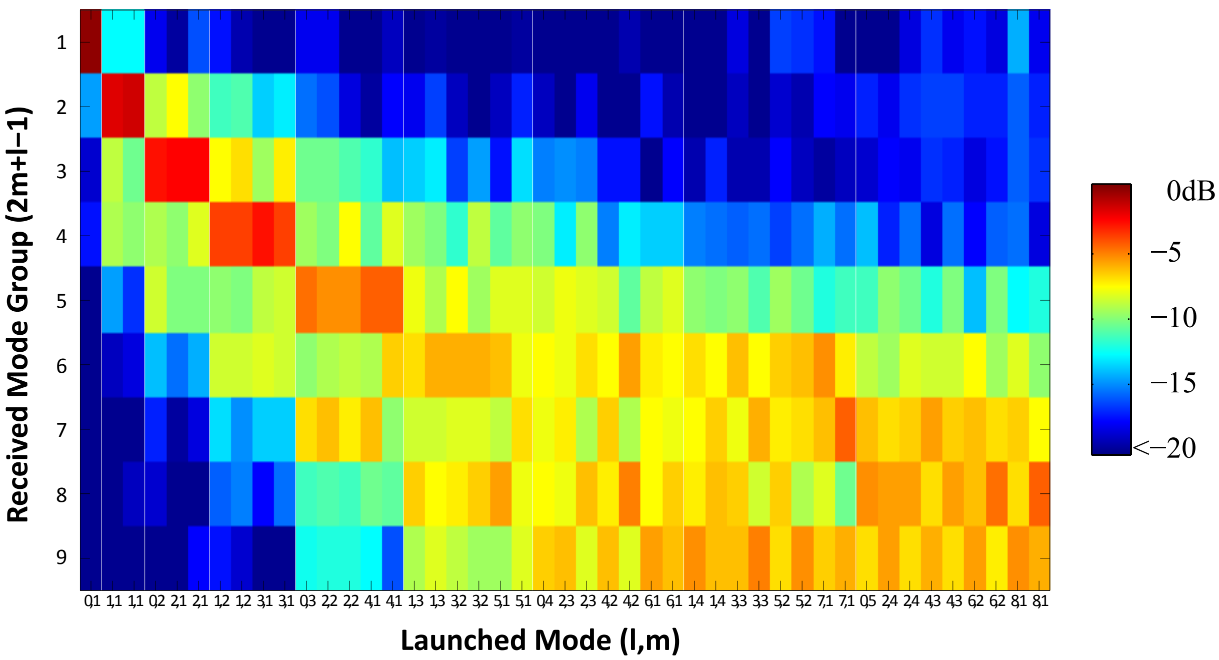

Figure 5.16: Mode-group transfer matrix of the unbent 10m OM3 patchcord used for bend radius testing.

seen there is significant power loss. This power loss is seen to increase with fibre curvature as well as with mode-group order. It is seen that for a 7.2mm bend radius there is 4dB additional power loss in the fibre when launching mode-group 9. Clearly, this indicates that power in the high-order mode groups is being coupled to other mode-groups or dissipated.

In order to confirm where this power is lost the total received power in mode-groups 1-6 when mode-groups 7, 8 and 9 are excited is plotted in Figure 5.18. It can be seen that almost no detectable additional power is coupled into mode-groups 1-6 when mode-groups 7, 8 and 9 are launched. This indicates that the power being lost as bend radius increases is being coupled into higher order modes and ultimately into leaky-modes whereby the power is dissipated in the cladding.

On this basis alone it can be seen that for consistent performance when using this mode multiplexing system over OM3 it is safest to use only mode-groups 1-5 if there are likely to be very tight bends. However, if bend radii are kept to Telecommunications Industry Association recommended limit of ∼30mm as described in Section 5.2.2 then it should still be possible to use mode-groups as high as order 9.

Figure 5.19 shows the ratio of power coupled into the same received mode-group as is transmitted to the power coupled into other mode-groups, termed *mode-group cross-coupling ratio*. This metric provides further insight into the effects of bending because the observed behaviour can now be categorised into 3 classes by mode-group. Class I, consisting of mode-groups 1-4, shows no significant change in power coupling between modes as fibre curvature is increased.

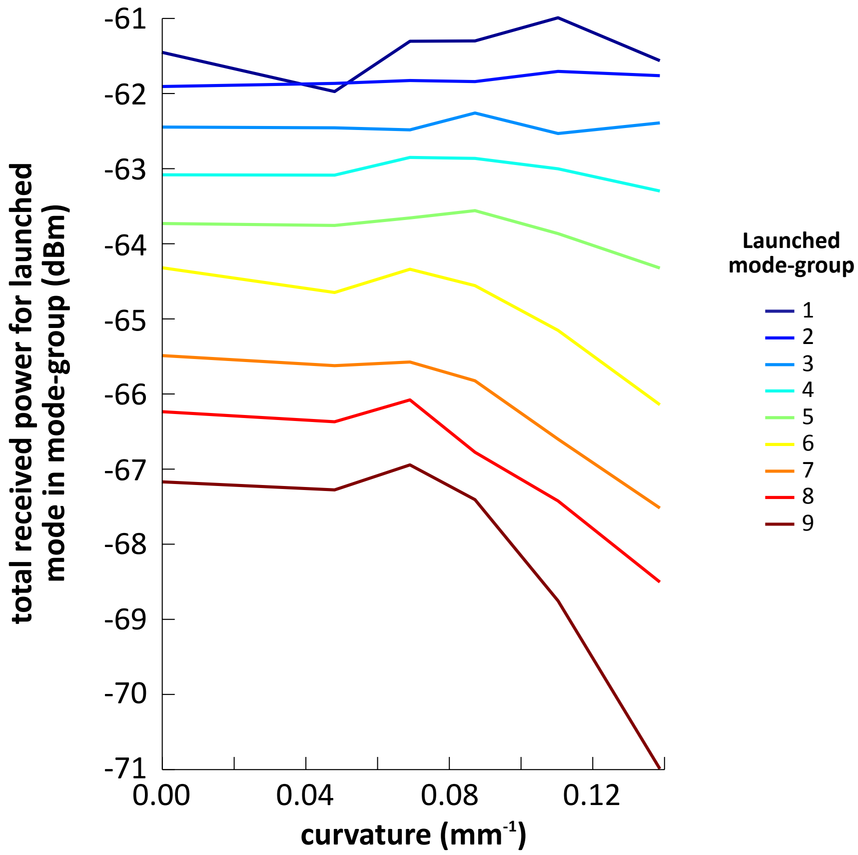

Figure 5.17: Total received power aggregated across all mode groups for different launched mode groups as fibre curvature is increased.

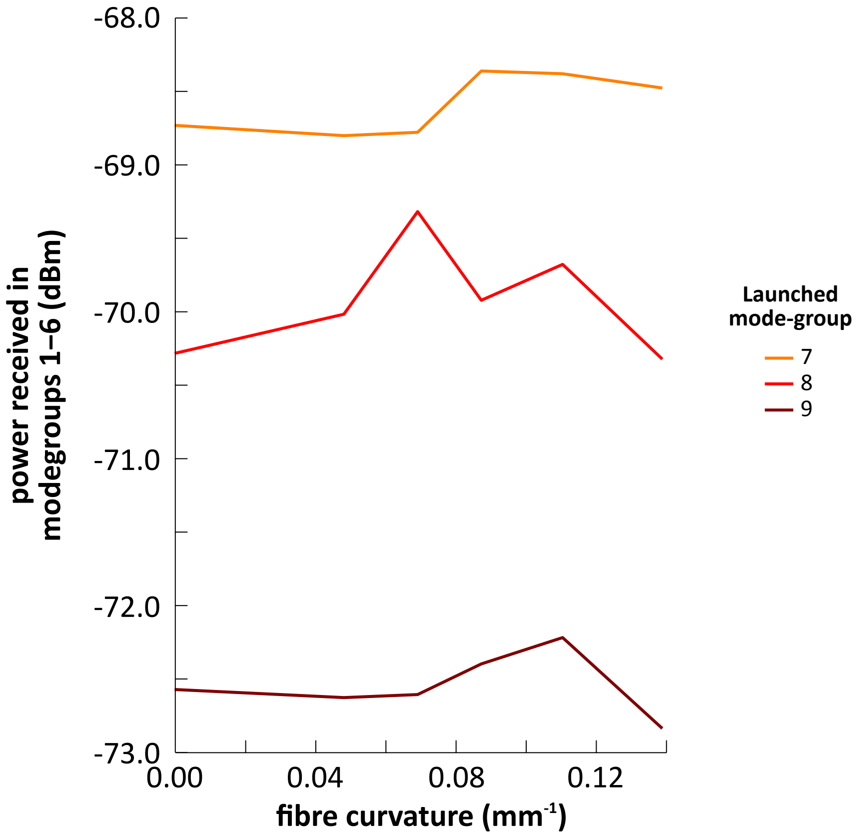

Figure 5.18: Total power received in mode-groups 1-6 when mode-groups 7-9 are excited as fibre curvature is increased.

Therefore these mode-groups are very reliable even for tight bend radii. Class II, consisting of mode-groups 5 and 6, exhibits an increase in mode-group cross-coupling ratio as curvature is increased because power that is normally coupled into mode-groups 7-9 is lost into the cladding. This improves the overall ratio by attenuating some of the leaked power. This class actually experiences slightly improved performance under tight bend radii.

Class III, consisting of mode-groups 7-9, exhibits a significant decrease in mode-group cross-coupling ratio as fibre curvature increases. This is partly explained by the loss of power into the cladding. However it is worth noting that while the total power reduction across all received mode-groups when mode-group 9 is launched is 4dB as seen in Figure 5.17, the decrease in the inter-mode-group coupling ratio is closer to 9dB. This indicates that there must also be coupling between these higher order mode groups (though not into lower order mode groups base on the results in Figure 5.18). For class III, the reduction in performance is a combination of increased coupling between mode-groups and dissipation of power into leaky modes in the cladding.

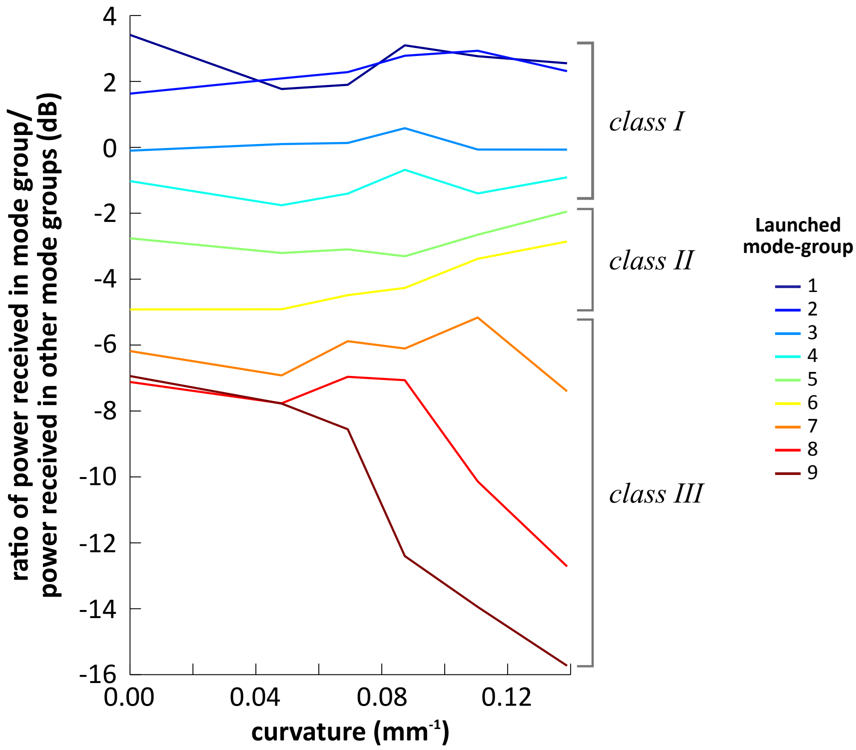

Figure 5.19: Ratio of power received in the same mode-group that is launched to power received in other mode-groups as fibre curvature is increased. Three different classes of behaviour are observed.

Figure 5.20 shows a histogram of all the received polarisation orientation angles for each mode-group launched. The distributions for mode-groups 1-6 appear similar in shape as fibre curvature is increased, with peaks corresponding to a rotated version of launched polarisation. However for mode-groups 7-9 the spread of the distributions appears to increase with fibre curvature. To further examine this the standard deviation of the received polarisation orientation angles across all mode groups is plotted in Figure 5.21. It can be seen that while for mode-groups 1-6 there is no clear trend common to all of them, for mode-groups 7-9 there is a consistently upwards trend and the standard deviation of the polarisation angles is seen to increase with fibre curvature. This means the received power is becoming more uniformly spread across a wide range of polarisation orientations. This is consistent with increased modal coupling caused by polarisation mode coupling and strong birefringence as discussed in Section 5.2.2. However, this effect is not detectable in lower order modes indicating that the bending induced birefringence is has much less effect on mode coupling.

It is worth noting though that from equation 5.12 at a bend radius of 7.2mm the bending induced birefringence is calculated to cause phase shifts between orthogonal received polarisations of 263 degrees over the test distance of 690mm. This is quite significant and so even though the mode coupling due to birefringence is not detectable, there may still be significant polarisation mode dispersion (PMD) causing pulse spreading and subsequent reduction in channel bandwidth.

Overall, it can be said that for mode groups of order 1-6 the modal behaviour is fairly stable, if not slightly improved, for tight bend radii. In higher order mode-groups both coupling and power loss are significantly greater. Mode-groups 1-6 are then the best choices for use in mode multiplexing over OM2 or OM3 fibre. Furthermore, such information could be used to create low-cost modal filters, simply by bending fibres to a pre-determined radius. This would enable the creation of simple mode multiplexing tools by, in effect, converting multimode fibres into few-mode fibres.

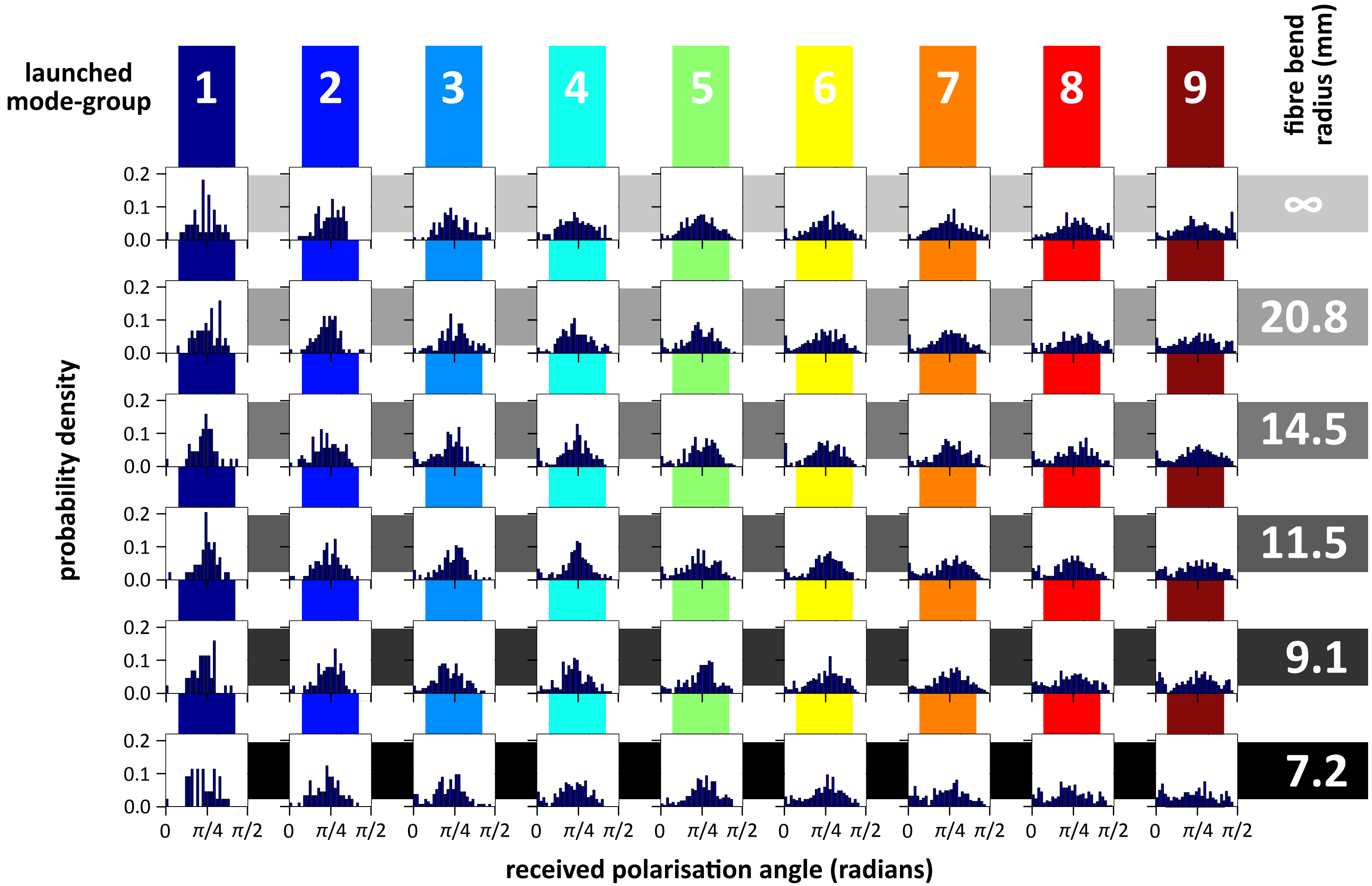

Figure 5.20: Histograms of the absolute value of the polarisation angles across all received modes for different transmitted mode-groups and fibre bend radii.

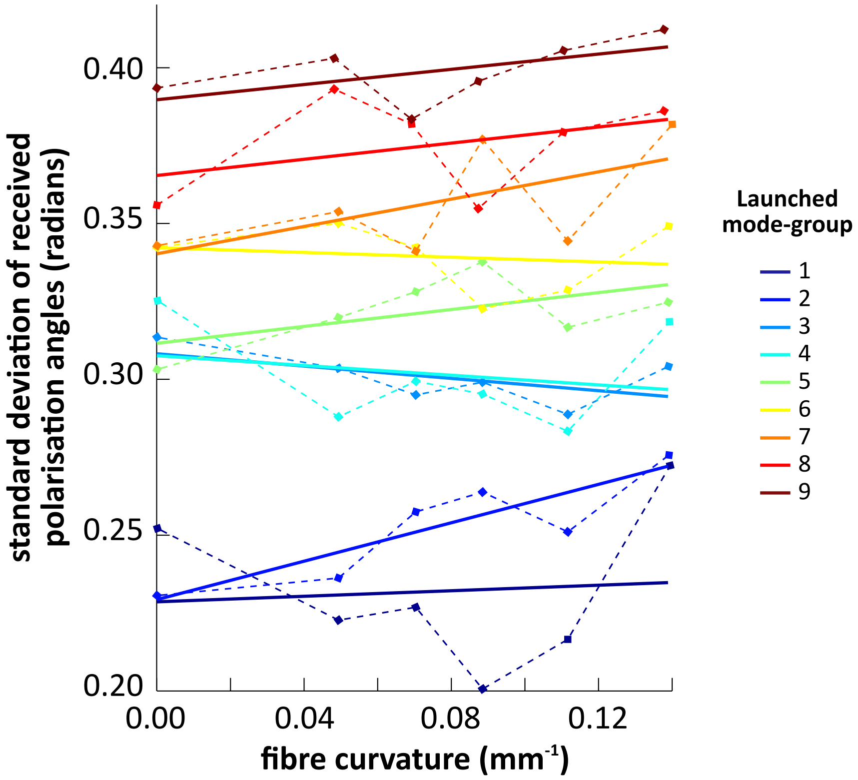

Figure 5.21: Standard deviation of received polarisation angles as fibre curvature is increased. Solid lines indicate trends.

5.5 Conclusions

In this chapter it is shown for a typical indoor DAS scenario that a 2×2 MIMO system mode division multiplexed over 2km of OM2 MMF is able to provide sufficient SNR performance to support channel capacities of 10bit/s/Hz over a bandwidth of 6GHz.

Further, using a second experimental set-up with a mode-selective switch at the receiver, it is possible to measure the mode-group transfer matrix of 2km of OM2 MMF for the first 9 mode-groups. The condition number is found to be $\leq$ 15dB across a 3GHz RF bandwidth for up to a 4×4 submatrix of this mode-group transfer matrix. This means that the system can readily support at least 4 independent MIMO streams over a single piece of 2km OM2 MMF.

Finally, it is found experimentally that when a fibre contains sharp bends of radius between 20mm and 7.2mm, mode-groups 1-6 experience either the same or slightly better performance than unbent fibre in terms of total power loss and inter-mode-group coupling. These mode-groups can therefore be used reliably and predictably for mode-multiplexing over OM2 and OM3 fibre.

The novel MDM system presented in this chapter has the potential to multiplex many more independent fibre modes, and hence MIMO RF spatial streams, than is currently possible. This represents an important advance in the design of indoor wireless infrastructure that must support a multitude of MIMO-enabled services offering large numbers of MIMO channels. This will be crucial to increasing wireless capacity available to users and preventing an imminent shortfall. Furthermore, this system represents a significant leap forwards in improving the data carry capacity of optical fibres in general and has immense potential to make a major impact on this field.

Chapter 6

Conclusions and Future Work

6.1 Overall Conclusions

Modern society is increasingly reliant on fast and ubiquitous access to wireless networks, driven in part by the proliferation of smart phones and the emergence of distributed intelligent sensing systems. As a result there is a huge demand on wireless networks and to avoid an imminent capacity shortfall, new strategies and technologies must be developed urgently. Wireless protocols are approaching their theoretical limits and almost every available form of multiplexing (time, frequency and spatial in the latest 4G and 802.11 standards) and advanced coding has been exploited. Therefore, attention must be turned to the design of wireless delivery infrastructure to enable further significant improvements in capacity. This is particularly important in indoor environments as this is where most mobile data traffic originates.

Up to this point distributed antenna systems (DAS) based on radio-over-fibre (RoF) technology, have been a popular infrastructure solution to improve coverage for wireless systems. However, to enable the very high speeds required in future mobile systems there must fundamentally be more wireless base stations for the same number of users in order to add capacity to a network. This could be implemented by using dense networks of small cells, or else by distributing capacity from centrally located base stations to a dense network of remote antenna units (RAUs) in a DAS. This means there is a need to re-design DASs so that they can be installed with a higher density of RAUs while incurring only minimal additional installation costs. Further, such DAS must be able to support the features of modern wireless protocols that enable high data rates, in particular multiple-input multiple-output (MIMO) technology. MIMO requires the simultaneous transmission of multiple spatially decorrelated radio signals using the same frequency channel. This poses a significant challenge in DAS design as it may require a method of sending multiple radio signals to a single RAU, whether by installing additional fibres or implementing a multiplexing scheme over a single fibre.

In this dissertation, a free-space optical system capable of enabling dense placement of RAUs in a DAS without requiring cabling is first demonstrated. Then the performance of such free-space links is examined and a useful design metric able to cope with the unusual nonlinear behaviour in such links is developed. Next, different possible layout designs for DASs that support MIMO protocols are compared using theoretical and experimental analyses and it is shown that if only small numbers of MIMO streams are used it may be possible to distribute the streams using existing DAS designs without the need to install additional fibres. Finally, for systems with larger numbers of MIMO streams a novel method of transporting multiple MIMO radio streams to a single RAU using mode-group multiplexing over a single multimode fibre is demonstrated. This, too, can be implemented within existing DAS deployments.

6.1.1 Radio over Free-Space Optical Links

In Chapter 2 it was first shown that fibre links in DAS can be replaced with low-cost, broadband free-space optical links, termed radio over free-space optics (RoFSO) links. These enable the implementation of very high density DAS without the need for prohibitively expensive or impractical cabling infrastructure. This makes it possible to create flexible DAS installations at low cost that can offer very high capacity. A 16m RoFSO link was experimentally demonstrated to provide a spurious-free dynamic range (SFDR) of >100dB/Hz$^{2/3}$ over a frequency range from 300MHz- 3.1GHz, demonstrating its potential as a broadband, multiservice alternative to RoF. Further, only approximate manual alignment is required, obviating the need for expensive and cumbersome automatic optical alignment systems.

The performance over 16m was then extrapolated to 50m and it was found that the link could provide an SFDR of > 109dB/Hz$^{2/3}$ over the same frequency range. The link was found to have an 802.11g EVM dynamic range of 36dB indicating its ability to support real wireless services requiring large dynamic range. This is the first such demonstration of a low-cost broadband RoFSO system.

The demonstration of RoFSO links for DAS is important for the design of future wireless infrastructure as it enables dense access networks to be deployed inside buildings without the need to install additional cabling, thereby significantly reducing costs. A RoFSO DAS could be used to dynamically allocate capacity from multiple centrally located base stations to many closely spaced RAUs, hence enabling a dense access network for users.

6.1.2 High Order Distortion in RoFSO links

Following this, in Chapter 3 the linearity performance of RoFSO links was examined in detail. Because of the high-power high-loss nature of RoFSO links the semiconductor lasers used to drive them, which were chosen over external modulators to minimise costs, are susceptible to unusual high-order nonlinear behaviour, often dominated by 7th, 9th or 11th order behaviour. This abruptly limits performance at higher powers and so is of great importance when quantifying dynamic range. Existing measures of dynamic range, such as SFDR, assume third-order nonlinearities only and so are inaccurate and less meaningful in the presence of dominant high-order effects. An alternative measure of dynamic range called dynamic-distortion-free dynamic range (DDFDR) was then proposed. This differs in that the upper limit is defined as the modulating power at which the peak optical modulation index (OMI) reaches unity. At this point the error vector magnitude (EVM) measured for a range of different wireless services starts to increase rapidly due to high-order distortion. This makes DDFDR a practical, service-independent metric of dynamic range. For two different wireless services it was observed experimentally that on average the DDFDR upper limit predicts the EVM knee point to within 1dB, while the third-order SFDR only predicts it to within 6dB. This represents the first detailed analysis of high-order distortion effects in lossy analogue optical links and DDFDR is the first metric able to usefully quantify the performance impacts of such behaviour.

DDFDR enables the accurate and reliable design of RoFSO because it enables simple measurements to provide an accurate estimate of the useful dynamic range. Matching this dynamic range to the requirements of the wireless services offered by the RoFSO DAS then enables other design metrics, such as allowable optical loss, tolerance to misalignment and required gain of amplifiers, to be determined more accurately.

6.1.3 Layout Designs for MIMO-enabled DAS

Next, the combination of emerging multiple-input multiple-output (MIMO) wireless protocols with existing DAS was examined. Because MIMO wireless protocols make use of multiple radio transceivers operating in parallel, they enable significantly higher data rates than traditional single antenna wireless systems. They will therefore form an integral part of most future wireless systems.

It was demonstrated that for systems with small numbers of MIMO streams (up to ~ 4), the full capacity benefit of MIMO can be attained in an existing DAS installation simply by distributing the MIMO streams amongst individual spatially separated remote antennas. Such systems are said to have an antenna replication factor of 1. This is in contrast to the prevailing paradigm of systems that replicate every MIMO spatial stream at each RAU, i.e. that have a replication factor of M for an $\mathrm{M} \times \mathrm{N}$ MIMO protocol. This was first shown theoretically through an examination of SNR as the number of spatial streams was increased. It was also seen from this analysis that for $\mathrm{M} > 4$ the performance advantage of DAS layouts with replication factors > 1 starts to increase.

Experimental results for two representative DAS propagation scenarios, one with significant line-of-sight propagation (LOS) and the other with no line-of-sight (NLOS), showed that the median channel of a 3×3 MIMO DAS with antenna replication factor of 1 is only $\sim$1% short of the median channel capacity of a 3×3 MIMO DAS with antenna replication factor 3. This compares with the advantage gained by using MIMO DAS over MIMO CAS which is 3.2% and 4.1% for the two propagation scenarios respectively. Therefore, there is minimal benefit to using a 3×3 MIMO DAS with antenna replication 3 in this case. A MIMO DAS with antenna replication 3 would provide almost the same performance while avoiding the additional installation costs.

The analysis was then extended to the multiple user case and with 20 users and 3 base stations a 3×3 MIMO DAS with antenna replication factor 1 was shown to offer median aggregate capacities of 259 bit/s/Hz and 233 bit/s/Hz for the LOS and NLOS cases respectively. This is only ~1% short of the capacity for the case with antenna replication factor 3 in both propagation scenarios.

It was concluded that existing DAS installations can provide the capacity benefits of MIMO services for small numbers of spatial streams. This result holds true for the multiuser case when additional base stations are operated over a single DAS infrastructure. This is an important result as it means that for emerging wireless protocols, such as 802.11n and 4G/LTE, that use up to 4×4 MIMO, pre-existing DAS infrastructures can provide most of the benefit of MIMO with very little upgrading required. A system of comparable performance can simply be constructed by distributing the spatial streams amongst different RAUs. This avoids the need for installation of additional fibres, a key cost driver in DAS deployment.

6.1.4 Broadband MIMO-enabled RoF systems using Mode-Division Multiplexing

The previous Chapter showed that for MIMO protocols with small numbers of spatial streams (typically ≤ 4) sending multiple MIMO streams to each RAU provides little performance benefit over distributing the streams amongst RAUs. However, the theoretical analysis also suggested that for MIMO protocols with a larger number of spatial streams, such as 802.11ac with up to 8 streams, this no longer holds true and that capacity is significantly enhanced by sending multiple MIMO streams to each RAU.

To be able to support such protocols over existing DAS infrastructures, thereby avoiding the cost associated with laying additional fibres, it is necessary to be able to simultaneously send multiple spatial streams over single multimode fibres. Multimode fibre is the most commonly found fibre in modern buildings, much of it pre-installed as part of a LAN infrastructure. As a result, it is also the most common type of fibre used for DAS.

In Chapter 5 a novel *mode division multiplexing (MDM)* system that sends each separate MIMO stream via a different propagation mode in a multimode fibre was demonstrated. Individual LP modes of a graded-index multimode fibre are launched and detected using computer generated holograms displayed on spatial light modulators (SLM). Combined channel measurements over 2km of mode-multiplexed graded-index MMF and a typical indoor radio environment showed in principle a 2×2 MIMO link providing capacities of 10bits/s/Hz over a bandwidth of 6GHz. Using a second experimental set-up it was shown that the system could feasibly support at least up to a 4×4 case over 2km of MMF with a condition number $\leq$15dB over a bandwidth of 3GHz, indicating a high degree of separability of the channels.

Finally, it was shown experimentally that when a fibre contains sharp bends (bend radius between 7.2mm and 20mm) the first 6 mode-groups used for multiplexing exhibit no additional power loss or cross-coupling compared with unbent fibre, although mode-groups 7, 8 and 9 are more severely affected. This indicates that at least 6×6 multiplexing is possible in standard fibre installations potentially involving tight fibre bends. Furthermore, this empirically determined knowledge of the effect of fibre bending on different propagation modes in real fibres could be used to create low-cost modally selective filters for future mode multiplexing systems.

The demonstration of this technique is very important as it offers a way of implementing MIMO DAS with larger numbers of spatial streams over record distances of MMF. This method does not require the installation of additional fibre to support additional spatial streams. It does, however, require further equipment at both ends of the link to implement the multiplexing scheme. Furthermore, this technique also has an important role to play in improving the transfer speed of digital data over fibre, an application with enormous potential.

Overall, in this dissertation several important new wireless infrastructure technologies and design methods were introduced and experimentally verified. These all represent advances in our ability to design wireless infrastructure capable of delivering ultra-high data rates to large numbers of wireless users – one of the biggest challenges in telecommunications today.

6.2 Areas of Future Research

So far this work has shown that is possible to effectively distribute wireless MIMO signals to antennas distributed around a building using both fibre optic and free-space optical links, and that doing so greatly enhances the wireless capacity available to users. This is a critically important step in redesigning wireless infrastructure to prevent networks being crippled by overwhelming user demand for data.

However, this work also forms a starting point for a diverse range of future research areas.

Dynamically reconfigurable, intelligent DAS

This newly gained insight into how DAS can exploit MIMO, combined with the ability to create low-cost and dense networks of distributed antennas using free-space optical links, opens the possibility of creating vast scale intelligent DAS serving multiple users from multiple base stations over a large area. In conventional wireless networks each radio transceiver serves a fixed geographical area or cell. It should be possible to dynamically alter this cell configuration based on demand, hence making the DAS 'intelligent'. Cells would be able to overlap with one another creating 'cells within cells' in response to spikes in user demand at particular locations – for example 300 people disembarking a plane at an airport. If users were more dispersed, the configuration could be changed to create a uniform ultra-dense network of high-speed cells – a configuration made economically feasible by radio over free-space optics links.

This will blur the boundaries of traditional cell-based wireless network design as these new intelligent networks gain the ability to dynamically create cells of varying shape, size, location and capacity. Not only will this lead to substantial improvements in available capacity but it also provides a new way to optimise energy efficiency – for example, in times of reduced demand some base stations could be switched off while the others cover a larger area. Further still, this opens up the possibility of utilising this network of distributed antennas as a large antenna array with hundreds – even thousands – of elements, creating an advanced *large scale antenna systems (LSAS)*. These antennas can be coordinated together to create highly directed radio signals, much like focussed beams of light [232]. This opens up the possibility of making substantial improvements in signal quality as well as the energy efficiency of such networks.

Mode-multiplexing for data communications

Another important development will be the extension of the mode multiplexing system described in Chapter 5 to increase the data capacity limits of multimode optical fibre. This will be of immense importance in backhaul links of mobile networks, where data from many wireless cells is aggregated requiring extremely high speeds. Although it is currently possible to measure the modal transfer matrix of the first 45 modes in an OM2 standard fibre, only two of these modes (or two linear combinations of modes) have been used simultaneously to transport data. This means that in practical terms our current system at most doubles the number of independent data channels in a fibre, and hence doubles the capacity. It should be possible to extend this to its full potential of as much as 8-10 independent channels by designing a new transmitter module capable of taking as input 8-10 optical streams and then using composite phase masks to excite different modes of the fibre with each of these streams. An example set-up to achieve this is illustrated in Figure 6.1. This system will also have hugely important implications in digital data transfer applications as it represents a whole new degree of freedom that can be exploited to maximise capacity.

This extended mode multiplexing system can be created with just two SLMs (one at the transmitter, one at the receiver) meaning it can be both low-cost and readily extendible to a larger number of streams. The system also has the potential to adapt itself to the individual properties of a particular fibre allowing optimal performance for a wide range of different optical fibres. This means that existing fibre infrastructure in buildings can be exploited to its maximum potential and the need for potentially costly new installations is reduced.

High-speed optical wireless links

Free-space optical links have further potential to bridge the shortfall in wireless capacity when used in the very last leg of a communication link: delivering data directly to end users. Such optical wireless systems could offer data rates of up to 1 terabit per second - over 1000 times what radio wireless can offer [95].

Work has been published on the possibility of implementing optical wireless using LED lighting, meaning that high-speed optical wireless could readily be made available ubiquitously at low cost [233]. There is potential to combine this new development with the MDM system described previously, putting it to a new use – modulating the shape of wavefronts to create multiple orthogonal lightbeams.

Recently, it has been shown possible to produce light in such a way that it is able to travel through space in a corkscrew (or helicoidal) path as shown in Figure 6.2. Helicoids of different pitch can be detected independently allowing a new basis over which to send multiple information streams simultaneously [95]. This is analogous to mode multiplexing in fibre, as discussed in Chapter 5, except that the propagation is not bounded and so there are many more possible

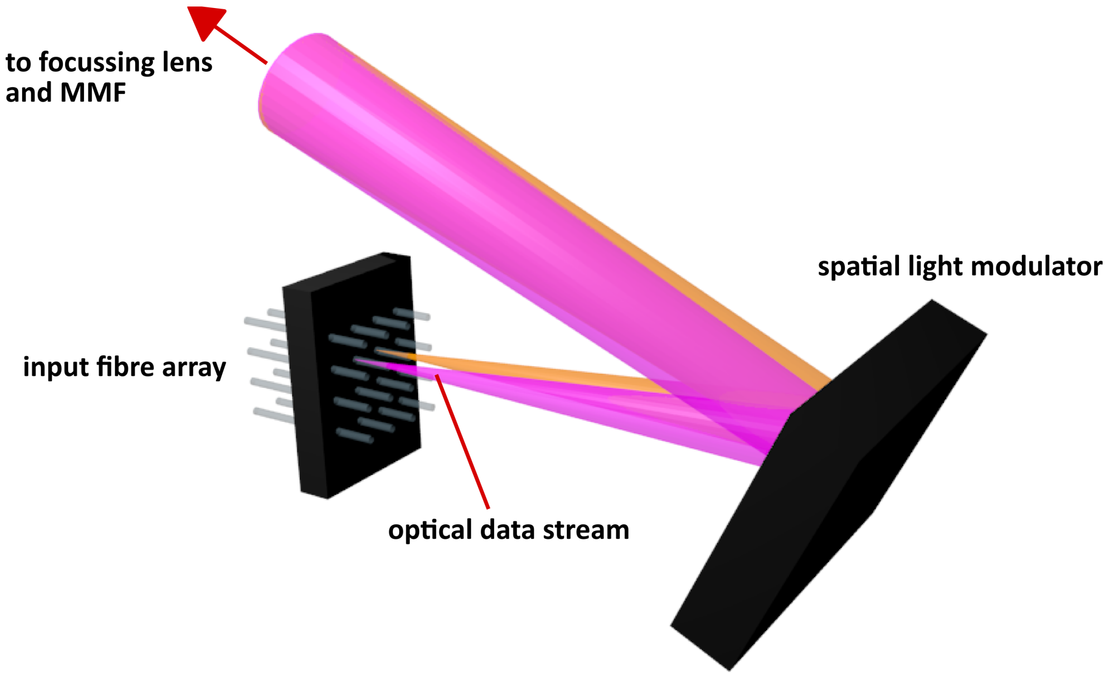

Figure 6.1: Illustration of the proposed principle for the new MDM system transmitter module. An SLM applies an orthogonal phase mask to each independent optical stream exiting a fibre array. The spatial separation of the fibres in the input array means that by superimposing gratings on the phase masks it is possible to apply different phase masks to each input stream. The resultant beams are then Fourier-transformed by a lens (not shown) and focussed onto the fibre, at which point each beam will then excite a particular combination of LP modes.

orthogonal modes. The next major challenge would be to develop a similar system capable of working using LEDs instead of lasers, making it cheaper and easier to scale.

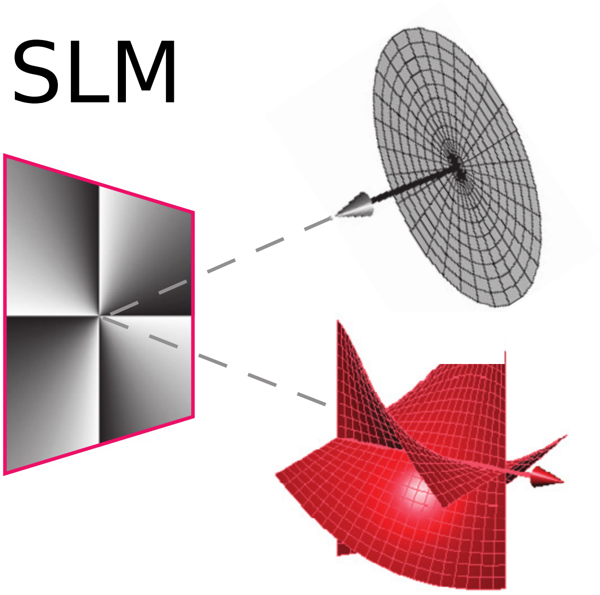

Figure 6.2: Illustration of the conversion of a conventional plane wave light beam to a twisted 'corkscrew' or helicoidal beam using a spatial light modulator (SLM), based on [95].

Modal analysis in sensing and PCB waveguide applications

Finally, the MDM system introduced in Chapter 5 has further applications in analysing the modal properties of a range of other optical waveguides. One such example is waveguides printed on circuit boards for high-speed optical buses between chips [234]. The modal properties of such links will become increasingly important as they are driven to their limits in future high speed computing applications. Knowing the modal propagation properties will enable a maximisation of the bandwidth of such links, particular if they must have sharp corners or have uneven thickness due to manufacturing constraints.

Similarly, the modal properties of exposed waveguides are also of great interest in sensing applications. When an exposed waveguide is coated with an appropriate dye, the presence of a target substance will alter the complex refractive index profile of the waveguide enabling an estimate of the concentration of that substance [235]. Currently, the optical loss occurring in such waveguides due to absorption by the dye/target substance combination is the primary concentration sensing mechanism. However, the modal propagation properties of a waveguide provide a much more comprehensive characterisation of the effect of the target substance on the refractive index. In fact, the absorption data is a subset of the full principal modal transfer matrix of such waveguides.

By doing a full modal analysis and determining the principal modes of the exposed waveguide it should be possible to greatly improve the sensitivity of such sensing systems and enable accurate calibration for determining concentration. Such devices could have great impact, for example, as portable devices used for analysing blood samples or contaminated water in remote locations.

References

[1] "Key Global Telecom Indicators for the World Telecommunication Service Sector," International Telecommuncation Union, Tech. Rep., 2011. [Online]. Available: http://www.itu.int/ITU-D/ict/statistics/at_glance/KeyTelecom.html

[2] J. Rebello, "Evolution of Standards Blurs Lines for Wireless Connectivity Applications," iSuppli Corporation, Tech. Rep., 2010. [Online]. Available: http://www.isuppli.com/Mobile-and-Wireless-Communications/Pages/Evolution-of-Standards-Blurs-Lines-for-Wireless-Connectivity-Applications.aspx?PRX

[3] "ITU Internet Reports 2005: The Internet of Things," International Telecommunications Union, Tech. Rep., 2005. [Online]. Available: http://www.itu.int/osg/spu/publications/internetofthings/

[4] R. Das and P. Harrop, "RFID Forecasts, Players & Opportunities 2006 - 2016," Tech. Rep., 2006. [Online]. Available: http://www.idtechex.com/research/reports/rfid_forecasts_players_and_opportunities_2006_2016_000137.asp

[5] "Data, data everywhere," *The Economist*, Feb. 2010.

[6] "Managing big data for smart grids and smart meters," IBM, Tech. Rep., 2012. [Online]. Available: ftp://public.dhe.ibm.com/software/pdf/industry/IMW14628USEN.pdf

[7] J. Ekholm and S. Fabre, "Forecast: Mobile Data Traffic and Revenue, Worldwide, 2010-2015," Gartner, Tech. Rep., 2011. [Online]. Available: http://www.gartner.com/DisplayDocument?ref=clientFriendlyUrl&id=1737114

[8] "Cisco Visual Networking Index : Global Mobile Data Traffic Forecast Update , 2011 2016," 2012. [Online]. Available: http://www.cisco.com/en/US/solutions/collateral/ns341/ns525/ns537/ns705/ns827/white_paper_c11-520862.pdf

[9] O. Oyman, J. Foerster, Y.-j. Tcha, and S.-c. Lee, "Toward enhanced mobile video services over WiMAX and LTE [WiMAX/LTE Update," *IEEE Communications Magazine*, vol. 48, no. 8, pp. 68–76, Aug. 2010.

[10] J. Genachowski, “The Clock is Ticking - Remarks on Broadband,” Washington, D.C., Tech. Rep., 2011. [Online]. Available: http://hraunfoss.fcc.gov/edocs_public/attachmatch/DOC-305225A1.pdf

[11] T. Norman, “Research forecast report - Wireless network traffic 2010-2015: forecasts and analysis,” Analysys Mason, Tech. Rep., 2010. [Online]. Available: http://www.analysysmason.com/Research/Custom/Reports/RDTN0_Wireless_traffic_forecast/Table-of-contents/

[12] “Visible light communication (vlc) - a potential solution to the global wireless spectrum shortage,” GBI Research, Tech. Rep., 2011.

[13] H. Friis, “A Note on a Simple Transmission Formula,” *Proceedings of the IRE*, vol. 34, no. 5, pp. 254–256, May 1946.

[14] R. Bultitude, “Measurement, Characterization and Modeling of Indoor 800/900 MHz Radio Channels for Digital Communications,” *IEEE Communications Magazine*, vol. 25, no. 6, pp. 5–12, 1987.

[15] D. Puccinelli and M. Haenggi, “Multipath fading in wireless sensor networks: measurements and interpretation,” in *Proceedings of the 2006 international conference on Wireless communications and mobile computing.* ACM, 2006, p. 1044.

[16] “Propagation data and prediction methods for the planning of indoor radiocommunication systems and radio local area networks in the frequency range 900 MHz to 100 GHz,” 2012. [Online]. Available: http://www.itu.int/rec/R-REC-P.1238-7-201202-I/en

[17] J.-P. M. G. Linmartz, *Wireless Communication, The Interactive Multimedia CD-ROM*, 1st ed. Amsterdam: Baltzer Science Publishers, 1996.

[18] C. Shannon, “Communication In The Presence Of Noise,” *Proceedings of the IEEE*, vol. 86, no. 2, pp. 447–457, Feb. 1949.

[19] “In-Building Wireless Systems to Exceed Revenue of $15 Billion by 2013, says ABI Research,” 2008. [Online]. Available: http://telecom.tekrati.com/research/10220/

[20] “United Kingdom Frequency Allocation Table,” UK office of communications, Tech. Rep. 17, 2013. [Online]. Available: http://stakeholders.ofcom.org.uk/binaries/spectrum/spectrum-information/UKFAT_2013.pdf

[21] F. Mlinarsky, M. Seymour, and P. Sangam, “The Road to 4G Wireless Agenda,” 2009. [Online]. Available: http://www.octoscope.com/English/Collaterals/Presentations/octoScope_Roadto4G_Interop_20090519.pdf

[22] D. Gesbert, M. Shafi, P. Smith, and A. Naguib, “From theory to practice: an overview of MIMO space-time coded wireless systems,” *IEEE Journal on Selected Areas in Communications*, vol. 21, no. 3, pp. 281–302, Apr. 2003.

[23] R. Stacey, E. Perahia, A. Stephens, A. Kasher, S. Trainin, M. Gong, R. Banerjea, H. Zhang, S. Srinivasa, Y. Liu, H. Ramamurthy, N. Zhang, and Y. Kim, "IEEE 802.11-09/0992r21 - IEEE P802.11 Wireless LANs Specification Framework for TGac," 2011.

[24] "Spectral Efficiency," Qualcomm, Tech. Rep., 2009. [Online]. Available: http://ecfsdocs.fcc.gov/filings/2009/12/22/6015503606.htmlhttp://apps.fcc.gov/ecfs//document/view.action?id=7020354191

[25] H. Hristov, R. Feick, and W. Grote, "Improving Indoor Signal Coverage by use of Through-Wall Passive Repeaters," in *IEEE Antennas and Propagation Society International*, 2001, pp. 158–161.

[26] D. Soldani and S. Dixit, "Wireless relays for broadband access [radio communications series]," *IEEE Communications Magazine*, vol. 46, no. 3, pp. 58–66, Mar. 2008.

[27] N. Esseling, B. Walke, and R. Pabst, "Performance Evaluation of a Fixed Relay Concept for Next Generation Wireless Systems," in *IEEE International Symposium on Personal, Indoor, and Mobile Radio Communications*, 2004, pp. 744–751.

[28] C.-X. Wang, X. Hong, X. Ge, X. Cheng, G. Zhang, and J. Thompson, "Cooperative MIMO channel models: A survey," *IEEE Communications Magazine*, vol. 48, no. 2, pp. 80–87, Feb. 2010.

[29] C. Chevallier, C. Brunner, A. Garavaglia, K. P. Murray, and K. R. Baker, *WCDMA UMTS Deployment Handbook*, C. Chevallier, C. Brunner, A. Garavaglia, K. Murray, and K. R. Baker, Eds. Chichester: John Wiley & Sons Ltd., 2006.

[30] D. Mavrakis, "Do we really need femto cells?" 2007. [Online]. Available: http://www.visionmobile.com/blog/2007/12/do-we-really-need-femto-cells/

[31] "Small Cell Market Status," informa and Small Cell Forum, Tech. Rep. 4, 2012. [Online]. Available: http://smallcellforum.org/smallcellforum/resources-white-papers

[32] A. Bleicher, "A Surge in Small Cell Sites," *IEEE Spectrum*, pp. 1–4, 2013.

[33] V. Chandrasekhar, J. Andrews, and A. Gatherer, "Femtocell networks: a survey," *IEEE Communications Magazine*, vol. 46, no. 9, pp. 59–67, Sep. 2008.

[34] A. Saleh, A. Rustako, and R. Roman, "Distributed antennas for indoor radio communications," *IEEE Transactions on Communications*, vol. 35, no. 12, pp. 1245–1251, Dec. 1987.

[35] P. Chow, A. Karim, V. Fung, and C. Dietrich, "Performance advantages of distributed antennas in indoor wireless communication systems," *Proceedings of IEEE Vehicular Technology Conference (VTC)*, no. 2, pp. 1522–1526, 1994.

[36] M. J. Crisp, "Radio Over Fibre Distributed Antenna Networks," Doctor of Philosophy, University of Cambridge, 2009.

[37] R. Heath, S. Peters, and K. LLC, "A Current Perspective on Distributed Antenna Systems for the Downlink of Cellular Systems," *IEEE Communications Magazine*, no. April, pp. 142–149, 2013.

[38] "Femtocells and Distributed Antenna Systems Complementary or Competitive?" ABI Research, Tech. Rep., 2009. [Online]. Available: http://host-68-194-68-109.ag2.uk.sharedband.net/research/1007100-Femtocells+and+Distributed+Antenna+Systems

[39] "Zinwave - Wideband active distributed antenna systems, DAS, for the wireless world indoors." [Online]. Available: www.zinwave.com

[40] P. Hartmann, X. Qian, R. Penty, and I. White, "Broadband multimode fibre (MMF) based IEEE 802.11a/b/g WLAN distribution system," in *2004 IEEE International Topical Meeting on Microwave Photonics (IEEE Cat. No.04EX859)*, vol. onpp. IEEE, 2004, pp. 173–176.

[41] M. J. Crisp, S. Li, R. Penty, A. Watts, and I. H. White, "Uplink and Downlink Coverage Improvements of 802.11g Signals Using a Distributed Antenna Network," *Journal of Lightwave Technology*, vol. 25, no. 11, pp. 3388–3395, Nov. 2007.

[42] H. Xia, a.B. Herrera, S. Kim, and F. Rico, "A CDMA-distributed antenna system for in-building personal communications services," *IEEE Journal on Selected Areas in Communications*, vol. 14, no. 4, pp. 644–650, May 1996.

[43] S. Sabesan, M. Crisp, R. V. Penty, and I. H. White, "An error free passive UHF RFID system using a new form of wireless signal distribution," in *2012 IEEE International Conference on RFID (RFID)*. IEEE, Apr. 2012, pp. 58–65.

[44] J. Winters, "Optimum Combining for Indoor Radio Systems with Multiple Users," *IEEE Transactions on Communications*, vol. 35, no. 11, pp. 1222–1230, Nov. 1987.

[45] C. Wheatley III, "Antenna system for multipath diversity in an indoor microcellular communication system," Nov. 1996. [Online]. Available: www.google.com/patents/US5577265

[46] J. Gambini, S. Savazzi, P. Castiglione, U. Spagnolini, and G. Matz, "Wireless over cable in femtocell systems: A case study from indoor channel measurements," in *2012 IEEE Wireless Communications and Networking Conference Workshops (WCNCW)*. IEEE, Apr. 2012, pp. 137–141.

[47] A. Attar, H. Li, and V. C. M. Leung, "Applications of fiber-connected distributed antenna systems in broadband wireless access," *2012 International Conference on Computing, Networking and Communications (ICNC)*, pp. 623–627, Jan. 2012.

[48] C. Ho and T. Rappaport, "Effects of antenna polarization and beam pattern on multipath delay spread and path loss in indoor obstructed wireless channels," in *1st International Conference on Universal Personal Communications - ICUPC '92 Proceedings*. Ieee, 1992, pp. 04.02/1–04.02/5.

[49] C. M. Peter Ho, T. S. Rappaport, and M. P. Koushik, "Antenna effects on indoor obstructed wireless channels and a deterministic image-based wide-band propagation model for in-building personal communication systems," *International Journal of Wireless Information Networks*, vol. 1, no. 1, pp. 61–76, Jan. 1994.

[50] X. H. Wu, S. Member, Z. N. Chen, and S. Member, "Comparison of planar dipoles in UWB applications," *IEEE Transactions on Antennas and Propagation*, vol. 53, no. 6, pp. 1973–1983, Jun. 2005.

[51] R. Nealy, W. Davis, and W. Stutzman, "Compact antennas for UWB applications," in *IEEE Conference on Ultra Wideband Systems and Technologies, 2003.* IEEE, 2003, pp. 205–208.

[52] D. Stamatelos and A. Ephremides, "Spectral efficiency and optimal base placement for indoor wireless networks," *IEEE Journal on Selected Areas in Communications*, vol. 14, no. 4, pp. 651–661, May 1996.

[53] T. Frühwirth and P. Brisset, "Optimal placement of base stations in wireless indoor telecommunication," in *Principles and Practice of Constraint ProgrammingCP98.* Springer, 1998, pp. 476–480. [Online]. Available: http://www.springerlink.com/index/JR7EH596MWQ4A297.pdf

[54] S. Haykin, "Cognitive radio: brain-empowered wireless communications," *IEEE Journal on Selected Areas in Communications*, vol. 23, no. 2, pp. 201–220, Feb. 2005.

[55] T. Yucek and H. Arslan, "A survey of spectrum sensing algorithms for cognitive radio applications," *IEEE Communications Surveys & Tutorials*, vol. 11, no. 1, pp. 116–130, 2009.

[56] S. Saunders and A. Aragon-Zavala, *Antennas and propagation for wireless communication systems.* Wiley, 2007.

[57] K. Kerpez, "A radio access system with distributed antennas," *IEEE Transactions on Vehicular Technology*, vol. 45, no. 2, pp. 265–275, May 1996.

[58] J. Zhang, G. D. L. Roche, and G. L. D. Roche, *Femtocells: Technologies and Deployment.* Chichester: Wiley & Sons Ltd., 2010.

[59] I. Stamopoulos, A. Aragon, and S. Saunders, "Performance Comparision of Distributed Antenna and Radiating Cable Systems for Cellular Indoor Environment in the DCS band," in *Twelfth International Conference on Antennas and Propagation, 2003 (ICAP 2003)*, no. 7, 2003, pp. 7–10.

[60] Y. Zhang, "Indoor radiated-mode leaky feeder propagation at 2.0 GHz," *IEEE Transactions on Vehicular Technology*, vol. 50, no. 2, pp. 536–545, Mar. 2001.

[61] A. Flatman, "In-Premises Optical Fibre Installed Base Analysis to 2007," 2007. [Online]. Available: http://www.ieee802.org/3/10GMMFSG/public/mar04/flatman_1_0304.pdf

[62] M. L. Yee, H. L. Chung, P. K. Tang, L. Ong, B. Luo, M. Zhou, Z. Shao, and M. Fujise, "850nm Radio-Over-Fiber EVM Measurements for IEEE 802.11g WLAN and Cellular Signal Distribution," in *Proceedings of the 36th European Microwave Conference*, Manchester, U.K., 2006, pp. 882–885.

[63] T.-S. Chu and M. Gans, "Fiber optic microcellular radio," *IEEE Transactions on Vehicular Technology*, vol. 40, no. 3, pp. 599–606, 1991.

[64] M. Fabbri and P. Faccin, "Radio over Fiber Technologies and Systems: New Opportunities," *2007 9th International Conference on Transparent Optical Networks*, vol. 00, pp. 230–233, Jul. 2007.

[65] P. Hartmann, "Robust transmission of RF signals over multimode fibre (MMF) beyond the fibre-bandwidth," Doctor of Philosophy, University of Cambridge, 2006.

[66] A. Krishnamoorthy, H. Schwetman, P. Koka, I. Shubin, and J. Cunningham, "Computer Systems Based on Silicon Photonic Interconnects," *Proceedings of the IEEE*, vol. 97, no. 7, pp. 1337–1361, Jul. 2009.

[67] B. Masella and X. Zhang, "Linearized Optical Single-Sideband MachZehnder Modulator for Radio-Over-Fiber Systems," *IEEE Photonics Technology Letters*, vol. 19, no. 24, pp. 2024–2026, Dec. 2007.

[68] B. Cai and A. Seeds, "Optical frequency modulation links: Theory and experiments," in *IEEE Transactions on Microwave Theory and*, vol. 45, no. 4. Ieee, Apr. 1997, pp. 505–511.

[69] C. Lim, A. Nirmalathas, M. Attygalle, D. Novak, and R. Waterhouse, "The merging of a WDM fiber-radio backbone with a 25 GHz WDM ring network," *IEEE MTT-S International Microwave Symposium Digest, 2003*, pp. 273–276, 2003.

[70] A. Chowdhury, H.-C. Chien, S.-H. Fan, J. Yu, and G.-K. Chang, "Multi-Band Transport Technologies for In-Building Host-Neutral Wireless Over Fiber Access Systems," *Journal of Lightwave Technology*, vol. 28, no. 16, pp. 2406–2415, Aug. 2010.

[71] H. Kim and Y. Chung, "Passive optical network for CDMA-based microcellular communication systems," *Journal of Lightwave Technology*, vol. 19, no. 3, pp. 301–311, Mar. 2001.

[72] "Digivance Indoor Coverage Solution 800 and 1900 MHz System Installation and Operation Manual." [Online]. Available: http://www.adc.com/us/en/Library/Techpub/75110.pdf?refer=Library&C=Wireless+Coverage+and+Capacity&L=Digivance+Indoor+Coverage+Solution

[73] T. Li, M. Crisp, R. Penty, and I. White, "Low bit rate digital radio over fibre system," in *Microwave Photonics, 2009. . . .* , 2009.

[74] P. Gamage, A. Nirmalathas, C. Lim, D. Novak, and R. Waterhouse, "Design and Analysis of Digitized RF-Over-Fiber Links," *Journal of Lightwave Technology*, vol. 27, no. 12, pp. 2052–2061, Jun. 2009.

[75] Y. Yamamoto and T. Kimura, "Coherent Optical Fiber Transmission Systems," *IEEE Journal of Quantum Electronics*, no. 6, 1981.

[76] C. H. I. Cox, *Analog Optical Links - Theory and Practice.* New York, NY, USA: Cambridge University Press, 2005, vol. 23.

[77] D. K. Mynbaev and L. L. Scheiner, *Fiber-optic communications technology.* Upper Saddle River, NJ: Prentice Hall, 2001.

[78] L. Raddatz, I. H. White, D. Cunningham, and M. C. Nowell, "An Experimental and Theoretical Study of the Offset Launch Technique for the Enhancement of the Bandwidth of Multimode Fiber Links," *Journal of Lightwave Technology*, vol. 16, no. 3, pp. 324–331, Mar. 1998.

[79] "LMR -1700 Flexible Low Loss Communications Coax." [Online]. Available: http://www.timesmicrowave.com/content/pdf/lmr/40-43.pdf

[80] X. Qian, "Optically-Amplified Radio-over-Fibre Systems," Doctor of Philosophy, University of Cambridge, 2006.

[81] G. Katz, S. Arnon, P. Goldgeier, Y. Hauptman, and N. Atias, "Cellular over optical wireless networks," *IEEE Proceedings on Optoelectronics*, vol. 153, no. 4, p. 195, 2006.

[82] L. Roselli, V. Borgioni, F. Zepparelli, F. Ambrosi, M, M. Comez, P. Faccin, and A. Casini, "Analog laser predistortion for multiservice radio-over-fiber systems," *Journal of Lightwave Technology*, vol. 21, no. 5, pp. 1211–1223, May 2003.

[83] M. J. Crisp, S. Sabesan, R. Penty, and I. H. White, "Mixed Wireless Communications and RFID Sensor Networks over Fibre," in *Microwave Photonics, 2009. MWP '09. International Topical Meeting on*, 2009.

[84] S. Hunziker and W. Baechtold, "Cellular remote antenna feeding: Optical fibre or coaxial cable?" *Electronics Letters*, vol. 34, no. 11, pp. 1038–1040, 1998.

[85] P. Yue, X. Yi, and Z.-j. Liu, "Research on Radio Frequency Assignment Mechanism of the Distributed Antenna System Based on Radio over Free Space Optics Technology," in *2010 IEEE Asia-Pacific Services Computing Conference*, no. Im. Ieee, Dec. 2010, pp. 526–530.

[86] H. Willebrand and B. Ghuman, "Fiber optics without fiber," *IEEE Spectrum*, vol. 38, no. 8, 2001.

[87] D. Plant, M. Venditti, E. Laprise, J. Faucher, K. Razavi, M. Teauneuf, A. Kirk, and J. Ahearn, "256-channel bidirectional optical interconnect using VCSELs and photodiodes on CMOS," *Journal of Lightwave Technology*, vol. 19, no. 8, p. 1093, 2001.

[88] P. Chen, S. Chang, S. Shuen-Te Ji, H. Lin, H. Tsay, P. Huang, W. Chiang, W. Lin, S. Lee, H. Tsao, and Others, "Demonstration of 16 channels 10 Gb/s WDM free space transmission over 2.16 km," *IEEE/LEOS Summer Topical Meetings, 2008 Digest of the*, pp. 235–236, 2008.

[89] "Canobeam DT-150 HD," 2008. [Online]. Available: http://www.usa.canon.com/html/industrial_bctv/pdf/CanobeamChallengeSheets(6.17.08).pdfhttp://www.usa.canon.com/html/industrial_bctv/pdf/CanobeamChallengeSheets(6.17.08).pdf

[90] "SONAbeam by fSONA." [Online]. Available: http://www.fsona.com/technology.php

[91] "LightPointe FlightStrata G," 2006. [Online]. Available: http://www.lightpointe.com/products/fs_g_carrier.cfm

[92] P. Gatenby and M. Grant, "Optical intersatellite links," *Electronics & Communication Engineering Journal*, vol. 3, no. 6, 1991.

[93] S. Williams, "IrDA: past, present and future," *IEEE Personal Communications*, vol. 38, no. 2, pp. 155–61, Aug. 2000.

[94] F. Gfeller and U. Bapst, "Wireless in-house data communication via diffuse infrared radiation," *Proceedings of the IEEE*, vol. 67, no. 11, pp. 1474–1486, 1979.

[95] J. Wang, J.-y. Yang, I. M. Fazal, N. Ahmed, Y. Yan, H. Huang, Y. Ren, Y. Yue, S. Dolinar, M. Tur, and A. E. Willner, "Terabit free-space data transmission employing orbital angular momentum multiplexing," *Nature Photonics*, vol. 6, no. 7, pp. 488–496, Jun. 2012.

[96] "Visible Light Communications Consortium." [Online]. Available: www.vlcc.net

[97] S. Bloom, E. Korevaar, J. Schuster, and H. Willebrand, "Understanding the performance of free-space optics [Invited]," *Journal of optical networking*, vol. 2, no. 6, pp. 178–200, 2003.

[98] C.-C. Chen and C. Gardner, "Impact of random pointing and tracking errors on the design of coherent and incoherent optical intersatellite communication links," *IEEE Transactions on Communications*, vol. 37, no. 3, pp. 252–260, Mar. 1989.

[99] A. Harris and T. Giuma, "Divergence and Power Variations in Mobile Free-Space Optical Communications," *Third International Conference on Systems (icons 2008)*, pp. 174–178, 2008.

[100] A. Acampora, S. Bloom, and S. Krishnamurthy, "UniNet: a hybrid approach for universal broadband access using small radio cells interconnected by free-space optical links," *IEEE Journal on Selected Areas in Communications*, vol. 16, no. 6, pp. 973–987, 1998.

[101] "IEC 60825-1 Safety of laser products Part 1: Equipment classification and requirements," 2007.

[102] T. Eitane, R. Manor, and I. Haber, “Optical wireless communications realignment,” Aug. 2007. [Online]. Available: www.google.com/patents/US20070031152

[103] I. I. Kim, R. Stieger, J. Koontz, C. Moursund, M. Barclay, P. Adhikari, J. Schuster, E. Korevaar, R. Ruigrok, and C. De Cusatis, “Wireless optical transmission of fast ethernet, FDDI, ATM, and ESCON protocol data using the TerraLink laser communication system,” *Optical Engineering*, vol. 37, no. 12, p. 3143, Dec. 1998.

[104] M. Jeganathan and P. Ionov, “Multi-Gigabits-per-second Optical Wireless Communications,” 2000. [Online]. Available: http://www.freespaceoptic.com/WhitePapers/Jeganathan(OpticalCrossing).pdf

[105] R. Ramirez-Iniguez and R. J. Green, “Optical antenna design for indoor optical wireless communication systems,” *International Journal of Communication Systems*, vol. 18, no. 3, pp. 229–245, 2005.

[106] E. Ciaramella, Y. Arimoto, G. Contestabile, M. Presi, A. D’Errico, V. Guarino, and M. Matsumoto, “1.28 terabit/s (32x40 Gbit/s) wdm transmission system for free space optical communications,” *IEEE Journal on Selected Areas in Communications*, vol. 27, no. 9, pp. 1639–1645, Dec. 2009.

[107] A. Scott, “Optical beam steering device,” 2002. [Online]. Available: www.google.com/patents/EP0470122B1?cl=en

[108] D. Wight, J. Heaton, B. Hughes, and J. Birbeck, “Novel phased array optical scanning device implemented using GaAs / AlGaAs technology,” *Applied Physics*, vol. 59, no. August, pp. 899–901, 1991.

[109] E. Bisaillon, D. F. Brosseau, T. Yamamoto, M. Mony, E. Bernier, D. Goodwill, D. V. Plant, and A. G. Kirk, “Free-Space Optical Link With Spatial Redundancy for Misalignment Tolerance,” *IEEE Photonics Technology Letters*, vol. 14, no. 2, pp. 242–244, 2000.

[110] D. Kedar and S. Arnon, “Urban optical wireless communication networks: the main challenges and possible solutions.” *IEEE Communications Magazine*, vol. 42, no. 5, pp. 2–7, 2004.

[111] R. Lawrence and J. Strohbehn, “A survey of clear-air propagation effects relevant to optical communications,” *Proceedings of the IEEE*, vol. 58, no. 10, pp. 1523–1545, 1970.

[112] H. H. Refai, “Transporting RF signals over free-space optical links,” *Proceedings of SPIE*, vol. 5712, pp. 46–54, 2005.

[113] F. Bucholtz, J. H. R. Burris, C. I. Moore, C. S. McDermitt, R. Mahon, M. R. Suite, J. V. Michalowicz, G. C. Gilbreath, and W. S. Rabinovich, “Statistical properties of a short analog RF free-space optical link,” in *Atmospheric Propagation VI*, L. M. W. Thomas and G. C. Gilbreath, Eds., vol. 7324, no. 1. SPIE, 2009, p. 73240D.

[114] F. Bucholtz, C. I. Moore, H. R. Burris, C. S. Mcdermitt, R. Mahon, M. R. Suite, J. V. Michalowicz, G. C. Gilbreath, and W. S. Rabinovich, "Free-Space Analog Optical Links : Systems , Performance and Statistical Properties," in *Applications of Lasers for Sensing and Free Space Communications*, 2010, p. LSMC4.

[115] K. Kazaura, T. Suzuki, K. Wakamori, M. Matsumoto, T. Higashino, K. Tsukamoto, and S. Komaki, "Experimental Demonstration of a Radio on Free Space Optics System for Ubiquitous Wireless," *Progress In Electromagnetics Research Symposium (PIERS) Online*, vol. 5, no. 3, pp. 235–240, 2009.

[116] K. Tsukamoto, T. Higashino, T. Nakamura, K. Takahashi, Y. Aburakawa, S. Komaki, K. Wakamori, T. Suzuki, K. Kazaura, A. Shah, and Others, "Development of Radio on Free Space Optics System for Ubiquitous Wireless," in *Progress In Electromagnetics Research Symposium*, Hangzhou, China, 2008, pp. 427–431.

[117] "ITU-T Rec. G.803, Architecture of transport networks based on the synchronous digital hierarchy (SDH)," Geneva, 2000.

[118] "MEF Introduces The Mobile Backhaul Initiative with First Integrated Suite to Resolve 4G/LTE Backhauls Most Costly Challenge," Metro Ethernet Forum, Los Angeles, Tech. Rep., 2012. [Online]. Available: http://www.metroethernetforum.org/MSWord_Documents/Press-Release-MEF-MBH-Initiative-2012-02-08-final.doc

[119] "Backhaul Evolution Strategies for LTE Operators," 2010. [Online]. Available: http://www.heavyreading.com/details.asp?sku_id=2534&skuitem_itemid=1255&promo_code=&aff_code=&next_url=/list.asp?page_type=all_reports

[120] L. Carter, D. Burnett, S. Drew, G. Marle, L. Hagadorn, D. Bartlett-McNeil, and N. Irvine, "Submarine cables and the oceans: connecting the world," United Nations Environment Programme World Con servation Monitoring Centre (UNEP-WCMC), Cambridge, Tech. Rep. 3, Sep. 2009. [Online]. Available: http://www.unep-wcmc.org/biodiversity-series-31_94.html

[121] D. J. Richardson, "Applied physics. Filling the light pipe." *Science (New York, N.Y.)*, vol. 330, no. 6002, pp. 327–8, Oct. 2010.

[122] J. Cai, Y. Cai, C. R. Davidson, D. G. Foursa, A. Lucero, O. Sinkin, W. Patterson, A. Pilipetskii, G. Mohs, and N. S. Bergano, "Transmission of 96100G pre-filtered PDM-RZ-QPSK channels with 300% spectral efficiency over 10,608km and 400% spectral efficiency over 4,368km," in *Optical Fiber Communication (OFC), collocated National Fiber Optic Engineers Conference, 2010 Conference on (OFC/NFOEC)*, 2010, pp. 8–10.

[123] H. R. Stuart, "Dispersive Multiplexing in Multimode Optical Fiber," *Science*, vol. 289, no. 5477, pp. 281–283, Jul. 2000.

[124] C. Oestges and B. Clerckx, *MIMO wireless communications : from real-world propagation to space-time code design*, 1st ed. Amsterdam: Elsevier, 2007.

[125] Z. Haas and M. Santoro, "A mode-filtering scheme for improvement of the bandwidth-distance product in multimode fiber systems," *Journal of Lightwave Technology*, vol. 11, no. 7, pp. 1125–1131, Jul. 1993.

[126] L. Geng, S. Lee, and K. William, "Symmetrical 2-D hermite-gaussian square launch for high bit rate transmission in multimode fiber links," *Optical Fiber . . .*, vol. 20, no. c, pp. 5–7, 2011.

[127] G. Stepniak, L. Maksymiuk, and J. Siuzdak, "Binary-Phase Spatial Light Filters for Mode-Selective Excitation of Multimode Fibers," *Journal of Lightwave Technology*, vol. 29, no. 13, pp. 1980–1987, Jul. 2011.

[128] J. Carpenter and T. D. Wilkinson, "Characterization of Multimode Fiber by Selective Mode Excitation," *Journal of Lightwave Technology*, vol. 30, no. 10, pp. 1386–1392, May 2012.

[129] C. P. Tsekrekos, M. de Boer, A. Martinez, F. M. J. Willems, and a. M. J. Koonen, "Demonstration of a Transparent 2-Input 2-Output Mode Group Diversity Multiplexing Link," *2006 European Conference on Optical Communications*, pp. 1–2, Sep. 2006.

[130] S. Berdagué and P. Facq, "Mode division multiplexing in optical fibers." *Applied optics*, vol. 21, no. 11, pp. 1950–5, Jun. 1982.

[131] R. Ryf, S. Randel, A. H. Gnauck, C. Bolle, A. Sierra, S. Mumtaz, M. Esmaeelpour, E. C. Burrows, R.-j. Essiambre, P. J. Winzer, D. W. Peckham, A. H. McCurdy, and R. Lingle, "Mode-Division Multiplexing Over 96 km of Few-Mode Fiber Using Coherent 6x6 MIMO Processing," *Journal of Lightwave Technology*, vol. 30, no. 4, pp. 521–531, Feb. 2012.

[132] J. Carpenter, B. Thomsen, and T. Wilkinson, "Degenerate Mode-Group Division Multiplexing," *Journal of Lightwave Technology*, no. c, pp. 1–1, 2012.

[133] M. Salsi, C. Koebele, D. Sperti, P. Tran, H. Mardoyan, P. Brindel, S. Bigo, A. Boutin, F. Verluise, P. Sillard, M. Astruc, L. Provost, and G. Charlet, "Mode-Division Multiplexing of 2x100 Gb/s Channels Using an LCOS-Based Spatial Modulator," *Journal of Lightwave Technology*, vol. 30, no. 4, pp. 618–623, Feb. 2012.

[134] N. Hanzawa and K. Saitoh, "Demonstration of mode-division multiplexing transmission over 10 km two-mode fiber with mode coupler," *Optical Fiber Communication Conference and Exposition (OFC/NFOEC), 2011 and the National Fiber Optic Engineers Conference*, no. c, pp. 19–21, 2011.

[135] J. Sakaguchi, B. J. Puttnam, W. Klaus, Y. Awaji, N. Wada, A. Kanno, T. Kawanishi, K. Imamura, H. Inaba, K. Mukasa, and R. Sugizaki, "19-core fiber transmission of 19100172-Gb/s SDM-WDM-PDM-QPSK signals at 305Tb/s," in *Optical Fiber Communication Conference and Exposition (OFC/NFOEC), 2012 and the National Fiber Optic Engineers Conference*, Mar. 2012, pp. 5–7.

[136] R. Ryf, A. Sierra, R. Essiambre, A. H. Gnauck, S. Randel, and M. Esmaeelpour, "Coherent 1200-km 6 x 6 MIMO Mode-Multiplexed Transmission over 3-core Microstructured Fiber," in *37th European Conference and Exposition on Optical Communications*, 2011, p. Th.13.C.1.

[137] M. Alatossava, A. Taparugssanagorn, V.-M. Holappa, and J. Ylitalo, "Measurement Based Capacity of Distributed MIMO Antenna System in Urban Microcellular Environment at 5.25 GHz," in *VTC Spring 2008 - IEEE Vehicular Technology Conference*. IEEE, May 2008, pp. 430–434.

[138] A. Chowdhury, H.-c. Chien, J. Wei, and G.-k. Chang, "Multi-service Multi-carrier Broadband MIMO Distributed Antenna Systems for In-building Optical Wireless Access," in *Optical Fiber Communication (OFC), collocated National Fiber Optic Engineers Conference, 2010 Conference on (OFC/NFOEC)*, 2010, pp. 26–28.

[139] A. van Zelst, "System for transporting multiple radio frequency signals of a multiple input, multiple output wireless communication system to/from a central processing base station," *US Patent App. 10/195,504*, 2004.

[140] K. Miyamoto, T. Tashiro, T. Higashino, K. Tsukamoto, S. Komaki, K. Hara, T. Taniguchi, J.-i. Kani, N. Yoshimoto, and K. Iwatsuki, "Experimental demonstration of MIMO RF signal transmission in RoF-DAS over WDM-PON," *2011 International Topical Meeting on Microwave Photonics jointly held with the 2011 Asia-Pacific Microwave Photonics Conference*, pp. 25–28, Oct. 2011.

[141] S. H. Lee, a. Wonfor, R. V. Penty, I. H. White, G. Busico, R. Cush, and M. Wale, "Uncooled DWDM transmission system using tunable laser sources with anti-mode-hop control protocol," *IEEE Photonic Society 24th Annual Meeting*, vol. 2, pp. 218–219, Oct. 2011.

[142] K. Zhu, M. J. Crisp, S. He, R. V. Penty, and I. H. White, "MIMO System Capacity Improvements Using Radio-over- Fibre Distributed Antenna System Technology," in *Optical Fiber Communication Conference, 2011*, 2011, pp. 6–8.

[143] R. Ibernon-Fernandez, J.-M. Molina-Garcia-Pardo, and L. Juan-Llacer, "Comparison Between Measurements and Simulations of Conventional and Distributed MIMO System," *IEEE Antennas and Wireless Propagation Letters*, vol. 7, pp. 546–549, 2008.

[144] L. Tarlazzi, P. Faccin, E. M. Vitucci, F. Fuschini, and V. Degli-Esposti, "Characterization of an Interleaved F-DAS MIMO indoor propagation channel," in *2010 Loughborough Antennas & Propagation Conference*, no. November. IEEE, Nov. 2010, pp. 505–508.

[145] W. Roh and A. Paulraj, "MIMO channel capacity for the distributed antenna," in *Proceedings IEEE 56th Vehicular Technology Conference*, vol. 2, no. 650. IEEE, 2002, pp. 706–709.

[146] E. Ohlmer, J. Hofrichter, S. Bittner, G. Fettweis, Q. Wang, H. Zhang, K. Wolf, and D. Plettemeier, "Urban Outdoor MIMO Experiments with Realistic Handset and Base Station Antennas," in *2010 IEEE 71st Vehicular Technology Conference*. Ieee, 2010, pp. 1–5.

[147] E. M. Vitucci, L. Tarlazzi, P. Faccin, and V. Degli-Esposti, "Analysis of the performance of LTE systems in an Interleaved F-DAS MIMO indoor environment," in *Antennas and Propagation (EUCAP), Proceedings of the 5th European Conference on*, Apr. 2011, pp. 2184–2186.

[148] H. Yonetani, I. Ushijima, T. Takada, and K. Shima, "Transmission characteristics of DFB laser modules for analog applications," *Journal of Lightwave Technology*, vol. 11, no. 1, pp. 147–153, 1993.

[149] A. Street, D. O'Brien, P. Stavrinou, and D. Edwards, "Indoor optical wireless systemsa review," *Optical and Quantum Electronics*, vol. 29, no. 3, pp. 349–378, 1997.

[150] H. Nyquist, "Thermal Agitation of Electric Charge in Conductors," *Phys. Rev.*, vol. 32, pp. 110–113, Jul. 1928.

[151] A. Papoulis, "High density shot noise and Gaussianity," *Journal of Applied Probability*, vol. 8, no. 1, pp. 118–127, 1971.

[152] Y. Yamamoto, "AM and FM quantum noise in semiconductor lasers–Part I: Theoretical analysis," *IEEE Journal of Quantum Electronics*, vol. 19, no. 1, pp. 34–46, Jan. 1983.

[153] J. E. Carroll, *Rate equations in semiconductor devices*. Cambridge: Cambridge University Press, 1985.

[154] G. Morthier and P. Vankwikelberge, *Handbook of Distributed Feedback Laser Diodes*. Norwood: Artech House, 1997.

[155] N. Kanaglekar, R. McIntosh, and W. Bryant, "Analysis of two-tone, third-order distortion in cascaded two-ports," *IEEE Transactions on Microwave Theory and Techniques*, vol. 36, no. 4, pp. 701–705, Apr. 1988.

[156] H. Al-Raweshidy and S. Komaki, *Radio over fiber technologies for mobile communications networks*. Artech House Boston, MA, 2002.

[157] "IEEE Standard for Information technology Telecommunications and information exchange between systems Local and metropolitan area networks Specific requirements Part 11: Wireless LAN Medium Access Control (MAC) and Physical Layer (PHY) Specifications," New York, NY, USA, 2007. [Online]. Available: http://standards.ieee.org/getieee802/download/802.11-2007.pdf

[158] "ETSI TS 125 141 V9.4.0 (2010-07) Technical Specification Universal Mobile Telecommunications System (UMTS); Base Station (BS) conformance testing (FDD) (3GPP TS 25.141 version 9.4.0 Release 9)," 2010.

[159] "IEEE Standard for Information technology Telecommunications and information exchange between systems Local and metropolitan area networks Specific requirements Part 11: Wireless LAN Medium Access Control (MAC) and Physical Layer (PHY) Specifications Am," 2009.

[160] A. Polishuk and S. Arnon, "Optical wireless communication network with adaptive transmitter array," in *Electrical and Electronics Engineers in Israel, 2002. The 22nd Convention of*, 2002, pp. 293–295.

[161] M. Abuelma'atti, "Nonlinear distortion performance of semiconductor laser diodes influenced by coherent reflected waves," *Journal of Lightwave Technology*, vol. 3, no. 6, pp. 1343–1350, 1985.

[162] G. S. D. Gordon, M. J. Crisp, R. V. Penty, and I. H. White (JLT GE), "High-Order Distortion in Directly Modulated Semiconductor Lasers in High-Loss Analogue Optical Links with Large RF Dynamic Range," *Journal of Lightwave Technology*, vol. 29, no. 23, pp. 3577–3586, 2011.

[163] G. S. D. Gordon, M. J. Crisp, R. V. Penty, and I. H. White, "Demonstration of a Low-Cost Broadband Radio over Free- Space Optics System," in *Semiconductor and Integrated Optoelectronics*, vol. 45, Cardiff, Mar. 2010.

[164] D. A. Marpaung, C. G. Roeloffzen, and W. C. van Etten, "A broadband high dynamic range analog photonic link using push-pull directly-modulated semiconductor lasers," in *2008 IEEE MTT-S International Microwave Symposium Digest.* Ieee, Jun. 2008, pp. 507–510.

[165] C. Cox, E. Ackerman, G. Betts, and J. Prince, "Limits on the performance of RF-over-fiber links and their impact on device design," *IEEE Transactions on Microwave Theory and Techniques*, vol. 54, no. 2, pp. 906–920, Feb. 2006.

[166] J. Helms, "Intermodulation and harmonic distortions of laser diodes with optical feedback," *Journal of Lightwave Technology*, vol. 9, no. 11, pp. 1567–1575, 1991.

[167] S. Ghoniemy, L. MacEachern, and S. Mahmoud, "Extended robust semiconductor laser modeling for analog optical link simulations," *IEEE Journal of Selected Topics in Quantum Electronics*, vol. 9, no. 3, pp. 872–878, May 2003.

[168] M. Haldar, K. Chia, and F. Mendis, "Dynamic considerations in overmodulation of semiconductor laser diodes," *Electronics Letters*, vol. 32, no. 7, p. 659, 1996.

[169] J. Le Bihan, "Approximate dynamic model for evaluating distortion in a semiconductor laser under overmodulation," *IEEE Photonics Technology Letters*, vol. 9, no. 3, pp. 303–305, Mar. 1997.

[170] I. Vurgaftman and J. Singh, "Dynamic instabilities in the power spectrum of deeply modulated semiconductor lasers," *Journal of Applied Physics*, vol. 76, no. 7, p. 4003, 1994.

[171] B. Wang and W. Way, "Large-signal spurious-free dynamic range due to static and dynamic clipping in direct and external modulation systems," *Journal of Lightwave Technology*, vol. 16, no. 10, pp. 1773–1785, 1998.

[172] T. Marozsak, A. Kovacs, E. Udvary, and T. Berceli, "Direct modulated lasers in radio over fiber applications," *International Topical Meeting on Microwave Photonics MWP-02*, pp. 129–132, 2002.

[173] D. M. Dobkin, *RF engineering for wireless networks: hardware, antennas, and propagation*. Boston, Mass.: Newnes, 2005.

[174] F. Bretenaker, G. Baili, M. Alouini, L. Morvan, D. Dolfi, and I. Sagnes, "Class-A semiconductor lasers for the transport and generation of optically carried RF analog signals," in *ISLC 2010 The 22nd IEEE International Semiconductor Laser Conference*, no. 978, Kyoto, Sep. 2010, pp. 188–189.

[175] P. Cruz and N. B. Carvalho, "PAPR Evaluation in Multi-Mode SDR Transceivers," *2008 38th European Microwave Conference*, no. October, pp. 1354–1357, Oct. 2008.

[176] R. L. Abrahams, "Troubleshooting Dual-Band WLAN Radios : Solutions Are Steadily Emerging To Meet The Unique Problems Encountered In The Design Of 802.11 Dual-Band Radios." *Wireless Systems Design*, 2003.

[177] G. Gordon, M. Crisp, R. Penty, and I. White, "Experimental Evaluation of Layout Designs for 3x3 MIMO-Enabled Radio-over-Fiber Distributed Antenna Systems," *IEEE Transactions on Vehicular Technology*, no. c, pp. 1–1, 2013.

[178] G. Gordon, J. Carpenter, M. Crisp, T. Wilkinson, R. Penty, and I. White, "Demonstration of Radio-over-Fibre Transmission of Broadband MIMO over Multimode Fibre using Mode Division Multiplexing," in *European Conference and Exhibition on Optical Communication*, no. 1, 2012.

[179] D. Gesbert, M. Kountouris, R. Heath Jr., C.-b. Chae, and T. Salzer, "Shifting the MIMO Paradigm," *IEEE Signal Processing Magazine*, vol. 24, no. 5, pp. 36–46, Sep. 2007.

[180] R. W. Heath Jr., T. Wu, Y. H. Kwon, and A. C. K. Soong, "Multiuser MIMO in Distributed Antenna Systems With Out-of-Cell Interference," *IEEE Transactions on Signal Processing*, vol. 59, no. 10, pp. 4885–4899, Oct. 2011.

[181] W. Feng, Y. Li, J. Gan, S. Zhou, J. Wang, and M. Xia, "On the Deployment of Antenna Elements in Generalized Multi-User Distributed Antenna Systems," *Mobile Networks and Applications*, vol. 16, no. 1, pp. 35–45, Oct. 2009.

[182] P. Kafle, A. Intarapanich, A. Sesay, J. Mcrory, and R. Davies, "Spatial correlation and capacity measurements for wideband MIMO channels in indoor office environment," *IEEE Transactions on Wireless Communications*, vol. 7, no. 5, pp. 1560–1571, May 2008.

[183] S. Büyükçorak and G. K. Kurt, "Spatial Correlation and MIMO Capacity at 2.4 GHz," *Procedia Technology*, vol. 3, pp. 9–17, Jan. 2012.

[184] D. Tse and P. Viswanath, *Fundamentals of Wireless Communication.* Cambridge: Cambridge University Press, 2005.

[185] S. Alamouti, "A simple transmit diversity technique for wireless communications," *IEEE Journal on Selected Areas in Communications*, vol. 16, no. 8, pp. 1451–1458, 1998.

[186] T. Lo, "Maximum ratio transmission," *IEEE Transactions on Communications*, vol. 47, no. 10, pp. 1458–1461, 1999.

[187] E. Telatar, "Capacity of Multi-antenna Gaussian Channels," *European Transactions on Telecommunications*, vol. 10, no. 6, pp. 585–595, Nov. 1999.

[188] A. Lozano, A. Tulino, and S. Verdú, "Mercury/waterfilling: optimum power allocation with arbitrary input constellations," in *International Symposium on Information Theory (ISIT)*, Adelaide, 2005.

[189] P. Wolniansky, G. Foschini, G. Golden, and R. Valenzuela, "V-BLAST: an architecture for realizing very high data rates over the rich-scattering wireless channel," in *1998 URSI International Symposium on Signals, Systems, and Electronics. Conference Proceedings (Cat. No.98EX167).* IEEE, 1998, pp. 295–300.

[190] G. Golden, C. Foschini, R. Valenzuela, and P. Wolniansky, "Detection algorithm and initial laboratory results using V-BLAST space-time communication architecture," *Electronics Letters*, vol. 35, no. 1, p. 14, 1999.

[191] G. Foschini, M. Gans, and J. Kahn, "Fading correlation and its effect on the capacity of multielement antenna systems," *IEEE Transactions on Communications*, vol. 48, no. 3, pp. 502–513, Mar. 2000.

[192] H. Yang and T. L. Marzetta, "Performance of Conjugate and Zero-Forcing Beamforming in Large-Scale Antenna Systems," *IEEE Journal on Selected Areas in Communications*, vol. 31, no. 2, pp. 172–179, Feb. 2013.

[193] A. F. Molisch and M. Z. Win, "Performance Analysis of Multiuser Diversity in MIMO Systems with Antenna Selection," *IEEE Transactions on Wireless Communications*, vol. 7, no. 1, pp. 15–21, Jan. 2008.

[194] H. Ozcelik, N. Czink, and E. Bonek, "What Makes a Good MIMO Channel Model?" *2005 IEEE 61st Vehicular Technology Conference*, vol. 1, no. c, pp. 156–160.

[195] A. Goldsmith, S. Jafar, N. Jindal, and S. Vishwanath, "Capacity limits of MIMO channels," *IEEE Journal on Selected Areas in Communications*, vol. 21, no. 5, pp. 684–702, Jun. 2003.

[196] G. Caire and S. Shamai, "On the achievable throughput of a multiantenna Gaussian broadcast channel," *IEEE Transactions on Information Theory*, vol. 49, no. 7, pp. 1691–1706, Jul. 2003.

[197] X. Li, M. Luo, M. Zhao, L. Huang, and Y. Yao, "Downlink Performance and Capacity of Distributed Antenna System in Multi-User Scenario," in *2009 5th International Conference on Wireless Communications, Networking and Mobile Computing.* IEEE, Sep. 2009, pp. 1–4.

[198] N. Jindal and A. Goldsmith, "Dirty-Paper Coding Versus TDMA for MIMO Broadcast Channels," *IEEE Transactions on Information Theory*, vol. 51, no. 5, pp. 1783–1794, May 2005.

[199] A.F. Molisch, M. Z. Win, J. H. Winters, and A. Molisch, "Reduced-complexity transmit/receive-diversity systems," in *IEEE VTS 53rd Vehicular Technology Conference, Spring 2001. Proceedings (Cat. No.01CH37202).* IEEE, 2001.

[200] C. Eugene, K. Sakaguchi, and K. Araki, "Experimental and analytical investigation of MIMO channel capacity in an indoor line-of-sight (LOS) environment," in *2004 IEEE 15th International Symposium on Personal, Indoor and Mobile Radio Communications (IEEE Cat. No.04TH8754).* IEEE, pp. 295–300.

[201] A. Saleh and R. Valenzuela, "A Statistical Model for Indoor Multipath Propagation," *IEEE Journal on Selected Areas in Communications*, vol. 5, no. 2, pp. 128–137, Feb. 1987.

[202] M. Mtumbuka and D. Edwards, "Investigation of tri-polarised MIMO technique," *Electronics Letters*, vol. 41, no. 3, p. 137, 2005.

[203] N. Das, T. Inoue, T. Taniguchi, and Y. Karasawa, "An experiment on MIMO system having three orthogonal polarization diversity branches in multipath-rich environment," in *IEEE 60th Vehicular Technology Conference, 2004. VTC2004-Fall. 2004*, no. 2. IEEE, 2004, pp. 1528–1532.

[204] T. Yamakami, T. Higashino, K. Tsukamoto, and S. Komaki, "An experimental investigation of applying MIMO to RoF ubiquitous antenna system," *2008 International Topical Meeting on Microwave Photonics jointly held with the 2008 Asia-Pacific Microwave Photonics Conference*, pp. 201–204, Sep. 2008.

[205] J. M. Senior, *Optical Fiber Communications*, third edit ed. Harlow: Prentice Hall, 2009.

[206] A. W. Snyder and J. D. Love, *Optical Waveguide Theory.* New York: Chapman and Hall, 1983.

[207] A. Alexeyev and T. Fadeyeva, "Optical vortices and the flow of their angular momentum in a multimode fiber," *Semiconductor Physics, Quantum Electronics & Optoelectronics*, vol. 1, no. 1, pp. 82–89, 1998.

[208] S. Fan and J. M. Kahn, "Principal modes in multimode waveguides." *Optics letters*, vol. 30, no. 2, pp. 135–7, Jan. 2005.

[209] R. Olshansky, "Mode Coupling Effects in Graded-index Optical Fibers." *Applied optics*, vol. 14, no. 4, pp. 935–45, Apr. 1975.

[210] P. F. Kolesar, E. Leichter, and A. Sengupta, "Bend Insensitive Multimode Fiber - Is The Reward Worth The Risk ?" 2011.

[211] J. Carpenter and T. D. Wilkinson, "All Optical Mode-Multiplexing Using Holography and Multimode Fiber Couplers," *Journal of Lightwave Technology*, vol. 30, no. 12, pp. 1978–1984, Jun. 2012.

[212] C. Koebele, M. Salsi, D. Sperti, P. Tran, P. Brindel, H. Mardoyan, S. Bigo, A. Boutin, F. Verluise, P. Sillard, M. Astruc, L. Provost, F. Cerou, and G. Charlet, "Two mode transmission at 2100 Gb/s, over 40 km-long prototype few-mode fiber, using LCOS-based programmable mode multiplexer and demultiplexer." *Optics express*, vol. 19, no. 17, pp. 16 593–600, Aug. 2011.

[213] M. B. Shemirani, W. Mao, R. A. Panicker, and J. M. Kahn, "Principal Modes in Graded-Index Multimode Fiber in Presence of Spatial- and Polarization-Mode Coupling," *Journal of Lightwave Technology*, vol. 27, no. 10, pp. 1248–1261, May 2009.

[214] E. A. J. Marcatili, "Bends in Optical Dielectric Guides," *Bell System Technical Journal*, vol. 48, no. 7, pp. 2103–2132, 1969.

[215] D. Marcuse, "Curvature loss formula for optical fibers," *Journal of the Optical Society of America*, vol. 66, no. 3, p. 216, Mar. 1976.

[216] M. Shemirani and J. Kahn, "Higher-Order Modal Dispersion in Graded-Index Multimode Fiber," *Journal of Lightwave Technology*, vol. 27, no. 23, pp. 5461–5468, Dec. 2009.

[217] R. Ulrich, S. C. Rashleigh, and W. Eickhoff, "Bending-induced birefringence in single-mode fibers." *Optics letters*, vol. 5, no. 6, pp. 273–5, Jun. 1980.

[218] J. Noda, K. Okamoto, and Y. Sasaki, "Polarization-maintaining fibers and their applications," *Journal of Lightwave Technology*, vol. 4, no. 8, pp. 1071–1089, 1986.

[219] "Minimum Optical Fiber Bend Radius," Corning Cable Systems LLC, Tech. Rep., 2006. [Online]. Available: http://csmedia.corning.com/CableSystems/%5CResource_Documents%5Capplication_engineering_notes_rl%5CAEN021.pdf

[220] S. R. Bickham, S. C. Garner, O. Kogan, and T. A. Hanson, "Theoretical and Experimental Studies of Macrobend Losses in Multimode Fibers," in *58th International Wire & Cable Symposium and Conference*, no. 1, 2009, pp. 1–8.

[221] W. Crossland, I. Manolis, M. Redmond, K. Tan, T. Wilkinson, M. Holmes, T. Parker, H. Chu, J. Croucher, V. Handerek, S. Warr, B. Robertson, I. Bonas, R. Franklin,

C. Stace, H. White, R. Woolley, and G. Henshall, “Holographic optical switching: the ”ROSES” demonstrator,” *Journal of Lightwave Technology*, vol. 18, no. 12, pp. 1845–1854, 2000.

[222] C. Henderson, D. Leyva, and T. Wilkinson, “Free space adaptive optical interconnect at 1.25 Gb/s, with beam steering using a ferroelectric liquid-crystal SLM,” *Journal of Lightwave Technology*, vol. 24, no. 5, pp. 1989–1997, May 2006.

[223] J. Carpenter and T. D. Wilkinson, “Computation of high-stability DC balancing scheme for ferroelectric liquid crystal on silicon holograms using graphics processing units,” *Opt. Lett.*, vol. 36, no. 8, pp. 1323–1325, Apr. 2011.

[224] A. Okamoto, K. Aoki, Y. Wakayama, D. Soma, and T. Oda, “Multi-Excitation of Spatial Modes using Single Spatial Light Modulator for Mode Division Multiplexing,” in *National Fiber Optic Engineers Conference*. Optical Society of America, 2012, p. JW2A.38.

[225] J. W. Goodman, *Introduction To Fourier Optics*, ser. McGraw-Hill physical and quantum electronics series. Roberts & Company, 1996.

[226] J. Carpenter, “Graphics processing unitaccelerated holography by simulated annealing,” *Optical Engineering*, vol. 49, no. 9, p. 095801, Sep. 2010.

[227] M. Born and E. Wolf, *Principles of Optics: Electromagnetic theory of propagation, interference and diffraction of light*. Cambridge: Cambridge University Press, 1980.

[228] J. Carpenter, “Holographic Mode Division Multiplexing in Optical Fibres,” Ph.D., University of Cambridge, 2012.

[229] “TIA/EIA-492AAAB: Detail Specification for 50-um Core Diameter/125-um Cladding Diameter Class Ia Graded-Index Multimode Optical Fibers.”

[230] C. H. Kwok, R. V. Penty, I. H. White, and D. G. Cunningham, “Novel Passive Launch Scheme for Ultimate Bandwidth Improvement of Graded-Index Multimode Fibers,” *Optical Fiber Communication Conference*, p. OWA3, 2010.

[231] N. Riesen and J. D. Love, “Design of mode-sorting asymmetric Y-junctions,” *Applied Optics*, vol. 51, no. 15, p. 2778, May 2012.

[232] T. L. Marzetta, “Noncooperative Cellular Wireless with Unlimited Numbers of Base Station Antennas,” *IEEE Transactions on Wireless Communications*, vol. 9, no. 11, pp. 3590–3600, Nov. 2010.

[233] L. Hanzo, H. Haas, S. Imre, D. O’Brien, M. Rupp, and L. Gyongyosi, “Wireless Myths, Realities, and Futures: From 3G/4G to Optical and Quantum Wireless,” *Proceedings of the IEEE*, vol. 100, no. Special Centennial Issue, pp. 1853–1888, May 2012.

[234] N. Bamiedakis, J. Beals, R. Penty, and I. H. White, “Cost-Effective Multimode Polymer Waveguides for High-Speed On-Board Optical Interconnects,” *IEEE Journal of Quantum Electronics*, vol. 45, no. 4, pp. 415–424, 2009.

[235] S. R. Bamiedakis, N. and Penty, R.V. and White, I.H. and Hutter, T. and Ellliott, "Low-cost PCB-integrated polymer waveguide sensor for gas detection," in *Lasers and Electro-Optics (CLEO), 2011 Conference on*, 2011.